

Contact Dynamics Modelling for Robotic Task Simulation

by

Yves Gonthier

A thesis
presented to the University of Waterloo
in fulfillment of the
thesis requirement for the degree of
Doctor of Philosophy
in
Systems Design Engineering

Waterloo, Ontario, Canada, 2007

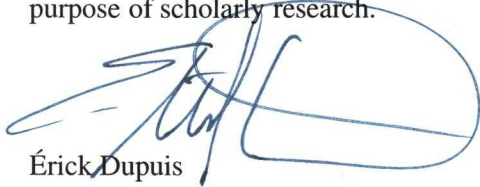
©Government of Canada, 2007

I hereby declare that I am the sole author of this thesis.



Yves Gonthier

Her Majesty the Queen in Right of Canada, acting through the Canadian Space Agency, hereby authorizes the University of Waterloo to lend this thesis to other institutions or individuals for the purpose of scholarly research.



Érick Dupuis
Robotics Section Manager
Canadian Space Agency

Her Majesty the Queen in Right of Canada, acting through the Canadian Space Agency, hereby authorizes the University of Waterloo to reproduce this thesis by photocopying or other means, in total or in part, at the request of other institutions or individuals for the purpose of scholarly research.



Érick Dupuis
Robotics Section Manager
Canadian Space Agency

Abstract

This thesis presents the theoretical derivations and the implementation of a contact dynamics modelling system based on compliant contact models. The system was designed to be used as a general-purpose modelling tool to support the task planning process space-based robot manipulator systems. This operational context imposes additional requirements on the contact dynamics modelling system beyond the usual ones of fidelity and accuracy. The system must not only be able to generate accurate and reliable simulation results, but it must do it in a reasonably short period of time, such that an operations engineer can investigate multiple scenarios within a few hours. The system is easy to interface with existing simulation facilities. All physical parameters of the contact model can be identified experimentally or can be obtained by other means through analysis or theoretical derivations based on the material properties. Similarly, the numerical parameters can be selected automatically or by using heuristic rules that give an indication of the range of values that would ensure that the simulations results are qualitatively correct. The contact dynamics modelling system is comprised of two contact models.

On one hand, a point contact model is proposed to tackle simulations involving bodies with non-conformal surfaces. Since it is based on Hertz theory, the contacting surfaces must be smooth and without discontinuity, i.e., no corners or sharp edges. The point contact model includes normal damping and tangential friction and assumes the contact surface is very small, such that the contact force is assumed to be acting through a point. An expression to set the normal damping as a function of the effective coefficient of restitution is given. A new seven-parameter friction model is introduced. The friction model is based on a bristle friction model, and is adapted to the context of 3-dimensional frictional impact modelling with introduction of load-dependent bristle stiffness and damping terms, and with the expression of the bristle deformation in vectorial form. The model features a dwell-time stiction force dependency and is shown to be able to reproduce the dynamic nature of the friction phenomenon.

A second contact model based on the Winkler elastic foundation model is then proposed to deal with a more general class of geometries. This so-called volumetric contact model is suitable for a broad range of contact geometries, as long as the contact surface can be approximated as being flat. A method to deal with objects where this latter approximation is not reasonable is also presented. The effect of the contact pressure distribution across the contact surface is accounted for in the form of the rolling resistance torque and spinning friction torque. It is shown that the contact forces and moments can be expressed in terms of the volumetric properties of the *volume of interference* between the two bodies, defined as the volume spanned by the intersection of the two undeformed geometries of the colliding bodies. The properties of interest are: the volume of the volume of interference, the position of its centroid, and its inertia tensor taken about the centroid. The analysis also introduces a new way of defining the contact normal; it is shown that the contact normal must correspond to one of the eigenvectors of the inertia tensor.

The investigation also examines how the Coulomb friction is affected by the relative motion

of the objects. The concept of average surface velocity is introduced. It accounts for both the relative translational and angular motions of the contacting surfaces. The average surface velocity is then used to find dimensionless factors that relate friction force and spinning torque caused by the Coulomb friction. These latter factors are labelled the Contensou factors. Also, the radius of gyration of the moment of inertia of the volume of interference about the contact normal was shown to correlate the spinning Coulomb friction torque to the translational Coulomb friction force. A volumetric version of the seven-parameter bristle friction model is then presented. The friction model includes both the tangential friction force and spinning friction torque. The Contensou factors are used to control the behaviour of the Coulomb friction.

For both contact models, the equations are derived from first principles, and the behaviour of each contact model characteristic was studied and simulated. When available, the simulation results were compared with benchmark results from the literature. Experiments were performed to validate the point contact model using a six degrees-of-freedom manipulator holding a half-spherical payload, and coming into contact with a flat plate. Good correspondence between the simulated and experimental results was obtained.

Acknowledgements

First and foremost I would like to thank my supervisor at the University of Waterloo Prof. John McPhee. He was always supportive and encouraging. It took me a long while to wrap-up my Ph.D. research and finally write the thesis. However, John was patient enough to allow me to get through it, even though I was raising a family and working full time at the CSA, and on the STVF project in particular. I benefited greatly from his rigorous insight and would not have reached my goals without his sharp input.

I am also grateful to Prof. Paul Calamai for allowing me to enter the Ph.D. program in the Department of Systems Design Engineering. Without his support, it would not have been possible.

I also want to thank Dr. Jean-Claude Piedboeuf for encouraging me to pursue this endeavour, and for acting as my co-supervisor. He supported me throughout the years as manager of the Robotics Section, and also afterwards. I am also grateful to Erick Dupuis for allowing me to pursue the work and releasing me of my other work duties in the past months, so that I could work effectively toward completing my degree.

Many thanks go to my colleague and friend Dr. Christian Lange, for his meticulous and thorough reviews of my thesis drafts, and also for being such a supportive colleague in the work at the CSA.

My mother always encouraged me to do this Ph.D degree from the start. In the last few months, she took care of the kids after school and made sure the homework was done. Without her help, I could not have accomplished so much progress this year. *Merci maman, sans ton aide cela n'aurait pas été possible, et aussi merci pour avoir cru en moi.*

My warmest thanks go to my wife Isabella. She followed me in this crazy adventure. We moved to the Waterloo so that I could complete my course requirements when our youngest son was only two months old. Over the years, her relentless support allowed me to continue making progress, even though it often seemed that there were "more important things to do". *Isabella, sans toi, je n'aurais jamais été capable de réussir. Merci, pour toujours.*

My final words go to my two sons Julien and Sacha. I want to thank them for helping me to put everything about my life in perspective. The important things always come first, and the rest follows after. My family always comes first. *Les enfants, je vous aime. J'espère qu'un jour vous lirez ces lignes, et comprendrez que ce qui a motivé tout ce travail c'est la curiosité. Je vous vois grandir tous le jours et je retrouve en vous cette même énergie. Puisse-t-elle vous amener vers les buts que vous vous donnerez.*

Contents

1	Introduction	1
1.1	Contact Dynamics in Space	1
1.1.1	The Operation of Space-Based Robotic Systems	1
1.1.2	Robotic Task Verification Using Pure Simulation	5
1.1.3	Contact Dynamics Simulation in an Operational Context	5
1.2	Contact Dynamics Modelling System Requirements	7
1.3	Document Structure	8
1.4	Original Contributions	8
1.4.1	Point Contact Model	9
1.4.2	Volumetric Contact Model	9
1.4.3	Implementation Framework	10
2	Literature Survey	11
2.1	Contact Dynamics Modelling	11
2.1.1	Historical Background	11
2.1.2	Rigid Body Contact Models	12
2.1.3	Regularized Contact Models	13
2.2	Contact Models Based on Hertz Theory	14
2.2.1	Hertz Theory	15
2.2.2	Models Based on Hertz Theory	16
2.2.3	Collision Detection, Penetration Depth	16
2.2.4	Contact Normal	18
2.2.5	Modelling Contact Between Objects with Complex Geometries	19
2.3	An Alternative to Hertz Theory	21
2.3.1	The Winkler Elastic Foundation Model	21
2.3.2	Obtaining Volumetric Information	22
2.4	Tangential Friction Models	24
2.4.1	Historical Background	25
2.4.2	Unlubricated Friction	25

2.4.3	Lubricated Friction	27
2.4.4	Dynamics of Friction	28
2.4.5	Modelling Friction in Multibody System Simulation	29
2.5	Research Focus	30
3	Point Contact Model	31
3.1	Point Contact Model Framework	31
3.1.1	Point of Action of the Contact Model	32
3.1.2	Contact Surface Normal Projection Matrices	34
3.1.3	Contact Model Components	35
3.2	Point Contact Sub-Models	35
3.2.1	Normal Contact Force Model	36
3.2.2	Tangential Friction Force Model	42
3.3	Point Contact Model Parameters	47
3.3.1	Normal Contact Force Model	48
3.3.2	Tangential Friction Force Model	49
4	Volumetric Contact Model	53
4.1	Elastic Foundation Model	53
4.1.1	Contact Model Hypothesis	54
4.1.2	Contact Surface	55
4.1.3	Adapting the Elastic Foundation Model for Modelling Contact	57
4.2	One Deformable Body Contact Model	59
4.2.1	Contact Model Framework	60
4.2.2	Normal Force Model	70
4.2.3	Rolling Resistance Torque Model	71
4.2.4	Tangential Friction Force Model	73
4.2.5	Spinning Friction Torque Model	74
4.3	Two Deformable Body Contact Model	75
4.3.1	Contact Model Framework	76
4.3.2	Contact Plate	82
4.3.3	Normal Force Model	93
4.3.4	Rolling Resistance Torque Model	95
4.3.5	Tangential Friction Force Model	96
4.3.6	Spinning Friction Torque Model	97
4.3.7	Contact Normal	99
4.4	Volumetric Friction Model	100
4.4.1	Coulomb Friction	100
4.4.2	Average Contact Surface Velocity	102

4.4.3	Volumetric Bristle Force Model	105
4.4.4	Tangential Friction Force Model	107
4.4.5	Spinning Friction Torque Model	109
4.5	Volumetric Contact Model Parameters	111
5	Numerical Simulation Results	113
5.1	Point Contact Model	113
5.1.1	Normal Contact Model	113
5.1.2	Tangential Friction Model	114
5.1.3	Multibody Dynamics Simulations	118
5.1.4	Experimental validation	128
5.2	Volumetric Contact Model	146
5.2.1	Simple Geometry Contacts	146
5.2.2	Complex Geometry Contacts	162
6	Conclusions	173
6.1	Review of the Contributions	174
6.1.1	Point Contact Model	174
6.1.2	Volumetric Contact Model	175
6.1.3	Implementation Framework	177
6.2	General Comments	178
6.3	Future Work	179
A	Contact Model Implementation Architecture	191
A.1	Contact Model Components	191
A.1.1	Geometric-Pair Components	192
A.1.2	Force Components	194
A.1.3	Contact Model Container	194
A.2	Geometric-Pair Models for the Point Contact Model	195
A.2.1	Sphere-Plane	195
A.2.2	Sphere-Edge	196
A.2.3	Sphere-Cylinder	199
A.2.4	Sphere-Cone	201
A.3	Volumetric Contact Model	204
A.3.1	LLG Polynomial Geometry Model	205
A.3.2	Geometric and Collision Metric Functions	205
A.3.3	Contact Normal	207
A.4	Complex Geometries	208
A.5	Contact Model C-Code Examples	210

A.6 Simulink Diagram Example	212
B The Multibody Toolbox (MuT)	213
B.1 Executive Summary	213
B.2 Description	213
B.3 Framework	214

List of Tables

- 3.1 Friction model parameters. 47

- 5.1 Friction model parameter values for Bowden and Leben stick-slip simulations. 116
- 5.2 Friction model parameter values for the bouncing ball simulations. 118
- 5.3 Friction model parameter values for double pendulum simulation. 124
- 5.4 Friction model parameter values for the contact experiment. 129
- 5.5 Normal contact model parameter values for the ball impacting a table simulation. 150
- 5.6 Friction model parameter values for the ball impacting a table simulation. 150
- 5.7 Normal contact model parameter values for the Tippe-Top simulations. 164
- 5.8 Friction model parameter values for the Tippe-Top simulations. 164
- 5.9 Normal contact model parameter values for the falling battery box simulation. 166
- 5.10 Friction model parameter values for the falling battery box simulation. 167

List of Figures

- 1.1 The Special Purpose Dexterous Manipulator – Dextre. 2
- 1.2 Dextre at the tip of Canadarm2. 2
- 1.3 The STVF concept. 4

- 2.1 The Winkler elastic foundation model. 22
- 2.2 Volumic renderings of the International Space Station. 23
- 2.3 A volumic model of Dextre. 24
- 2.4 Contact topology schematic. 26
- 2.5 Fractal topology model. 27
- 2.6 A typical Stribeck curve. 28
- 2.7 The Bowden and Leben stick-slip experiment. 29

- 3.1 Point of action and penetration depth for a sphere-plane pair. 32
- 3.2 The normal and tangential components of the vector \mathbf{u} 34
- 3.3 Linear vs. hysteretic damping in a normal contact force model. 37
- 3.4 Dimensionless damping factor d as a function of e_{eff} 39
- 3.5 The asperity contact sites. 43

- 4.1 Two bodies with conformal geometries: a battery box and its worksite. 54
- 4.2 Concave and convex objects. 56
- 4.3 A sphere in contact with a corner. 56
- 4.4 The modified Winkler elastic foundation model. 57
- 4.5 The contact surface between two deformable bodies. 58
- 4.6 Parameters for the Winkler elastic foundation model. 59
- 4.7 The volume of interference and contact surface centroids. 61
- 4.8 The position vector ρ_s and its normal and tangential components. 63
- 4.9 The normal force acting on a sphere and a cube. 71
- 4.10 The rolling resistance torque acting on a sphere and a cube. 72
- 4.11 The tangential friction force acting on a sphere and a cube. 74
- 4.12 The spinning friction torque acting on a sphere and a cube. 76
- 4.13 The contact plate normal offset ρ_n 86

4.14	The contact plate normal offset ρ_n for rigid bodies.	87
4.15	The flexible plate when $k_{v,i} \approx k_{v,j}$	88
4.16	Body velocities relative to the contact plate for $k_{v,i} = k_{v,j}$	92
4.17	The Contensou effect.	102
4.18	The bristle local deformation.	106
5.1	Effective coefficient of restitution for two models of d	115
5.2	Contact force vs. indentation for various values of e_{eff}	115
5.3	The Bowden and Leben stick-slip experimental apparatus.	116
5.4	Bowden and Leben stick-slip experiment for $ \mathbf{v}_t = 0.05$ m/s.	117
5.5	Bowden and Leben stick-slip experiment for $ \mathbf{v}_t = 0.1$ m/s.	117
5.6	Bowden and Leben stick-slip experiment for $ \mathbf{v}_t = 0.15$ m/s.	118
5.7	Trajectory of the ball impacting an inclined plane.	119
5.8	Ball impacting an inclined plane: velocity components vs. time.	120
5.9	Trajectory of the ball impacting a cylinder (2D motion).	121
5.10	Ball impacting a cylinder: velocity components vs. time (2D motion).	121
5.11	Trajectory of the ball impacting a cylinder (3D motion).	122
5.12	Ball impacting a cylinder: velocity components vs. time (3D motion).	122
5.13	Ball impacting a cylinder: total system energy for 3D motion.	123
5.14	Double pendulum: schematic diagram.	123
5.15	Double pendulum: joint positions.	124
5.16	Double pendulum: joint velocities.	125
5.17	Double pendulum: X - Y plot of end-effector positions.	125
5.18	Double pendulum: dwell state s_{dw} of friction model.	126
5.19	Double pendulum: total system energy.	126
5.20	Benchmark double pendulum: case (a).	127
5.21	Benchmark double pendulum: case (b).	128
5.22	The half-sphere and the worksite force-plate.	129
5.23	The SMT and the worksite force-plate.	130
5.24	SMT-robot: frame definitions.	134
5.25	SMT joint positions (unconstrained motion).	136
5.26	SMT joint velocities (unconstrained motion).	137
5.27	SMT joint moments (unconstrained motion).	138
5.28	SMT joint moments (corrected) (unconstrained motion).	139
5.29	Cartesian position of SMT end-effector (normal motion only).	141
5.30	Worksite force-plate measurements (normal motion only).	142
5.31	Cartesian position of SMT end-effector (normal and tangential motion).	144
5.32	Worksite force-plate measurements (normal and tangential motion).	145
5.33	LLG model of the ball rolling in the cylinder.	147

5.34	Trajectory of the ball impacting a cylinder (volumetric).	148
5.35	Ball impacting a cylinder: position and velocity components vs. time (volumetric).	149
5.36	Ball impacting a cylinder: total system energy (volumetric).	149
5.37	Trajectory of the ball impacting a table.	150
5.38	Ball impacting a table: ball centre motion.	151
5.39	Ball impacting a table: forces acting at the ball centre.	152
5.40	Ball impacting a table: moments acting at the ball centre.	153
5.41	Ball impacting a table: contact normal angle relative to the Y -axis.	154
5.42	Ball impacting a table: dwell state s_{dw} of the friction model.	154
5.43	Ball impacting a table: total system energy.	155
5.44	Simulation results using ode23tb: force in Z .	156
5.45	Simulation results using ode23tb: total system energy.	157
5.46	Simulation results using ode23tb: force in Z – zoomed.	157
5.47	Simulation results using ode23tb: total system energy – zoomed.	158
5.48	Simulation results using ode3: force in Z .	158
5.49	Simulation results using ode3: total system energy.	159
5.50	Y -position of the ball centre over time.	160
5.51	Y -position of the ball centre over time – zoomed.	160
5.52	Simulation results comparison: force in Z .	161
5.53	Simulation results comparison: total system energy.	162
5.54	The Tippe-Top geometry.	163
5.55	Time-history of the inclination of the Tippe-Top (original).	164
5.56	Time-history of the inclination of the Tippe-Top (modified).	165
5.57	Time-history of the global Z -angular velocity Ω_z .	166
5.58	Cellular LLG models for a battery box and its worksite.	167
5.59	The battery box translational velocities.	168
5.60	The battery box angular velocities.	168
5.61	The battery box forces at the micro-fixtured.	169
5.62	The battery box moments at the micro-fixtured.	169
5.63	The battery box force in X – zoomed.	170
5.64	The battery box falling into the worksite.	171
A.1	Schematic diagram for the sphere-plane pair.	196
A.2	Schematic diagram for the sphere-edge pair.	197
A.3	Sphere-edge pair cross-section.	199
A.4	Schematic diagram for the sphere-cylinder pair.	201
A.5	Schematic diagram for the sphere-cone pair.	202
A.6	Sphere-cone pair cross-section in the \mathbf{p}_{cn-s} - \mathbf{a} plane.	203
A.7	C-code for a frictional sphere-cone contact model.	210

A.8	C-code for a frictionless sphere-edge contact model.	211
A.9	C-code for a frictional LLG-pair contact model.	211
A.10	Simulink diagram for the ball-cylinder simulation using the point contact model. .	212

Nomenclature

Scalars

α	· empirically determined constant that relate the normal velocity at impact to the coefficient of restitution. It is valid for a limited range of impact velocities.
θ_ϵ	· angular threshold used in the convergence test of the implementation of the inverse iteration method.
θ_n	· angular displacement about \mathbf{n} applied at \mathbf{s}_c to get the local bristle deformation at \mathbf{s} .
$\dot{\theta}_n$	· first time-derivative of θ_n .
$\dot{\theta}_{sl}$	· slip-mode angular velocity for the spinning bristle friction torque model.
$\dot{\theta}_{st}$	· stick-mode angular velocity for the spinning bristle friction torque model.
λ	· hysteresis damping factor.
λ_{HC}	· hysteresis damping factor obtained with the Hunt and Crossley model.
λ_{LN}	· hysteresis damping factor obtained with the Lankarani and Nikravesh model.
λ_n	· eigenvalue of \mathbf{J}_s or \mathbf{J}_v corresponding to the eigenvector \mathbf{n} .
μ_C	· Coulomb friction coefficient (kinetic friction).
μ_{max}	· maximum stiction coefficient value (dwell-time dependent).
μ_S	· stiction friction coefficient (static friction).
ρ_n	· magnitude of ρ_n .
$\rho_{v,n,avg}$	· average value of $\rho_{v,n}$ over the volume of interference V .
σ_0	· bristle stiffness relative to the normal load.
σ_1	· bristle damping relative to the normal load.
σ_2	· viscous damping coefficient relative to the normal load.
τ_{br}	· bristle dynamics time constant. It is equal to σ_1/σ_0 .
τ_{dw}	· dwell-time dynamics time constant.
τ_s	· magnitude of the spinning friction torque.
τ_{sc}	· magnitude of the spinning Coulomb friction torque.
τ_{max}	· maximum spinning friction torque (dwell-time dependent).
τ_r	· numerical constraint relaxation time constant.
ω_n	· magnitude of ω_n .
$\omega_{n,i}$	· magnitude of $\omega_{n,i}$.
$\omega_{n,j}$	· magnitude of $\omega_{n,j}$.
a	· damping factor in the normal contact force model.
A_c	· contact surface area.

a_i	· damping factor of the body \mathcal{B}_i normal contact force model.
a_j	· damping factor of the body \mathcal{B}_j normal contact force model.
C_ω	· Contensou factor in translation.
$C_{\omega,s}$	· stick-state dependent Contensou factor in translation.
C_v	· Contensou factor in rotation.
$C_{v,s}$	· stick-state dependent Contensou factor in rotation.
d	· dimensionless damping factor in the normal contact force model.
d_{HC}	· dimensionless damping factor in the normal contact force model obtained with the Hunt and Crossley model.
d_{LN}	· dimensionless damping factor in the normal contact force model obtained with the Lankarani and Nikravesh model.
e_{eff}	· effective coefficient of restitution.
e_{emp}	· empirically obtained coefficient of restitution.
f_k	· part of the magnitude of \mathbf{f}_n due to the stiffness of the body material deformation(s).
f_n	· magnitude of \mathbf{f}_n .
$f_{n,i}$	· magnitude of $\mathbf{f}_{n,i}$.
$f_{n,j}$	· magnitude of $\mathbf{f}_{n,j}$.
f_{max}	· maximum tangential friction force (dwell-time dependent).
h_f	· depth of the Winkler elastic foundation mattress.
h_p	· the height of contact plate with respect to \mathcal{K}_w in the direction of \mathbf{n} .
h_v	· average height of the volume of interference over the contact surface.
$h_{v,i}$	· average height of the volume of deformation of body \mathcal{B}_i over the contact surface.
$h_{v,j}$	· average height of the volume of deformation of body \mathcal{B}_j over the contact surface.
k_f	· elastic modulus of the Winkler elastic foundation.
k_l	· linear spring stiffness.
k_v	· volumetric stiffness.
$k_{v,i}$	· volumetric stiffness of body \mathcal{B}_i .
$k_{v,j}$	· volumetric stiffness of body \mathcal{B}_j .
n_i	· maximum number of iterations of the inverse iteration method implementation.
r_{gyr}	· radius of gyration of the volume-inertia tensor about \mathbf{n} .
r_i	· ratio relating the size of the volume of deformation V_i of body \mathcal{B}_i to the volume of interference V .
r_j	· ratio relating the size of the volume of deformation V_j of body \mathcal{B}_j to the volume of interference V .
r_n	· ratio used to set the eigenvector estimate for the implementation of the inverse iteration method.
s_{dw}	· dwell-stick state.
\dot{s}_{dw}	· first time-derivative of the dwell-stick state.

v_ϵ	· numerical tolerance for a small velocity.
v_{avg}	· average surface velocity.
v_{cn}	· magnitude of the component of \mathbf{v}_c in the direction of \mathbf{n} .
v_{cn}^i	· magnitude of the component of \mathbf{v}_c in the direction of \mathbf{n} at the first instant of impact.
V	· volume of the volume of interference.
V_i	· volume of deformation of body \mathcal{B}_i .
V_j	· volume of deformation of body \mathcal{B}_j .
v_n	· magnitude of the component of \mathbf{v}_r in the direction of \mathbf{n} .
v_n^i	· magnitude of the component of \mathbf{v}_r in the direction of \mathbf{n} at the first instant of impact.
v_n^o	· magnitude of the component of \mathbf{v}_r in the direction of \mathbf{n} at the last instant of the contact phase.
$v_{n,i}$	· magnitude of the component of $\mathbf{v}_{r,i}$ in the direction of \mathbf{n}_i .
$v_{n,i}^i$	· magnitude of the component of $\mathbf{v}_{r,i}$ in the direction of \mathbf{n}_i at the first instant of impact.
$v_{n,j}$	· magnitude of the component of $\mathbf{v}_{r,j}$ in the direction of \mathbf{n}_j .
$v_{n,j}^i$	· magnitude of the component of $\mathbf{v}_{r,j}$ in the direction of \mathbf{n}_j at the first instant of impact.
v_S	· Stribeck velocity.
x	· minimum distance and penetration depth measure. The value is positive when the bodies are not colliding and negative when there is inter-penetration. Contact occurs/is lost when $x = 0$.
x_r	· relaxed penetration depth.
$x_{r,o}$	· reference position of the relaxed penetration depth.
$\dot{x}_{r,o}$	· first time-derivative of $x_{r,o}$.

Functions

$\text{dir}_\epsilon(\mathbf{u}, u_\epsilon)$	· returns a unit vector along the direction of \mathbf{u} and uses the relaxed sign convention near a small tolerance u_ϵ .
$f_s(\mathbf{s})$	· total elastic foundation deformation depth of the bodies \mathcal{B}_i and \mathcal{B}_j at a point \mathbf{s} of the contact surface.
$f_{s,i}(\mathbf{s})$	· elastic foundation deformation depth of the body \mathcal{B}_i at a point \mathbf{s} of the contact surface.
$f_{s,j}(\mathbf{s})$	· elastic foundation deformation depth of the body \mathcal{B}_j at a point \mathbf{s} of the contact surface.
$f_{s,p}(\mathbf{s})$	· flexible plate deformation at the point \mathbf{s} of the contact surface.
$h_i(\boldsymbol{\rho}_i, \mathbf{n}_i)$	· height function of the surface of body \mathcal{B}_i with respect to \mathcal{K}_i measured in the direction of \mathbf{n}_i .

$h_j(\boldsymbol{\rho}_j, \mathbf{n}_j)$ · height function of the surface of body \mathcal{B}_j with respect to \mathcal{K}_j measured in the direction of \mathbf{n}_j .

$\text{sat}(\mathbf{u}, u_{\max})$ · returns a vector along the direction of \mathbf{u} and saturates its magnitude to u_{\max} when $|\mathbf{u}| > u_{\max}$.

Matrices

\mathbf{R}_i · rotation matrix giving the orientation of frame \mathcal{K}_i relative to \mathcal{K}_w .

\mathbf{R}_j · rotation matrix giving the orientation of frame \mathcal{K}_j relative to \mathcal{K}_w .

Vectors

$\boldsymbol{\theta}_n$ · angular displacement vector for a small rotation about \mathbf{n} at \mathbf{s}_c to get the local bristle deformation at \mathbf{s} .

$\dot{\boldsymbol{\theta}}_n$ · first time-derivative of $\boldsymbol{\theta}_n$.

$\boldsymbol{\rho}_i$ · position of a point \mathbf{s} on the contact surface relative to \mathcal{K}_i .

$\boldsymbol{\rho}_j$ · position of a point \mathbf{s} on the contact surface relative to \mathcal{K}_j .

$\boldsymbol{\rho}_n$ · position of the centroid \mathbf{s}_c of the surface of contact relative to the centroid \mathbf{p}_c of the volume of interference. Component of $\boldsymbol{\rho}_s$ in the direction of \mathbf{n}

$\boldsymbol{\rho}_{n,i}$ · position of the centroid $\mathbf{s}_{c,i}$ of the surface of contact relative to the centroid $\mathbf{p}_{c,i}$ of the deformation volume V_i of body \mathcal{B}_i . Component of $\boldsymbol{\rho}_{s,i}$ in the direction of \mathbf{n}_i .

$\boldsymbol{\rho}_{n,j}$ · position of the centroid $\mathbf{s}_{c,j}$ of the surface of contact relative to the centroid $\mathbf{p}_{c,j}$ of the deformation volume V_j of body \mathcal{B}_j . Component of $\boldsymbol{\rho}_{s,j}$ in the direction of \mathbf{n}_j .

$\boldsymbol{\rho}_s$ · position of a point \mathbf{s} on the contact surface relative to the centroid \mathbf{p}_c of the volume of interference.

$\boldsymbol{\rho}_{s,i}$ · position of a point \mathbf{s} on the contact surface relative to the centroid $\mathbf{p}_{c,i}$ of the deformation volume V_i of body \mathcal{B}_i .

$\boldsymbol{\rho}_{s,j}$ · position of a point \mathbf{s} on the contact surface relative to the centroid $\mathbf{p}_{c,j}$ of the deformation volume V_j of body \mathcal{B}_j .

$\boldsymbol{\rho}_t$ · position of a point \mathbf{s} on the contact surface relative to the centroid \mathbf{s}_c of the contact surface. Component of $\boldsymbol{\rho}_s$ perpendicular to the direction of \mathbf{n} .

$\boldsymbol{\rho}_{t,i}$ · position of a point \mathbf{s} on the contact surface relative to the centroid $\mathbf{s}_{c,i}$ of the contact surface. Component of $\boldsymbol{\rho}_{s,i}$ perpendicular to the direction of \mathbf{n}_i .

$\boldsymbol{\rho}_{t,j}$ · position of a point \mathbf{s} on the contact surface relative to the centroid $\mathbf{s}_{c,j}$ of the contact surface. Component of $\boldsymbol{\rho}_{s,j}$ perpendicular to the direction of \mathbf{n}_j .

$\boldsymbol{\rho}_v$ · position of a point \mathbf{p} in the volume of interference relative to the centroid \mathbf{p}_c of the volume of interference.

$\boldsymbol{\rho}_{v,n}$ · component of $\boldsymbol{\rho}_v$ in the direction of \mathbf{n} .

$\boldsymbol{\rho}_{v,t}$ · component of $\boldsymbol{\rho}_v$ perpendicular to the direction of \mathbf{n} .

$\boldsymbol{\tau}_{br}$ · bristle friction torque.

τ_i	· torque applied by the contact model to body \mathcal{B}_i .
τ_j	· torque applied by the contact model to body \mathcal{B}_j .
τ_r	· rolling resistance torque.
$\tau_{r,i}$	· rolling resistance torque from body \mathcal{B}_i .
$\tau_{r,j}$	· rolling resistance torque from body \mathcal{B}_j .
τ_s	· spinning friction torque.
$\tau_{s,i}$	· spinning friction torque from body \mathcal{B}_i .
$\tau_{s,j}$	· spinning friction torque from body \mathcal{B}_j .
τ_{sc}	· spinning Coulomb friction torque.
ω_i	· angular velocity of body \mathcal{B}_i relative to frame \mathcal{K}_w .
ω_j	· angular velocity of body \mathcal{B}_j relative to frame \mathcal{K}_w .
ω_n	· component of ω_r in the direction of \mathbf{n} .
$\omega_{n,i}$	· component of $\omega_{r,i}$ in the direction of \mathbf{n}_i .
$\omega_{n,j}$	· component of $\omega_{r,j}$ in the direction of \mathbf{n}_j .
ω_p	· angular velocity of the contact plate relative to \mathcal{K}_w .
ω_r	· relative angular velocity of body \mathcal{B}_i with respect to body \mathcal{B}_j .
$\omega_{r,i}$	· relative angular velocity of body \mathcal{B}_i with respect to the contact plate.
$\omega_{r,j}$	· relative angular velocity of body \mathcal{B}_j with respect to the contact plate.
ω_t	· component of ω_r perpendicular to the direction of \mathbf{n} .
$\omega_{t,i}$	· component of $\omega_{r,i}$ perpendicular to the direction of \mathbf{n}_i .
$\omega_{t,j}$	· component of $\omega_{r,j}$ perpendicular to the direction of \mathbf{n}_j .
\mathbf{f}_{br}	· bristle friction force.
\mathbf{f}_C	· point contact model Coulomb friction force.
\mathbf{f}_c	· contact force.
$\mathbf{f}_{c,i}$	· contact force on body \mathcal{B}_i .
$\mathbf{f}_{c,j}$	· contact force on body \mathcal{B}_j .
\mathbf{f}_i	· force applied by the contact model to body \mathcal{B}_i at \mathcal{K}_i .
\mathbf{f}_j	· force applied by the contact model to body \mathcal{B}_j at \mathcal{K}_j .
\mathbf{f}_n	· component of \mathbf{f}_c in the direction of \mathbf{n} .
$\mathbf{f}_{n,i}$	· component of $\mathbf{f}_{c,i}$ in the direction of \mathbf{n}_i .
$\mathbf{f}_{n,j}$	· component of $\mathbf{f}_{c,j}$ in the direction of \mathbf{n}_j .
\mathbf{f}_t	· component of \mathbf{f}_c perpendicular to the direction of \mathbf{n} .
$\mathbf{f}_{t,i}$	· component of $\mathbf{f}_{c,i}$ perpendicular to the direction of \mathbf{n}_i .
$\mathbf{f}_{t,j}$	· component of $\mathbf{f}_{c,j}$ perpendicular to the direction of \mathbf{n}_j .
\mathbf{f}_{tc}	· volumetric contact model Coulomb friction force.
\mathbf{n}	· normal of the contact surface pointing from body \mathcal{B}_j toward body \mathcal{B}_i .
\mathbf{n}_i	· normal of the contact surface pointing from body \mathcal{B}_i toward body \mathcal{B}_j .
\mathbf{n}_j	· normal of the contact surface pointing from body \mathcal{B}_j toward body \mathcal{B}_i .

\mathbf{p}	· position of a point in the volume of interference relative to \mathcal{K}_w .
\mathbf{p}_c	· position of the centroid the volume of interference relative to \mathcal{K}_w .
$\mathbf{p}_{c,i}$	· position of the centroid the deformation volume V_i of body \mathcal{B}_i relative to \mathcal{K}_w .
$\mathbf{p}_{c,j}$	· position of the centroid the deformation volume V_j of body \mathcal{B}_j relative to \mathcal{K}_w .
\mathbf{p}_a	· position of the point of action relative to \mathcal{K}_w .
\mathbf{r}_i	· position of frame \mathcal{K}_i relative to \mathcal{K}_w .
\mathbf{r}_j	· position of frame \mathcal{K}_j relative to \mathcal{K}_w .
\mathbf{s}	· position of a point on the contact surface relative to \mathcal{K}_w .
\mathbf{s}_c	· position of the centroid of the contact surface relative to \mathcal{K}_w .
$\mathbf{s}_{c,i}$	· position of the centroid of the contact surface of body \mathcal{B}_i relative to \mathcal{K}_w .
$\mathbf{s}_{c,j}$	· position of the centroid of the contact surface of body \mathcal{B}_j relative to \mathcal{K}_w .
\mathbf{u}	· an arbitrary vector.
\mathbf{u}_n	· component of \mathbf{u} in the direction of \mathbf{n} .
\mathbf{u}_t	· component of \mathbf{u} perpendicular to the direction of \mathbf{n} .
\mathbf{v}_i	· translational velocity of frame \mathcal{K}_i with respect to \mathcal{K}_w .
\mathbf{v}_j	· translational velocity of frame \mathcal{K}_j with respect to \mathcal{K}_w .
\mathbf{v}_c	· the relative translational velocity of body \mathcal{B}_i with respect to body \mathcal{B}_j at the centroid \mathbf{p}_c .
$\mathbf{v}_{c,i}$	· the relative translational velocity of body \mathcal{B}_i with respect to the contact plate at the centroid $\mathbf{p}_{c,i}$.
$\mathbf{v}_{c,j}$	· the relative translational velocity of body \mathcal{B}_j with respect to the contact plate at the centroid $\mathbf{p}_{c,j}$.
\mathbf{v}_{cn}	· the component of \mathbf{v}_c in the direction of \mathbf{n} .
$\mathbf{v}_{cn,i}$	· the component of $\mathbf{v}_{c,i}$ in the direction of \mathbf{n}_i .
$\mathbf{v}_{cn,j}$	· the component of $\mathbf{v}_{c,j}$ in the direction of \mathbf{n}_j .
\mathbf{v}_{ct}	· the component of \mathbf{v}_c perpendicular to the direction of \mathbf{n} .
$\mathbf{v}_{ct,i}$	· the component of $\mathbf{v}_{c,i}$ perpendicular to the direction of \mathbf{n}_i .
$\mathbf{v}_{ct,j}$	· the component of $\mathbf{v}_{c,j}$ perpendicular to the direction of \mathbf{n}_j .
\mathbf{v}_n	· the component of \mathbf{v}_r in the direction of \mathbf{n} .
$\mathbf{v}_{n,i}$	· the component of $\mathbf{v}_{r,i}$ in the direction of \mathbf{n}_i .
$\mathbf{v}_{n,j}$	· the component of $\mathbf{v}_{r,j}$ in the direction of \mathbf{n}_j .
\mathbf{v}_r	· the relative translational velocity of body \mathcal{B}_i with respect to body \mathcal{B}_j at \mathbf{p}_a (point contact model) or at a point \mathbf{s} of the contact surface (volumetric contact model).
$\mathbf{v}_{r,i}$	· the relative translational velocity of body \mathcal{B}_i with respect to the contact plate at a point \mathbf{s} of the contact surface.
$\mathbf{v}_{r,j}$	· the relative translational velocity of body \mathcal{B}_j with respect to the contact plate at a point \mathbf{s} of the contact surface.

\mathbf{v}_{sct}	· the relative velocity of body \mathcal{B}_i with respect to body \mathcal{B}_j at \mathbf{s}_c in the direction perpendicular to \mathbf{n} .
$\mathbf{v}_{\text{sct},i}$	· the relative velocity of body \mathcal{B}_i with respect to the contact plate at $\mathbf{s}_{c,i}$ in the direction perpendicular to \mathbf{n}_i .
$\mathbf{v}_{\text{sct},j}$	· the relative velocity of body \mathcal{B}_j with respect to the contact plate at $\mathbf{s}_{c,j}$ in the direction perpendicular to \mathbf{n}_j .
\mathbf{v}_t	· the component of \mathbf{v}_r perpendicular to the direction of \mathbf{n} .
$\mathbf{v}_{t,i}$	· the component of $\mathbf{v}_{r,i}$ perpendicular to the direction of \mathbf{n}_i .
$\mathbf{v}_{t,j}$	· the component of $\mathbf{v}_{r,j}$ perpendicular to the direction of \mathbf{n}_j .
\mathbf{z}	· bristle deformation.
$\dot{\mathbf{z}}$	· first time-derivative of \mathbf{z} .
\mathbf{z}_{sc}	· bristle deformation at \mathbf{s}_c .
$\dot{\mathbf{z}}_{\text{sc}}$	· first time-derivative of \mathbf{z}_{sc} .
$\dot{\mathbf{z}}_{\text{sl}}$	· slip-mode translational velocity for the tangential friction bristle force model.
$\dot{\mathbf{z}}_{\text{st}}$	· stick-mode translational velocity for the tangential friction bristle force model.

Tensors/Dyadic Operators

\mathbf{I}	· unit dyad
$\mathbf{J}_{\rho_s, \text{avg}}$	· average surface-inertia tensor.
\mathbf{J}_s	· surface inertia-tensor.
$\mathbf{J}_{s,i}$	· surface inertia-tensor for the body \mathcal{B}_i deformation.
$\mathbf{J}_{s,j}$	· surface inertia-tensor for the body \mathcal{B}_j deformation.
\mathbf{J}_t	· surface-inertia tensor expressed relative to the surface centroid \mathbf{s}_c .
\mathbf{J}_v	· moment of inertia of the volume of interference V , also called the volume-inertia tensor in the thesis.
\mathbf{N}	· projection operator projecting any vector onto \mathbf{n} .
\mathbf{T}	· projection operator projecting any vector perpendicularly \mathbf{n} .

Frames

- \mathcal{K}_w · inertial ‘world’ frame.
- \mathcal{K}_i · frame attached to body \mathcal{B}_i .
- \mathcal{K}_j · frame attached to body \mathcal{B}_j .

Names

- \mathcal{B}_i · name of the body corresponding to index i .
- \mathcal{B}_j · name of the body corresponding to index j .
- S · name of the contact surface.

Chapter 1

Introduction

1.1 Contact Dynamics in Space

This thesis presents a generic framework to include contact dynamics models into multibody simulation systems. Contact dynamics simulation is of primary interest to Canadian Space Agency (CSA) robotics community. The findings presented in this thesis are derived from the research work done by the author over the last 8 years in support of the internal research and development projects led by the Robotics Section at the CSA.

1.1.1 The Operation of Space-Based Robotic Systems

Canada's contribution to the International Space Station (ISS) endeavour is the Mobile Servicing System (MSS) (Stieber et al., 2000). A major component of the MSS is the Special Purpose Dexterous Manipulator (SPDM or Dextre) shown in Figure 1.1. While the Space Station Remote Manipulator System (SSRMS or Canadarm2) will assemble the ISS, Dextre will be required for performing maintenance tasks. Essentially, Dextre will manipulate the Orbital Replacement Units, the components of the ISS systems replaceable on orbit. Dextre will operate directly connected to the ISS or to the tip of Canadarm2, as shown in Figure 1.2. Both Canadarm2 and Dextre are tele-operated from inside the ISS. To assist the operators conducting contact operations and ensure safety, force and moment accommodation (FMA) control will be used (Nguyen et al., 1991; Aghili et al., 2001), whereby the force and moment applied by Dextre are adjusted automatically while the operator controls the velocity of the end-effector via a set of hand-controllers.

The cost and risks associated with the execution of robotic tasks around the ISS require that all procedures are verified on earth prior to their execution in space. Canada is responsible for the verification of all the tasks involving Dextre. The CSA has developed the SPDM Task Verification Facility (STVF), a series of simulation and analysis tools used for verifying the kinematics (clearance, interface reach, degrees of freedom) and dynamics (insertion forces, flexibility) of the Dextre operations. One of the main technical challenges with the STVF is the verification of the feasibility

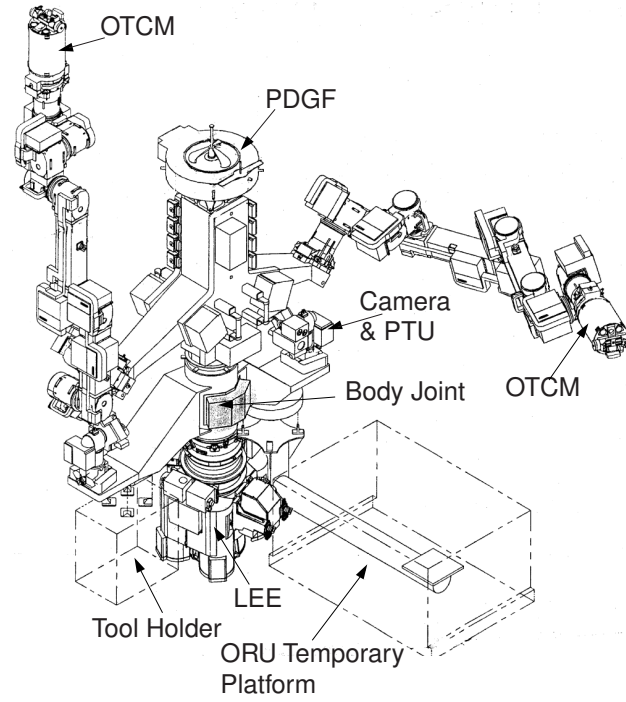


Figure 1.1: The Special Purpose Dexterous Manipulator – Dextre.

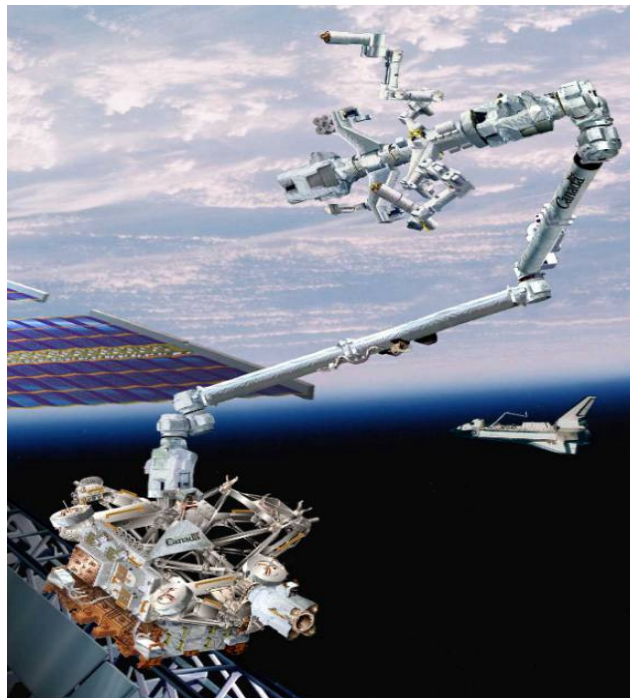


Figure 1.2: Dextre at the tip of Canadarm2.

of the insertion or extraction tasks. The forces involved are the result of complex frictional contact between the payloads and their respective worksite. A critical goal for the STVF is to be able to accurately replicate these forces by using a hardware emulator of Dextre (Piedbœuf et al., 2001).

The emulation of a space robot on ground is a challenging task because space manipulators cannot support their own weight on Earth. Different possibilities exist for the ground emulation of a space robot. The first one is to use a flat floor as done for Shuttle Remote Manipulator System. However, the motion is limited to a plane which is not representative of real contact task. A second possibility is to use a scaled-down version of the space manipulator. While attractive in theory, this is very difficult to realize in practise especially for a robot having flexibility. The third option is to use counterweights to build a system that will be dynamically equivalent to the space robot. This is an interesting option but matching the frequency response of the space robot is difficult. In addition, Dextre will often be mounted on Canadarm2 which itself is very flexible. A self-balancing system is not able to represent the flexible motion of the base. Another option is to use hardware-in-the-loop simulation (HLS) as done by the CSA (Piedbœuf et al., 1999; Aghili et al., 1999) but also by DLR¹ (Krenn and Schäfer, 1999) and NASA² (Ananthakrishnan et al., 1996). In HLS, a ground robot is driven by the output of the space robot simulator as shown in Figure 1.3.

At CSA, the HLS consists of the SMT³ robot and the MOTS⁴, a real-time simulation and visualization engine. The Dextre operator sends joystick commands to the real-time Dextre simulator that predicts a corresponding motion response. The resulting Dextre endpoint motion then becomes a set point for the SMT robot controller. The SMT performs contact operations with real hardware. Real contact forces are measured using force/moment sensors, and fed back into the simulator allowing the dynamics simulation engine to react to these external contact forces. Once the HLS has been performed, further analysis and parametric studies are done using the MDSF-NRT⁵, a non-real time high-fidelity simulator for the MSS (Ma et al., 1997).

This concept is very flexible since it can accommodate vibrations of the space robot base or other phenomena. The main difficulty in HLS is to have good performance, i.e., ensuring that the impedance of the ground robot is the same as the one of the space robot, while keeping the system stable in free space and in contact (Zhu et al., 2002; Aghili et al., 2004). This type of simulation creates instability problems similar to those encountered with force control of master/slave systems. Furthermore, the validation of a facility such as STVF is a challenging task because there exists little experimental evidence to validate against (Martin et al., 2004). In effect, the simulation of contact behaviour can be compared to experimental data only when the shape of the contacting surfaces are geometrically simple, and the data is obtained in a very controlled experiment, i.e., using only one or two dimensional motion (Sharf et al., 2002; Agar et al., 2005).

¹German Aerospace Centre (German: Deutsches Zentrum für Luft- und Raumfahrt)

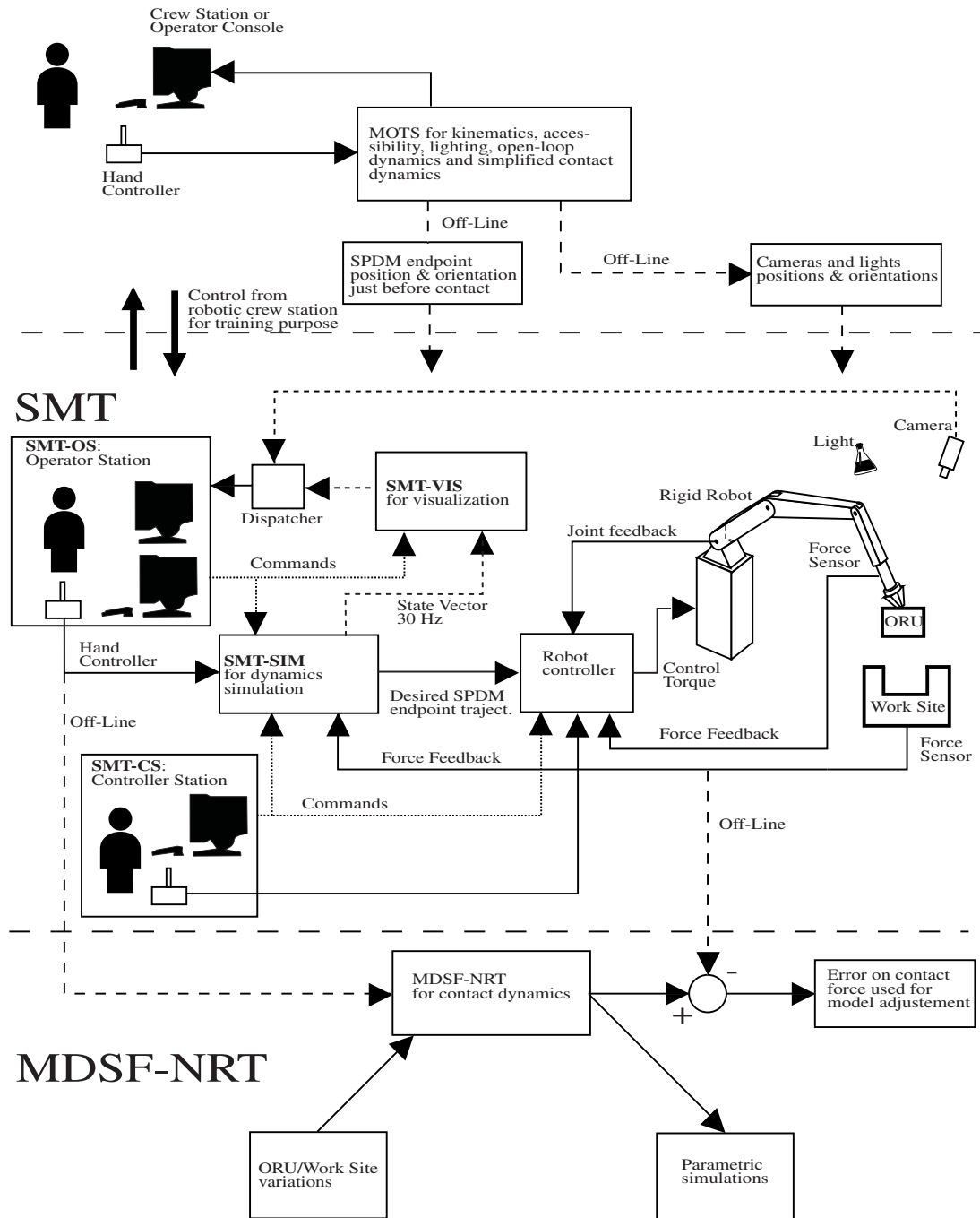
²National Aeronautics and Space Administration

³STVF Manipulator Testbed

⁴MSS Operation and Training Simulator

⁵Manipulator Development and Simulation Facility

MOTS

Figure 1.3: The STVF concept with hardware-in-the-Loop simulation.⁶

⁶Permission to reproduce this figure was given by Érick Dupuis (mailto:Erick.Dupuis@space.gc.ca), Robotics Section Manager, Canadian Space Agency.

1.1.2 Robotic Task Verification Using Pure Simulation

On the other hand, numerical simulation provides a flexible and cost-effective alternative to hardware testing (Wang et al., 2006), but entails the challenge of obtaining accurate models and their corresponding parameters for both the robotic systems comprising the MSS and the environment with which they interact. While the characterization and simulation of robotic systems is a well-understood topic, the modelling of contact dynamics is an active subject of on-going research. Validated contact models for objects with simple geometries have been around for some time (Wang and Mason, 1992). However, modelling contact between objects that have complex geometries is more difficult, particularly when friction is present.

A large spectrum of methods have been proposed to perform numerical simulations of bodies with complex shapes in contact, each tackling the contact modelling and simulation problem from a different perspective. The method that is best suited for a given problem depends on the purpose for which the simulation is being performed. In general, when selecting a particular method, a trade-off is made between accuracy and speed and/or numerical robustness.

At one end of the spectrum are the so-called “dynamics engine” targeted toward video games or computer animation systems such as *Havok*⁷, *Open Dynamics Engine*⁸, *Vortex*⁹, *PhysX*¹⁰ and *Falling Bodies*¹¹. Here, the contact modelling system is tuned for numerical robustness and speed, and is usually based on simplified rigid-body methods, one notable exception being *Falling Bodies*. They allow interactive simulations based on Newtonian physics that *look good*, but where accuracy or physical correctness is of a lesser concern.

At the other other end of the spectrum are the continuum models that allow the detailed modelling of the deformations of bodies occurring during a contact event. These models are implemented using Finite Element Methods (FEM), e.g., (Laursen and Simo, 1993; Eberhard, 1999; Puso and Laursen, 2004), and their application is restricted to non real-time simulation because of the large computational overhead associated with FEM.

1.1.3 Contact Dynamics Simulation in an Operational Context

The CSA has a team of engineers dedicated to the planning and verification of all MSS operations. These operations engineers rely heavily on multibody dynamics simulation tools to investigate and evaluate MSS mission plans. For tasks that require insertion or extraction of payloads, contact dynamics models are needed. However, the use of contact models in simulators within an operational context is a challenging task and imposes specific requirements.

On one hand, the simulation facility must produce the data in a relatively short time-frame such that the operations engineer can investigate multiple scenarios in a reasonable amount of time. If

⁷<http://www.havok.com>

⁸<http://www.ode.org>

⁹<http://www.cm-labs.com>

¹⁰<http://www.ageia.com>

¹¹<http://www.animats.com>

the investigation is done in support of a on-going space mission, then the engineer will have at most a few hours to reach the conclusion. The time constraint therefore often excludes the FEM approach as a practical alternative. On the other hand, it is imperative that the simulation results are accurate enough such that the appropriate conclusions are drawn, and in particular, that the set of selected robot control parameters will ensure mission success. In other words, the results from the robotic system simulators, including the contact dynamics models, must be reliable.

A major difficulty in implementing reliable robotic simulation system is lack of well-defined process to determine the parameters of the contact models. These parameters are typically divided in two categories: those related to physical properties of the contacting bodies, and those that are purely numerical by nature, e.g., numerical tolerances. A robust parameter-selection process would ensure that the simulated results are consistent with observed physical behaviour, or at least, it would provide a reasonably high level of confidence in the results. This process can only be established if the nature of all physical parameters is well understood and how each numerical setting affects the simulation results.

Furthermore, a contact model is always based on certain modelling assumptions, and the numerical implementation usually imposes additional restrictions. It is therefore imperative to have a good understanding of these assumptions and restrictions such that the contact model parameters are selected judiciously and that the simulation scenarios do not violate the modelling assumptions. For example, a simplified contact model may be able to compute the contact forces between the edges of two objects only when the edges are not parallel. In this case, the simulation scenario should avoid this problematic situation.

Hence, a contact modelling system designed for an operational context would need to be based on formulations that allow the physical parameters to be correlated directly with a physical behaviour, e.g., higher stiffness means less penetration. Additionally, it is best to avoid contact models that have ‘special cases’ to deal with and especially those which have problematic cases, such as the example given above. If the contact model must have degenerate cases, then these should be well identified such that they can be detected and avoided. The implementation should allow all numerical parameters to be selected automatically, or with some heuristic ‘rule-of-thumb’.

The operations engineer using a contact dynamics modelling system will expect the contact model to produce realistic contact forces, such that the simulation yields reliable results. In this context, ‘realistic’ implies that the contact forces should be physically correct, as perceived through the actuators of the robotic system, such that the simulation of the robot dynamics is accurate. Hence, the concern here is that the overall contact force felt at the joint level is correct, but that the details of how that force is obtained are irrelevant. In essence, the contact force must be physically correct only on a macroscopic scale, but must include all aspects of the physical phenomena occurring during a contact event.

Finally, the contact dynamics modelling system must be used with existing simulation facilities at the CSA. These simulation systems utilize fixed-step explicit solvers such as Runge-Kutta or

even Euler to maintain a predictable computation time. The contact models must therefore be compatible with explicit Ordinary Differential Equation (ODE) solvers.

1.2 Contact Dynamics Modelling System Requirements

The objective of this thesis is to develop a contact dynamics modelling framework that addresses the needs of engineers responsible for the MSS operations task planning. The goal is to develop a general-purpose contact modelling tool that could be used as an alternative to the currently-used contact dynamics simulation software or the STVF. The tool could also be used for other types of multibody simulations. The requirements for the proposed contact dynamics modelling system are:

- Realistic force: the model should be able to reproduce physically observed behaviour. The level of fidelity should allow accurate simulation of the dynamics of a robotic system in contact with its environment.
- Identifiable model parameters: related to a physical property and can be obtained through experiments or analysis, e.g., doing a finite element analysis to obtain the contact stiffness.
- Compatible with explicit fixed-step ODE solvers.
- Capable of handling objects with complex shapes.
- Have as few as possible numerical parameters, with clear guidelines to select these settings.
- Allow for visualization.
- Have a robust implementation where the user does not have to hand-tune parameters related to the implementation, e.g., selecting a contact normal *a priori*.
- Have a flexible implementation framework that allows different level of complexity in the contact model to be implemented easily, e.g., using more complex or simple friction models.
- Easy to implement contact geometries and easy setup of the contact model.

The contact modelling system must be accurate and allow for experimental validation, such that the numerically generated contact forces are a valid approximation of the actual forces felt by the robotic subsystems of the MSS. It should include all relevant contact phenomena that will affect the dynamic behaviour of the robotic system during tasks involving inserting or extracting an object into or from its receptacle. With trustworthy models for the contact dynamics, the operations engineer responsible for the planning of the robotic tasks will be able to select the appropriate control parameters, and in particular the FMA gains, such that a stable and predictable robot behaviour will be obtained.

1.3 Document Structure

The main focus of this thesis is the theoretical development of contact models, complete with normal damping and friction. The core of the thesis derives and presents the equations needed to implement two contact models. The contact model implementation is covered in Appendix A.

Chapter 2 reviews the state-of-the-art in modelling contacts and friction. The survey indicates that compliant contact models are well suited to meet the contact modelling system requirements given in this chapter. The focus then turns to how compliant contact models are implemented. In particular, the discussion covers the methods used to treat contact between objects with complicated geometries. A discussion of the friction phenomenon follows and a review of friction models in the literature is given.

Chapter 3 introduces a new contact model for objects that have non-conformal geometries, i.e., where the shape of the two bodies have sufficiently dissimilar profiles, such that the contact regions are small in comparison to the size of either body. Since, it is based on Hertz theory, the contacting surfaces must be smooth and without discontinuity, i.e., no corners or sharp edges. A new bristle friction model is presented that includes the modelling of the dynamics of friction.

For objects that have more complex geometries or have non-smooth features, the Hertz theory models cannot be used. An alternative contact modelling approach based on the Winkler elastic foundation model is presented in Chapter 4. The resulting so-called volumetric contact model uses information about the shape of the colliding bodies to compute the contact forces and moments acting on the contact surface. This volumetric contact model can handle contact between objects with non-smooth features and when the contact surface is small or large. A new volumetric bristle friction model, complete with tangential and spinning friction force and torque is also presented.

Chapter 5 presents numerical simulation results using the contact models presented in Chapters 3 and 4. Some results are compared to benchmark results from the literature. The behaviour of the total system energy is also examined to verify that the model effectively conserves or dissipates energy in a physically correct manner.

Chapter 6 presents a discussion on the features and possible applications of the proposed contact models. The conclusions are given and some topics are suggested to further the research.

Appendix A gives an overview of an object-oriented contact dynamics modelling infrastructure. The framework facilitates the creation of contact models by providing the necessary hooks and functionalities to automatically integrate the contact models into a numerical simulation environment. The implementation of the structure for handling contact models for complex objects—objects that include many sub-parts—is also presented.

1.4 Original Contributions

The contributions from this work fall in three categories: those related to the point and volumetric contact models, and a novel software architecture used to integrate the contact models under a

common framework.

1.4.1 Point Contact Model

Chapter 3 introduces a contact model suitable for modelling collisions between objects with non-conformal geometries. The key contributions related to this contact model are:

- A reformulation of the hysteretic damping term from the Hunt-Crossley contact model such that the normal energy dissipation is controlled via a single parameter called the damping factor. The new formulation separates the hysteresis term into its damping and stiffness parts, thereby directly relating the energy dissipation to the damping factor.
- A new expression for the damping factor as a function of the effective coefficient of restitution. The new definition is derived from the exact solution of the equation of motion of two spheres in direct central impact. It can be used to obtain the damping factor over a wide range of values of the coefficient of restitution and is not restricted to values close to unity like other previously proposed definitions.
- A new seven-parameter bristle friction model. The bristle friction model is adapted to the context of 3-dimensional frictional impact modelling with introduction of load-dependent bristle stiffness and damping terms, and with the expression of the bristle deformation in vectorial form. The model features a dwell-time stiction force dependency and is shown to be able to reproduce the dynamic nature of the friction phenomenon. Section 3.3.2 proposes methods to identify the friction model parameter or ways to simplify the friction model depending on the required level of modelling fidelity.
- Experimental validation of the contact model was performed using the STVF. Good correspondence between the simulated and experimental results was obtained. The experiments allowed the identification of the normal contact stiffness and damping as well the stiction and Coulomb friction coefficients.

1.4.2 Volumetric Contact Model

In Chapter 4, a contact model based on volumetric properties is presented. The key contributions related to this contact model are:

- The analysis of the volumetric contact model assumptions: the model properties are derived assuming the elastic behaviour of the contacting objects can be approximated using a modified Winkler elastic foundation model, and that the contact surface is approximately flat. A method to deal with the cases where this latter assumption is not valid is also presented.
- The new contact plate concept. It is introduced as a mechanism to “measure” the contact forces and torques acting between two bodies.

- The demonstration that the contact forces and moments can be expressed in terms of the volumetric properties of the *volume of interference* between the two bodies, defined as the volume spanned by the intersection of the two undeformed geometries of the colliding bodies. The properties of interest are: the volume of the volume of interference, the position of its centroid, and the inertia tensor about its centroid.
- The demonstration that the two deformable body contact model equations are in fact identical to the ones for one deformable body case, with the exception that the contact stiffness of the two deformable body contact model corresponds to an equivalent stiffness defined in terms of the stiffness of each body.
- The demonstration that the contact normal corresponds to one of the eigenvectors of the volume of interference inertia tensor.
- The new concept of average surface velocity. It gives a measure of motion that accounts for both the relative translational and angular motions.
- The finding of dimensionless factors called the *Contensou factors*. These factors relate the friction force and spinning torque caused by the Coulomb friction, and how these vary as a function of the relative motion between the bodies.
- A volumetric version of the seven-parameter bristle friction model. The friction model includes both the tangential friction force and spinning friction torque. The model uses the Contensou factors to control the behaviour of the Coulomb friction.
- A new general-purpose contact model based on volumetric properties that includes the normal contact force and damping, rolling resistance torque and tangential and spinning friction force and torque. It features a contact stiffness proportional to the contact area and leads automatically to the correct selection of the point of action of the force. This volumetric contact model can be used to model contact dynamics for a broad range of object shapes because the volumetric quantities that serve as input to the contact model can be determined for any object shape. In particular, the volumetric contact model is able to handle contacts between objects that have edges and corners, and where the dimension of the contact surface can be large with respect to the size of the objects.

1.4.3 Implementation Framework

Although it is not reported in detail in the present document, a important contribution of the work accomplished in this research is the implementation of an open-architecture and object-oriented framework that facilitates the creation of contact models based on compliance, and their integration into a numerical simulation environment. Appendix A provides more details on the framework and explains how it is used to implement a number of variations of the proposed contacts models.

Chapter 2

Literature Survey

This chapter reviews the literature on contact dynamics modelling methods for use in a multibody dynamics simulation system. The first section presents a review of the main contact modelling approaches and provides the rationale for the method selected in this work: contact models based on compliance. In Section 2.2, the Hertz theory model is reviewed and its use and limitations for modelling contact between objects with simple and complex geometries is investigated. Section 2.3 gives the background on an alternative to the Hertz theory for modelling elastic contacts: the Winkler elastic foundation model. Section 2.4 presents an analysis of the contact friction phenomena and the various models that have been proposed to model its behaviour. Finally, Section 2.5 summarizes the principal references that serve as basis for the contributions presented in this work.

2.1 Contact Dynamics Modelling

This section presents the state-of-the-art of contact modelling methods. The reviewed methods are suitable for use in an operational environment, where simulation results must be obtained quickly and reliably.

2.1.1 Historical Background

The physical phenomena occurring during the impact of two or more bodies are a topic of continuous research. Nowadays, with the aid of increasingly powerful computer hardware and advanced software the realistic modelling and fast simulation of complex impact situations of two or more bodies is feasible. Already in 1639 Marci derived first relations of impacting bodies based on experiments. Huygens found then in 1669 that for the fully elastic impact the normal velocities before and after the impact have the same magnitude but opposite direction. This kinematic relation was then extended by Newton in 1686 who derived experimentally the coefficient of restitution and postulated the impact hypothesis for central impacts with kinetic energy loss. In 1738 Euler describes the contact of two fully elastic impacting bodies with a massless spring, herewith defining

the impact as a continuous process. Poisson divides in 1835 the impact into a compression and restitution phase and postulates the impulse hypothesis, which says that the impulses in the two impact phases can be related by a coefficient of restitution.

Hertz interpreted in 1882 the elastic normal impact as a quasi-static process and derives a static solution, neglecting elastic wave propagation within the bodies. He showed that within the contact region, there is an elliptical distribution of the contact pressure. Integrating the pressure over the area, he determined the compressive reaction force. He then obtained the normal displacement at the surface of the body from the Boussinesq solution for a force applied normal to the surface of an elastic half space (Goldsmith, 1960; Timoshenko and Goodier, 1970). The resulting force approach law features a stiffness coefficient that depends on the material properties and geometries of the colliding bodies. A graphical procedure not only considering the normal but also tangential impulse changes due to friction was demonstrated by Routh in 1889. However, this graphical approach is not easily extensible to the three-dimensional case.

The motivation for contact modelling and simulation shows a great variety. For design, analysis as well as model-based control a very detailed investigation of the dynamics of complex mechanical, often multibody, systems is needed. In general, two main approaches for the description of impacts can be distinguished, those that assume the colliding bodies are perfectly rigid and those that assume some form of compliance. Depending on the application they bear certain advantages and disadvantages. A more detailed overview thereof can for instance be found in Szabó (1987) and in Lüder (2000). As indicated in Section 1.1.3, continuum models based on FEM are not included in the present analysis because of the large computational overhead associated with these methods.

2.1.2 Rigid Body Contact Models

The rigid-body approach is only concerned with the description of the global impact response, i.e., the motion after the impact depending on the motion at the beginning of the impact. Impact hypotheses are applied such as Newton's kinematic (Han and Gilmore, 1993) or Poisson's (Glocker and Pfeiffer, 1992) impulse or Stronge's (Stronge, 2000) energy based impact hypothesis, to derive a complete set of equations. Hereby, the equations of motion are derived by balancing the system's momenta before and after the impact, i.e., without explicitly considering contact compliances. This approach assumes the collision to be an instantaneous and discontinuous phenomenon, i.e., a *discrete* event, and a momentum balance is performed to calculate the velocity jumps. This is also known as piecewise analysis (Lankarani, 1996) and stereo-mechanical theory (Stronge, 2000).

Klarbring (1990) investigates a contact problem with friction involving one contact point and two degrees-of-freedom. Lankarani and Pereira (2001) classified the planar frictional impact problem in seven cases, and account for all modes of impact i.e., sliding, sticking, and reverse sliding in the compression and restitution phases. The classification is based on the pre-impact system configuration and velocities. Friction during the impact is accounted for through the introduction of a

friction impulse. Stronge (2000) introduced the concept of an infinitesimal deformable particle to obtain the changes in velocity as a function of the impulse during the infinitesimal contact period. This allows following the evolution of the contact process and variation in relative velocity across the contact patch as a function of the impulse.

Some contact dynamics simulation systems never compute the contact forces, and only use collision impulses to enforce the non-penetration constraint, i.e., the equations of motion are solved at the velocity level only (Mirtich and Canny, 1995). For lasting contact, Pfeiffer and Glocker (1996) show that the resulting dynamic equations can be setup as a linear complementary problem, where the contact accelerations are used as complementary variables to the contact force. To avoid deviations from the geometric constraints, the contact distance can be used instead of acceleration as a variable complementary to the contact force (Hotz et al., 1999). A comprehensive presentation of the rigid-body contact dynamics fundamentals is given by Glocker (2001). Sharf and Zhang (2006) propose an alternative approach for solving the non-colliding contact problem for objects of any shape. The method is also based on rigid-body dynamics but leads to an explicit closed-form solution for the normal contact force.

However, these rigid-body approaches fall short in representing the underlying impact phenomena by neglecting the small displacements during collision. Moreover, the utilized coefficient of restitution is often defined independently of the normal component of the relative velocity, which contradicts experimental measurements (Goldsmith, 1960). Also, in the case of Dextre, the manipulator itself is inherently flexible, and, when the manipulator comes into contact with its environment, the impact durations are significantly larger than the sampling period of the discrete-time control system of the manipulator. As a result, the impact duration cannot be assumed to be instantaneous. In the context of robotic operations, the time-history of the force profile is of critical importance, as it affects the ability of the robotic system to remain stable while performing contact tasks. Also, recent studies have shown that the stiffness of the contact greatly influences the stability of robotic systems under discrete-time control (Kövecses et al., 2007). Consequently, rigid body models, which assume the stiffness to be infinite, provide an inadequate reference for validating the performance of space robotic systems in contact.

2.1.3 Regularized Contact Models

The second class of contact models are the regularized contact models. The term regularized describes the reformulation of a problem to derive a solvable formulation (Lichtenberg and Liebermann, 1992). In this particular case, the regularization consists in changing the nature of the impact from a discontinuous process into a continuous one. The contact forces are described as a function of the contact deformation by smoothening the discontinuity of the impact and friction forces in the constraints (Brogliato, 1996; Vielsack, 1996). This approach is often referred to as the penalty method, whereby the model returns a measure of the constraint violation; the larger the violation, the higher the penalty.

In contrast to the contact models based on the rigid body assumption, compliant models describe the rate-dependent normal and tangential compliance relations over time. Herewith, a velocity-dependent coefficient of restitution is easily incorporated, a behaviour consistent with experimental observation (Goldsmith, 1960). These models can be easily integrated within the existing simulation systems at the CSA, which are based on standard ODE solvers. Using this contact modelling approach, it is also easy to add sophisticated friction models, such as the dwell-time dependent friction model proposed in Gonthier et al. (2004), and which will be described in detail in Section 3.2.2.

Another key feature of compliant contact models is that they naturally handle contact between flexible systems. The joints of robotic systems designed for space are usually equipped with planetary gears or harmonic drives to maximize the torque output since the available power is very limited. These gear reduction systems introduce significant joint flexibility in addition to the inherent link flexibility. These flexibilities are typically associated with some form of damping, e.g., joint viscous friction. Hence, the flexibilities affect the overall system dynamics, particularly during impacts. If the robotic systems were perfectly rigid, the impacts would be instantaneous. Instead, the real robotic systems deform during the collisions and remain in contact for significant time periods. The damping associated with the manipulator flexibilities also increases the amount of energy dissipated during the impact and therefore effectively lowers the coefficient of restitution of the impact process. These dynamic interactions are not as easily included in the discrete contact modelling approach.

Finally, the stiffness properties of the compliance can be directly related to the colliding object geometries and to the material Young's modulus. Hence, a model more related to physical quantities and thus more intuitive can be derived. For these reasons, the compliant modelling approach was selected for the proposed contact modelling method. The main difficulty in using this method lies in the fact that the resulting set of equations become numerically stiff and have very small time constants when the contact stiffness is high. But these issues are mitigated by the fact that the contact events are occurring at low velocities, and that the existing simulation facilities are designed to operate with small integration step sizes.

2.2 Contact Models Based on Hertz Theory

The discussion from the preceding section indicates that the regularized model approach is better suited to meet the requirements for the contact model specified in Section 1.2. This section looks in more detail at the literature regarding the implementation of compliant contact models in multibody simulations. These models are essentially non-linear spring models used to predict the force acting to separate the colliding bodies. This force will be hereafter called the *normal contact force* to distinguish it from the frictional forces acting in a direction tangential to the contact surface.

2.2.1 Hertz Theory

The first published work on the subject of contact mechanics was written by Hertz (1896). His analysis of the contact between two elastic bodies remains today one of the most important examples of a solution to a classical problem in the theory of elasticity. Since then, a large volume of work has been published on solving contact mechanics problem using the classical theory of elasticity.

In order to apply the theory of elasticity to the contact mechanics problem, the bodies are assumed to be homogeneous, isotropic and linearly elastic, and the plastic flows are treated quasi-statically. Solutions have been found for classical contact problems, where the colliding bodies have simple geometries such as spheres or cylinders (Gladwell, 1980; Johnson, 1985; Barber, 1992; Fischer-Cripps, 2000). Alexandroff and Pozharskii (2001) reported results for non-classical three-dimensional contact problems.

On the other hand, the use of contact models derived from Hertz theory should be restricted to contact between bodies with non-conformal geometries, i.e., where the shape of the two bodies have sufficiently dissimilar profiles, such that the contact regions are small in comparison to the size of either body. This restriction is imposed by the half-space approximation used to solve the contact mechanics problem. In this theory, the deformations are assumed negligible outside the small contact region. In these circumstances, the contact stresses comprise a local ‘stress concentration’ which can be considered independent of the stresses in the bulk of the two bodies.

The Hertz contact force law (Goldsmith, 1960; Timoshenko and Goodier, 1970) establishes that for two spheres i and j in direct-central impact, the normal contact force f_k is a function of the relative local inter-penetration (or indentation) and is given by

$$f_k = k |x|^p, \quad (2.1)$$

where the relative local inter-penetration x is defined as the maximum distance between the undeformed surfaces of the two spheres. The force-approach law based on Hertzian theory yields $p = 3/2$ when the two contacting bodies are linearly elastic spheres. The generalized parameter k depends on the material properties and the radii R_i and R_j of the spheres, i.e.,

$$k = \frac{4}{3\pi(h_{m,i} + h_{m,j})} \left(\frac{R_i R_j}{R_i + R_j} \right)^{1/2}, \quad (2.2)$$

where the material properties h_m for the spheres i and j are

$$h_{m,l} = \frac{1 - \nu_l^2}{\pi E_l} \quad \text{with } l = i, j. \quad (2.3)$$

The variables ν_l and E_l are the Poisson’s ratio and the Young’s modulus associated with each sphere respectively. Note that the form of Equation (2.1) is also valid for other types of geometries,

and that Equation (2.2) represents the special case of two elastic spheres. To model the contact force of a sphere and a plane, one of the radii is set to infinity, and Equation (2.2) simplifies to

$$k = \frac{4}{3\pi(h_{m,i} + h_{m,j})} R_i^{1/2}, \quad (2.4)$$

where i refers to the properties of the sphere and j to the properties of the plane as defined above.

2.2.2 Models Based on Hertz Theory

Typical regularized models consist of a combination of spring and damper elements with linear or nonlinear force characteristics. For direct central and frictionless impacts Hunt and Crossley (1975), Khulief and Shabana (1987), and Lankarani and Nikravesh (1988) use a continuous contact model with a local compliance in the normal direction. The energy dissipation is a function of a damping constant which can be related to the impact velocity and the coefficient of restitution e . Marhefka and Orin (1999) demonstrated the validity of the expression for the damping, and that the derived formulations are only valid for e close to unity.

Compliant contact models based on Hertz's Theory are typically expressed in the form of an equation relating the depth of inter-penetration of two bodies to the contact force. This distance is obtained using specialized geometric algorithms in order to detect the occurrence of collisions and compute some relevant metric feeding into the compliance models. These algorithms will be referred to hereafter as *collision detection* and *collision metric* algorithms. These topics are covered next.

2.2.3 Collision Detection, Penetration Depth

Many surveys have been published that discuss the techniques that have been developed to efficiently detect collisions (Lin and Gottschalk, 1998; Jimenez et al., 2001). Most of these techniques focus on the problem of detecting collisions between two or more rigid body objects that are defined either by a large set of polygons, or a set of quadratic surfaces.

The fastest methods currently available for detecting collisions between rigid body objects combine extensive preprocessing with assumptions about temporal coherence and geometric or topological properties. Other techniques make fewer assumptions about the type of objects they will be applied to. The latter use a multi-level collision detection scheme to concentrate the search to regions where collisions have a potential of occurring. To this end, bounding boxes are set up around the objects and collision tests are first performed on these simpler geometries. As a result, the heavy computational effort required for the detailed geometry collision tests is restricted to a subset of objects in close proximity. Different researchers have experimented with bounding shapes such as axis-aligned bounding boxes (AABBs), spheres, object-oriented bounding boxes (OBBs) and others; see O'Brien (2000) for a more extensive discussion on the subject.

The work presented here will focus on the detailed modelling and simulation of contact forces between arbitrary geometries and not on the high level sweep-and-prune methods. The two commonly used methods to perform the low-level geometric collision tests are: (1) an exact mathematical formulation of the contact distance between selected geometrical features of the objects, and (2) an optimization method to converge on the location of the closest point.

Closest Feature Algorithms

The main advantage of the collision detection algorithms based on closest feature detection is that they provide an *exact* measure of the contact distance. Typical feature pairs are the vertex-face pairs and edge-edge pairs found in geometries represented by a set of polygons. A good example of this type of collision detection system is *V-Clip*, which is well adapted to three dimensional collision detection system for contact dynamics simulation (Mirtich, 1998).

Closest feature algorithms can be defined for other geometric features, such as cylinders or disks (Kecskeméthy et al., 2000), but this requires a case by case analysis and is not easily applicable to any geometric feature pair. Furthermore, this approach is prone to geometric singularities and is context dependent. For example, when two disks are overlapping on each other, but not intersecting, which one is on top? Are they contacting through their surfaces or through their edges? The answers to these questions depend on the context within which the geometric feature pair is considered.

Hence, closest feature algorithms are typically used only for polygonal geometries. On the other hand, they are very efficient since the resulting equations are simple to solve. Additionally, these algorithms can be easily tailored to return a penetration distance and a contact normal direction when objects are colliding. This feature makes them readily suitable for the implementation of contact force models based on the penetration distance. The penetration distance is most commonly (and arbitrarily) defined as the length of the shortest relative translation that results in the objects losing contact. However, a more robust definition is given by Heidelberg et al. (2004).

Optimization Algorithms

An alternative formulation for the collision detection problem relies on an optimization approach. Here, the object geometries can be described by quadratic surfaces, and the minimal separation or inter-penetration distance of two objects is found using an optimization method. One of the first algorithms proposed in this category is the GJK algorithm (Gilbert et al., 1988). Van Den Bergen (1999) implemented an enhanced version of the GJK algorithm (Cameron, 1997) in combination with AABB trees that can also compute the penetration distance. Sharf and Nahon (1995) proposed to define the interference distance as the distance by which objects should be shrunk until contact is lost. The latter definition also works for objects bounded by quadratic surfaces.

Collision detection algorithms based on optimization methods can handle objects bounded by quadratic surfaces, but at the cost of introducing one or more numerical tolerances required by the optimization algorithm. If the objects under consideration are very stiff, then the convergence threshold must be set very small in order to minimize a corresponding contact force “noise” resulting from the numerical imprecision of the collision detection technique. As a result, collision detection algorithms using an optimization scheme to identify the contact distance or penetration depth are not necessarily the best choice for modelling the contact dynamics of stiff objects.

2.2.4 Contact Normal

The determination of the contact normal, i.e., the direction along which the resultant force preventing penetration must act, is a parallel problem to the determination of the penetration depth. It has been less formally investigated, perhaps because of its seemingly intuitive solution. However, there are situations where the contact normal cannot be determined by simple observation. For example, when two cubes touching each other at the corners the interaction becomes complex and a more robust and reliable method is required. Ideally, the user of the contact dynamics simulation system should not have to figure out *a priori* the direction of the contact normal.

For collision algorithms based on closest feature distance, the contact normal problem is trivial: the contact normal is the direction along which the penetration distance is measured. For the example above, a two-corner intersection between two cubes would yield a list of 6 point-face pairs (there are two corner points facing three faces each) and 9 edge-edge pairs (there are three edges connected at each of the two corners), each of which gives a contact distance and corresponding penetration direction. Mirtich (1998) discusses how to obtain the contact force from a set of resulting contacting feature pairs. For algorithms based on an optimization method, the answer is not as straight-forward, but solutions have been proposed (Van Den Bergen, 2001).

Another approach is used by Nagle¹ and Tenaglia et al. (1999) to obtain the contact normal. The idea is to “wrap” the objects into a viscoelastic shell of uniform thickness, or skin, and simply use the minimum distance direction evaluated by the collision detection algorithm as the contact normal. Of course, the skin thickness and stiffness must be selected such that inter-penetration never exceeds the combined skin thickness of both objects. This shortcut solves two problems at once: the same algorithm can be used for collision detection and penetration and the contact normal is always well defined.

Alternatively, the contact surface normal can be determined as a function of the curve defined by the intersection of the two undeformed body surfaces. When the curve lies within a plane, then the contact normal is simply set as the normal of the plane. When this curve is not inscribed within a plane, i.e., it is three-dimensional, then a best-fit plane is found such that it minimizes the distance to each point of the curve, or, alternatively, that it maximizes the projected surface area of the intersection curve. The contact surface normal is then set to the normal of the best-fit

¹See Patent No. 5,644,204 on Animats website: www.animats.com

plane. This definition for the contact normal based on the intersection curve ensures that the contact normal will always change direction smoothly as the colliding bodies move with respect to each other. This method for determining the contact normal is commonly used by multibody dynamics simulation software packages such as ADAMS² and Working Model³.

The various definitions for the contact normal presented above share a common deficiency: they are nothing more than an arbitrary choice for the contact normal definition. These choices are not based on the mechanical analysis of the problem, and, as such, there is no justification that any of these methods yield a physically representative selection of the contact surface normal.

2.2.5 Modelling Contact Between Objects with Complex Geometries

The continuous approach has often been disregarded in the context of real-time or near real-time simulation because of a perceived lack of computational efficiency. While it is true that the numerical integration of the differential equations through an impact phase requires that the solver takes relatively small steps at that time, it is not clear however that the overall process is less efficient than the discrete approach. Indeed, there are at least two contact dynamics simulation systems using the continuous approach to model contact dynamics, and both of them are targeted for use in the context of real-time simulation of low velocity robotic tasks involving hard contact with the external environment (Ma, 2000; Tenaglia et al., 1999). In the world of computer animation, *Falling Bodies* stands out as being the only physically-based animation system using the continuous approach.

On the other hand, these latter contact dynamics simulation systems often take simplifying “shortcuts” to generalize the use of simple contact models, e.g., using a model of two spheres colliding with each other to calculate the contact forces between objects with more complicated shapes. In general, such generalizations are not representative of the physical phenomena at work during contact, and, hence, are not correct. The deficiencies related to these simplifying assumptions are best explained by looking at examples. Two cases are presented next.

Case Study 1: Falling Bodies

The software product *Falling Bodies* sold by Animats is a good example of a contact dynamics system based on a regularized approach. Fortunately, (or unfortunately) their technology has been patented, so the information on the technology is public domain.

Falling Bodies uses the enhanced GJK (Cameron, 1997) collision detection algorithm combined with the patented skin approach to determine the contact distance, penetration distance and contact normal. The problem of contact force noise discussed in Section 2.2.3 is avoided by selecting a spring model with an exponential force profile. With such a model, the “local stiffness” of the spring is low when the penetration depth is small, and becomes high when the penetration distance is in the order of the skin thickness.

²Personal conversation with Mr. Rajiv Rampalli (MSC Software).

³<http://www.workingmodel.com/vn4d/faqlist.html>

The contact force noise is only noticeable when the contact force varies slowly, such as when the system is in static equilibrium. In static equilibrium, the magnitude of the contact force is much smaller than the magnitude of the contact force during impact. For stiff materials, the difference is by several orders of magnitude. Thus, by introducing an exponential spring instead of Hertz-type model, *Falling Bodies* can significantly reduce the numerical force noise by using a lower spring stiffness coefficient, since the spring model will naturally increase the stiffness when the penetration depths become larger. Hence, it can be concluded that the spring model used in *Falling Bodies* was selected for its numerical properties and not because of the physics of the collision process.

Another problem when using an optimization scheme like the GJK algorithm is that the location where the maximum object inter-penetration occurs can move instantaneously from one location to another. The case where a square block rests on a plane in static equilibrium is considered. If the block is slightly perturbed, then one corner will start sinking into the plane. The GJK algorithm will therefore converge to this corner and this is where the contact force will be applied. Then, the contact force will push that corner up. This will cause the collision detection algorithm to converge to another corner, which will be also pushed up, and so forth. Hence, a cycling behaviour will appear as a result of the method of determination of the contact force location. In turn, there will be a resulting moment “noise” about the block’s centre of mass due to these sudden changes in the location of the contact force point of action, even if the force itself does not change in magnitude. Again, this behaviour is not consistent with the actual behaviour of the contact interaction.

Case Study 2: Contact Force With *V-Clip*

The block resting on a plane example discussed in the previous section is now reconsidered. The contact force location cycling behaviour can be avoided if separate contact models are assigned at each corner of the block, such that a force is always acting at each point, and that the overall load of the block is distributed among the four contact models.

Here, each feature pair (e.g., vertex-face and edge-edge) is assigned to individual contact models, and a contact force is applied at each corner whenever this corner of the block penetrates the plane. What was just described is the implementation of a contact dynamics system using a closest feature-type of collision detection algorithm. In Section 2.2.3 the *V-Clip* collision detection system was introduced. *V-Clip* is a closest feature collision detection algorithm designed to return the list of closest (or penetrating) features. Hence, the force cycling problem is avoided when using a closest-feature contact force approach.

On the other hand, there are other situations where this modelling approach yields physically inconsistent behaviour. First, a particularity of this modelling approach is that the contact stiffness is directly proportional to the number of features in contact. This is a property of the contact modelling system, not of the physical phenomena.

Another inconsistency occurs when the objects are rotating with respect to each other. The

same block resting on a plane example is considered again, but when it is sliding and spinning with respect to the plane. During the motion, it may happen that one of its corners becomes stationary. If the contact models used at each vertex-face feature pair includes some model of the stick-slip frictional effect, the corner of the block that is not moving will stick, while the other corners would be sliding. However, the entire contact surface is undergoing the translational and rotational motion; it just happens that one point on it is not moving. Hence, it is best to consider the contact surface as a whole and not just at the corners.

It may also happen that the point that is locally stationary is not be located at a corner. In this case, the contact models located at the four corner points would simply miss the phenomenon. This behaviour is an artifact of the modelling system and is not consistent with the physics of stick slip phenomenon, i.e., either the face touching the plane is sticking or it is sliding. But it will not have one corner sticking while the others are sliding.

2.3 An Alternative to Hertz Theory

In the previous section, it was observed that contact dynamics modelling systems that rely on compliant contact models often drastically simplify the interaction of complexly shaped bodies to simple cases, or even point contacts. The significance of the shapes of the colliding bodies on the resulting contact forces is generally not taken into account, or not modelled in a consistent manner for all components of the contact force, namely, normal and tangential force, rolling and spinning resistance torques. The Hertzian contact model, which assumes an elastic half-space approximation, is often used to model contact phenomena.

2.3.1 The Winkler Elastic Foundation Model

Strictly speaking, Hertz theory should be used to model contact mechanics only when colliding body surfaces can be described by second-order polynomials. In practise however, its application can be extended to bodies with smooth surfaces as long as the resulting contact area remains small with respect to the dimensions of the bodies. Even though the geometric boundary conditions may not be exactly fulfilled, the Hertz theory's assumption that the pressure distribution over the contact area is elliptical will still apply, or at least provide a good approximation, such that the theory still applies (Johnson, 1985).

On the other hand, there are situations where the dimensions of contact areas are significant with respect to the size of the bodies and the assumption of elliptical pressure distribution is no longer valid. This situation occurs when the geometries of the colliding bodies are conforming, i.e., they have similar shapes such that the resulting contact area becomes large. Johnson suggested to use the Winkler elastic foundation as a simple approximation for the contact pressure distribution. The foundation model can be used in complex situations where half-space theory would be very cumbersome:

The difficulties of elastic contact stress theory arise because the displacement at any point in the contact surface depends upon the distribution of the pressure throughout the whole contact. To find the pressure at any point in the contact of solids of given profiles, therefore, requires the solution of an integral equation for the pressure. This difficulty is avoided if the solids can be modelled by a simple Winkler elastic foundation, or ‘mattress’ rather than an elastic half-space. (Johnson, 1985).

Figure 2.1 shows the foundation model, where k_f is the elastic modulus of the foundation and h_f is the arbitrarily chosen depth of the foundation mattress. The SI units of k_f and h_f are $[\text{N}/\text{m}^2]$ and $[\text{m}]$, respectively.

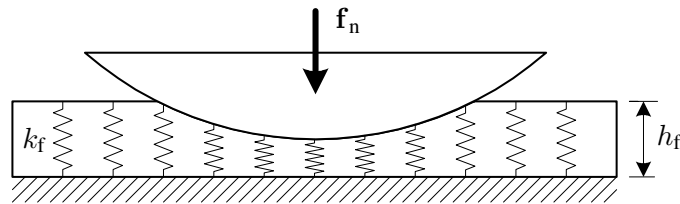


Figure 2.1: The Winkler elastic foundation model.

Hippmann (2004) uses this approach to deal with complex, i.e., conforming, geometries and suggests methods of how to obtain the foundation depth and stiffness. However, the method assumes the geometries are composed of polygons, and hence it is not very well suited for objects with curved surfaces. The global body-to-body contact force is obtained by numerically summing up the force contribution from each contacting polygon. The local polygon normal force magnitude is readily found as a function of the polygon area and the inter-penetration depth, while its direction is determined arbitrarily using some heuristic rules. The model also includes a simple tangential friction model. Hasegawa and Sato (2004) used a similar approach to implement a real-time rigid body simulation for a haptic device using a more sophisticated friction model with state transitions between the static and dynamic friction forces. Their contact force model uses the contact volume as a metric to evaluate the contact force. O’Brien (2000) also suggested using the contact volume to obtain the contact force, but without justifying it.

2.3.2 Obtaining Volumetric Information

The authors cited in the previous section used polygonal models to obtain the contact volume and the contact force thereof. However, the polygonization of a geometry introduces undesirable side-effects in the modelling of contact forces. For example, a sphere that is perfectly round will not roll in the same way as a faceted sphere made out of polygons. Typically, the contact dynamics is very sensitive to these geometric nuances. The alternative is to use a geometric description system that describes the shapes exactly, without the polygon approximation.

Projective geometry is a fundamental branch of geometry, invented in the 17th century and formalized in the 19th century. Almost forgotten since then, it has recently been reconsidered by Rotgé (1997) because of its remarkable algorithmic attributes. The classical Euclidean geometry is a subset of affine geometry, which is itself a subset of projective geometry. Projective geometry is a method of describing geometry that focuses on the relative relationship between the features of a geometry, rather than looking at the dimensions of the object, e.g., position and length, which correspond to a Euclidean representation.

The relational nature of the geometric description in projective space allows an *exact* definition of the geometries, not subject to floating point imprecision and not requiring a polygonal discretization. The resulting solid modelling technology uses instead polynomials to characterize projective algebraic surfaces (Rotgé and Farret, 2007). It represents objects using simple projective primitives, e.g., quadric, cubics, quartics, etc. In fact, this polynomial technology uses the projective algebraic surfaces as primitives and functional expressions as structural relationship descriptors. In this approach, the basic idea is that complex solids can be represented as compositions of the primitive by means of arithmetic and logical operators. The result is a solid modelling technology that provide the means to render and manipulate exact *volumes* and extract volumetric information; see Figures 2.2 and 2.3.

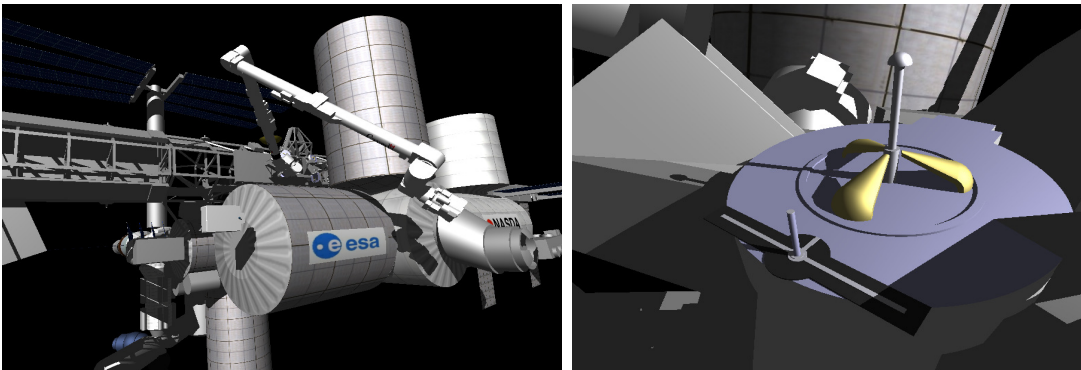


Figure 2.2: Volumetric renderings of the International Space Station.

The contact model for conforming contacts presented in Chapter 4 relies on the polynomial technology to obtain the volumetric information it needs to evaluate the contact force. Parallel Geometry Inc.⁴ (LLG), which promotes this technology, has developed for the CSA a suite of collision detection and collision metrics functions that permit the implementation of the proposed contact modelling framework. The technology also includes a novel ellipsoid-based high-level pruning technology that optimizes the collision detection queries. This approach is different than usual sweep-and-prune methods described in Section 2.2.3, which are typically based on boxes or spheres. Here the advantage is that the ellipsoid can be stretched or squeezed around the object

⁴<http://www.llgeometry.com>

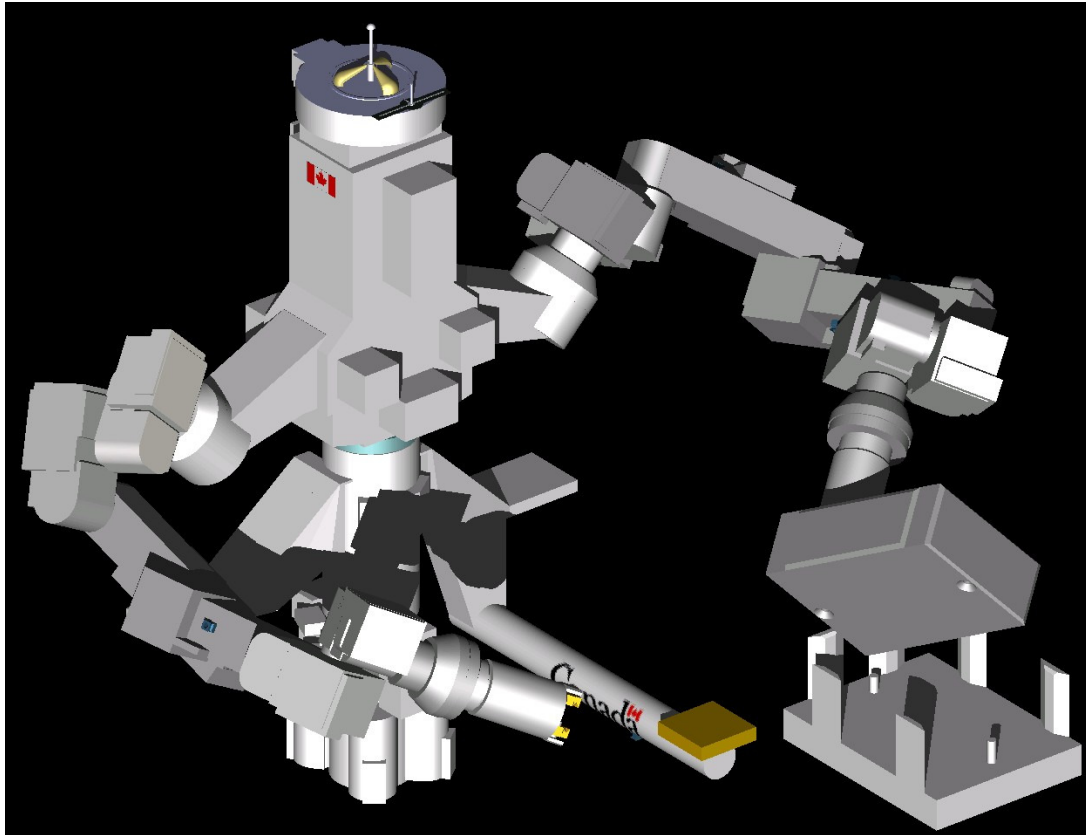


Figure 2.3: A volumic model of Dextre.

shapes to get a very close fit. The resulting collision detection system can therefore be optimized for highly complex environments, and yet remain very efficient (Doyon et al., 2004).

The literature survey has up to now mainly focused on the normal contact force acting to prevent inter-body penetration. However, friction plays an equally important role in the modelling of body-to-body interaction forces. This topic is presented in the next section.

2.4 Tangential Friction Models

The interaction forces between two moving bodies is the result of complex physical phenomena. Two aspects are inherently present when computing contact loads. These are friction and normal contact. Historically, these two aspects were treated separately, despite the fact that in reality they constitute a single physical phenomena. This section presents a review and analysis of the contact friction phenomena.

Portions of the text in this section are extracted from de Carufel et al. (2000), an unfinished document prepared as part of an internal research project lead by the Robotics Section at the CSA.

Authorization to reproduce the text was obtained⁵ and the contribution from the original authors is acknowledged. Some of the text and figures from the original document are included in this thesis because the original document was never published.

2.4.1 Historical Background

Tribology as a science was born in England at the beginning of this century. However, the study of friction is relatively old. Leonardo da Vinci at the end of the XVth century described in his *Notebooks* the analysis of the motion of a brick on an inclined flat wall. His statements reflected what is known today as the fundamental laws of friction. However, it is only some two centuries after and apparently without the knowledge of da Vinci's work that Guillaume Amontons⁶ stated the laws of friction in 1699 (Bennewitz, 2007). They are summarized as:

1. The friction force is a force opposing the motion, proportional to the normal load.
2. The friction force is independent of the contact area.

One of the most substantial contributions to tribology is the work of a French army engineer, Charles Augustin Coulomb. Stimulated by the French war industry, he established scientifically the basic laws of tribology. His statements on the relation that exists between the micro-structure of the interfacing bodies in contact and the friction force has survived up until now. In his model, the surface roughness was represented by bristles and the friction force was explained by the effort necessary to move two brushes relative to each other, with their bristles in contact. Using this analogy, the difference between static and kinetic friction could be explained by the fact that, at higher speeds, the bristles may jump over gaps resulting in a less opposition to the motion. The reduction of friction due to lubrication could also be explained by lubricant filling up the gaps.

In the 1930s and 1940s, and with the intention of understanding wear and lubrication for industrial purposes, Bowden and Tabor (1939) investigated the microscopic behaviour of solids in contact. Tribology as it is defined today was born. The rate of publication in tribology has been increasing ever since. An impressive amount of publications, treating both experimental and theoretical studies, is available today. The following discussion is a summary of the ideas that emerged from these investigations and that are considered fundamental to tribology.

2.4.2 Unlubricated Friction

In his work, Coulomb used the bristle model to represent the topography of the contact surface. A generalization of the bristle was introduced by Bowden and Tabor: the asperity model. While

⁵Permission to reproduce the text from the document "CDMLib Reference Manual–CSA Internal Project" was given by Érick Dupuis (Erick.Dupuis@space.gc.ca), Robotics Section Manager, Canadian Space Agency.

⁶Presentation at the European Academy (1699).

bristles are long and thin by definition, asperities can have any height and size. This generalization directly led to the concept of apparent and true surface of contact.

A study of the topography of the contact area is necessary to explain and understand friction. Consider the situation where two bodies \mathcal{B}_i and \mathcal{B}_j are in contact over a finite dimension area A_c (Figure 2.4). The protuberance of each surface are called asperities. They may have different height, slopes and radius of curvature of the tip, and the slopes may differ in different directions. In reality, the two bodies are in contact only over a portion of the total area A_c . The sum of those microscopic contact surfaces is called the true area of contact A_t as opposed to the apparent area of contact A_c .

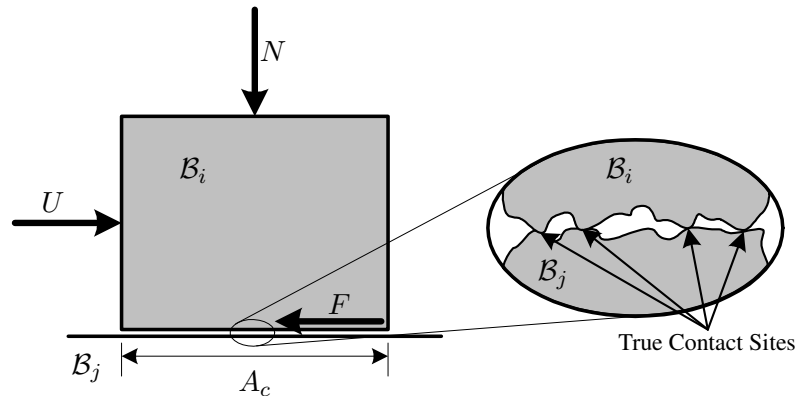


Figure 2.4: Contact topology schematic.

With this representation, friction can be intuitively analyzed. Although the stress at the contact surface appears relatively low, the stress at the true contact sites may become extremely high. Assuming constant normal loads N , any increase in the tangential force F contributes to bring the true contact sites to their plasticity limits. When they all reach that level, breakaway occurs and sliding is initiated. This observation is in agreement with the work of Rabinowicz (1956) and Dahl (1968) who suggested pre-sliding microscopic displacement occurring during stiction (Dahl effect). This model also explains the dissipative behaviour of the friction process, both in stiction and in sliding.

The asperity model can also explain other important observations on the macroscopic behaviour of friction. For example, it can explain the reduction in friction forces in the kinetic regime. During sliding, some asperities are brought in contact and are deformed up to the plasticity limit. In that process however, some asperities are freed, releasing a certain amount of elastic strain energy that can be partly used to deform newly contacting asperities, thus reducing the amount of work necessary to maintain motion. Finally, the asperity model can also explain one of the fundamental laws of friction. The increase in normal load is reflected at the asperity level by an increase in true contact surface. As a result, the amount of tangential force necessary to bring all contact sites to the plasticity limit is also increased. Analysis have demonstrated that for most materials, the true

contact area is a linear function of normal load, and that the static friction force is a linear function of the true contact area. This corresponds to the second law of Amontons.

The topography of different surfaces have later been measured using precise profilometric instruments. This demonstrated the validity of the asperity model (Majumbar and Bhushan, 1991; Greenwood and Williamson, 1966; Mann et al., 1994; Bailey and Sayles, 1991). Throughout the years, researchers have used contact mechanics to study the asperity contact problem. Various models were developed using elasticity and elasto-plasticity approaches (Rigney and Hirth, 1979; Avitzur et al., 1984; Chang et al., 1987; Chang and Ling, 1992).

A realistic view of asperities is given in (Majumbar and Bhushan, 1991). Asperities are most likely as represented in Figure 2.5. There are various levels of asperities, ranging from machining-level to molecular-level protuberances. Each level plays an important role in the friction phenomena. This was captured in their fractal model of the topography.

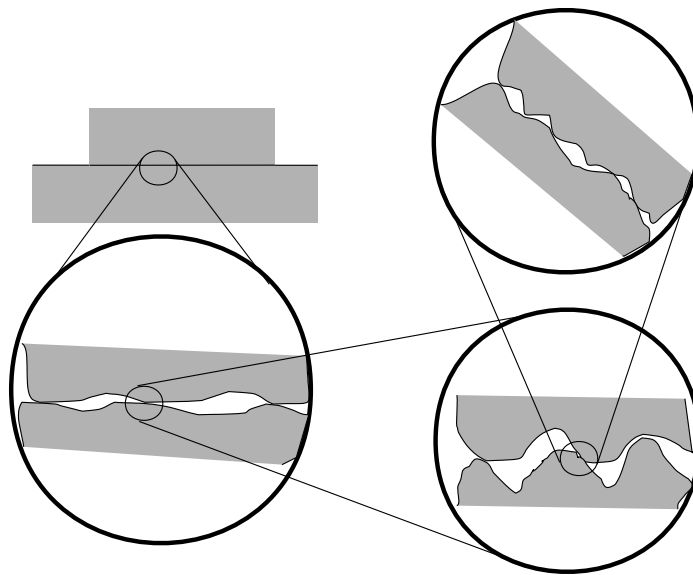


Figure 2.5: Fractal topology model.

2.4.3 Lubricated Friction

Lubrication has been used for a long time to reduce friction and wear. Obviously, lubrication and tribology are very closely related. Wear is essentially a result of friction. Again for industrial and military purposes, the problem of lubrication was studied in great detail in the XIXth century. A good approach for the understanding of lubrication in frictional contacts is through the analysis of the Stribeck curves presented in Figure 2.6 relating the relative velocity between the lubricated contacting surfaces and the friction force for constant normal loads.

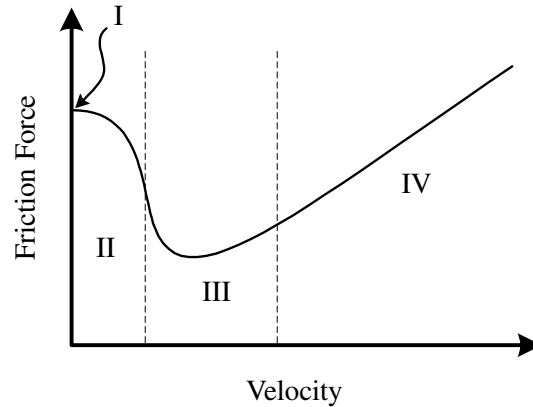


Figure 2.6: A typical Stribeck curve.

There are four distinctive regions to the Stribeck curve; see Armstrong-Helouvry et al. (1994). Region I is called the stiction region. In this regime, the lubricant fills up the voids at the contact surface without preventing the contact of asperities. Consequently, the friction can be explained using the same argument as those used for static dry contacts. Region II is the boundary lubrication region. The lubricant, trapped in the gaps between asperities, moves to the true contact sites and forms along both surfaces a boundary layer preventing rubbing between the molecular level asperities. The result is a decrease in friction associated with the flow development of the lubricant and the onset of motion. This phenomenon is referred to as the Stribeck effect. Region III is the partially lubricated region. As the flow develops, the fluid film increases in thickness, pushing apart the two surfaces and reducing the amount of asperities that may come in contact. However, as the flow is developing, the shear stress present in the film becomes the dominant effect of friction. As a result, friction keeps on reducing up to a point where the reduction in asperity contacts becomes insignificant with respect to the increase in shear stress. Finally, region IV is the full fluid lubrication region. The flow is fully developed and the dominant effect on the variation of the friction force is the shear stress in the fluid, proportional to the relative velocity for Newtonian fluids. The residual Coulomb friction force is due to the interaction present between asperities with height greater than the fluid film thickness.

2.4.4 Dynamics of Friction

In the previous subsections, friction was viewed as a static process that could be described by algebraic equations only. However, it was clearly demonstrated that some phenomena associated with friction are dynamic in nature. Some researchers (Rabinowicz, 1956; Dahl, 1968; Hess and Soom, 1990) performed experimental studies that suggested some behaviours clearly associated with dynamics present in friction. The most important experiment is the stick-slip experiment (Rabinowicz, 1956) for which a schematic is shown in Figure 2.7(a). It simply consists of a slider attached to a

fixed wall with a spring and a damper resting on a conveyor. The conveyor motion is then controlled in velocity to provide some measurement of the friction force (Bell and Burdekin, 1969).

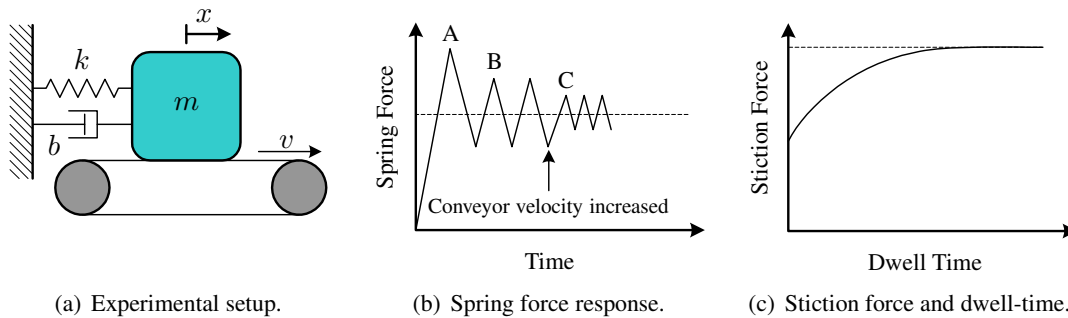


Figure 2.7: The Bowden and Leben stick-slip experiment.

A typical spring force response is also presented in Figure 2.7(b). At first, the static friction is dominant and the force builds up in the spring. When the breakaway force is reached, the slider starts to move backward due to the reduction in the friction force associated with kinetic friction. When the relative motion between the slider and the conveyor reaches zero, the slider sticks and the process is repeated. If the damper is selected to be such that the position at which stiction re-occurs is near the equilibrium between spring force and kinetic friction, the stick-slip process is avoided. From the static analysis presented in the preceding sections, this explanation makes sense. However, it cannot predict the difference between the point A, B and C. In fact, it has been observed that the maximum stiction force is a function of the dwell time as shown in Figure 2.7(c). Consequently, the level of stiction present at the first breakaway (point A) is higher than under steady state operation (point B). Also, when the speed of the conveyor is increased, the stiction force is reduced (point C). If it is increased to a certain level, stick-slip disappears and the spring force corresponds to the value shown by the dotted line. A similar result is obviously reached if the spring is stiffened. These observations cannot be explained using the static arguments of the preceding section.

2.4.5 Modelling Friction in Multibody System Simulation

A general contact model must include a sub-model for the tangential friction forces such that oblique-frictional impacts can be treated as well. To obtain these forces, the stiction and Coulomb friction coefficients μ_S and μ_C are applied to relate normal and tangential forces during the sticking and sliding states, as shown in Whittaker (1937), Keller (1986), Han and Gilmore (1993), Wang and Mason (1992), and Battle (1993). These coefficients are also known as static and kinetic coefficients of friction respectively. An extension of the above mentioned models can be found in Lüder (2000) in which the impact of rigid bodies, including friction and energy dissipation, is modelled using a regularized approach with spring, dash-pot elements and hysteresis in

normal and tangential directions. Stronge (2000) shows that contact models with compliance in the directions normal and tangential to the contact surface area provide a good prediction of experimental results for oblique impacts. As was seen in Section 2.4.2, friction models using local compliance are also known as bristle models (Canudas de Wit et al., 1995). Tenaglia et al. (1999), and Ma (2000) also extended the direct central contact force model to three dimensions by adding a tangential compliance effect to model the friction.

2.5 Research Focus

The research presented in this thesis extends and combines the results presented in previous work. This section summarizes the principal references that are the foundation for this work. The theoretical results fall in two categories: (1) a contact model for bodies that have non-conformal geometries and (2) a general contact model appropriate for a wide range of object geometries.

The contact model for non-conforming geometries is treated in Chapter 3. For this case, the Hertz theory is applicable and the proposed normal contact model is based on the non-linear spring model proposed by Hunt and Crossley (1975), and introduces a new method of defining the hysteretic damping term. A new bristle friction model is presented that extends the work from Canudas de Wit et al. (1995) and de Carufel et al. (2000), and in particular, it is adapted to the context of multibody simulation with impact with the introduction of a load-dependent tangential stiffness term. The friction model is expressed in vector form and includes dynamic effects such as the dwell-time dependency of the stiction force.

To handle a more general class of geometries, the Winkler elastic foundation model (Johnson, 1985) is used in Chapter 4 as the theoretical basis for the derivations of a general contact model. The resulting contact model normal and tangential components uses the same parameter set as the model presented in Chapter 3, but the model includes the rolling resistance and spinning friction torque effects as well. A formal definition for the contact normal is given and the behaviour of friction when the contact surface is large is investigated.

Appendix A presents a flexible object-oriented framework that can be used to implement a very wide variety of contact models, including the models presented in Chapters 3 and 4.

Chapter 3

Point Contact Model

In this chapter a contact model based on Hertz theory is presented. This modelling hypothesis imposes that the contact region be small compared to the dimensions of the colliding bodies and, hence, that the colliding bodies have non-conformal geometries. A more general contact model, which can handle conformal as well as non-conformal geometries and which includes both spinning friction and rolling resistance effects will be presented in Chapter 4. The first section of this chapter presents the multibody framework within which the contact model resides, and Section 3.2 presents the normal and tangential components of the contact model. Finally, Section 3.3 discusses methods to obtain or estimate the contact model parameter values.

3.1 Point Contact Model Framework

The contact model for non-conformal geometries takes the form of a lumped-parameter non-linear spring. The relationship between the spring deformation and the resulting force can be derived when each body is approximated as a semi-infinite elastic solid bounded by a surface. This idealization simplifies the boundary conditions and makes available the large body of elasticity theory results that has been developed for the elastic half-space. A simple function relating the local surface deformation to the force causing this deformation is then readily obtained. The local deformation can be parameterized as a function of the penetration depth of the undeformed bodies. This analysis produces a single algebraic expression relating the penetration depth to the normal contact force i.e., a spring model.

To include the contact model into a multibody dynamics simulation system, it is also necessary to specify the point where the contact force will be applied. Since the contact region is assumed to be very small, the moments generated by the local deformations in the contact region are neglected. Obviously, the contact force should act in the direction that minimizes the constraint violation and, hence, the direction of the normal contact force should also be determined.

This section will demonstrate how to set up the proposed contact model for the simulation of collisions between two rigid bodies with arbitrary non-conformal shapes. The case of the sphere-

plane pair will be presented as an example.

3.1.1 Point of Action of the Contact Model

The contact model presented in Section 2.2.1 computes the contact force f_k between two non-conforming rigid bodies as a function of the penetration depth x . For a given non-conforming geometric pair, a *point of action* \mathbf{p}_a is defined as the point where the equal contact forces with opposite directions are applied to the two bodies. In the case of the sphere-plane pair, the Hertz force approach law is based on the deepest penetration distance. The point of action is selected as the point along the sphere surface at which the sphere surface normal is exactly opposite to the plane normal. This choice is convenient since by measuring the height of the point of action with respect to the plane surface, the desired penetration distance is obtained.

The states of two arbitrary bodies \mathcal{B}_i and \mathcal{B}_j are described by defining body-fixed frames \mathcal{K}_i and \mathcal{K}_j attached to \mathcal{B}_i and \mathcal{B}_j , respectively. The origin of each frame is located by the position vectors \mathbf{r}_i and \mathbf{r}_j relative to an inertial “world” frame \mathcal{K}_w . Their orientation relative to \mathcal{K}_w is described by the rotation matrices \mathbf{R}_i and \mathbf{R}_j . The frames translate at a velocity \mathbf{v}_i and \mathbf{v}_j and rotate with an angular velocity $\boldsymbol{\omega}_i$ and $\boldsymbol{\omega}_j$. For the sphere-plane example, the position of the centre of the sphere (\mathcal{B}_i) with respect to \mathcal{K}_i is \mathbf{p}_{sph} , and the sphere radius is R . The surface of the plane (\mathcal{B}_j) is located at a height h_j along the plane normal \mathbf{n} from the origin of \mathcal{K}_j ; see Figure 3.1. When performing vectorial operations, all vectorial quantities are resolved in \mathcal{K}_w . Typically, \mathbf{p}_{sph} and \mathbf{n} are specified in local frame coordinates, but they can be easily transformed into \mathcal{K}_w by using \mathbf{R}_i and \mathbf{R}_j .

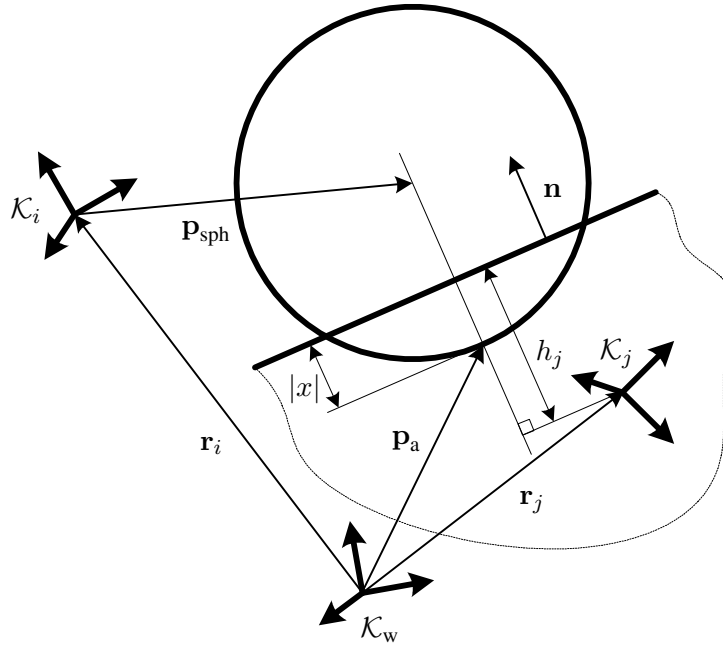


Figure 3.1: Point of action and penetration depth for a sphere-plane pair.

In the case of the sphere-plane geometric pair, the point of action is found as

$$\mathbf{p}_a = \mathbf{r}_i + \mathbf{p}_{\text{sph}} - R \mathbf{n} , \quad (3.1)$$

where \mathbf{n} points from \mathcal{B}_j to \mathcal{B}_i . The height x of the point of action with respect to the plane is given by

$$x = (\mathbf{p}_a - \mathbf{r}_j) \cdot \mathbf{n} - h_j , \quad (3.2)$$

which is the expression for the penetration depth needed to evaluate Equation (2.1). This same expression can be used to detect contact, i.e., when $x \leq 0$, so a separate collision detection algorithm is not needed for this case. In the general case, \mathbf{p}_a must first be identified using a collision detection algorithm. Then, \mathbf{p}_a is arbitrarily assumed to belong to one of the bodies, say \mathcal{B}_i , after which the surface normal \mathbf{n} and height h to the surface of the other body \mathcal{B}_j can be found as a function of $(\mathbf{p}_a - \mathbf{r}_j)$. In this thesis, the contact normal \mathbf{n} will always be interpreted as pointing from body \mathcal{B}_j toward body \mathcal{B}_i . Accordingly, the relative translational velocity of \mathcal{B}_i with respect to \mathcal{B}_j at the point of action is given by

$$\mathbf{v}_r = \mathbf{v}_i + \boldsymbol{\omega}_i \times (\mathbf{p}_a - \mathbf{r}_i) - \mathbf{v}_j - \boldsymbol{\omega}_j \times (\mathbf{p}_a - \mathbf{r}_j) . \quad (3.3)$$

Once the force generated from the local surface deformations has been computed, its contribution to the forces \mathbf{f}_i and \mathbf{f}_j and moments $\boldsymbol{\tau}_i$ and $\boldsymbol{\tau}_j$ acting on the bodies at their respective body-fixed frames \mathcal{K}_i and \mathcal{K}_j is given by

$$\begin{aligned} \mathbf{f}_i &= \mathbf{f}_c & ; & & \boldsymbol{\tau}_i &= (\mathbf{p}_a - \mathbf{r}_i) \times \mathbf{f}_c \\ \mathbf{f}_j &= -\mathbf{f}_c & ; & & \boldsymbol{\tau}_j &= -(\mathbf{p}_a - \mathbf{r}_j) \times \mathbf{f}_c \end{aligned} , \quad (3.4)$$

where \mathbf{f}_c is the total contact force and includes both the normal force acting to prevent constraint violation and the frictional forces. A more sophisticated model for the normal contact force will be presented in Section 3.2.1, while Section 3.2.2 will introduce a novel friction model.

The proposed contact model adds little computational overhead to the multibody dynamics simulation since Equation (2.1) is a simple explicit expression, and thus it is suitable for a real-time implementation. For the case of arbitrary geometries, the extra computational effort will be focused on finding the location of the point of action, the penetration depths and the direction along which it is measured. The determination of these quantities has been intensely investigated in the past decade, and for which very efficient algorithms are available, e.g., Lin and Gottschalk (1998) and Jimenez et al. (2001).

3.1.2 Contact Surface Normal Projection Matrices

Although the model presented here assumes that the size of the contact area is negligible compared to the size of the colliding bodies, the contact surface nonetheless has a normal \mathbf{n} along which the normal contact force acts. For the derivations in the coming sections, it is useful to partition the vectorial quantities into sub-components that are tangential and normal to \mathbf{n} . To this end, the projection operator \mathbf{N} that projects any vector \mathbf{u} onto the surface normal \mathbf{n} is defined as

$$\mathbf{u}_n = \mathbf{n}(\mathbf{n} \cdot \mathbf{u}) = \mathbf{n}\mathbf{n} \cdot \mathbf{u} = \mathbf{N} \cdot \mathbf{u} . \quad (3.5)$$

Hence, \mathbf{N} is a dyadic operator. The matrix operation for $\mathbf{n}\mathbf{n}$ is $[\mathbf{n}][\mathbf{n}]^T$ and is sometimes referred to as the “outer product” as opposed to the “inner product” operator $[\mathbf{n}]^T[\mathbf{n}]$. Here, the brackets $[\cdot]$ indicate the vector \mathbf{n} is treated as a column matrix with the components of \mathbf{n} resolved in some frame. Clearly $\mathbf{N} \cdot \mathbf{n} = \mathbf{n}$ and using \mathbf{N} , \mathbf{u} can be decomposed into a vector \mathbf{u}_n normal to the contact surface S and \mathbf{u}_t tangential to the surface such that $\mathbf{u} = \mathbf{u}_t + \mathbf{u}_n$; see Figure 3.2. \mathbf{u}_t and \mathbf{u}_n are given as

$$\mathbf{u} = (\mathbf{I} - \mathbf{N} + \mathbf{N}) \cdot \mathbf{u} = (\mathbf{I} - \mathbf{N}) \cdot \mathbf{u} + \mathbf{N} \cdot \mathbf{u} = \mathbf{u}_t + \mathbf{u}_n , \quad (3.6)$$

and

$$\begin{aligned} \mathbf{u}_n &= \mathbf{N} \cdot \mathbf{u} = u_n \mathbf{n} , \\ \mathbf{u}_t &= (\mathbf{n} \times \mathbf{u}) \times \mathbf{n} = \mathbf{u} - \mathbf{n}(\mathbf{n} \cdot \mathbf{u}) = (\mathbf{I} - \mathbf{N}) \cdot \mathbf{u} = \mathbf{T} \cdot \mathbf{u} , \end{aligned} \quad (3.7)$$

where $u_n = \mathbf{n} \cdot \mathbf{u}$, \mathbf{I} is the unit dyad and $\mathbf{T} = \mathbf{I} - \mathbf{N}$ is the projection operator projecting the vector \mathbf{u} on the plane tangential to \mathbf{n} . Hence, by definition

$$\mathbf{N} + \mathbf{T} = \mathbf{I} . \quad (3.8)$$

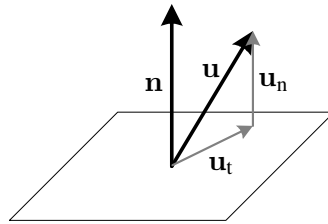


Figure 3.2: The normal and tangential components of the vector \mathbf{u} .

3.1.3 Contact Model Components

The contact model presented in this chapter includes compliance in both the normal and tangential directions. With \mathbf{n} defined as the outward unit vector normal to the contact surface and pointing from \mathcal{B}_j toward \mathcal{B}_i , the contact force \mathbf{f}_c is decomposed into normal \mathbf{f}_n and tangential \mathbf{f}_t components:

$$\mathbf{f}_c = \mathbf{f}_n + \mathbf{f}_t = f_n \mathbf{n} + \mathbf{f}_t, \quad (3.9)$$

where the magnitude of the normal force is f_n . Similarly, the relative velocity \mathbf{v}_r at the point of action \mathbf{p}_a is expressed in terms of its normal and tangential components \mathbf{v}_n and \mathbf{v}_t as

$$\mathbf{v}_r = \mathbf{v}_n + \mathbf{v}_t = v_n \mathbf{n} + \mathbf{v}_t, \quad (3.10)$$

where the magnitude of the normal velocity is v_n .

3.2 Point Contact Sub-Models

As was seen in Section 2.2.5, contact models derived from the Hertz theory have been used for modelling contact forces in multibody dynamics simulation packages. One of their key features is that the contact force can be expressed directly in terms of a geometrically identifiable metric—the penetration depth. Today, many collision detection packages can also provide a penetration depth estimation when a geometric ‘overlap’ is detected. As a result, the implementation of a Hertz theory-based contact model into a multibody dynamics package is fairly straightforward. The previous section showed how this is done for the case of a sphere-plane geometric pair.

Hertz’s theory provides a good approximation of the contact force between hard compact bodies where the contact region remains small in comparison with the size of either body. For non-conforming elastic bodies, the local deformations in the contact region resulting from the reaction forces will create a small area where the surface of the bodies conform exactly. The multi-body dynamics simulation packages that use Hertz theory-based contact force models generally do not consider the moments produced in the contact region, although these effects have been carefully studied (Johnson, 1985). Since the contact area is small with respect to the size of the bodies, the moment arm of the contact force about each body’s centre of mass will typically produce a moment that is much larger than the moment resulting from the rolling and spinning frictional effect occurring in the contact region. However, for a realistic simulation these effects may be important, and neglecting them may result in a qualitatively unrealistic simulation; see Section 5.1.

The Hertz force-approach law described in Section 2.2.1 only provides information about the force acting to separate two colliding bodies and is valid for direct-central frictionless impacts only. To implement a general point contact model, the tangential forces must also be modelled such that oblique-frictional impacts can be treated as well. The next two sub-sections present sub-models for

the normal contact and tangential friction forces.

3.2.1 Normal Contact Force Model

The normal contact force model derived in this section belongs to a special class of non-linear spring models. Given that the Hertz non-linear spring behaviour is a well understood phenomena, the analysis presented here will concentrate on the mechanism through which the energy is dissipated. The work presented here is based on previous derivation by Hunt and Crossley (1975) and Lankarani and Nikravesh (1990). A brief overview of their work is presented next.

Previous Work

The compliant normal-force model proposed by Hunt and Crossley (1975) for direct central and frictionless impacts is a non-linear spring-damper model of the form

$$f_n = \lambda |x|^p \dot{x} + k |x|^p, \quad (3.11)$$

where x and $\dot{x} = v_n$ are the penetration depth and velocity, λ is the *hysteresis*¹ damping factor and k is the spring constant. Section 3.1 shows how x and v_n are computed for a sphere-plane geometric pair. The force-approach law based on Hertz theory yields $p = 3/2$ when the two contacting bodies are linearly elastic spheres. Non-linear spring models for other geometric pairs have been derived (Johnson, 1985). As discussed in Hunt and Crossley (1975), this damping model is consistent with the expectation that the total contact force should vanish when the indentation goes to zero. See Figure 3.3 for comparison of the effect of a linear damping term vs. the hysteretic damping term on the contact force during impact.

Clearly, in the case of the spring with the linear damping term, the contact force can be seen to be positive and non-zero at the start of the impact phase, and negative and non-zero at the end of the impact phase. This behaviour contradicts two characteristics that should be expected from a consistent contact model: that the contact force should be zero at zero penetration, and that the contact force should always be positive, i.e., there should not be any any “sticking” effect. Note that in both figures, the energy dissipated during the impact corresponds to the area inside the loop.

It has been shown that at low impact velocities and for most linear materials with an elastic range (Goldsmith, 1960), the coefficient of restitution can be approximated by

$$e_{\text{emp}} = 1 - \alpha v_n^i, \quad (3.12)$$

where α is an empirically determined constant that is valid for a limited range of impact velocities and v_n^i is the normal relative velocity at the start of the impact phase. For steel, bronze or ivory, α is

¹The terminology used by Hunt and Crossley is inappropriate. The dynamic behaviour associated with the damping term does not have hysteresis. The output of the model only depends on the current state of the system.

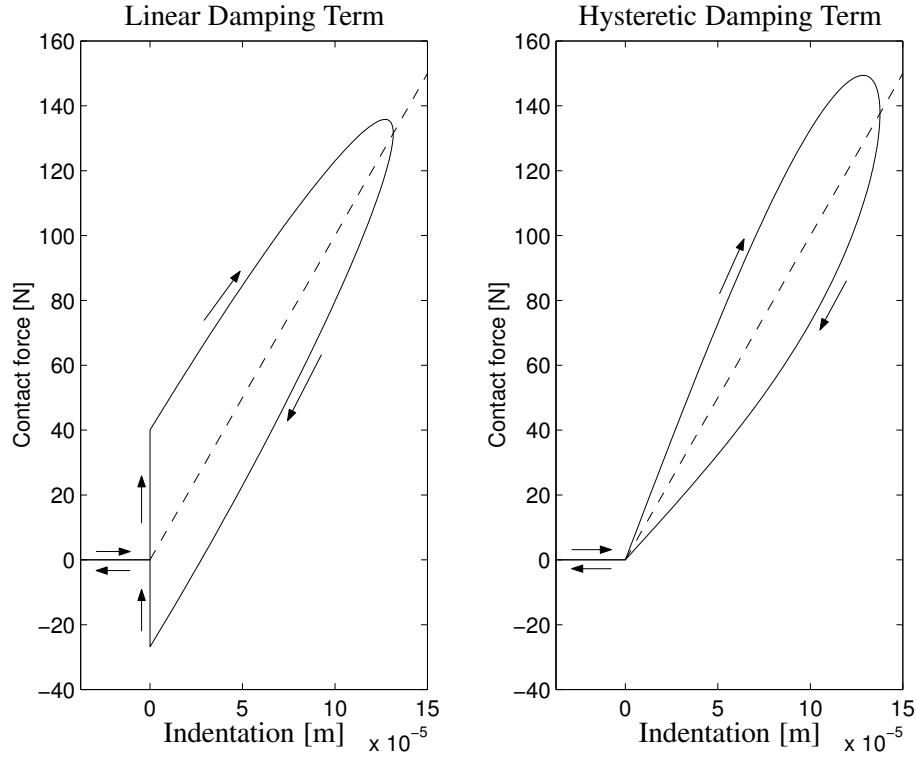


Figure 3.3: Linear vs. hysteretic damping in a normal contact force model.

equal to 0.08... 0.32 s/m. Assuming that the energy dissipated during the compressive phase and during expansion phase are equal, Hunt and Crossley approximated the hysteresis damping factor as a function of the restitution coefficient and v_n^i as

$$\lambda_{\text{HC}} = \frac{3}{2} (1 - e_{\text{eff}}) \frac{1}{v_n^i} k, \quad (3.13)$$

where the effective coefficient of restitution for the contact model e_{eff} is defined as:

$$e_{\text{eff}} = -v_n^o / v_n^i, \quad (3.14)$$

and v_n^o is the normal relative velocity at the end of the impact phase. Using the definition of e_{emp} for e_{eff} , Equation (3.13) simplifies to

$$\lambda_{\text{HC}} = \frac{3}{2} \alpha k. \quad (3.15)$$

Lankarani and Nikravesh performed a similar analysis, but they instead assumed that the amount of energy dissipated was much less than the energy stored in compression. This assumption allowed them to express the velocity at any point during the compression phase as a function of the initial impact velocity. Using this result, they then evaluated the integral of the energy dissipated during

the impact phase, and assuming again symmetric distribution of the energy dissipation around the hysteresis loop, they obtain an expression for the hysteresis damping factor as follows

$$\lambda_{\text{LN}} = \frac{3}{4} (1 - e_{\text{eff}}^2) \frac{1}{v_{\text{n}}^i} k, \quad (3.16)$$

or

$$\lambda_{\text{LN}} = \frac{3}{2} \alpha k \left(1 - \frac{\alpha v_{\text{n}}^i}{2} \right), \quad (3.17)$$

when e_{eff} is estimated using e_{emp} . A comparative study of these damping factor definitions as well as others is given by Zhang and Sharf (2004), including a definition based on the analytical solution of the equations of motion. However, the latter definition was initially proposed by the author (Gonthier et al., 2002) and is presented in the next section.

A New Damping Factor Definition

If the colliding bodies i and j have a mass m_i and m_j , respectively, then the effective mass m can be obtained from $m^{-1} = m_i^{-1} + m_j^{-1}$ (Lankarani and Nikravesh, 1990). Defining the damping factor a by $\lambda = a k$, the equation of relative motion $m \ddot{x} = -f_{\text{n}}$ can be written as

$$m \dot{v}_{\text{n}} + k |x|^p (1 + a v_{\text{n}}) = 0, \quad (3.18)$$

where the Hunt and Crossley contact model has been expressed in the form

$$f_{\text{n}} = k |x|^p (1 + a v_{\text{n}}), \quad (3.19)$$

and the bodies are assumed to be in contact when $x < 0$. To prevent the contact model from applying tensile forces, a must be selected such that

$$1 + a v_{\text{n}} \geq 0 \quad \forall v_{\text{n}}. \quad (3.20)$$

As Marhefka and Orin (1999) and Stronge (2000) showed, Equation (3.18) is separable and can be integrated over the impact phase as follows

$$\int_{v_{\text{n}}^i}^{v_{\text{n}}^o} \frac{v_{\text{n}}}{1 + a v_{\text{n}}} dv_{\text{n}} + \frac{k}{m} \int_{x^i}^{x^o} x^p dx = 0, \quad (3.21)$$

where x^i , x^o are the penetration depths at the start and end of the impact phase. The second integral term of Equation (3.21) is the work done by the elastic term over the collision event and is therefore equal to zero. Hence, v_{n}^o depends exclusively on v_{n}^i and a , and is independent of the system's effective mass, stiffness, or the type of spring model used. To get a better understanding

of the relationship between v_n^i , v_n^o and a , the definition for e_{eff} is substituted into Equation (3.21) and the first integral term is solved. The result is

$$a v_n^i - \ln(1 + a v_n^i) + e_{\text{eff}} a v_n^i + \ln(1 - e_{\text{eff}} a v_n^i) = 0. \quad (3.22)$$

Since a and v_n^i always appear together in Equation (3.22), a dimensionless factor d defined as $d = e_{\text{eff}} a v_n^i$ is introduced and a closed-form relationship for d and e_{eff} independent of v_n^i is obtained. The solution to Equation (3.21) simplifies to

$$\frac{1 + d/e_{\text{eff}}}{1 - d} = e^{d(1+1/e_{\text{eff}})}. \quad (3.23)$$

The solution for the closed-form expression has multiple branches (one of them being $d = 0$). However, a valid solution for this problem should be such that Equation (3.20) is satisfied. Noting that for $v_n^i < 0$, the value of v_n is limited by $v_n^i < v_n < -e_{\text{eff}} v_n^i$. Hence, the valid solution branch for d will be such that $d \leq 1$ for any e_{eff} . On the other hand, the damping factor cannot be negative since this would cause energy to be gained during impact. Hence, $0 \leq d \leq 1$. Figure 3.4 shows the corresponding solution branch for d . Clearly, d is always less than or equal to 1 and goes to zero at $e_{\text{eff}} = 1$. The solution can be obtained by solving Equation (3.23) with a numerical bisection algorithm. A good initial guess, $d_{\text{est}} = 1 - e_{\text{eff}}^2$ is provided.

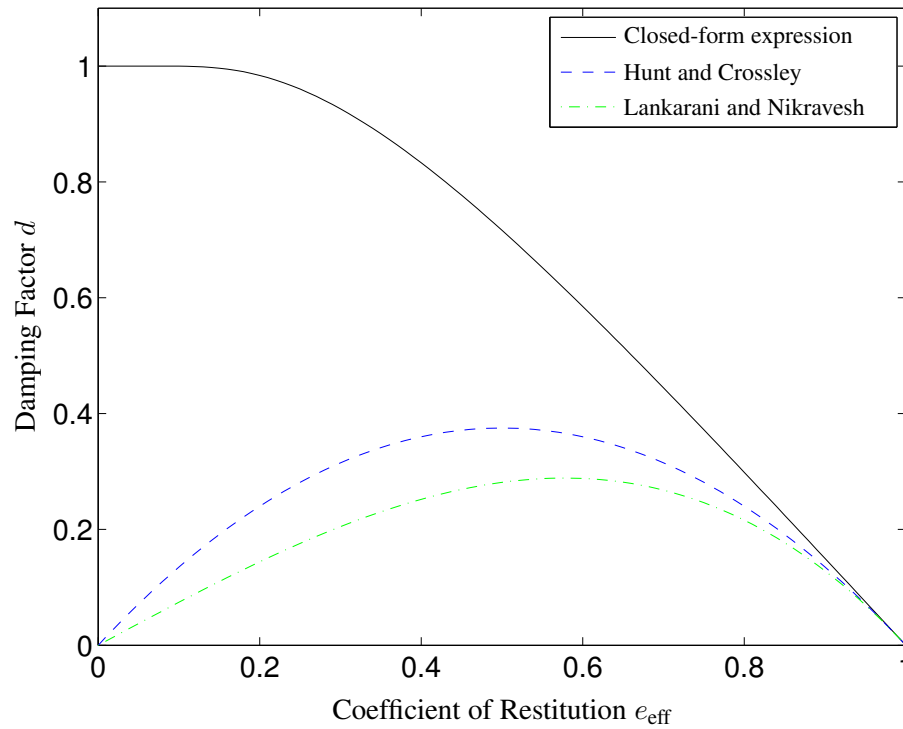


Figure 3.4: Dimensionless damping factor d as a function of e_{eff} .

Since the relationship between e_{eff} and d is constant, the solution can be found a-priori and does not need to be computed during the simulation. This branch uniquely defines the damping factor d as a function of e_{eff} . Therefore, $a v_n^i = d/e_{\text{eff}}$ is also a function of e_{eff} only, which is a constant for a given impact. Thus, the damping factor a is always inversely proportional to v_n^i (and v_n^o) for any e_{eff} and for any impact velocity. The expression for a is

$$a = \frac{d}{e_{\text{eff}} v_n^i}, \quad (3.24)$$

and the hysteresis damping factor is now given as

$$\lambda = \frac{k d}{e_{\text{eff}} v_n^i}. \quad (3.25)$$

Equation (3.25) predicts that λ will become very large as e_{eff} becomes small, an observation that is consistent with the need to have high energy dissipation in plastic impacts.

A definition of d_{HC} corresponding to the model proposed by Hunt and Crossley can be obtained by setting Equation (3.25) equal to Equation (3.13) yielding

$$d_{\text{HC}} = \frac{3}{2} e_{\text{eff}} (1 - e_{\text{eff}}). \quad (3.26)$$

Similarly, a definition of d_{LN} corresponding to the model by Lankarani and Nikravesh gives the following expression

$$d_{\text{LN}} = \frac{3}{4} e_{\text{eff}} (1 - e_{\text{eff}}^2). \quad (3.27)$$

Figure 3.4 shows that both the Hunt and Crossley and the Lankarani and Nikravesh definitions for d approximates the solution of the closed-form expression (Equation (3.23)) only in the region where e_{eff} is near unity. Of the two, the Hunt and Crossley definition appears to give a better approximation. However, for a simulation using either d_{HC} or d_{LN} for $e_{\text{eff}} \neq 1$, the condition $v_n^i = -e_{\text{eff}} v_n^o$ is violated by the results.

Physical Nature of Normal Energy Dissipation

The hysteretic damping formulation in Equation (3.11) is a convenient mathematical instrument to express on a macroscopic scale the complex dynamic effects occurring at the microscopic level. The hysteretic damping term from Equation (3.11) is an energy dissipation mechanism that eliminates the system energy in a manner that is consistent with the overall physical process, but it does so by neglecting the details of the actual phenomena. In essence, the hysteretic damping is a special kind of non-linear damper, and it dissipates energy as a function of the motion of the contact surface. However, the actual phenomena is different.

During impact, the energy is mainly dissipated by the plastic deformation of the surface as-

perities coming into normal contact and through vibrational waves propagating through the elastic bodies. In the latter case, the resulting energy loss is due to a transfer of energy from the overall kinetic energy of the body into internal vibrational energy. The pressure waves associated with these internal vibrations propagate through the bodies and are eventually damped out by the material. This latter mode of energy dissipation exists when the collisions occur at relatively low velocities, such that the speed of the internal pressure waves is significantly higher than the relative body velocity. Hu and Schiehlen (2003) present more detailed investigation on the effects of wave propagation and structural vibration on the modelling of multibody systems with impact.

Stoianovici and Hurmuzlu (1996) experimentally investigated the validity of the rigid-body assumption. They studied how the flexibility of a body affects the effective coefficient of restitution of an impact and defined a criterion to distinguish compact rigid bodies from elongated flexible ones. Their findings indicate that the hysteretic damping correctly models the normal energy dissipation for bodies satisfying the compact rigid-body criterion. Hence, although the hysteretic damping mathematically corresponds to a non-linear damper, it accurately reproduces the effect of energy dissipated in vibrational impact. On the other hand, because the hysteretic damping approximates this effect realistically does not imply that the surface motion behaviour is that of non-linear spring-damper mechanism. The hysteretic damping “mimics” the energy dissipation of the asperity plastic deformation and the material vibration.

In reality, as the bodies collide, there are small local deformations due to the plastic deformations of the surface asperities that occur on top of the overall contact surface deformation that causes the bulk of the contact pressure. The size of these small plastic deformations is comparable to that of the asperities, and is therefore negligible. Additionally, the contact surfaces undergo small but rapid oscillations caused by the displacement of the pressure waves. The magnitude of the pressure wave increases with the force of the collision, and therefore cause more damping. However, these oscillations are not modelled explicitly in the contact model; only their energy dissipation effect is in the form of hysteretic damping. Hence, the model represents the shape of the contact surface that corresponds *on average* to the shape of the quasi-static deformation. That is, the shape of the deformed surfaces is assumed to correspond to the mean value of the oscillations. This latter observations will be useful in Chapter 4 to develop a better formulation for the volumetric contact model. It however highlights the fact that the contact model should not be interpreted as corresponding to a non-linear spring-damper mechanism; only its mathematical representation does.

While the damping in the normal contact force is a significant phenomenon through which energy is dissipated during the impact phase, it is also important to consider the effects of the friction acting along the surface of the contacting bodies in the region of contact. This is considered next.

3.2.2 Tangential Friction Force Model

Unlike the derivation done in the previous section, where the magnitude of the normal contact force was derived using scalar equations, the surface friction force is a vectorial quantity by nature. For oblique and/or non-collinear impacts, the dynamics of motion will in general be coupled in all directions. Thus, it would be incorrect to use two independent, one-dimensional friction models for the friction forces acting along a two-dimensional surface. Furthermore, the stick-slip transitions cannot be considered in the context of an arbitrary direction, e.g., when two colliding bodies are moving with respect to each other; they cannot be sticking in one direction, and sliding in another.

Bristle Friction Force Model

Canudas de Wit et al. (1995) introduced a one-dimensional dynamic friction model that combines the stick-slip behaviour and Stribeck effects, which is characterized by decreasing friction with increasing velocity at low velocity (Armstrong, 1991). To model these frictional effects, it is postulated that the two rigid bodies make contact through elastic bristles. The friction force is modelled as a function of the bristle deformation z and deformation rate \dot{z} ; essentially a simple linear spring-damper model. The dissipative nature of this bristle model is consistent with the dissipative behaviour of the friction process of the asperity model presented in Section 2.4.2. However, the original bristle friction model was introduced in a context where the normal load acting between the two bodies was constant. For modelling impacting bodies, this simplification is not appropriate. It is therefore useful to re-consider the physical analysis that lead to the selection of the spring-damper elements as the bristle model.

The asperity model also suggests that the true area of contact constitutes in fact only a fraction of the total contact area between two bodies. The true contact area corresponds to the sum of the areas where the surface asperities come in contact; see Figure 3.5. It is the interaction of these surface asperities that causes the friction phenomena. These asperities interact in two ways.

First, under a constant normal load, an increase in tangential load will bring the contact sites to their plasticity limits. When they all reach their limits, breakaway occurs and sliding is initiated. This breakaway is preceded by a pre-sliding microscopic displacement: the Dahl effect. The model therefore suggests that the friction force behaves like a spring model when the tangential load does not exceed the breakaway limit. The stiffness of this pre-sliding spring model is related to the number of the asperities in contact and to the size of each individual contact site, or in other words, to the size of the true area of contact.

Secondly, the size of the true contact area has been shown to increase linearly as a function of the normal load. This implies that an increase in normal load will increase the number of asperities in contact and increase the size of the local contact sites. Figures 3.5(a) and 3.5(b) show the change in size of the contact sites as the load increases. Hence, the plasticity limit of each asperity contact site will increase, and because the number of contact sites will also increase, the

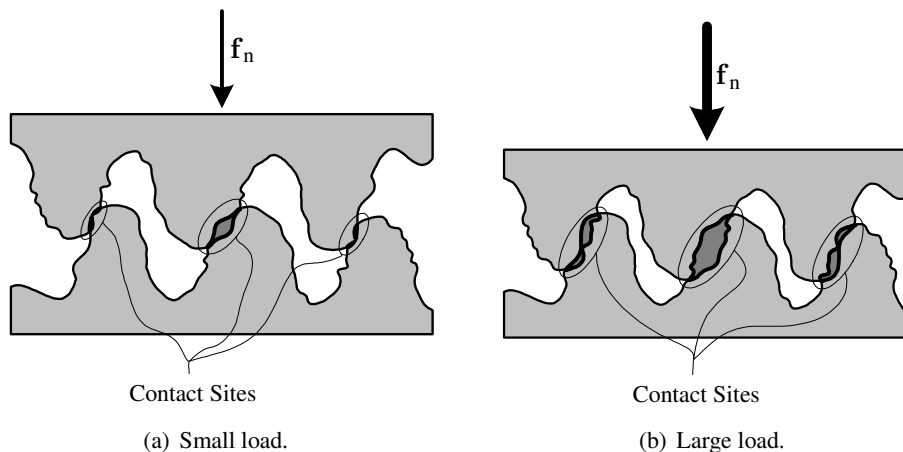


Figure 3.5: The asperity contact sites.

tangential breakaway force will increase as well. This behaviour is consistent with the observation by Coulomb, whereby the friction force increases linearly with the normal load, i.e., the friction force is directly proportional to the size of the true area of contact.

However, it was just observed that the tangential stiffness of the pre-sliding spring model behaviour of the friction is also related to the size of the true area of contact. Hence, an increase in normal load should also affect the stiffness of the pre-sliding spring behaviour in the frictional phenomena. It is therefore suggested that the stiffness of the bristle used to model the pre-sliding spring behaviour be made proportional to the load. A similar argument can be made for the dissipative behaviour of the friction process, i.e., that it should be proportional to the size of the true area of contact, which is itself proportional to the normal load.

The bristle model proposed by Canudas de Wit et al. (1995) can easily be transformed into a vectorized friction model by simply expressing the bristle deformation z as a vectorial quantity, \mathbf{z} , without affecting the model properties. It is then further modified by making its effective stiffness and damping proportional to the normal load f_n as follows

$$\mathbf{f}_{br} = f_n \sigma_0 \mathbf{z} + f_n \sigma_1 \dot{\mathbf{z}} = f_n (\sigma_0 \mathbf{z} + \sigma_1 \dot{\mathbf{z}}) , \quad (3.28)$$

where \mathbf{f}_{br} is the friction force generated from the bending of the bristle, σ_0 and σ_1 are the relative stiffness and damping coefficients and have SI units of m^{-1} and $\text{s} \cdot \text{m}^{-1}$ respectively.

The bristle state will be defined at the velocity level, and integrated to obtain local deformation. However, the use of the original Canudas de Wit et al. model results in ordinary differential equations (ODEs) that are very stiff at low relative velocities (i.e. small \mathbf{v}_t), and cannot be solved using explicit ODE solvers. The bristle state dynamics can be shown to have a time constant of $1/|\mathbf{v}_t|$, which becomes very large at low velocities, while the time constant associated with the relative

body motion dynamics are small and constant during stick. A new definition for the bristle state is therefore needed, and it is presented next.

Bristle Dynamics Model

The bristle dynamics model for $\dot{\mathbf{z}}$ is reformulated into two distinct sub-models: $\dot{\mathbf{z}}_{st}$ for the sticking regime and $\dot{\mathbf{z}}_{sl}$ for the sliding regime. A sticking state function s is introduced to transition smoothly between the stick-slip friction regimes. The deformation rate is now expressed as

$$\dot{\mathbf{z}} = s \dot{\mathbf{z}}_{st} + (1 - s) \dot{\mathbf{z}}_{sl} , \quad (3.29)$$

where

$$s = e^{-\frac{\mathbf{v}_t \cdot \mathbf{v}_t}{v_s^2}} , \quad (3.30)$$

and v_s is the velocity at which the Stribeck effect occurs. With this formulation, $\dot{\mathbf{z}}$ becomes $\dot{\mathbf{z}}_{st}$ (sticking case) when \mathbf{v}_t approaches zero, i.e., $(1 - s) \rightsquigarrow 0$. If \mathbf{v}_t increases, $\dot{\mathbf{z}}$ becomes $\dot{\mathbf{z}}_{sl}$ (sliding case), i.e., $s \rightsquigarrow 0$.

When the friction state is in the stiction regime, the relative motion of the bristles should match exactly the relative motion of the rigid bodies, i.e. the surfaces stick together. Hence, $\dot{\mathbf{z}}_{st}$ is defined as

$$\dot{\mathbf{z}}_{st} = \mathbf{v}_t . \quad (3.31)$$

The sliding rate $\dot{\mathbf{z}}_{sl}$ is defined in terms of the Coulomb friction force \mathbf{f}_C that acts while the two bodies are sliding with respect to each other. Coulomb friction acts in a direction opposite to the relative velocity \mathbf{v}_t between the two bodies and its magnitude is $\mu_C f_n$, where μ_C is the Coulomb friction coefficient. To simplify the notation, the negative sign for the Coulomb friction will be included in the formulation later on. The friction force \mathbf{f}_C is thus described by

$$\mathbf{f}_C = \mu_C f_n \text{dir}_\epsilon(\mathbf{v}_t, v_\epsilon) , \quad (3.32)$$

where dir_ϵ returns a unit vector along the direction of \mathbf{v}_t . The function dir_ϵ uses the relaxed sign convention near a small velocity tolerance v_ϵ to regularize the function at small vector magnitudes and avoid the possibility of dividing by zero. It is therefore suitable for a numeric implementation and is given as

$$\text{dir}_\epsilon(\mathbf{u}, u_\epsilon) = \begin{cases} \frac{\mathbf{u}}{|\mathbf{u}|} & ; \quad |\mathbf{u}| \geq u_\epsilon \\ \frac{\mathbf{u}}{u_\epsilon} \left(\frac{3}{2} \cdot \frac{|\mathbf{u}|}{u_\epsilon} - \frac{1}{2} \left(\frac{|\mathbf{u}|}{u_\epsilon} \right)^3 \right) & ; \quad |\mathbf{u}| < u_\epsilon \end{cases} , \quad (3.33)$$

where \mathbf{u} and u_ϵ are a vector and a scalar value, respectively. While the two rigid bodies are sliding with respect to each other, the friction force \mathbf{f}_{br} applied by the bristle should be \mathbf{f}_C . Setting Equation (3.28) equal to Equation (3.32), and solving for $\dot{\mathbf{z}} \approx \dot{\mathbf{z}}_{\text{sl}}$ yields

$$\dot{\mathbf{z}}_{\text{sl}} = \frac{1}{\sigma_1} \mu_C \text{dir}_\epsilon(\mathbf{v}_t, v_\epsilon) - \frac{\sigma_o}{\sigma_1} \mathbf{z}. \quad (3.34)$$

Equation (3.34) is a first order ODE and has a time constant $\tau_{\text{br}} = \sigma_1/\sigma_o$. The bristle dynamics time constant τ_{br} controls how fast the bristles reach a steady-state deformation when two rigid bodies are moving at a constant relative velocity. Interestingly, although the bristle force itself is proportional to the normal load f_n , the bristle velocity is not. It is a function of the tangential relative velocity direction and the constant parameters σ_o , σ_1 and μ_C only.

To summarize, the bristle deformation rate is given as

$$\dot{\mathbf{z}} = s \mathbf{v}_t + (1 - s) \left(\frac{1}{\sigma_1} \mu_C \text{dir}_\epsilon(\mathbf{v}_t, v_\epsilon) - \frac{\sigma_o}{\sigma_1} \mathbf{z} \right). \quad (3.35)$$

Dwell Time Dependency of Friction

While the two rigid bodies are sticking to each other, the maximum friction force is limited by the stiction force $\mu_S f_n$, where μ_S is the stiction coefficient. Experimental observations (Rabinowicz, 1956; Bell and Burdekin, 1969) have shown that the full magnitude of the stiction force does not come into effect as soon as the relative velocity becomes zero. Instead, the maximum stiction force gradually increases over time, and eventually reaches the upper limit $\mu_S f_n$. This phenomenon is also called dwell-time dependency.

On the other hand, the temporal lag effect associated with the dwell-time is only present for the slip-stick transition, i.e., it takes some time for the microscopic asperities to settle into each other and for the molecular bonding to take place. As soon a stick-slip transition occurs, these bonds shatter at once. Hence, there is a need to include two time constants to correctly model the dwell-time effect on the maximum stiction force. A new state, s_{dw} , is introduced to model the effect of the dwell-time on the maximum stiction force

$$\dot{s}_{\text{dw}} = \begin{cases} \frac{1}{\tau_{\text{dw}}}(s - s_{\text{dw}}) & ; \quad s - s_{\text{dw}} \geq 0 \\ \frac{1}{\tau_{\text{br}}}(s - s_{\text{dw}}) & ; \quad s - s_{\text{dw}} < 0 \end{cases}, \quad (3.36)$$

where τ_{dw} is the dwell-time dynamics time constant and τ_{br} is the bristle dynamics time constant, as before. Typically, τ_{dw} should be at least an order of magnitude larger than τ_{br} . With the definition proposed for \dot{s}_{dw} in Equation (3.36), s_{dw} simply follows the value of s with a long time delay as s goes to 1 (sticking) while it follows it very quickly (as fast as the bristle dynamics allow) when s

goes to zero (sliding). The maximum stiction coefficient μ_{\max} can now be defined as

$$\mu_{\max} = \mu_C + (\mu_S - \mu_C) s_{dw} , \quad (3.37)$$

such that the maximum stiction force f_{\max} is

$$f_{\max} = \mu_{\max} f_n . \quad (3.38)$$

As mentioned previously, the bristle friction force should never exceed f_{\max} at any time. In particular, the stick-slip friction regime transition can only happen if the magnitude of the bristle force becomes saturated, such that the surfaces of the two rigid bodies can start accelerating with respect to each other and the relative velocity increases beyond v_S . To this end, the saturation function $\text{sat}(\mathbf{u}, u_{\max})$ is defined as

$$\text{sat}(\mathbf{u}, u_{\max}) = \begin{cases} \mathbf{u} & ; \quad |\mathbf{u}| \leq u_{\max} \\ \frac{\mathbf{u}}{|\mathbf{u}|} u_{\max} & ; \quad |\mathbf{u}| > u_{\max} \end{cases} . \quad (3.39)$$

The magnitude of both \mathbf{f}_{br} and f_{\max} are proportional to f_n ; see Equations (3.28) and (3.38). Hence, the saturation of \mathbf{f}_{br} by f_{\max} can be written as

$$\text{sat}(\mathbf{f}_{\text{br}}, f_{\max}) = f_n \text{sat}(\sigma_o \mathbf{z} + \sigma_1 \dot{\mathbf{z}}, \mu_{\max}) . \quad (3.40)$$

When the magnitude of the bristle force exceeds f_{\max} , $\dot{\mathbf{z}}$ needs to be re-computed to ensure the result for Equation (3.28) is consistent with the scaling of \mathbf{f}_{br} . Setting Equation (3.28) equal to Equation (3.40) the new expression to compute $\dot{\mathbf{z}}$ is

$$\dot{\mathbf{z}} = \frac{1}{\sigma_1} \text{sat}(\sigma_o \mathbf{z} + \sigma_1 \dot{\mathbf{z}}, \mu_{\max}) - \frac{\sigma_o}{\sigma_1} \mathbf{z} . \quad (3.41)$$

Again, Equation (3.41) shows that the bristle dynamics is independent of f_n , and is governed by $\tau_{\text{br}} = \sigma_1/\sigma_o$ which is constant. This feature ensures that the friction model will never cause numerical problems, even when the relative velocity is low, which is a key advantage over the formulation proposed by Canudas de Wit et al. (1995).

In Section 3.2.2 it was established that both the bristle stiffness and damping should be proportional to the true area of contact and hence to the normal load. To include the effect of lubrication in the friction model, a viscous damping term is added and it is also made proportional to the normal load. The rationale here is that the shear stress from the lubrication fluid increases when the fluid film thickness decreases. Hence, with a higher normal load, the fluid film thickness will shrink and the shear stress will increase.

The tangential friction force \mathbf{f}_t can now be computed. A term proportional to the relative

tangential velocity and to the normal load is added to account for viscous friction so that

$$\mathbf{f}_t = -f_n (\text{sat}(\sigma_0 \mathbf{z} + \sigma_1 \dot{\mathbf{z}}, \mu_{\max}) + \sigma_2 \mathbf{v}_t) , \quad (3.42)$$

where σ_2 is the relative viscous damping coefficient. It is seen that Equation (3.42) is very similar to Equation (3.28), except for the addition of the saturation function and the viscous damping term. Equation (3.42) also includes the negative sign to ensure that the friction model force acts against the motion. Clearly, at any point in time, the friction model will always return a friction force that is proportional to the normal. This behaviour is consistent with the observations by Coulomb.

The proposed friction model is a seven parameter model; see Table 3.1 for a list of the friction model parameters. Note that the bristle dynamics time constant is inferred from σ_0 and σ_1 , and a numerical tolerance v_ϵ must also be specified. As a guideline the v_ϵ should be at most one tenth of v_S . This minimizes the impact of the dir_ϵ function regularization on the system dynamics when $|\mathbf{v}_t| < v_\epsilon$ since the friction model will have already switched into the “stick” mode in this velocity range; see Equations (3.29) and (3.30). The value of $v_\epsilon = 1/100 v_S$ was used for all simulation examples presented in this thesis. The next section proposes methods to establish the values for the all contact model parameters.

Parameter	Description
μ_S	Stiction friction coefficient (static friction)
μ_C	Coulomb friction coefficient (kinetic friction)
σ_0	Load-dependent bristle stiffness
σ_1	Load-dependent bristle damping coefficient
σ_2	Load dependent viscous damping coefficient
v_S	Stribeck velocity
τ_{dw}	Dwell-time dynamics time constant

Table 3.1: Friction model parameters.

3.3 Point Contact Model Parameters

To use the contact model in a multibody dynamics simulation, the parameters of the model must be known or selected. This section will discuss how each parameter of the contact model could be obtained experimentally in general terms. The goal of the discussion in this section is to show that all the contact model parameters can be obtained through an experimental procedure, or otherwise inferred from relevant data.

However, in an operational context, it may not always be feasible to perform all the necessary experiments to find values for these parameters. Most often, only the most important values will be known, such as the contact stiffness, or the Coulomb friction coefficient(s). The discussion in the section will therefore also focus on general rules to select these parameters, such that appropriate

values can be quickly identified to get a simulation running. First the parameters for the normal contact model will be examined followed by a discussion on the friction model parameters.

3.3.1 Normal Contact Force Model

The normal contact model has two types of parameters which can be independently set: the parameters for the stiffness and those affecting the damping behaviour.

The contact stiffness parameter can be found using the Hertz theory; see Equation (2.2) and in the literature (Gladwell, 1980; Johnson, 1985; Barber, 1992; Alexandroff and Pozharskii, 2001; Fischer-Cripps, 2000). The stiffness can also be identified experimentally (Lange and Gonthier, 2003; Agar et al., 2005), essentially by curve fitting a force versus indentation depth plot when the force is applied quasi-statically.

The damping term for the proposed contact model is directly a function of the coefficient of restitution. One option is to measure this coefficient directly by performing an impact experiment and measuring the velocity just before and after the impact, or by simply tuning the parameter such that position history curves match with the experimental data (Stoianovici and Hurmuzlu, 1996). Finally, the impact behaviour of many materials has been studied (Goldsmith, 1960) and the coefficient of restitution can be found using Equation (3.12).

The normal contact model was developed under the assumption that there is an impact cycle with incoming and outgoing velocities. Obviously, when the contact occurs at very low velocities, the bodies may never bounce away from each other when an external force such as gravity is acting on the system. Hence, in the actual implementation, the contact model includes a minimal velocity threshold v_{small} that must be specified. When the initial impact velocity is less than v_{small} , the hysteretic damping factor becomes constant, i.e.,

$$a = \frac{d}{e v_{\text{small}}} . \quad (3.43)$$

Experimentally, v_{small} can be determined by measuring the last initial impact velocity before the bodies stop bouncing with respect to each other. If this information is not available, the value selected for v_{small} should be small compared to the expected impact velocities of the simulation scenarios, e.g., less than 1 mm/s for a typical robotic task. v_{small} is not a numerical threshold parameter like v_ϵ ; its value affects a physical phenomenon, i.e., the last impact velocity before lasting contact occurs. Its value should in general be larger than v_ϵ because v_ϵ is a purely numerical tolerance.

The primary role of tolerance v_ϵ is avoid the numerical problem associated with a division by zero. However, the regularization of the dir_ϵ when the magnitude of the relative tangential velocity is less than v_ϵ also has an essential role in the numerical implementation. When the relative velocity is very small, its direction will become numerically indeterminate, i.e., will be directly a function of the noise in the numerical solution of the ODE. Hence, it is important filter out these meaningless

values of direction.

One additional parameter was added to the normal contact model implementation for Simulink. When using fixed-step solvers, Simulink does not allow the detection of the exact time at which the collision occurs. Instead, the contact force starts being applied at the first time step *after* the bodies come into contact. Hence, the contact force is not applied as soon as the bodies start touching and this “error” can cause an increase in total system energy. To avoid the artificial increase in energy, the penetration depth at the time the contact is first detected is used as a reference position to calculate a relaxed penetration depth estimate x_r as follows

$$x_r = x - x_{r,0} \quad (3.44)$$

where $x_{r,0}$ is set equal to the current penetration depth at the instant the impact is detected. The relaxed depth estimate is then used in place of the true penetration depth to calculate the normal contact force. As a result, the contact force at the detected instant of impact is zero. The reference position $x_{r,0}$ is then slowly brought back to zero using a first order ODE with a slow time constant. Hence, the numerical relaxation introduces an additional state x_r for which the solver must find the solution. The resulting numerical relaxation ODE is given as

$$\dot{x}_{r,0} = -\frac{1}{\tau_r} x_{r,0} , \quad (3.45)$$

where τ_r is the numerical constraint relaxation time constant. This time constant should be selected large enough so that the dynamics of the numerical relaxation does not affect the dynamics of the system. A suggested range of values is $\tau_r \geq 1$ s. The numerical relaxation of the constraint is a compromise solution to deal with the drawback of the fixed-step solver implementation in Simulink: a temporary error in position is introduced, but the artificial energy gain is avoided. It should be noted that the numerical constraint relaxation process has no impact on the system dynamics when a variable-step solver is used in Simulink. In this case, Simulink iterates to find the exact time of impact at machine-precision accuracy and, hence, the initial penetration depth is zero.

3.3.2 Tangential Friction Force Model

The friction model unavoidably requires a value for the Coulomb friction coefficient μ_C . Without this value, is it impossible to know how much friction needs to be applied. However, most of the other parameters of the friction model can be inferred from this value and a few general estimates.

The Coulomb friction coefficient can be determined by applying a normal load on a contact surface at a constant velocity and measuring the tangential force. Performing the same experiment at different velocities yields both the Coulomb friction coefficient μ_C and the relative viscous damping coefficient σ_2 , which can be inferred from the slope of the force versus velocity curve. If the simulation scenario involves relative motion occurring at low velocities, the effect of σ_2 can

usually be neglected, i.e., $\sigma_2 \approx 0$. This is the case for most space-based manipulator tasks.

The stiction coefficient μ_S can be obtained using the apparatus shown in Figure 2.7(a). However, if the pre-sliding distance can be measured, then this latter experiment will also provide the value for the stiction coefficient. To measure the pre-sliding distance, the contacting objects must be at rest and a constant normal load must be applied. Then a slowly increasing tangential force should be applied and the relative displacement of the objects is measured. Once the stiction limit is reached, the objects will start to rapidly accelerate with respect to each other, i.e., a stick-slip transition is provoked. This latter experiment provides a value for the stiction force, and since the normal force is known, the stiction coefficient μ_S is readily obtained. The same experiment can be performed at various loads to obtain more reliable data. Alternatively, if the simulation does not require the friction to include a stick-slip behaviour, then μ_S can be set arbitrarily equal to μ_C , which in effect deactivates the stick-slip modelling mechanism of the friction model.

The pre-sliding experiment also provides a measure for the pre-sliding displacement δz . If the tangential force is increased very slowly during the experiment, then the relative velocity at the contact surface should be very small and bristle stiffness parameter can be inferred directly from the pre-sliding displacement measurement. Setting Equation (3.28) equal to $\mu_S f_n$, and noting that at the time the tangential force reaches the breakaway limit force, the bristle deformation is δz and the bristle velocity $\dot{z} \approx 0$, the bristle relative stiffness is found simply as

$$\sigma_o = \frac{\mu_S}{\delta z} \quad (3.46)$$

Alternatively, if the pre-sliding experiment data is not available, it is possible to simply pick a value that would be suitable for a given simulation scenario. For example, an operations engineer would not necessarily care that the simulation accurately replicates the pre-sliding displacement behaviour. In this case using a value much smaller than the size of the objects involved would be adequate, e.g., $\delta z = 0.1$ mm for a typical robotic payload.

Obtaining a value for σ_1 is more tricky. If the pre-sliding displacement δz can be measured, then one option is to hit one object with a tangential impacting force that is small enough not to cause the object to slide, but large enough to generate some measurable oscillations. The second object should be held firmly to the ground. The magnitude of the oscillations will be in the order of δz but will decay in time. While in stiction, the oscillating system essentially behaves as a mass held stationary by a spring-damper. The equation of motion is as follows:

$$m \ddot{x} + f_n \sigma_1 \dot{x} + f_n \sigma_o x = 0, \quad (3.47)$$

where m is the mass of the object hit by the impacting force. If the normal force corresponds to the weight of the object, then $f_n = mg$, where g is the acceleration due to gravity. In this case,

Equation (3.47) simplifies to

$$\ddot{x} + g \sigma_1 \dot{x} + g \sigma_0 x = 0 . \quad (3.48)$$

A general form for second order differential equation is

$$\ddot{x} + 2\zeta \omega_d \dot{x} + \omega_d^2 x = 0 , \quad (3.49)$$

where ζ is the damping ratio and ω_d is the damped frequency of the system. Normally, the value for ζ should be in the range from 0 to 1, with the value of 1 corresponding to the critically damped case. Values over 1 correspond to an over-damped system. When $\zeta = 1$, then $\omega_d = \omega_{\text{nat}} = \sqrt{g \sigma_0}$, where ω_{nat} is the natural undamped frequency of the system. The parameters ω_d and ζ can be found by looking at the frequency and the rate of decay of the oscillations. Comparing Equations (3.48) and (3.49), it is clear that σ_0 and σ_1 can be identified from the impact experiment, i.e.,

$$\begin{aligned} \sigma_0 &= \frac{\omega_d^2}{g} , \\ \sigma_1 &= \frac{2\zeta \omega_d}{g} . \end{aligned} \quad (3.50)$$

On the other hand, performing the impact experiment may not always be possible. The example of the operations engineer is considered once more. If the value for the pre-sliding displacement was based on engineering judgement, then it makes no sense to identify σ_1 experimentally. Some heuristic rule should be used instead.

A body sliding freely on a rough surface is considered. If no other external forces act on this body, it will eventually stop moving under the action of the friction force, and its total kinetic energy will vanishes as soon as it stops. The kinetic energy associated with the translational motion does not get converted into internal vibrational energy. The kinetic energy is simply dissipated by the plastic deformation of the surface asperities. Hence, the vibrational energy associated with the oscillations discussed above should also vanish quickly. The value for σ_1 must therefore be selected such that the friction model dissipates energy quickly when the stiction phase is initiated and that the tangential oscillations are minimized. In other words, it is desirable to have high damping and maintain a quick system response. These conditions are obtained when the oscillating system is critically damped, i.e., ζ is set 1. Using this setting, σ_1 is set simply as

$$\sigma_1 = 2\sqrt{\frac{\sigma_0}{g}} , \quad (3.51)$$

which implies that the bristle time constant $\tau_{\text{br}} = \sigma_1/\sigma_0$ is

$$\tau_{\text{br}} = \frac{2}{\sqrt{g \sigma_0}} = \frac{2}{\omega_{\text{nat}}} . \quad (3.52)$$

Next, to obtain the dwell-time dynamics time constant τ_{dw} , it is necessary to perform the Bowden and Leben stick-slip experiment described in Section 2.4.4 for various conveyor-belt velocities. These experiments will determine the range of relative surface velocity at which the dwell-time dynamics have an influence. The behaviour can then be reproduced in simulation to identify a representative value for τ_{dw} . However, if this value cannot be determined experimentally, or the modelling of the dwell-time dynamics is not relevant to the simulation scenario, then a value can be selected by picking a value greater than τ_{br} by an order of magnitude since the model assumes the bristle dynamics time-constant to be much faster than the dwell-time dynamics.

Alternatively, the dwell-time dynamics feature of the friction model can be disabled altogether by setting s_{dw} equal to s in the friction model instead of using the first order ODE in Equation (3.36). This later choice effectively removes the dwell-time dependency feature of the friction model. In effect, τ_{dw} is set to zero, i.e., there is no delay between s and s_{dw} .

Finally, the Stribeck velocity can be determined as follows. When the magnitude of the relative tangential velocity reaches twice the value of the Stribeck velocity parameter v_S , Equation (3.30) shows that the sliding mode coefficient $(1 - s) = (1 - e^{-4}) = 0.98$, i.e., the friction model is in sliding mode. Hence, the range of values of the velocity in the region III of the Stribeck curve shown in Figure 2.6 corresponds roughly to twice the value of the Stribeck parameter of the friction model. The exact estimate for v_S must be found experimentally by tuning the value of v_S to fit the experimental data. However, when it is not possible to perform these experiments, a value much smaller than the expected relative tangential velocities should be used, e.g., 1 mm/s for a typical robotic task.

Chapter 4

Volumetric Contact Model

This chapter presents a new contact modelling approach based on volumetric properties. The chapter provides the derivations from first principles of all the contact model components. The presented theoretical derivations are based on a Winkler elastic foundation model, a simplified version of elastic stress theory. Unlike the model presented in Chapter 3, which was based on the Hertz theory, the use of this new contact model is not restricted to bodies with non-conformal geometries.

4.1 Elastic Foundation Model

Figure 4.1 shows an example of bodies with conformal geometries. The figure shows a typical payload Dextre will be handling, and the worksite into which it must insert or from which it must extract the payload. Because the two bodies have many flat sub-surfaces, the resulting area of contact can become relatively large, thereby invalidating the fundamental assumption of small area of contact upon which the Hertz theory is built. A different compliant contact modelling scheme is therefore needed to tackle this type of simulation.

This chapter introduces an alternative contact modelling approach that can address the contact mechanics problem for bodies of arbitrary shape, whether they are conforming or not. This new modelling method is based on a compliant contact model approach but uses information related to the volume of inter-penetration of the colliding bodies. This volume is defined as the volume spanned by the intersection of the two undeformed geometries of the colliding bodies and will be called hereafter the *volume of interference*. In contrast to most other compliant modelling methods, which are commonly based on the point of deepest penetration, the proposed method yields a contact force proportional to the volume of interference, specifies that the force should be applied at the centroid of this volume and that the rolling resistance and spinning friction torques are proportional to the geometric inertia tensor of the volume of interference. This chapter presents detailed derivations demonstrating why the volumetric properties can be used to correctly account for all components of the contact forces acting between two colliding bodies, and introduces a new method to determine the normal of the contact surface. The volumetric contact model derivations

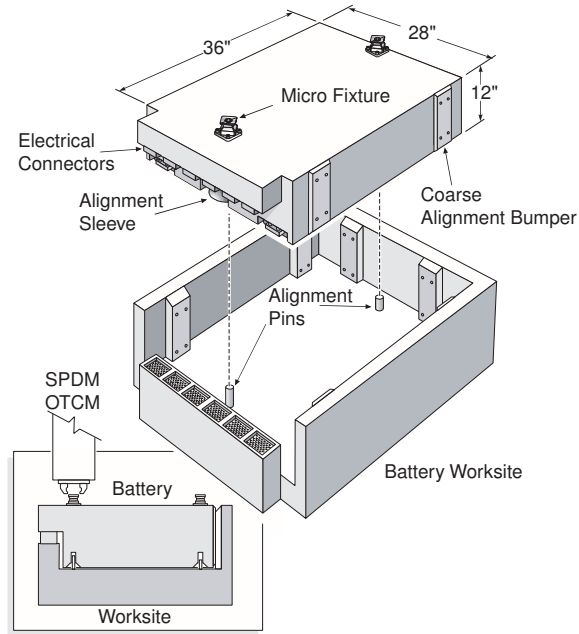


Figure 4.1: Two bodies with conformal geometries: a battery box and its worksite.

are based on the Winkler elastic foundation model approximation presented in Section 2.3.1. The next section explains how the foundation model is adapted to the context of contact modelling for a multibody simulation.

4.1.1 Contact Model Hypothesis

Before establishing the volumetric contact model theory, it is necessary to consider the context in which the contact model will be used. For typical robotic tasks, it is expected that:

1. The maximum contact force is bounded and will never exceed the material elastic limit.
2. The contacting bodies are stiff.
3. The impacts occur at low velocities.
4. The Amontons laws of friction are applicable.

The first hypothesis indicates the normal contact forces can suitably be modelled using a compliant contact model based on the elastic properties of the contacting object material. In other words, the contact force will never plastically deform the object. In the context of space robot operations, the first hypothesis is in fact a requirement for any robotic task operation. A space-based robotic system should *never* damage any of the payloads or the environment, given the cost of launching the payloads and the enormous effort required if they need to be replaced.

The second hypothesis, considered in conjunction with the first one, indicates that the inter-penetration depth between objects in contact should be small. Basically, the space-based robotic systems will be applying small forces to fairly rigid objects, so it is reasonable to assume that the inter-penetration depths to be orders of magnitude smaller than the object sizes, i.e., negligible. For example, the maximum force Dextre¹ was designed to apply is 111 N, whereas the payloads it must manipulate are made of aluminium, titanium or steel.

The third hypothesis suggests that the dissipative nature of the contact phenomena can be modelled by including a hysteretic damping term in the normal contact force law. This type of energy dissipation mechanism is appropriate to model low-speed impacts, as seen in Section 2.2.2.

The last hypothesis is a prerequisite to be able to include any Coulomb-type of friction model, with or without stick-slip modelling. The law stipulates that the friction force is proportional to the normal load. This has a significant implication on the implementation of the contact model: the friction force acts perpendicular to the normal load, or otherwise the normal load would not be “normal”.

4.1.2 Contact Surface

To tackle the derivations of the contact model properties using the elastic foundation model assumption, the fourth assumption from the previous section must be generalized to the whole contact model: it will be assumed that the contact surface is *flat*.

This latter assumption has two consequences: first the contact normal is constant over the contact area, and second that the normal force of the contact model will be perpendicular to the tangential friction force. Given that the inter-penetration depth has already been established as very small, the flat surface assumption does allow the modelling of contact between convex geometries — conforming or not. In these cases, the object shapes never ‘wrap around’ each other, such that motion perpendicular to the normal contact direction is not hindered by the geometry of the objects, and is affected only by the frictional forces.

Figure 4.2(a) shows two convex geometries in contact, a cube and a sphere, with the sphere shown at three different locations. An arrow shows the normal contact force acting on the sphere at each location. For all the positions of the sphere, it is seen that any motion of the sphere perpendicular to the normal force can only result in frictional forces. The shape of the cube will not constrain the sphere from moving ‘sideways’ to the normal contact force direction.

However, when dealing with a convex-concave geometric pair this is no longer the case. An object can be inserted into another, such that sideways motion will not only induce frictional forces, but will also cause new parts of the geometries to come into contact, thus introducing normal forces from a different direction. Figure 4.2(b) shows such a case. Here, when the sphere is moved to the right, a new contact force appears and blocks its right-wise motion. This force is not frictional by nature. It corresponds to the normal contact force from the wall to the right of the sphere. To

¹SPAR-SS-SG-2899 SPDM Specification - Rev. C

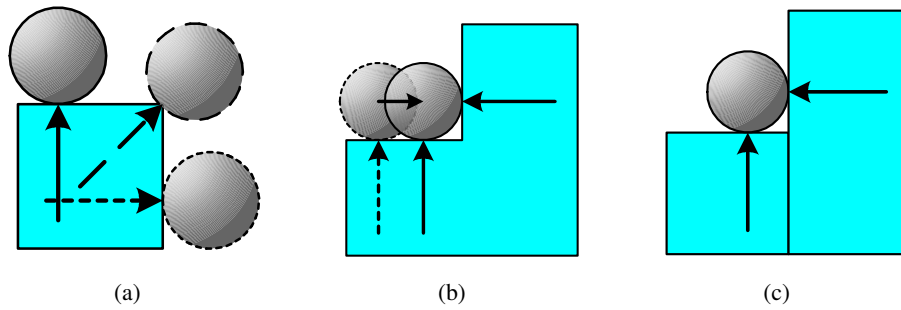


Figure 4.2: Concave and convex objects.

deal with this problematic case, all objects must be decomposed in convex sub-parts such that the contribution of contact forces from each individual convex sub-component is accounted for. This solution is illustrated in Figure 4.2(c), where the concave shape is split into two separate convex shapes, such that two different objects contribute to the contact force acting on the sphere.

The convex-object subdivision process can be considered for a curved concave surface as well. The case of a contact between a sphere and a corner is considered again, assuming this time the contact is frictionless. Figure 4.3(a) shows the sphere touching the corner in two places. Again, when the sphere is moved to the right this will affect only the contact force of the vertical wall to the right of the sphere, but will not affect the force between the horizontal part of the corner and the sphere: these forces correspond to two distinct physical phenomena and should be treated separately. As before, the corner is split into two distinct (and convex) parallelepipeds such that two contact forces are applied.

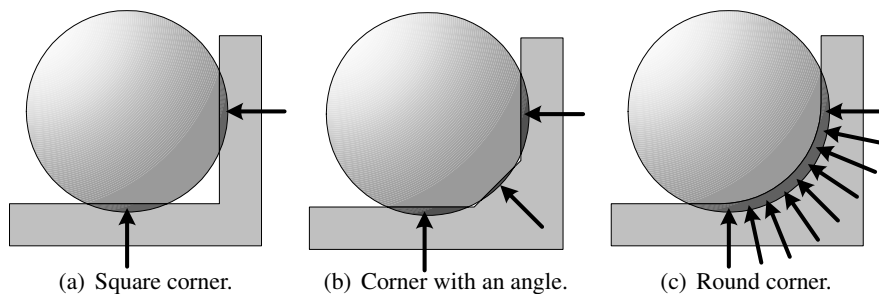


Figure 4.3: A sphere in contact with a corner.

Next, consider the forces acting on the sphere when an angle is introduced in the corner, as shown in Figure 4.3(b). There are now three distinct forces acting on the sphere. Again, the additional force could be modelled by introducing a prism geometry in addition to the two parallelepipeds, thus resulting in three distinct contact models. The same process can be repeated as the number of angles increases even further, thus resulting in even more contact models. Eventually,

with a fine enough discretization, the corner surface will become smooth, and the forces will appear continuous, as shown in Figure 4.3(c). In the end, the number of convex sub-objects needed to accurately represent a concave curved surface will depend on the accuracy requirements of the simulation scenario.

It should be noted that increasing the number of contact elements will not increase the overall contact force since the force of each contact sub-element is proportional to the volume of interference contained in that element, and that the overall volume is independent of the number of contact elements. Hence, with this volumetric approach, the modelling of contact between objects with complex shapes can be accomplished by splitting the objects into a sufficiently large number of convex sub-objects without affecting the stiffness properties of the contact phenomena.

4.1.3 Adapting the Elastic Foundation Model for Modelling Contact

The basic concept for the Winkler elastic foundation model was presented in Section 2.3.1. The foundation model is usually conceptualized as a flat mattress of springs into which a hard non-flat object is pressed; see Figure 2.1. However, since the contact model assumes the contact surface is flat, it is more convenient to imagine that it is the flat surface which is hard and that it is the non-flat object that is deforming.

Furthermore, in this work the elastic foundation model will be interpreted in a figurative sense. It is usually construed as a mattress of springs in compression when the two bodies collide. Instead, the foundation model will be interpreted as a set of *tensile* springs attached to the undeformed surfaces of the colliding objects, and acting to separate them. In other words, the colliding body surfaces are allowed to pass through each other and the foundation springs pull on the inside surface of each body to bring them apart. Figure 4.4 shows the new elastic foundation concept, with the

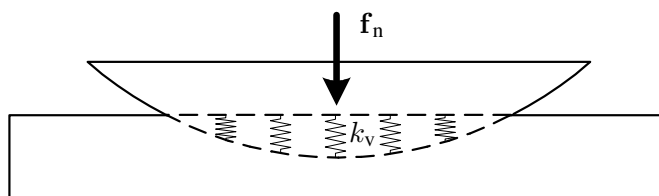


Figure 4.4: The modified Winkler elastic foundation model.

normal contact force \mathbf{f}_n and where the volumetric stiffness is $k_v = k_f/h_f$. The parameter k_v has SI units of $[\text{N}/\text{m}^3]$. This interpretation of the foundation model has the advantage of avoiding the need to explicitly define the foundation depth h_f and it emphasizes the relationship between the shape of the volume of interference and the normal contact force. In Figure 4.4, the contour of the volume of interference is shown in dashed lines.

A few additional definitions are now introduced to help define the Winkler elastic foundation

contact model in terms of body-fixed quantities. To model the contact of two deformable bodies, a thin, flat, rigid and massless plate is inserted between the two deformable bodies such that the contacting surface of each body conforms exactly to the plate, called hereafter the *contact plate*; see Figure 4.5. The contact plate ensures the flatness of the surface of contact. It is also assigned the same frictional properties as the surfaces of the two colliding bodies.

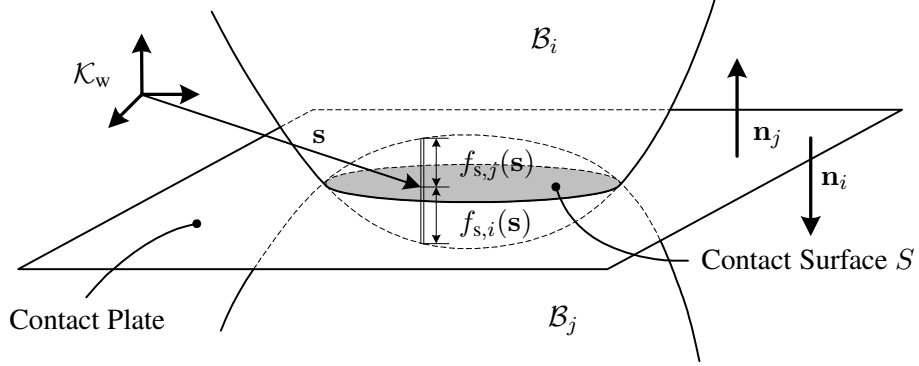


Figure 4.5: The contact surface between two deformable bodies.

Figure 4.5 shows the resultant contact surface S obtained by inserting the contact plate between the bodies \mathcal{B}_i and \mathcal{B}_j . The vector \mathbf{s} shows the location of an infinitesimal surface element dS relative to inertial reference ‘world’ frame \mathcal{K}_w . The orientation and position of the plate will be investigated in further detail in Section 4.3.7. The local elastic foundation deformation depths of bodies \mathcal{B}_i and \mathcal{B}_j at \mathbf{s} are obtained with the body shape functions $f_{s,i}(\mathbf{s})$ and $f_{s,j}(\mathbf{s})$ respectively, where $f_{s,i}(\mathbf{s})$ and $f_{s,j}(\mathbf{s})$ correspond to the distance by which the foundation spring is “stretched” on each side of the contact plate and are measured along the normal directions \mathbf{n}_i and \mathbf{n}_j respectively. \mathbf{n}_i and \mathbf{n}_j are selected to be pointing out of bodies \mathcal{B}_i and \mathcal{B}_j , such that $\mathbf{n}_j = -\mathbf{n}_i$. The contact surface normal \mathbf{n} is defined as pointing out of \mathcal{B}_j toward \mathcal{B}_i following the convention adopted in Section 3.1 and, hence, $\mathbf{n} = \mathbf{n}_j = -\mathbf{n}_i$.

Similarly as was done in Section 3.1, the states of the two bodies \mathcal{B}_i and \mathcal{B}_j are defined using two body-fixed frames \mathcal{K}_i and \mathcal{K}_j . The origin of each frame is defined by the position vectors \mathbf{r}_i and \mathbf{r}_j relative to \mathcal{K}_w ; see Figure 4.6. Their orientation with respect to \mathcal{K}_w is assumed to be described by the rotation matrices \mathbf{R}_i and \mathbf{R}_j . The frames translate at a velocity \mathbf{v}_i and \mathbf{v}_j and rotate with an angular velocity $\boldsymbol{\omega}_i$ and $\boldsymbol{\omega}_j$. Now, let $\boldsymbol{\rho}_i$ and $\boldsymbol{\rho}_j$ represent the location of a point \mathbf{s} on the contact surface S relative to bodies \mathcal{B}_i and \mathcal{B}_j respectively, and given as

$$\begin{aligned} \boldsymbol{\rho}_i &= \mathbf{s} - \mathbf{r}_i, \\ \boldsymbol{\rho}_j &= \mathbf{s} - \mathbf{r}_j. \end{aligned} \tag{4.1}$$

Figure 4.6 also shows $h_i(\boldsymbol{\rho}_i, \mathbf{n}_i)$ and $h_j(\boldsymbol{\rho}_j, \mathbf{n}_j)$ which give the body surface heights above $\boldsymbol{\rho}_i$

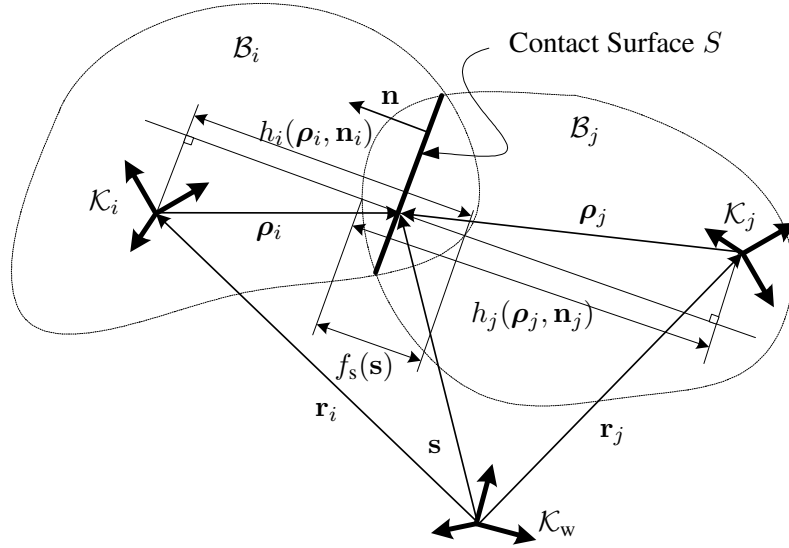


Figure 4.6: Parameters for the Winkler elastic foundation model.

and ρ_j , measured along the directions \mathbf{n}_i and \mathbf{n}_j with respect to the body reference frames \mathcal{K}_i and \mathcal{K}_j , respectively. The lengths $h_i(\rho_i, \mathbf{n}_i)$ and $h_j(\rho_j, \mathbf{n}_j)$ are defined by the geometry of bodies \mathcal{B}_i and \mathcal{B}_j , and their values depend only on the tangential components of ρ_i and ρ_j , respectively, i.e., $h_i(\rho_i, \mathbf{n}_i) = h_i(\mathbf{T} \cdot \rho_i, \mathbf{n}_i)$ and $h_j(\rho_j, \mathbf{n}_j) = h_j(\mathbf{T} \cdot \rho_j, \mathbf{n}_j)$, where \mathbf{T} is the projection operator defined in Section 3.1.2. The shape functions $f_{s,i}(\mathbf{s})$ and $f_{s,j}(\mathbf{s})$ are defined in terms of the surface height function as follows,

$$\begin{aligned} f_{s,i}(\mathbf{s}) &= h_i(\rho_i, \mathbf{n}_i) - \mathbf{n}_i \cdot \rho_i = -h_i(\rho_i, \mathbf{n}) + \mathbf{n} \cdot \rho_i, \\ f_{s,j}(\mathbf{s}) &= h_j(\rho_j, \mathbf{n}_j) - \mathbf{n}_j \cdot \rho_j = h_j(\rho_j, \mathbf{n}) - \mathbf{n} \cdot \rho_j, \end{aligned} \quad (4.2)$$

where $h_i(\rho_i, \mathbf{n}_i) = -h_i(\rho_i, \mathbf{n})$ and $h_j(\rho_j, \mathbf{n}_j) = h_j(\rho_j, \mathbf{n})$. The shape function $f_s(\mathbf{s}) = f_{s,i}(\mathbf{s}) + f_{s,j}(\mathbf{s})$ of the volume of interference as a function of the location \mathbf{s} on the contact surface S is then

$$f_s(\mathbf{s}) = h_j(\mathbf{s} - \mathbf{r}_j, \mathbf{n}) - h_i(\mathbf{s} - \mathbf{r}_i, \mathbf{n}) + \mathbf{n} \cdot (\mathbf{r}_j - \mathbf{r}_i). \quad (4.3)$$

Equations (4.2) and (4.3) constitute the basic foundation model expressions that relate the pattern of deformation of the bodies to their geometry.

4.2 One Deformable Body Contact Model

This section presents the derivations for a contact model between one deformable body and one perfectly rigid one. Here, it will be assumed that the body \mathcal{B}_i is deformable while the body \mathcal{B}_j

is rigid. The contact plate is therefore attached to \mathcal{B}_j and only the deformation of \mathcal{B}_i will be considered. In other words, the contact surface of \mathcal{B}_j is flat and $f_{s,j}(\mathbf{s}) = 0 \forall \mathbf{s}$. This simplification has two important consequences. First, the contact pressure felt at any point of the contact surface is directly a function of $f_s(\mathbf{s}) = f_{s,i}(\mathbf{s})$, and secondly, the contact normal direction is known since it corresponds to a flat surface on \mathcal{B}_j .

This simplified model will facilitate the derivations of a number of fundamental relationships that are needed in the next section to complete the derivation and analysis for the two deformable body contact model. But first, a few basic relationships must be introduced.

4.2.1 Contact Model Framework

This subsection introduces a number of definitions and relationships defined in terms of the shape function $f_s(\mathbf{s})$. Although the contact model presented in this section assumes the body \mathcal{B}_j is rigid, the derivations from this subsection are not subject to this restriction and hence, are equally valid when $f_{s,j}(\mathbf{s}) \neq 0$.

Volume of Interference and Centroids

The volume V of the volume of interference is given by

$$V = \int_S f_s(\mathbf{s}) dS = \int_V dV . \quad (4.4)$$

From Equation (4.4), it is seen that $f_s(\mathbf{s})dS = dV$. The centroid \mathbf{p}_c of the volume of interference is found using

$$\mathbf{p}_c = \frac{1}{V} \int_V \mathbf{p} dV , \quad (4.5)$$

where \mathbf{p} is the position vector of an infinitesimal volume element dV relative to \mathcal{K}_w . The contact surface area A_c , is given as

$$A_c = \int_S dS , \quad (4.6)$$

and the location of the weighted centroid \mathbf{s}_c on S is defined as

$$\mathbf{s}_c = \frac{1}{V} \int_S \mathbf{s} f_s(\mathbf{s}) dS . \quad (4.7)$$

Here, $f_s(\mathbf{s})$ is analogous to a variable density function of the surface. Equations (4.5) and (4.7) correspond to the mean value vector definition from the First and Second Mean Value Theorems respectively. Similarly, an average volume ‘height’ can be defined in terms of the area A_c by applying the First Mean Value Theorem definition to the surface integral definition of Equation (4.4).

as follows,

$$\mathbf{s}_c = \mathbf{T} \cdot \mathbf{s}_c + \mathbf{N} \cdot \mathbf{s}_c = \mathbf{T} \cdot \mathbf{s}_c + h_p \mathbf{n} . \quad (4.12)$$

When comparing Equations (4.11) and (4.12), it is obvious that

$$\mathbf{T} \cdot \mathbf{s}_c = \mathbf{T} \cdot \mathbf{p}_c . \quad (4.13)$$

Next, the position vector $\boldsymbol{\rho}_s$ of a point on the surface relative to the volume of interference centroid \mathbf{p}_c is defined as

$$\boldsymbol{\rho}_s = \mathbf{s} - \mathbf{p}_c . \quad (4.14)$$

Integrating $\boldsymbol{\rho}_s$ over the contact area S gives

$$\int_S \boldsymbol{\rho}_s f_s(\mathbf{s}) dS = \int_S (\mathbf{s} - \mathbf{s}_c) f_s(\mathbf{s}) dS + (\mathbf{s}_c - \mathbf{p}_c) \int_S f_s(\mathbf{s}) dS . \quad (4.15)$$

Using Equations (4.4) and (4.7), the first integral on the right-hand side of Equation (4.15) is evaluated to be

$$\int_S (\mathbf{s} - \mathbf{s}_c) f_s(\mathbf{s}) dS = \int_S \mathbf{s} f_s(\mathbf{s}) dS - \mathbf{s}_c \int_S f_s(\mathbf{s}) dS = V \mathbf{s}_c - V \mathbf{s}_c = 0 . \quad (4.16)$$

Hence, Equation (4.15) becomes simply

$$\int_S \boldsymbol{\rho}_s f_s(\mathbf{s}) dS = (\mathbf{s}_c - \mathbf{p}_c) V . \quad (4.17)$$

The vector $\mathbf{s}_c - \mathbf{p}_c$ is decomposed and simplified using Equation (4.13) as follows

$$\mathbf{s}_c - \mathbf{p}_c = \mathbf{T} \cdot \mathbf{s}_c - \mathbf{T} \cdot \mathbf{p}_c + \mathbf{N} \cdot (\mathbf{s}_c - \mathbf{p}_c) = \mathbf{N} \cdot (\mathbf{s}_c - \mathbf{p}_c) . \quad (4.18)$$

Hence, $\mathbf{s}_c - \mathbf{p}_c$ is parallel to \mathbf{n} , as indicated by Equation (4.11). Expressing $\boldsymbol{\rho}_s$ in terms of its normal component $\boldsymbol{\rho}_n$ and tangential component $\boldsymbol{\rho}_t$ gives

$$\boldsymbol{\rho}_s = (\mathbf{s} - \mathbf{s}_c) + (\mathbf{s}_c - \mathbf{p}_c) = \boldsymbol{\rho}_t + \boldsymbol{\rho}_n = \boldsymbol{\rho}_t + \rho_n \mathbf{n} , \quad (4.19)$$

where $\rho_n = \mathbf{n} \cdot \boldsymbol{\rho}_n$. Clearly, $\mathbf{s} - \mathbf{s}_c$ is tangential to S and it has just been shown that $\mathbf{s}_c - \mathbf{p}_c$ is normal to S . Therefore, it can be concluded that

$$\begin{aligned} \boldsymbol{\rho}_t &= \mathbf{s} - \mathbf{s}_c \\ \boldsymbol{\rho}_n &= \mathbf{s}_c - \mathbf{p}_c \end{aligned} . \quad (4.20)$$

Hence, $\boldsymbol{\rho}_n$ locates \mathbf{s}_c relative to \mathbf{p}_c ; see Figure 4.8.

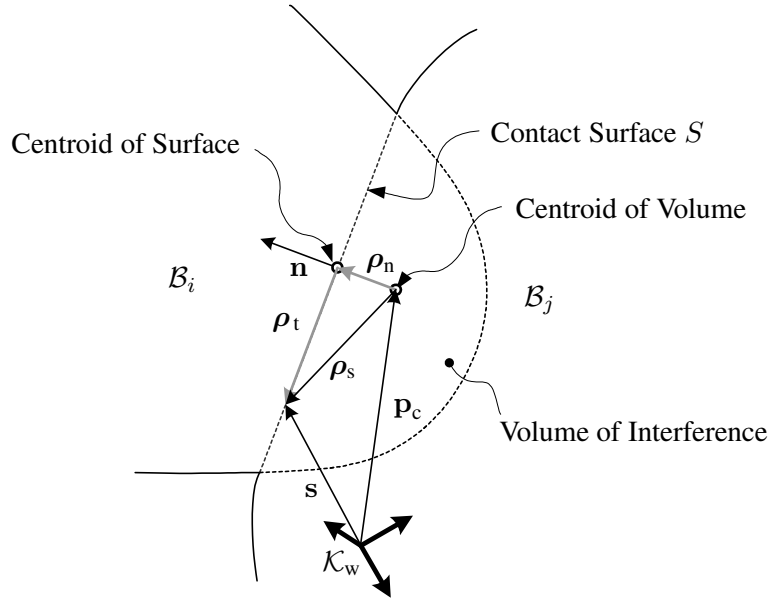


Figure 4.8: The position vector ρ_s and its normal and tangential components.

For the two deformable body contact model, the determination of ρ_n is not necessarily straightforward. However, it is easy to obtain here since the location of the contact surface is known. When the body B_j is rigid and h_p is known, then ρ_n is given as

$$\rho_n = h_p \mathbf{n} - \mathbf{N} \mathbf{p}_c . \quad (4.21)$$

Using the definitions for ρ_t and ρ_n , Equations (4.16) and (4.17) become simply

$$\int_S \rho_t f_s(\mathbf{s}) dS = \int_S \mathbf{s} f_s(\mathbf{s}) dS - \mathbf{s}_c \int_S f_s(\mathbf{s}) dS = 0 \quad (4.22)$$

and

$$\int_S \rho_s f_s(\mathbf{s}) dS = \rho_n V . \quad (4.23)$$

Equations (4.22) and (4.23) are useful relationships and will be used in the next section to simplify the contact model equations. Also, for the following derivations, all quantities will be derived relative to the volume of interference centroid \mathbf{p}_c .

Volume-Inertia and Surface Inertia Tensors

Finally, one additional quantity (or property) is defined: the contact surface *weighted second moment of area*, \mathbf{J}_s , and is given as follows

$$\mathbf{J}_s \cdot \boldsymbol{\omega}_r = \int_S (\boldsymbol{\rho}_s \times (\boldsymbol{\omega}_r \times \boldsymbol{\rho}_s)) f_s(\mathbf{s}) dS ; \quad (4.24)$$

where $\boldsymbol{\omega}_r$ could be any vector, but in this work will correspond to the relative angular velocity between the bodies \mathcal{B}_i and \mathcal{B}_j . \mathbf{J}_s can also be expressed using dyadic notation in the form of a second order tensor

$$\mathbf{J}_s = \int_S ((\boldsymbol{\rho}_s \cdot \boldsymbol{\rho}_s) \mathbf{I} - \boldsymbol{\rho}_s \boldsymbol{\rho}_s) f_s(\mathbf{s}) dS . \quad (4.25)$$

By virtue of the Second Mean Value Theorem, an average tensor $\mathbf{J}_{\rho_s, \text{avg}}$ can be found such that

$$\mathbf{J}_s = \mathbf{J}_{\rho_s, \text{avg}} \int_S f_s(\mathbf{s}) dS = V \mathbf{J}_{\rho_s, \text{avg}} , \quad (4.26)$$

where $\mathbf{J}_{\rho_s, \text{avg}}$ depends exclusively on the shape of the contact surface. One can think of \mathbf{J}_s as the inertia tensor for a volume of unit density about the centroid \mathbf{p}_c . \mathbf{J}_s appears in a recurring fashion in the coming derivations and is one of the three volumetric properties on which the proposed contact model is based. The other volumetric properties are the volume V of the volume of interference and its centroid \mathbf{p}_c .

The expression for \mathbf{J}_s can be simplified when its constitutive equation is re-written in terms of normal and tangential components. The vectors $\boldsymbol{\rho}_s$ and $\boldsymbol{\omega}_r$ are expressed as $\boldsymbol{\rho}_n + \boldsymbol{\rho}_t$ and $\boldsymbol{\omega}_n + \boldsymbol{\omega}_t$, respectively. The vectorial part of Equation (4.24) is thus written as

$$\begin{aligned} \boldsymbol{\rho}_s \times (\boldsymbol{\omega}_r \times \boldsymbol{\rho}_s) &= (\boldsymbol{\rho}_n + \boldsymbol{\rho}_t) \times ((\boldsymbol{\omega}_n + \boldsymbol{\omega}_t) \times (\boldsymbol{\rho}_n + \boldsymbol{\rho}_t)) \\ &= (\boldsymbol{\rho}_n + \boldsymbol{\rho}_t) \times (\boldsymbol{\omega}_n \times \boldsymbol{\rho}_n + \boldsymbol{\omega}_n \times \boldsymbol{\rho}_t + \boldsymbol{\omega}_t \times \boldsymbol{\rho}_n + \boldsymbol{\omega}_t \times \boldsymbol{\rho}_t) \\ &= \boldsymbol{\rho}_n \times (\boldsymbol{\omega}_n \times \boldsymbol{\rho}_t) + \boldsymbol{\rho}_n \times (\boldsymbol{\omega}_t \times \boldsymbol{\rho}_n) + \boldsymbol{\rho}_n \times (\boldsymbol{\omega}_t \times \boldsymbol{\rho}_t) \\ &\quad + \boldsymbol{\rho}_t \times (\boldsymbol{\omega}_n \times \boldsymbol{\rho}_t) + \boldsymbol{\rho}_t \times (\boldsymbol{\omega}_t \times \boldsymbol{\rho}_n) + \boldsymbol{\rho}_t \times (\boldsymbol{\omega}_t \times \boldsymbol{\rho}_t) . \end{aligned} \quad (4.27)$$

Simplifying the cross-product terms between parallel vectors, e.g., $\mathbf{n} \times \mathbf{n} = 0$, yields

$$\begin{aligned} \boldsymbol{\rho}_s \times (\boldsymbol{\omega}_r \times \boldsymbol{\rho}_s) &= \boldsymbol{\rho}_t \times (\boldsymbol{\omega}_n \times \boldsymbol{\rho}_t) + \boldsymbol{\rho}_t \times (\boldsymbol{\omega}_t \times \boldsymbol{\rho}_t) + \boldsymbol{\rho}_n \times (\boldsymbol{\omega}_t \times \boldsymbol{\rho}_n) \\ &\quad + \boldsymbol{\rho}_n \times (\boldsymbol{\omega}_n \times \boldsymbol{\rho}_t) + \boldsymbol{\rho}_t \times (\boldsymbol{\omega}_t \times \boldsymbol{\rho}_n) . \end{aligned} \quad (4.28)$$

The second line of Equation (4.28) is now examined in more detail. The triple vector cross-product

identity² is applied to the terms in the second line of Equation (4.28) yielding,

$$\begin{aligned} \boldsymbol{\rho}_n \times (\boldsymbol{\omega}_n \times \boldsymbol{\rho}_t) + \boldsymbol{\rho}_t \times (\boldsymbol{\omega}_t \times \boldsymbol{\rho}_n) &= (\boldsymbol{\rho}_n \cdot \boldsymbol{\rho}_t) \boldsymbol{\omega}_n - (\boldsymbol{\rho}_n \cdot \boldsymbol{\omega}_n) \boldsymbol{\rho}_t \\ &\quad + (\boldsymbol{\rho}_t \cdot \boldsymbol{\rho}_n) \boldsymbol{\omega}_t - (\boldsymbol{\rho}_t \cdot \boldsymbol{\omega}_t) \boldsymbol{\rho}_n, \\ &= -(\boldsymbol{\rho}_n \cdot \boldsymbol{\omega}_n) \boldsymbol{\rho}_t - (\boldsymbol{\rho}_t \cdot \boldsymbol{\omega}_t) \boldsymbol{\rho}_n, \end{aligned} \quad (4.29)$$

where the dot-products of perpendicular vectors have been eliminated, e.g., $\boldsymbol{\rho}_n \cdot \boldsymbol{\rho}_t = 0$. Placing the resulting expression back into the original integral from Equation (4.24), and moving terms that do not depend on \mathbf{s} outside the integral gives

$$-(\boldsymbol{\rho}_n \cdot \boldsymbol{\omega}_n) \int_S \boldsymbol{\rho}_t f_s(\mathbf{s}) dS - \left(\int_S \boldsymbol{\rho}_t f_s(\mathbf{s}) dS \cdot \boldsymbol{\omega}_t \right) \boldsymbol{\rho}_n = 0, \quad (4.30)$$

since the integrals in Equation (4.30) evaluate to zero (Equation (4.22)). Hence, the terms in the second line of Equation (4.28) can be neglected because they do not contribute to the final result of the integral. Applying the triple cross-product identity to the first line of Equation (4.28) yields

$$[(\boldsymbol{\rho}_t \cdot \boldsymbol{\rho}_t) \mathbf{I} - \boldsymbol{\rho}_t \boldsymbol{\rho}_t] (\boldsymbol{\omega}_n + \boldsymbol{\omega}_t) + (\boldsymbol{\rho}_n \cdot \boldsymbol{\rho}_n) \boldsymbol{\omega}_t = [(\boldsymbol{\rho}_t \cdot \boldsymbol{\rho}_t) \mathbf{I} - \boldsymbol{\rho}_t \boldsymbol{\rho}_t] \boldsymbol{\omega}_r + (\boldsymbol{\rho}_n \cdot \boldsymbol{\rho}_n) \boldsymbol{\omega}_t, \quad (4.31)$$

where $\boldsymbol{\rho}_n \cdot \boldsymbol{\omega}_t = 0$ was used to simplify the expression. Summarizing, the derivations show that Equation (4.27) simplifies into

$$\begin{aligned} \boldsymbol{\rho}_s \times (\boldsymbol{\omega}_r \times \boldsymbol{\rho}_s) &= \boldsymbol{\rho}_t \times (\boldsymbol{\omega}_r \times \boldsymbol{\rho}_t) + \boldsymbol{\rho}_n \times (\boldsymbol{\omega}_t \times \boldsymbol{\rho}_n) \\ &= [(\boldsymbol{\rho}_t \cdot \boldsymbol{\rho}_t) \mathbf{I} - \boldsymbol{\rho}_t \boldsymbol{\rho}_t] \boldsymbol{\omega}_r + (\boldsymbol{\rho}_n \cdot \boldsymbol{\rho}_n) \boldsymbol{\omega}_t. \end{aligned} \quad (4.32)$$

Hence, \mathbf{J}_s can be expressed in the form

$$\mathbf{J}_s = [\mathbf{J}_t + (\boldsymbol{\rho}_n \cdot \boldsymbol{\rho}_n) V \mathbf{I}], \quad (4.33)$$

or alternatively,

$$\begin{aligned} \mathbf{J}_s \cdot \boldsymbol{\omega}_t &= [\mathbf{J}_t + (\boldsymbol{\rho}_n \cdot \boldsymbol{\rho}_n) V \mathbf{I}] \cdot \boldsymbol{\omega}_t, \\ \mathbf{J}_s \cdot \boldsymbol{\omega}_n &= \mathbf{J}_t \cdot \boldsymbol{\omega}_n, \end{aligned} \quad (4.34)$$

where

$$\mathbf{J}_t = \int_S ((\boldsymbol{\rho}_t \cdot \boldsymbol{\rho}_t) \mathbf{I} - \boldsymbol{\rho}_t \boldsymbol{\rho}_t) f_s(\mathbf{s}) dS. \quad (4.35)$$

\mathbf{J}_t corresponds to the surface-inertia tensor expressed relative to the surface centroid \mathbf{s}_c . Equation (4.33) shows that the surface inertia taken about \mathbf{p}_c corresponds to the inertia \mathbf{J}_t to which the term $\boldsymbol{\rho}_n^2 V$ is added to account for the position offset from \mathbf{p}_c to \mathbf{s}_c , where the ‘mass’ of the surface-

² $\mathbf{a} \times (\mathbf{b} \times \mathbf{c}) = (\mathbf{a} \cdot \mathbf{c}) \mathbf{b} - (\mathbf{a} \cdot \mathbf{b}) \mathbf{c} = (\mathbf{a} \cdot \mathbf{c}) \mathbf{b} - \mathbf{c} (\mathbf{a} \cdot \mathbf{b}) = [(\mathbf{a} \cdot \mathbf{c}) \mathbf{I} - \mathbf{c} \mathbf{a}] \mathbf{b}$

inertia tensor is the volume V . This offset term corresponds to the parallel-axis theorem shift value for the change in axis of rotation location from \mathbf{s}_c to \mathbf{p}_c .

The surface-inertia tensor \mathbf{J}_s is closely related to the volume-inertia tensor \mathbf{J}_v of the volume of interference. The term ‘volume-inertia’ is used to distinguish it from the more commonly used ‘mass-inertia’ tensor, i.e., the former has SI units of $[\text{m}^5]$ whereas the later has units of $[\text{kg} \cdot \text{m}^2]$. When post-multiplied by the angular velocity $\boldsymbol{\omega}_r$, \mathbf{J}_v is defined as

$$\begin{aligned} \mathbf{J}_v \cdot \boldsymbol{\omega}_r &= \int_V (\boldsymbol{\rho}_v \times (\boldsymbol{\omega}_r \times \boldsymbol{\rho}_v)) dV \\ &= \int_V ((\boldsymbol{\rho}_v \cdot \boldsymbol{\rho}_v) \mathbf{I} - \boldsymbol{\rho}_v \boldsymbol{\rho}_v) dV \cdot \boldsymbol{\omega}_r, \end{aligned} \quad (4.36)$$

where $\boldsymbol{\rho}_v = \mathbf{p} - \mathbf{p}_c$. The second integral form yields the usual volume-inertia tensor expressed relative to the centroid \mathbf{p}_c . The vector $\boldsymbol{\rho}_v$ can be decomposed into normal and tangential components $\boldsymbol{\rho}_{v,n}$ and $\boldsymbol{\rho}_{v,t}$ as follows

$$\begin{aligned} \boldsymbol{\rho}_{v,n} &= \mathbf{N} \cdot (\mathbf{p} - \mathbf{p}_c), \\ \boldsymbol{\rho}_{v,t} &= \mathbf{T} \cdot (\mathbf{p} - \mathbf{p}_c) = \mathbf{T} \cdot \mathbf{p} - \mathbf{T} \cdot \mathbf{p}_c = \mathbf{s} - \mathbf{s}_c = \boldsymbol{\rho}_t. \end{aligned} \quad (4.37)$$

The definitions from Equations (4.37) can be substituted into Equation (4.36), and simplified in the same manner as was done for \mathbf{J}_s by using Equations (4.28). The terms in the second line of Equations (4.28) are re-written as was done in Equation (4.29) and can also be shown to evaluate to zero when they are placed back into the integral (4.36), but the proof is different than for the case of \mathbf{J}_s and it is given next.

First, the position of a point \mathbf{p} in the volume of interference is expressed in terms the position of its projection \mathbf{s} on the contact surface and its height h with respect to this projected position. The height is measured in the direction of \mathbf{n} ; see Figure 4.7. The expression for \mathbf{p} is given as

$$\mathbf{p} = \mathbf{s} - h \mathbf{n} = \boldsymbol{\rho}_t + \mathbf{s}_c - h \mathbf{n}, \quad (4.38)$$

which implies that

$$\begin{aligned} \boldsymbol{\rho}_{v,n} &= \boldsymbol{\rho}_n - h \mathbf{n}, \\ \boldsymbol{\rho}_{v,t} &= \boldsymbol{\rho}_t. \end{aligned} \quad (4.39)$$

The volume V of the volume of interference can now be found by splitting the volume integral Equation (4.4) into a double integral of the position of point \mathbf{p} relative to the contact plate, integrated over the surface S of the contact surface as

$$\int_V dV = \int_S \int_{-f_s(\mathbf{s})}^0 dh dS = \int_S [h]_{-f_s(\mathbf{s})}^0 dS = \int_S f_s(\mathbf{s}) dS = V. \quad (4.40)$$

Second, the integral of $\rho_{v,n}$ over the height h of the contact plate is evaluated as

$$\begin{aligned}
\int_{-f_s(\mathbf{s})}^0 \rho_{v,n} dh &= \int_{-f_s(\mathbf{s})}^0 (\rho_n - h \mathbf{n}) dh , \\
&= \rho_n \int_{-f_s(\mathbf{s})}^0 dh - \int_{-f_s(\mathbf{s})}^0 h dh \mathbf{n} , \\
&= [h]_{-f_s(\mathbf{s})}^0 \rho_n - \left[\frac{h^2}{2} \right]_{-f_s(\mathbf{s})}^0 \mathbf{n} , \\
&= f_s(\mathbf{s}) \left(\rho_n - \frac{f_s(\mathbf{s})}{2} \right) \mathbf{n} ,
\end{aligned} \tag{4.41}$$

where the term in parentheses corresponds to the position of mid-point of $f_s(\mathbf{s})$ along the height h relative to the position of the centroid \mathbf{p}_c . The mid-point position $f_{s,m}(\mathbf{s})$ is thus given as

$$f_{s,m}(\mathbf{s}) = \rho_n - \frac{f_s(\mathbf{s})}{2} . \tag{4.42}$$

Using the result from Equation (4.41), the expressions from Equation (4.29) can be substituted into the volume integral (4.36) and evaluated as follows

$$\begin{aligned}
& - \int_V [(\rho_{v,n} \cdot \boldsymbol{\omega}_n) \boldsymbol{\rho}_t + (\boldsymbol{\rho}_t \cdot \boldsymbol{\omega}_t) \rho_{v,n}] dV = \\
& = - \int_S \left(\int_{-f_s(\mathbf{s})}^0 \rho_{v,n} dh \cdot \boldsymbol{\omega}_n \right) \boldsymbol{\rho}_t dS - \int_S (\boldsymbol{\rho}_t \cdot \boldsymbol{\omega}_t) \int_{-f_s(\mathbf{s})}^0 \rho_{v,n} dh dS \\
& = -\omega_n \int_S f_{s,m}(\mathbf{s}) f_s(\mathbf{s}) \boldsymbol{\rho}_t dS - \left[\left(\int_S f_{s,m}(\mathbf{s}) f_s(\mathbf{s}) \boldsymbol{\rho}_t dS \right) \cdot \boldsymbol{\omega}_t \right] \mathbf{n} .
\end{aligned} \tag{4.43}$$

Invoking the Second Mean Value Theorem, the mid-point height value $f_{s,m}(\mathbf{s})$ inside the integrals of Equation (4.43) can be replaced by a constant mid-point height value $f_{s,m,avg}(\mathbf{s})$ averaged over the entire surface S . Equation (4.43) is thus re-written as

$$\begin{aligned}
& - \int_V [(\rho_{v,n} \cdot \boldsymbol{\omega}_n) \boldsymbol{\rho}_t + (\boldsymbol{\rho}_t \cdot \boldsymbol{\omega}_t) \rho_{v,n}] dV = \\
& = -\omega_n f_{s,m,avg}(\mathbf{s}) \int_S f_s(\mathbf{s}) \boldsymbol{\rho}_t dS - \left[\left(f_{s,m,avg}(\mathbf{s}) \int_S f_s(\mathbf{s}) \boldsymbol{\rho}_t dS \right) \cdot \boldsymbol{\omega}_t \right] \mathbf{n} , \\
& = 0 ,
\end{aligned} \tag{4.44}$$

since the integral terms in Equation (4.44) evaluate to zero, see Equation (4.22).

Hence, the terms of Equation (4.29) evaluate to zero when they are placed back into the integral (4.36), and only the terms in the first line of Equation (4.28) remain to be evaluated to obtain \mathbf{J}_v . The expression for \mathbf{J}_v thus becomes

$$\mathbf{J}_v \cdot \boldsymbol{\omega}_r = \mathbf{J}_t \cdot \boldsymbol{\omega}_r + \int_V (\rho_{v,n} \cdot \rho_{v,n}) dV \boldsymbol{\omega}_t , \tag{4.45}$$

where \mathbf{J}_t is defined as before. The integral term in Equation (4.45) can be simplified by virtue of the First Mean Value Theorem as follows

$$\int_V (\boldsymbol{\rho}_{v,n} \cdot \boldsymbol{\rho}_{v,n}) dV = \rho_{v,n,\text{avg}}^2 V, \quad (4.46)$$

where $\rho_{v,n,\text{avg}}$ is a value representing the average distance in the direction of the normal \mathbf{n} of all points in the volume of interference relative to \mathbf{p}_c . The value of $\rho_{v,n,\text{avg}}$ can only be determined if the shape of the volume V is known, while the value ρ_n in \mathbf{J}_s is invariant with respect to the surface integral, i.e., ρ_n is not a function of \mathbf{s} . \mathbf{J}_v can now be expressed in a general form as

$$\mathbf{J}_v = [\mathbf{J}_t + V \rho_{v,n,\text{avg}}^2 \mathbf{T}] . \quad (4.47)$$

Equations (4.33) and (4.47) show the close relationship between \mathbf{J}_v and \mathbf{J}_s . The difference between the two is $V(\rho_{v,n,\text{avg}}^2 - \rho_n^2) \mathbf{T}$ which has a small value for three reasons. First, the values for $\rho_{v,n,\text{avg}}$ and ρ_n will in general be small and in the same order of magnitude because the inter-penetration depth is expected to be small. Secondly, the values are squared, which reduces the volume-inertia tensor difference further by one order of magnitude. Finally, the values are subtracted, therefore resulting in an even smaller difference value.

\mathbf{J}_v is the volume-inertia tensor of the volume of interference and can be obtained either numerically or analytically. Hence, for the implementation of the contact model, \mathbf{J}_v will be used as an approximation of \mathbf{J}_s . In fact, \mathbf{J}_v approximates \mathbf{J}_s exactly when multiplied by $\boldsymbol{\omega}_n$, i.e., $\mathbf{J}_v \cdot \boldsymbol{\omega}_n = \mathbf{J}_s \cdot \boldsymbol{\omega}_n$, and the error is small when multiplied by $\boldsymbol{\omega}_t$, i.e., $\mathbf{J}_v \cdot \boldsymbol{\omega}_t \simeq \mathbf{J}_s \cdot \boldsymbol{\omega}_t$.

Expressing Local Velocities Relative to the Centroid

To include energy dissipation effects into the contact model, expressions for the relative translational velocity \mathbf{v}_r at a point \mathbf{s} on the contact surface is found as

$$\mathbf{v}_r = \mathbf{v}_i + \boldsymbol{\omega}_i \times \boldsymbol{\rho}_i - \mathbf{v}_j - \boldsymbol{\omega}_j \times \boldsymbol{\rho}_j . \quad (4.48)$$

Also, the relative angular velocity $\boldsymbol{\omega}_r$ of the surfaces at any point on S is given as

$$\boldsymbol{\omega}_r = \boldsymbol{\omega}_i - \boldsymbol{\omega}_j . \quad (4.49)$$

Substituting $\boldsymbol{\rho}_i$ and $\boldsymbol{\rho}_j$ as given in Equation (4.1) and expressing \mathbf{s} in terms of \mathbf{p}_c and $\boldsymbol{\rho}_s$ as defined in Equation (4.14), the relative velocity given in Equation (4.48) becomes

$$\mathbf{v}_r = (\mathbf{v}_i + \boldsymbol{\omega}_i \times (\mathbf{p}_c - \mathbf{r}_i)) - (\mathbf{v}_j + \boldsymbol{\omega}_j \times (\mathbf{p}_c - \mathbf{r}_j)) + \boldsymbol{\omega}_r \times \boldsymbol{\rho}_s . \quad (4.50)$$

The first two terms in Equation (4.50) correspond to the relative velocity of the surfaces of the two bodies, as if the centroid of the volume \mathbf{p}_c was located on the contact surface, while the third term

is a correction term to account for the fact that \mathbf{p}_c is not on the contact surface. Note that in general the volume of interference centroid is *not* on the contact surface. However in these derivations, no such assumption was made and therefore the relative velocity at the centroid \mathbf{v}_c can be defined as

$$\mathbf{v}_c = (\mathbf{v}_i + \boldsymbol{\omega}_i \times (\mathbf{p}_c - \mathbf{r}_i)) - (\mathbf{v}_j + \boldsymbol{\omega}_j \times (\mathbf{p}_c - \mathbf{r}_j)) . \quad (4.51)$$

The relative velocity \mathbf{v}_r at a point s of the surface S can now be simply expressed as a function of the relative velocity at the centroid \mathbf{v}_c and the relative angular velocity $\boldsymbol{\omega}_r$ as follows

$$\mathbf{v}_r = \mathbf{v}_c + \boldsymbol{\omega}_r \times \boldsymbol{\rho}_s . \quad (4.52)$$

Decomposing the Relative Velocity into Tangential and Normal Components

Equation (3.7) can be used to determine \mathbf{v}_t , \mathbf{v}_n , $\boldsymbol{\omega}_t$, and $\boldsymbol{\omega}_n$. Equation (4.52) can now be decomposed into two equations, one for the tangential direction and one for the normal direction. For the latter, \mathbf{v}_r is multiplied by \mathbf{N} and Equation (4.52) becomes

$$\mathbf{v}_n = \mathbf{N} \cdot \mathbf{v}_c + \mathbf{N} \cdot (\boldsymbol{\omega}_t \times \boldsymbol{\rho}_t) + \mathbf{N} \cdot (\boldsymbol{\omega}_t \times \boldsymbol{\rho}_n) + \mathbf{N} \cdot (\boldsymbol{\omega}_n \times \boldsymbol{\rho}_s) . \quad (4.53)$$

The last two terms in Equation (4.53) are zero, since the second factor of each expression is perpendicular to \mathbf{n} . Taking the dot product of Equation (4.53) with \mathbf{n} , the equation simplifies to

$$v_n = v_{cn} + \mathbf{n} \cdot (\boldsymbol{\omega}_t \times \boldsymbol{\rho}_t) , \quad (4.54)$$

where $v_{cn} = \mathbf{n} \cdot \mathbf{v}_c$. Similarly, the tangential component of \mathbf{v}_r is obtained by pre-multiplying Equation (4.52) by \mathbf{T} , i.e.,

$$\mathbf{v}_t = \mathbf{T} \cdot \mathbf{v}_c + \mathbf{T} \cdot (\boldsymbol{\omega}_t \times \boldsymbol{\rho}_t + \boldsymbol{\omega}_t \times \boldsymbol{\rho}_n + \boldsymbol{\omega}_n \times \boldsymbol{\rho}_t + \boldsymbol{\omega}_n \times \boldsymbol{\rho}_n) . \quad (4.55)$$

Equation (4.55) can be simplified by noting that $\boldsymbol{\omega}_n \times \boldsymbol{\rho}_n = 0$ and that $\boldsymbol{\omega}_t \times \boldsymbol{\rho}_t$ produces a vector perpendicular to the surface. Furthermore, since $\boldsymbol{\omega}_t \times \boldsymbol{\rho}_n$ and $\boldsymbol{\omega}_n \times \boldsymbol{\rho}_t$ produce a vector perpendicular to \mathbf{n} , it follows that

$$\mathbf{v}_t = \mathbf{v}_{ct} + \boldsymbol{\omega}_t \times \boldsymbol{\rho}_n + \boldsymbol{\omega}_n \times \boldsymbol{\rho}_t , \quad (4.56)$$

with $\mathbf{v}_{ct} = \mathbf{T} \cdot \mathbf{v}_c$. The first two terms on the right-hand side of Equation (4.56) do not depend on s and can be combined as follows

$$\mathbf{v}_t = \mathbf{v}_{sct} + \boldsymbol{\omega}_n \times \boldsymbol{\rho}_t , \quad (4.57)$$

where

$$\mathbf{v}_{\text{sct}} = \mathbf{v}_{\text{ct}} + \boldsymbol{\omega}_{\text{t}} \times \boldsymbol{\rho}_{\text{n}} . \quad (4.58)$$

The term $\boldsymbol{\omega}_{\text{t}} \times \boldsymbol{\rho}_{\text{n}}$ corresponds to the velocity of \mathbf{s}_{c} relative to \mathbf{p}_{c} in the direction tangential to \mathbf{n} . Hence, \mathbf{v}_{sct} is the relative tangential velocity at \mathbf{s}_{c} . Equation (4.58) shows that whenever $\boldsymbol{\omega}_{\text{t}}$ or $\boldsymbol{\rho}_{\text{n}}$ is small and negligible, $\mathbf{v}_{\text{sct}} = \mathbf{v}_{\text{ct}}$. In the context of simulation of robotic tasks, it is expected that $\boldsymbol{\omega}_{\text{t}}$ will never be large and that inter-penetration depth will be small, and therefore $\boldsymbol{\rho}_{\text{n}}$ will be small. As a result, it will generally be acceptable to assume $\mathbf{v}_{\text{sct}} \approx \mathbf{v}_{\text{ct}}$.

4.2.2 Normal Force Model

The contact force produced by the deformation of the contacting surfaces can be found by integrating the pressure on the contact surface over the contact area. The Winkler elastic foundation provides an approximation for the stiffness of the contact model only, and does not include any damping effect to dissipate energy during the contact process. In compliant contact models, the energy dissipation can be modelled using a hysteretic damping term as shown in Section 3.2.1. A modified Winkler elastic foundation model is proposed to obtain the local contact pressure $p(\mathbf{s})$, and which includes the hysteretic damping effect as follows

$$p(\mathbf{s}) = \frac{df_{\text{n}}}{dS} = k_{\text{v}} f_{\text{s}}(\mathbf{s}) (1 + a v_{\text{n}}) , \quad (4.59)$$

where $f_{\text{s}}(\mathbf{s})$ is the normal elastic displacement of the foundation as before, and a is the hysteretic damping factor. a is a function of the coefficient of restitution and of the initial normal impact velocity v_{n}^{i} ; see Equation (3.24). The normal contact force $\mathbf{f}_{\text{n}} = f_{\text{n}} \mathbf{n}$ is therefore given as

$$f_{\text{n}} = \int_S df_{\text{n}} = k_{\text{v}} \int_S f_{\text{s}}(\mathbf{s}) dS + k_{\text{v}} a \int_S v_{\text{n}} f_{\text{s}}(\mathbf{s}) dS . \quad (4.60)$$

The first integral term is solved using Equation (4.4) and results in $k_{\text{v}} V$. This part corresponds to the normal force due to the material stiffness. The second integral is solved using Equation (4.54) as

$$f_{\text{n}} = k_{\text{v}} V + k_{\text{v}} V a v_{\text{cn}} + k_{\text{v}} a \mathbf{n} \cdot \left(\boldsymbol{\omega}_{\text{t}} \times \int_S \boldsymbol{\rho}_{\text{t}} f_{\text{s}}(\mathbf{s}) dS \right) . \quad (4.61)$$

The integral term of Equation (4.61) is zero; see (4.22). Hence, the normal contact force is found to be simply

$$\mathbf{f}_{\text{n}} = k_{\text{v}} V (1 + a v_{\text{cn}}) \mathbf{n} , \quad (4.62)$$

where

$$a = \frac{d}{e_{\text{eff}} v_{\text{cn}}^i}, \quad (4.63)$$

and v_{cn}^i corresponds to initial normal impact velocity at s_c . Figure 4.9 shows how \mathbf{f}_n acts on a sphere-box pair (non-conformal geometries) and a cube-box pair (conformal geometries).

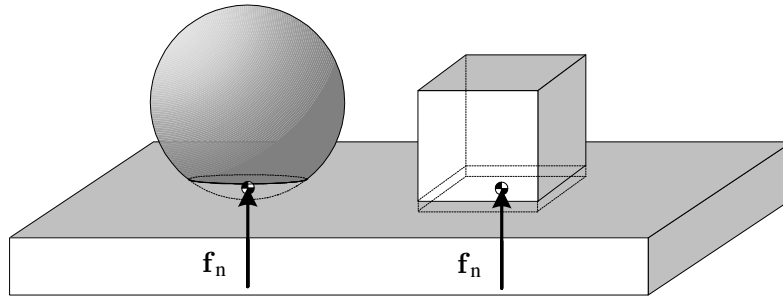


Figure 4.9: The normal force acting on a sphere and a cube.

It is interesting to note that although the derivation presented in this section is based on the pressure distribution across the area of contact, it is not necessary to determine the shape and location of the contact area to evaluate Equation (4.62). Instead, only the volume V of the volume of interference and its centroid \mathbf{p}_c must be determined. These quantities can be obtained either analytically or numerically. Since the contact plate is attached to \mathcal{B}_j , the direction of the contact normal is readily known. As a result, the magnitude and direction of \mathbf{f}_n can be determined using purely geometric and kinematic information. The stiffness term in f_n can be expressed as $k_v V = (k_v A_c) h_v$ where h_v is directly related to the inter-penetration depth; see Equation (4.8). Hence, the resulting linear stiffness $k_l = k_v A_c$ of the contact model is proportional to the contact surface area.

To implement the contact model in the context of a multibody dynamics simulation, the point of action of the contact force must be selected; see Section 3.1.1. The correct point of action where \mathbf{f}_n should be applied is the centroid of the distributed load, a location that has not yet been identified in the current derivation. Instead, it is proposed to use the centroid of the volume of interference as point of action of the contact force. This change in location may cause a moment that must be accounted for to correctly model the normal contact force. This extra torque is considered next.

4.2.3 Rolling Resistance Torque Model

Since the pressure at the contact surface is a function of the normal displacement and velocity at each point, the load distribution profile is generally not symmetric about the centroid of the volume of interference. It is therefore necessary to consider the moments generated by the contact pressure

distribution. To this end, the infinitesimal rolling resistance torque $d\tau_r$ is defined as follows

$$d\tau_r = \rho_s \times df_n . \quad (4.64)$$

Using Equations (4.59) and (4.54), $d\tau_r$ can be integrated over the contact area S . Substituting Equation (4.54) and moving all the terms that do not depend on s outside of the integral gives

$$\begin{aligned} \tau_r = & k_v (1 + a v_{cn}) \left[\int_S \rho_s f_s(s) dS \right] \times \mathbf{n} \\ & + k_v a \int_S (\rho_s \times (\omega_t \times \rho_s)) f_s(s) dS . \end{aligned} \quad (4.65)$$

The integral term in the first line of Equation (4.65) can be simplified employing Equation (4.23) and noting that $\rho_n \times \mathbf{n}$ is zero. Re-writing the second term using dyadic notation yields

$$\tau_r = k_v a \int_S ((\rho_s \cdot \rho_s) \mathbf{I} - \rho_s \rho_s) f_s(s) dS \cdot \omega_t \quad (4.66)$$

or

$$\tau_r = k_v a \mathbf{J}_s \cdot \omega_t . \quad (4.67)$$

Figure 4.10 shows how τ_r acts on a sphere-box pair and a cube-box pair.

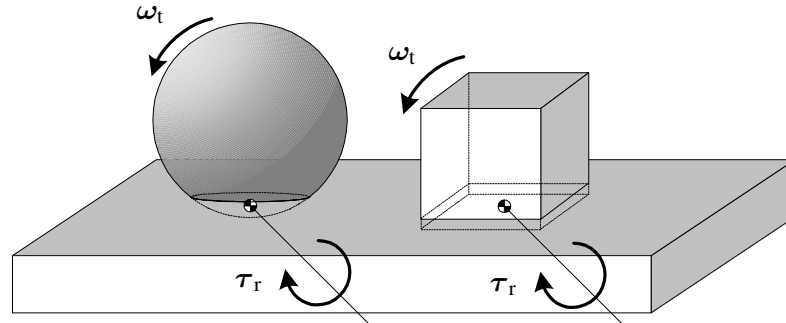


Figure 4.10: The rolling resistance torque acting on a sphere and a cube.

When the bodies are rolling with respect to each other, then τ_r is a rolling resistance torque acting to prevent the rolling. Equation (4.67) shows that if the two bodies are not rolling with respect to each other, i.e., $|\omega_t| = 0$, then the normal force is distributed symmetrically around the volume of interference centroid, so the net moment at the centroid is zero. See also that τ_r does not depend on f_n . Hence, the centroid of the volume of interference is a logical choice as the point of action of the contact force f_n . For any other choice, an additional moment proportional to f_n and the moment arm about the centroid would be required.

4.2.4 Tangential Friction Force Model

The forces resulting from friction in the tangential direction are considered next. In order to keep the formulation as general as possible, a friction force that is both dependent on relative surface velocity and load will be considered. Once the general formulation is derived, it can be specialized for Coulomb friction or viscous friction for example. The infinitesimal frictional force element $d\mathbf{f}_t$ is defined as

$$d\mathbf{f}_t = \mu \mathbf{v}_t df_n, \quad (4.68)$$

where μ is some constant that will be defined in the model implementation. It is interesting to note that if the normal force is kept constant, μ will be a viscous friction coefficient, while if the magnitude of \mathbf{v}_t is set to one, μ would represent either the static or kinetic friction coefficient. Substituting the definition of df_n as given in Equation (4.59) into Equation (4.68), the tangential friction force is found by integrating the force $d\mathbf{f}_t$ over the area,

$$\mathbf{f}_t = \mu k_v \int_S (1 + a v_n) \mathbf{v}_t f_s(\mathbf{s}) dS. \quad (4.69)$$

By recalling the expression for \mathbf{v}_t from (4.57), Equation (4.69) can be written as

$$\mathbf{f}_t = \mu k_v \int_S (1 + a v_n) f_s(\mathbf{s}) dS \mathbf{v}_{\text{sct}} + \boldsymbol{\omega}_n \times \left[\mu k_v \int_S (1 + a v_n) \boldsymbol{\rho}_t f_s(\mathbf{s}) dS \right]. \quad (4.70)$$

The first term in the equation above corresponds to Equation (4.60), and can be simplified in the same manner. The second term can be shown to be zero. Substituting Equation (4.54) into the integral of the second term, called I_1 hereafter, gives

$$I_1 = \mu k_v (1 + a v_{\text{cn}}) \int_S \boldsymbol{\rho}_t f_s(\mathbf{s}) dS + a \mu k_v \int_S (\mathbf{n} \cdot (\boldsymbol{\omega}_t \times \boldsymbol{\rho}_t)) \boldsymbol{\rho}_t f_s(\mathbf{s}) dS. \quad (4.71)$$

The integral first term of Equation (4.71) is evaluated to zero using Equation (4.22), while the second term can be shown to be zero by virtue of the chain rule, i.e., $\int u dv = uv - \int v du$ and setting dv to

$$dv = (\mathbf{n} \cdot (\boldsymbol{\omega}_t \times \boldsymbol{\rho}_t)) f_s(\mathbf{s}) dS, \quad (4.72)$$

and solving for v gives

$$v = \mathbf{n} \cdot \left[\boldsymbol{\omega}_t \times \left(\int_S \boldsymbol{\rho}_t f_s(\mathbf{s}) dS \right) \right]. \quad (4.73)$$

Using the Equation (4.22), the integral is evaluated, showing that $v = 0$, and therefore $I_1 = 0$. \mathbf{f}_t can now be evaluated and simplifies to

$$\mathbf{f}_t = \mu k_v V (1 + a v_{cn}) \mathbf{v}_{sct} , \quad (4.74)$$

or

$$\mathbf{f}_t = \mu f_n \mathbf{v}_{sct} . \quad (4.75)$$

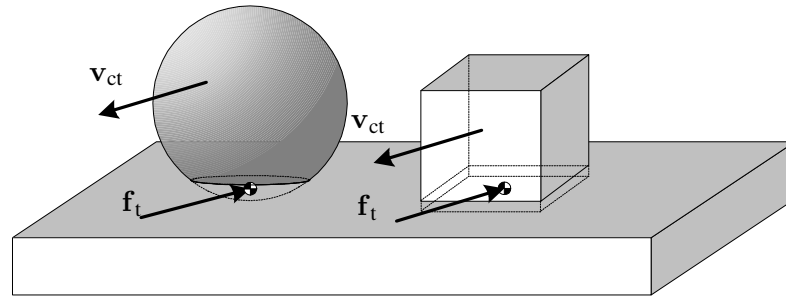


Figure 4.11: The tangential friction force acting on a sphere and a cube.

Figure 4.11 shows how \mathbf{f}_t acts on a sphere-box pair and a cube-box pair. As discussed previously, $|\rho_n|$ will typically be small for fairly rigid bodies and can be usually neglected. Hence, \mathbf{v}_{sct} in Equation (4.75) can be substituted by \mathbf{v}_{ct} without affecting the friction model behaviour significantly.

4.2.5 Spinning Friction Torque Model

In the previous section, the effect of friction due to translational motion was studied. When the contacting surface has a non-negligible area, this tangential friction force will also produce a moment that acts to prevent the bodies from turning with respect to each other. More precisely, the spinning friction is a torque that acts to prevent motion when the bodies have a non-zero relative angular velocity ω_n with respect to each other. Similar to the steps followed in Section 4.2.3, an infinitesimal spinning friction torque $d\tau_s$ is defined as follows

$$d\tau_s = \rho_t \times d\mathbf{f}_t . \quad (4.76)$$

The spinning torque is found by integrating Equation (4.76) over the area. Substituting the definition for $d\mathbf{f}_t$ from Equation (4.68), the integral to evaluate is

$$\tau_s = \mu k_v \int_S (1 + a v_n) (\rho_t \times \mathbf{v}_t) f_s(\mathbf{s}) dS . \quad (4.77)$$

Substituting the definition for \mathbf{v}_t from Equation (4.57), $\boldsymbol{\tau}_s$ becomes

$$\begin{aligned} \boldsymbol{\tau}_s = & \left[\mu k_v \int_S (1 + a v_n) \boldsymbol{\rho}_t f_s(\mathbf{s}) dS \right] \times \mathbf{v}_{sct} \\ & + \mu k_v \int_S (1 + a v_n) (\boldsymbol{\rho}_t \times (\boldsymbol{\omega}_n \times \boldsymbol{\rho}_t)) f_s(\mathbf{s}) dS . \end{aligned} \quad (4.78)$$

The first integral term of Equation (4.78) is exactly I_1 from Equation (4.70), and has been shown to be zero. Therefore, Equation (4.78) simplifies to

$$\boldsymbol{\tau}_s = \mu k_v \int_S (1 + a v_n) (\boldsymbol{\rho}_t \times (\boldsymbol{\omega}_n \times \boldsymbol{\rho}_t)) f_s(\mathbf{s}) dS . \quad (4.79)$$

Replacing the definition for v_n from Equation (4.54) into Equation (4.79) gives

$$\begin{aligned} \boldsymbol{\tau}_s = & \mu k_v (1 + a v_{cn}) \int_S (\boldsymbol{\rho}_t \times (\boldsymbol{\omega}_n \times \boldsymbol{\rho}_t)) f_s(\mathbf{s}) dS \\ & + \mu k_v a \int_S (\boldsymbol{\rho}_t \times (\boldsymbol{\omega}_n \times \boldsymbol{\rho}_t)) (\mathbf{n} \cdot (\boldsymbol{\omega}_t \times \boldsymbol{\rho}_t)) f_s(\mathbf{s}) dS . \end{aligned} \quad (4.80)$$

The second integral in Equation (4.80) can be integrated in parts and can be shown to be zero; see Equations (4.72) and (4.73). The double cross product in the first integral involving $\boldsymbol{\rho}_t$, can be replaced by a double cross product involving $\boldsymbol{\rho}_s$ since it operates on $\boldsymbol{\omega}_n$ and the $\boldsymbol{\rho}_n$ component in $\boldsymbol{\rho}_s$ will not contribute in the final result. In other words, the moment of inertia about $\boldsymbol{\omega}_n$ is not affected by the relative location along \mathbf{n} about which it is evaluated. Hence, Equation (4.25) can be used to find a simple expression for the spinning friction

$$\boldsymbol{\tau}_s = \mu k_v (1 + a v_{cn}) \mathbf{J}_s \cdot \boldsymbol{\omega}_n , \quad (4.81)$$

or

$$\boldsymbol{\tau}_s = \mu \frac{f_n}{V} \mathbf{J}_s \cdot \boldsymbol{\omega}_n . \quad (4.82)$$

Figure 4.12 shows how $\boldsymbol{\tau}_s$ acts on a sphere-box pair and a cube-box pair.

4.3 Two Deformable Body Contact Model

The two deformable body contact model is based on the theoretical framework of the one deformable body model. However, there is a key difference: the location and orientation of the contact plate are no longer known. The derivations presented in this section will therefore focus on the body deformation processes occurring on both sides of the contact plate to determine its location and orientation.

The deformation of each body as it is pressed onto the contact plate can be described in terms of its *deformation volume*, defined as the section of the undeformed body geometry that is located

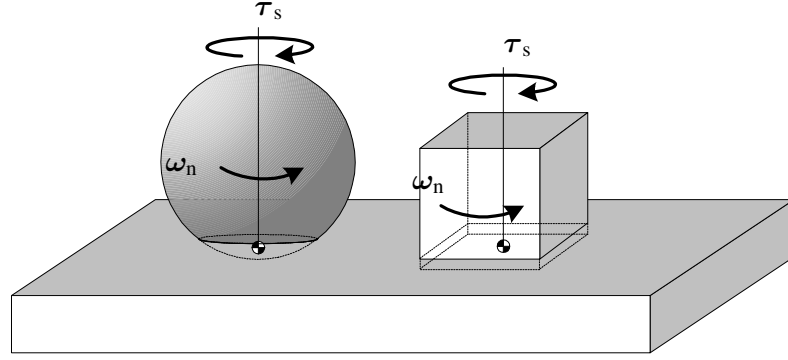


Figure 4.12: The spinning friction torque acting on a sphere and a cube.

below the contact plate surface. This volume corresponds to the volume of interference used by the one deformable body contact model. Hence, the forces and torques generated by the deformation of each body can be obtained using the one deformable body contact model. The contact plate position, orientation and motion will be determined by studying the combined effects of the forces and torques generated by the deformation of the two bodies.

Since the derivations involve the analysis of the deformations on each side of the contact plate, the quantities related to each body will be distinguished by adding the body index to the variable. Thus, quantities relating to \mathcal{B}_i and \mathcal{B}_j will be denoted by the subscripts i and j , respectively. The quantities without either subscript will be understood to relate to the entire volume of interference.

4.3.1 Contact Model Framework

This subsection introduces quantities pertaining to the volumes of deformation of bodies \mathcal{B}_i and \mathcal{B}_j , and relates them to the corresponding quantity of the volume of interference, as defined in Section 4.2.

Volume of Interference and Centroids

The resulting deformation volumes V_i and V_j on each side of the plate are found by obtaining the surface deformation depths $f_{s,i}(\mathbf{s})$ and $f_{s,j}(\mathbf{s})$ at a point \mathbf{s} on the contact surface and integrating over the contact surface area S such that

$$V_i = \int_S f_{s,i}(\mathbf{s}) dS \quad , \quad V_j = \int_S f_{s,j}(\mathbf{s}) dS \quad . \quad (4.83)$$

V_i and V_j are related to the total deformation volume V since $f_s(\mathbf{s}) = f_{s,i}(\mathbf{s}) + f_{s,j}(\mathbf{s})$, thus

$$V = \int_S f_s(\mathbf{s}) dS = \int_S f_{s,j}(\mathbf{s}) dS + \int_S f_{s,i}(\mathbf{s}) dS = V_i + V_j \quad . \quad (4.84)$$

The centroids $\mathbf{p}_{c,i}$ and $\mathbf{p}_{c,j}$ of deformation volumes V_i and V_j , respectively, are found using

$$\mathbf{p}_{c,i} = \frac{1}{V_i} \int_{V_i} \mathbf{p} dV \quad , \quad \mathbf{p}_{c,j} = \frac{1}{V_j} \int_{V_j} \mathbf{p} dV . \quad (4.85)$$

The deformation volumes share the same contact area A_c and have an average volume ‘height’

$$h_{v,i} = V_i/A_c \quad , \quad h_{v,j} = V_j/A_c . \quad (4.86)$$

For each deformation volume, the location of the weighted contact surface centroids $\mathbf{s}_{c,i}$ and $\mathbf{s}_{c,j}$ are defined as

$$\mathbf{s}_{c,i} = \frac{1}{V_i} \int_S \mathbf{s} f_{s,i}(\mathbf{s}) dS \quad , \quad \mathbf{s}_{c,j} = \frac{1}{V_j} \int_S \mathbf{s} f_{s,j}(\mathbf{s}) dS . \quad (4.87)$$

The centroid \mathbf{s}_c can be expressed in terms of $\mathbf{s}_{c,i}$ and $\mathbf{s}_{c,j}$ as using the relationship from Equation (4.84) as

$$V \mathbf{s}_c = (V_i + V_j) \mathbf{s}_c = \int_S \mathbf{s} f_s(\mathbf{s}) dS = \int_S \mathbf{s} f_{s,i}(\mathbf{s}) dS + \int_S \mathbf{s} f_{s,j}(\mathbf{s}) dS = V_i \mathbf{s}_{c,i} + V_j \mathbf{s}_{c,j} . \quad (4.88)$$

For now, $\mathbf{s}_{c,i}$ will be *selected* to be equal to $\mathbf{s}_{c,j}$. Section 4.3.2 will show that this choice is not arbitrary, and that it is in fact an equilibrium condition defining the orientation of the contact plate. Using this assumption, Equation (4.88) shows that

$$\mathbf{s}_c = \mathbf{s}_{c,i} = \mathbf{s}_{c,j} . \quad (4.89)$$

The position vectors $\boldsymbol{\rho}_{s,i}$ and $\boldsymbol{\rho}_{s,j}$ of a point \mathbf{s} on the surface S relative to deformation volumes centroids $\mathbf{p}_{c,i}$ and $\mathbf{p}_{c,j}$ are defined as

$$\boldsymbol{\rho}_{s,i} = \mathbf{s} - \mathbf{p}_{c,i} \quad , \quad \boldsymbol{\rho}_{s,j} = \mathbf{s} - \mathbf{p}_{c,j} . \quad (4.90)$$

As was demonstrated in Section 4.2.1, $\boldsymbol{\rho}_{s,i}$ and $\boldsymbol{\rho}_{s,j}$ can be decomposed into components normal and tangential to the contact plate as

$$\begin{aligned} \boldsymbol{\rho}_{n,i} &= \mathbf{s}_{c,i} - \mathbf{p}_{c,i} \quad , \quad \boldsymbol{\rho}_{n,j} = \mathbf{s}_{c,j} - \mathbf{p}_{c,j} , \\ \boldsymbol{\rho}_{t,i} &= \mathbf{s} - \mathbf{s}_{c,i} \quad , \quad \boldsymbol{\rho}_{t,j} = \mathbf{s} - \mathbf{s}_{c,j} . \end{aligned} \quad (4.91)$$

Comparing Equations (4.91) and (4.89), it becomes clear that

$$\boldsymbol{\rho}_{t,i} = \boldsymbol{\rho}_{t,j} = \boldsymbol{\rho}_t = \mathbf{s} - \mathbf{s}_c . \quad (4.92)$$

As derived in Section 4.2.1, it can be shown that $(\mathbf{s}_c - \mathbf{p}_{c,i})$ and $(\mathbf{s}_c - \mathbf{p}_{c,j})$ are also parallel to \mathbf{n} , and therefore it follows that $\mathbf{p}_{c,i}$, $\mathbf{p}_{c,j}$, \mathbf{p}_c , and \mathbf{s}_c are collinear.

Surface Inertia Tensors

Finally, the surface inertia tensors $\mathbf{J}_{s,i}$ and $\mathbf{J}_{s,j}$ of each deformation volume are defined with respect to the centroid of the total volume of interference \mathbf{p}_c . These are given as

$$\begin{aligned}\mathbf{J}_{s,i} &= \int_S ((\boldsymbol{\rho}_s \cdot \boldsymbol{\rho}_s) \mathbf{I} - \boldsymbol{\rho}_s \boldsymbol{\rho}_s) f_{s,i}(\mathbf{s}) dS = V_i \mathbf{J}_{\boldsymbol{\rho}_s, \text{avg}} , \\ \mathbf{J}_{s,j} &= \int_S ((\boldsymbol{\rho}_s \cdot \boldsymbol{\rho}_s) \mathbf{I} - \boldsymbol{\rho}_s \boldsymbol{\rho}_s) f_{s,j}(\mathbf{s}) dS = V_j \mathbf{J}_{\boldsymbol{\rho}_s, \text{avg}} ,\end{aligned}\tag{4.93}$$

where $\mathbf{J}_{\boldsymbol{\rho}_s, \text{avg}}$ is defined as in Section 4.2.1. Again, it follows that

$$\mathbf{J}_{s,i} + \mathbf{J}_{s,j} = (V_i + V_j) \mathbf{J}_{\boldsymbol{\rho}_s, \text{avg}} = V \mathbf{J}_{\boldsymbol{\rho}_s, \text{avg}} = \mathbf{J}_s .\tag{4.94}$$

Body Velocities With Respect to the Contact Plate

In Section 4.2, the contact plate is attached to the body \mathcal{B}_j . Hence, its motion corresponds to the motion of that body. Here however, the contact plate moves between the two bodies since both bodies deform during impact. Essentially, the contact plate behaves as a 6 degrees-of-freedom body constrained by the deformation forces from \mathcal{B}_i and \mathcal{B}_j . To characterize the plate position, orientation and motion, the forces acting on it must be determined. These forces also depend on the translational and angular velocity of the plate relative to each body. In this section, expressions for these relative velocities are derived.

The plate motion will be characterized in terms of the motion of the weighted surface centroid \mathbf{s}_c . Recall that \mathbf{s}_c has been assumed to be located at the same position as the weighted surface centroids $\mathbf{s}_{c,i}$ and $\mathbf{s}_{c,j}$ of the deformation volumes V_i and V_j on each side of the plate. As was shown in the derivation for \mathbf{v}_r in Equation (3.3), the translational motion of a point \mathbf{s} on the contact plate relative to \mathcal{B}_i is given as

$$\mathbf{v}_{r,i} = (\mathbf{v}_p + \boldsymbol{\omega}_p \times \boldsymbol{\rho}_t) - (\mathbf{v}_i + \boldsymbol{\omega}_i \times \boldsymbol{\rho}_i) ,\tag{4.95}$$

where \mathbf{v}_p and $\boldsymbol{\omega}_p$ are the translational and angular velocities of the contact plate at \mathbf{s}_c . Note that the contact plate motion could have been characterized by using any other point on the plate, thus yielding a different value for \mathbf{v}_p and $\boldsymbol{\omega}_p$. However, since \mathbf{s}_c is already defined, it is convenient to use this location on the contact plate. The angular motion of the contact plate relative to \mathcal{B}_i is simply given as

$$\boldsymbol{\omega}_{r,i} = \boldsymbol{\omega}_p - \boldsymbol{\omega}_i .\tag{4.96}$$

Substituting the definition for $\boldsymbol{\rho}_i$ in Equation (4.95), and expressing \mathbf{s} in terms of $\mathbf{p}_{c,i}$ and $\boldsymbol{\rho}_{s,i}$, the

relative motion is expressed as

$$\mathbf{v}_{r,i} = \mathbf{v}_{c,i} + \boldsymbol{\omega}_{r,i} \times \boldsymbol{\rho}_{s,i} , \quad (4.97)$$

where $\mathbf{v}_{c,i}$ is defined as

$$\mathbf{v}_{c,i} = (\mathbf{v}_p - \boldsymbol{\omega}_p \times \boldsymbol{\rho}_{n,i}) - (\mathbf{v}_i + \boldsymbol{\omega}_i \times (\mathbf{p}_{c,i} - \mathbf{r}_i)) \quad (4.98)$$

and describes the relative velocity of body \mathcal{B}_i with respect to the contact plate at $\mathbf{p}_{c,i}$. By definition, $\mathbf{p}_{c,i} = \boldsymbol{\rho}_n - \boldsymbol{\rho}_{n,i} + \mathbf{p}_c$, and therefore Equation (4.98) can be written in terms of \mathbf{p}_c as

$$\mathbf{v}_{c,i} = (\mathbf{v}_p - \boldsymbol{\omega}_{r,i} \times \boldsymbol{\rho}_{n,i} - \boldsymbol{\omega}_i \times \boldsymbol{\rho}_n) - (\mathbf{v}_i + \boldsymbol{\omega}_i \times (\mathbf{p}_c - \mathbf{r}_i)) . \quad (4.99)$$

Similarly, the translational motion of a point s on the contact plate relative to \mathcal{B}_j is given as

$$\mathbf{v}_{r,j} = (\mathbf{v}_p + \boldsymbol{\omega}_p \times \boldsymbol{\rho}_t) - (\mathbf{v}_j + \boldsymbol{\omega}_j \times \boldsymbol{\rho}_j) , \quad (4.100)$$

and the relative angular motion is given as

$$\boldsymbol{\omega}_{r,j} = \boldsymbol{\omega}_p - \boldsymbol{\omega}_j , \quad (4.101)$$

such that

$$\mathbf{v}_{r,j} = \mathbf{v}_{c,j} + \boldsymbol{\omega}_{r,j} \times \boldsymbol{\rho}_{s,j} , \quad (4.102)$$

where $\mathbf{v}_{c,j}$ is expressed as

$$\mathbf{v}_{c,j} = (\mathbf{v}_p - \boldsymbol{\omega}_{r,j} \times \boldsymbol{\rho}_{n,j} - \boldsymbol{\omega}_j \times \boldsymbol{\rho}_n) - (\mathbf{v}_j + \boldsymbol{\omega}_j \times (\mathbf{p}_c - \mathbf{r}_j)) . \quad (4.103)$$

Now, \mathbf{v}_c was defined in Equation (4.51) and is related to $\mathbf{v}_{c,i}$ and $\mathbf{v}_{c,j}$ as

$$\mathbf{v}_c = (\mathbf{v}_{c,j} - \mathbf{v}_{c,i}) + (\boldsymbol{\omega}_{r,j} \times \boldsymbol{\rho}_{n,j} - \boldsymbol{\omega}_{r,i} \times \boldsymbol{\rho}_{n,i} - \boldsymbol{\omega}_r \times \boldsymbol{\rho}_n) . \quad (4.104)$$

In Equation (4.104), the terms inside the second parentheses on the right hand-side only contribute velocities tangential to the contact plate. Hence, it is concluded that

$$\mathbf{N} \cdot \mathbf{v}_c = v_{cn} \mathbf{n} = \mathbf{N} \cdot (\mathbf{v}_{c,j} - \mathbf{v}_{c,i}) = v_{cn,j} \mathbf{n}_j - v_{cn,i} \mathbf{n}_i , \quad (4.105)$$

where $v_{cn,i} = \mathbf{n}_i \cdot \mathbf{N} \cdot \mathbf{v}_{c,i}$ and $v_{cn,j} = \mathbf{n}_j \cdot \mathbf{N} \cdot \mathbf{v}_{c,j}$. Substituting the convention for \mathbf{n}_i and \mathbf{n}_j gives

$$v_{cn} = v_{cn,i} + v_{cn,j} . \quad (4.106)$$

Similarly, the normal velocity at any point s on the contact surface is obtained by pre-multiplying Equations (4.97) and (4.102) by \mathbf{N} . Simplifying Equation (4.54) leads to

$$\begin{aligned}\mathbf{N} \cdot \mathbf{v}_{r,i} &= \mathbf{v}_{n,i} = v_{cn,i} \mathbf{n}_i + (\boldsymbol{\omega}_{t,i} \times \boldsymbol{\rho}_t) , \\ \mathbf{N} \cdot \mathbf{v}_{r,j} &= \mathbf{v}_{n,j} = v_{cn,j} \mathbf{n}_j + (\boldsymbol{\omega}_{t,j} \times \boldsymbol{\rho}_t) ,\end{aligned}\quad (4.107)$$

when recalling that $\boldsymbol{\rho}_{t,i} = \boldsymbol{\rho}_{t,j} = \boldsymbol{\rho}_t$. Writing the expressions in scalar form gives

$$\begin{aligned}v_{n,i} &= \mathbf{n}_i \cdot \mathbf{v}_{n,i} = v_{cn,i} + \mathbf{n}_i \cdot (\boldsymbol{\omega}_{t,i} \times \boldsymbol{\rho}_t) , \\ v_{n,j} &= \mathbf{n}_j \cdot \mathbf{v}_{n,j} = v_{cn,j} + \mathbf{n}_j \cdot (\boldsymbol{\omega}_{t,j} \times \boldsymbol{\rho}_t) .\end{aligned}\quad (4.108)$$

By applying the convention for \mathbf{n}_i and \mathbf{n}_j , the normal velocities $v_{n,i}$ and $v_{n,j}$ are related to v_n as follows

$$\begin{aligned}v_n &= \mathbf{n} \cdot (v_{n,j} \mathbf{n}_j - v_{n,i} \mathbf{n}_i) = v_{n,j} + v_{n,i} \\ &= v_{cn,i} + v_{cn,j} + \mathbf{n} \cdot [(\mathbf{T}(\boldsymbol{\omega}_p - \boldsymbol{\omega}_j) - \mathbf{T}(\boldsymbol{\omega}_p - \boldsymbol{\omega}_i)) \times \boldsymbol{\rho}_t] \\ &= v_{cn} + \mathbf{n} \cdot (\boldsymbol{\omega}_t \times \boldsymbol{\rho}_t) ,\end{aligned}\quad (4.109)$$

which corresponds to the definition from Equation (4.54). Hence, in vectorial form the relationship for the relative velocities in the normal direction is simply

$$\mathbf{v}_n = \mathbf{v}_{n,j} - \mathbf{v}_{n,i} . \quad (4.110)$$

The relationship for the normal angular velocity can be obtained by pre-multiplying Equation (4.49), (4.96) and (4.101) by \mathbf{N} , and noting that $\boldsymbol{\omega}_r = \boldsymbol{\omega}_{r,j} - \boldsymbol{\omega}_{r,i}$, hence,

$$\boldsymbol{\omega}_n = \boldsymbol{\omega}_{n,j} - \boldsymbol{\omega}_{n,i} . \quad (4.111)$$

Equation (4.111) can be expressed in scalar form by taking the dot product with \mathbf{n} on both sides

$$\omega_n = \omega_{n,i} + \omega_{n,i} , \quad (4.112)$$

where the convention for \mathbf{n}_i and \mathbf{n}_j was used.

A relationship for the relative velocities at the centroids \mathbf{s}_c , $\mathbf{s}_{c,i}$ and $\mathbf{s}_{c,j}$ in the tangential direction can also be obtained from Equation (4.104). Re-writing it as

$$(\mathbf{v}_c + \boldsymbol{\omega}_r \times \boldsymbol{\rho}_n) = (\mathbf{v}_{c,j} + \boldsymbol{\omega}_{r,j} \times \boldsymbol{\rho}_{n,j}) - (\mathbf{v}_{c,i} + \boldsymbol{\omega}_{r,i} \times \boldsymbol{\rho}_{n,i}) \quad (4.113)$$

and pre-multiplying both side by the projection operator \mathbf{T} yields

$$(\mathbf{v}_{ct} + \boldsymbol{\omega}_t \times \boldsymbol{\rho}_n) = (\mathbf{v}_{ct,j} + \boldsymbol{\omega}_{t,j} \times \boldsymbol{\rho}_{n,j}) - (\mathbf{v}_{ct,i} + \boldsymbol{\omega}_{t,i} \times \boldsymbol{\rho}_{n,i}) , \quad (4.114)$$

where the cross-product operations between the parallel parts of the vectors have been removed. In Equation (4.114), the terms inside the parentheses correspond to the relative velocities at \mathbf{s}_c , $\mathbf{s}_{c,i}$ and, $\mathbf{s}_{c,j}$ respectively. Hence it is seen that

$$\mathbf{v}_{\text{sct}} = \mathbf{v}_{\text{sct},j} - \mathbf{v}_{\text{sct},i} , \quad (4.115)$$

where

$$\begin{aligned} \mathbf{v}_{\text{sct},i} &= \mathbf{v}_{\text{ct},i} + \boldsymbol{\omega}_{t,i} \times \boldsymbol{\rho}_{n,i} \\ \mathbf{v}_{\text{sct},j} &= \mathbf{v}_{\text{ct},j} + \boldsymbol{\omega}_{t,j} \times \boldsymbol{\rho}_{n,j} . \end{aligned} \quad (4.116)$$

The tangential velocity of a point \mathbf{s} located at $\boldsymbol{\rho}_t$ from the surface centroid \mathbf{s}_c and relative to the centroids $\mathbf{s}_c = \mathbf{s}_{c,i} = \mathbf{s}_{c,j}$ is obtained by adding $\boldsymbol{\omega}_n \times \boldsymbol{\rho}_t = (\boldsymbol{\omega}_{n,j} - \boldsymbol{\omega}_{n,i}) \times \boldsymbol{\rho}_t$ to the surface centroid velocity expressions, namely,

$$(\mathbf{v}_{\text{sct}} + \boldsymbol{\omega}_n \times \boldsymbol{\rho}_t) = (\mathbf{v}_{\text{sct},j} + \boldsymbol{\omega}_{n,j} \times \boldsymbol{\rho}_{t,j}) - (\mathbf{v}_{\text{sct},i} + \boldsymbol{\omega}_{n,i} \times \boldsymbol{\rho}_{t,i}) , \quad (4.117)$$

where the relationship between the normal angular velocities given in Equation (4.111) was used while recalling that $\boldsymbol{\rho}_t = \boldsymbol{\rho}_{t,i} = \boldsymbol{\rho}_{t,j}$. Equation (4.117) corresponds to the definition of the tangential velocity expression for \mathbf{v}_t given in Equation (4.57). Hence it is concluded that

$$\mathbf{v}_t = \mathbf{v}_{t,j} - \mathbf{v}_{t,i} , \quad (4.118)$$

where

$$\begin{aligned} \mathbf{v}_{t,i} &= \mathbf{v}_{\text{sct},i} + \boldsymbol{\omega}_{n,i} \times \boldsymbol{\rho}_{t,i} , \\ \mathbf{v}_{t,j} &= \mathbf{v}_{\text{sct},j} + \boldsymbol{\omega}_{n,j} \times \boldsymbol{\rho}_{t,j} . \end{aligned} \quad (4.119)$$

The relationship for the tangential angular velocities can be obtained by pre-multiplying Equations (4.49), (4.96) and (4.101) by \mathbf{T} and noting that $\boldsymbol{\omega}_r = \boldsymbol{\omega}_{r,j} - \boldsymbol{\omega}_{r,i}$, i.e.,

$$\boldsymbol{\omega}_t = \boldsymbol{\omega}_{t,j} - \boldsymbol{\omega}_{t,i} . \quad (4.120)$$

Given that $\mathbf{v}_{r,i} = \mathbf{v}_{n,i} + \mathbf{v}_{t,i}$ and $\mathbf{v}_{r,j} = \mathbf{v}_{n,j} + \mathbf{v}_{t,j}$, and according to the definitions of \mathbf{v}_r , $\boldsymbol{\omega}_r$, $\mathbf{v}_{r,i}$, $\boldsymbol{\omega}_{r,i}$, $\mathbf{v}_{r,j}$ and $\boldsymbol{\omega}_{r,j}$ it can be seen that

$$\begin{aligned} \mathbf{v}_r &= \mathbf{v}_{r,j} - \mathbf{v}_{r,i} , \\ \boldsymbol{\omega}_r &= \boldsymbol{\omega}_{r,j} - \boldsymbol{\omega}_{r,i} . \end{aligned} \quad (4.121)$$

4.3.2 Contact Plate

The position and orientation of the contact plate are directly affected by the contact pressure acting on each side of the plate. On the other hand, the amount of deformation causing the contact pressure is determined by the position and orientation of the contact plate. Hence, the two problems are inter-dependent and must be solved at the same time.

Equivalent Stiffness

To determine the pressures acting on the contact plate, the body-to-body interaction is studied under quasi-static loading conditions. The quasi-static normal contact forces $\mathbf{f}_{n,i} = f_{n,i} \mathbf{n}_i$ and $\mathbf{f}_{n,j} = f_{n,j} \mathbf{n}_j$ pushing on each side of the plate are found by integrating the contact pressure over the contact area S , i.e.,

$$\begin{aligned} f_{n,i} &= \int_S k_{v,i} f_{s,i}(\mathbf{s}) dS = k_{v,i} V_i , \\ f_{n,j} &= \int_S k_{v,j} f_{s,j}(\mathbf{s}) dS = k_{v,j} V_j , \end{aligned} \quad (4.122)$$

where $k_{v,i}$ and $k_{v,j}$ are the volumetric stiffness of \mathcal{B}_i and \mathcal{B}_j respectively. Note that in general $k_{v,i} \neq k_{v,j}$. The normal contact force \mathbf{f}_n is the result of the force applied on each side of the plate, and therefore

$$\mathbf{f}_n = f_{n,j} \mathbf{n}_j = -f_{n,i} \mathbf{n}_i , \quad (4.123)$$

where \mathbf{f}_n is taken to have a positive value when it points in the direction of $\mathbf{n}_j = \mathbf{n}$. It follows that

$$2\mathbf{f}_n = f_{n,j} \mathbf{n}_j - f_{n,i} \mathbf{n}_i = (k_{v,i} V_i + k_{v,j} V_j) \mathbf{n} . \quad (4.124)$$

On the other hand, the contact plate is massless: it will always be in equilibrium. As a result, the sum of the normal forces acting on the contact plate should be zero. The sum of the normal forces acting on the contact plate is therefore given as

$$f_{n,i} \mathbf{n}_i + f_{n,j} \mathbf{n}_j = 0 , \quad (4.125)$$

which yields

$$k_{v,i} V_i = k_{v,j} V_j . \quad (4.126)$$

Equation (4.126) indicates that the volume on each side of the contact plate will be different when $k_{v,i} \neq k_{v,j}$. Combining Equations (4.84) and (4.126) gives expressions for V_i and V_j in terms of V

$$\begin{aligned} V_i &= r_i V, \quad \text{where } r_i = \frac{k_{v,j}}{k_{v,i} + k_{v,j}}, \\ V_j &= r_j V, \quad \text{where } r_j = \frac{k_{v,i}}{k_{v,i} + k_{v,j}}. \end{aligned} \quad (4.127)$$

The ratios r_i and r_j relate the size of the volume of deformation of the bodies to the size of the total volume of deformation V , i.e., the volume of interference. When the stiffness of one body is much larger than the stiffness of the other body, the ratios reduce to values of 0 and 1 as follows

$$\begin{aligned} r_i &= 0 ; r_j = 1, \quad \text{when } k_{v,i} \gg k_{v,j} \quad (\mathcal{B}_i \text{ rigid}), \\ r_i &= 1 ; r_j = 0, \quad \text{when } k_{v,i} \ll k_{v,j} \quad (\mathcal{B}_j \text{ rigid}), \end{aligned} \quad (4.128)$$

and therefore

$$\begin{aligned} V_i &= 0 ; V_j = V, \quad \text{when } k_{v,i} \gg k_{v,j} \quad (\mathcal{B}_i \text{ rigid}), \\ V_i &= V ; V_j = 0, \quad \text{when } k_{v,i} \ll k_{v,j} \quad (\mathcal{B}_j \text{ rigid}). \end{aligned} \quad (4.129)$$

The Equation (4.129) confirms the fact that rigid bodies do not deform, i.e., $V_i = 0$ when \mathcal{B}_i is rigid and $V_j = 0$ when \mathcal{B}_j is rigid. This observation will play a key role in the determination of the contact plate velocities later in this section.

Next, a new equivalent contact stiffness k_v is defined such that

$$2V k_v = k_{v,i} V_i + k_{v,j} V_j. \quad (4.130)$$

Substituting the expressions for V_i and V_j given above results in

$$2V k_v = k_{v,i} r_i V + k_{v,j} r_j V. \quad (4.131)$$

The V can be eliminated in the expression above such that an expression for k_v only in terms of $k_{v,i}$ and $k_{v,j}$ is found as

$$k_v = \left(\frac{1}{k_{v,i}} + \frac{1}{k_{v,j}} \right)^{-1}. \quad (4.132)$$

Interestingly, when one of the bodies becomes rigid, for example \mathcal{B}_i and therefore $k_{v,i} \gg k_{v,j}$, then Equation (4.132) indicates that $k_v = k_{v,j}$. Similarly, if \mathcal{B}_j is rigid, then $k_v = k_{v,i}$. Hence, when the stiffness of one body is set to infinity, the definition of k_v reduces to the one deformable body case, i.e., k_v corresponds to the stiffness of the deformable body.

Comparing Equations (4.124) and (4.131), it is obvious that

$$\mathbf{f}_n = k_v V \mathbf{n} . \quad (4.133)$$

Hence, k_v and V can be used to obtain the total quasi-static normal contact force even when the two bodies do not have the same stiffness. It is not necessary to find the values of V_i and V_j independently. Only V needs to be computed.

Contact Plate Orientation

The contact plate orientation is determined exclusively by the moments acting on it. Since it is massless, the moments acting on the plate should always add up to zero. Taking the moments of the pressures from the deformation of \mathcal{B}_i acting on the plate about the centroid $\mathbf{s}_{c,i}$ gives

$$\int_S \boldsymbol{\rho}_{t,i} \times d\mathbf{f}_{n,i} = k_{v,i} \int_S (\mathbf{s} - \mathbf{s}_{c,i}) f_{s,i}(\mathbf{s}) dS \times \mathbf{n}_i . \quad (4.134)$$

The right hand side of Equation (4.134) is easily solved using Equation (4.83) yielding

$$\int_S \boldsymbol{\rho}_{t,i} \times d\mathbf{f}_{n,i} = k_{v,i} \left[\int_S \mathbf{s} f_{s,i}(\mathbf{s}) dS - \mathbf{s}_{c,i} V_i \right] \times \mathbf{n}_i = 0 . \quad (4.135)$$

The term in brackets of Equation (4.135) evaluates to zero; see the definition of $\mathbf{s}_{c,i}$ given in Equation (4.87). Hence, the contact pressure induced by the deformation of body \mathcal{B}_i is equally distributed about the centroid $\mathbf{s}_{c,i}$. Similarly, it can be shown that the contact pressure resulting from the deformation of body \mathcal{B}_j is equally distributed about $\mathbf{s}_{c,j}$.

The above derivations indicate that the moment generated by the deformation of \mathcal{B}_i is zero at $\mathbf{s}_{c,i}$ and the moment generated by the deformation of \mathcal{B}_j is zero at $\mathbf{s}_{c,j}$. Hence, no external moments will be applied to the contact plate when $\mathbf{s}_{c,i} = \mathbf{s}_{c,j}$. In other words, under quasi-static loading conditions, the contact plate will naturally “adapt” its orientation such that $\mathbf{s}_{c,i} = \mathbf{s}_{c,j}$, thereby ensuring the net resultant moment acting on it is zero. This conclusion validates the hypothesis presented in Section 4.3.1, namely that $\mathbf{s}_{c,i} = \mathbf{s}_{c,j}$ and therefore that $\mathbf{s}_c = \mathbf{s}_{c,i} = \mathbf{s}_{c,j}$.

Contact Plate Position

Given that $\mathbf{s}_c = \mathbf{s}_{c,i} = \mathbf{s}_{c,j}$, it follows that the centroids \mathbf{p}_c , $\mathbf{p}_{c,i}$ and $\mathbf{p}_{c,j}$ of the volumes V , V_i and V_j , respectively, are located along the same line since $\boldsymbol{\rho}_n$, $\boldsymbol{\rho}_{n,i}$ and $\boldsymbol{\rho}_{n,j}$ are parallel vectors. However, V_i and V_j are sub-volumes of V such that $V_i + V_j = V$. Therefore, the location of the centroid \mathbf{p}_c can be expressed as a weighted summation of the centroids $\mathbf{p}_{c,i}$ and $\mathbf{p}_{c,j}$ as

$$V \mathbf{p}_c = V_i \mathbf{p}_{c,i} + V_j \mathbf{p}_{c,j} . \quad (4.136)$$

Subtracting $V \mathbf{s}_c = (V_i + V_j) \mathbf{s}_c$ from both sides of Equation (4.136) and using the definitions for ρ_n , $\rho_{n,i}$ and $\rho_{n,j}$ results in

$$V \rho_n = V_i \rho_{n,i} + V_j \rho_{n,j} . \quad (4.137)$$

Now, V_i and V_j can be expressed in terms of V (Equation (4.127)), and then dividing through by V , giving

$$\rho_n = r_i \rho_{n,i} + r_j \rho_{n,j} . \quad (4.138)$$

Equation (4.138) shows that ρ_n corresponds to either $\rho_{n,i}$ or $\rho_{n,j}$ when one of the bodies is rigid. If a body is rigid, then its deformation volume is zero and, therefore, its corresponding offset from the zero-volume centroid to the contact surface is also zero. Hence, when one body is rigid Equation (4.138) simplifies to

$$\rho_n = \rho_{n,j} , \quad \text{when } k_{v,i} \gg k_{v,j} \text{ } (\mathcal{B}_i \text{ rigid}) , \quad (4.139)$$

$$\rho_n = \rho_{n,i} , \quad \text{when } k_{v,i} \ll k_{v,j} \text{ } (\mathcal{B}_j \text{ rigid}) . \quad (4.140)$$

Not knowing *a priori* what are the shapes of V_i and V_j it is not possible to determine $\rho_{n,i}$ and $\rho_{n,j}$. However, Equations (4.8) and (4.86) give information of the average volume height for a given contact surface area A_c . If the volume of interference between the bodies is assumed to have a constant cross-section area, then the centroids of the volumes V_i and V_j are located at $\frac{1}{2} h_{v,i} \mathbf{n}_i$ and $\frac{1}{2} h_{v,j} \mathbf{n}_j$ from the contact plate. Hence, the contact plate is located at $\rho_{n,i} = -\frac{1}{2} h_{v,i} \mathbf{n}_i$ from $\mathbf{p}_{c,i}$ and $\rho_{n,j} = -\frac{1}{2} h_{v,j} \mathbf{n}_j$ from $\mathbf{p}_{c,j}$. Using this approximation, the estimated values for the centroid locations $\rho_{n,i}$ and $\rho_{n,j}$ are substituted in Equation (4.138). It follows that

$$\rho_n = -r_i \frac{V_i}{2 A_c} \mathbf{n}_i - r_j \frac{V_j}{2 A_c} \mathbf{n}_j , \quad (4.141)$$

where the values for $h_{v,i}$ and $h_{v,j}$ have been replaced following Equation (4.86). Expressing V_i and V_j in terms of V and noting that $V = h_v A_c$ gives

$$\rho_n = (r_i^2 - r_j^2) \frac{h_v}{2} \mathbf{n} \quad (4.142)$$

or

$$\rho_n = \left(\frac{k_{v,j} - k_{v,i}}{k_{v,i} + k_{v,j}} \right) \frac{h_v}{2} \mathbf{n} . \quad (4.143)$$

Equation (4.143) indicates that when $k_{v,i} < k_{v,j}$ and $V_i > V_j$, ρ_n points in the same direction as \mathbf{n} , i.e., toward body \mathcal{B}_i . Figure 4.13 illustrates the change in position of the contact plate location for two cases. The dashed line shows the plate location when $k_{v,i} = k_{v,j}$, and therefore $\mathbf{p}_c = \mathbf{s}_c$.

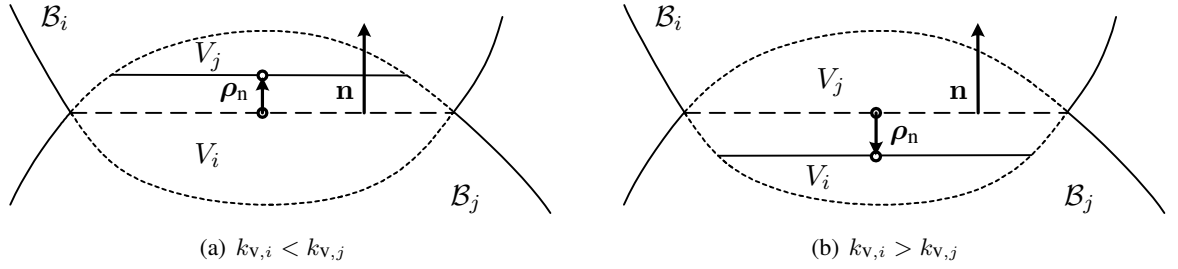


Figure 4.13: The contact plate normal offset ρ_n .

Figure 4.13(a) shows the case when $k_{v,i} < k_{v,j}$ and therefore $\rho_n \cdot \mathbf{n} > 0$. It can be seen that the contact plate moves toward \mathcal{B}_i , thereby increasing the size of V_i and reducing the size of V_j . Figure 4.13(b) illustrates the reverse.

Equation (4.143) can be used to obtain an estimate of the contact surface offset distance from the centroid of the volume of interference \mathbf{p}_c . However, it requires computing a value for h_v , which in turn means the area of the contact surface A_c must be determined, i.e., $h_v = V/A_c$. If the volume and the direction of the contact normal \mathbf{n} are known, then it is possible to project the volume of interference onto the contact plate along \mathbf{n} and obtain the resulting area of contact A_c . This can be done analytically or numerically.

Equation (4.143) can also be used to find an estimate for the offset in the extreme cases when one body is rigid and the other flexible. In this case the equation simplifies into

$$\rho_n = -\frac{h_v}{2} \mathbf{n}, \quad \text{when } k_{v,i} \gg k_{v,j} \text{ } (\mathcal{B}_i \text{ rigid}), \quad (4.144)$$

$$\rho_n = \frac{h_v}{2} \mathbf{n}, \quad \text{when } k_{v,i} \ll k_{v,j} \text{ } (\mathcal{B}_j \text{ rigid}). \quad (4.145)$$

Figure 4.14 shows the resulting contact plate position offset ρ_n when one of the bodies is rigid and the other is compliant and has a constant cross section area. In this case, Equations (4.144) and (4.145) yield the exact result.

Equation (4.143) emphasizes the dependence of ρ_n on the stiffness of the two bodies. When these stiffnesses are similar, then the value of ρ_n becomes small. For the type of simulation scenarios selected in this work this assumption is valid. Furthermore, it is also expected that the inter-penetration depths will be small. As a result, h_v will be small as well. Hence, the value of ρ_n is very small or negligible. As a result, the contact model implementation will assume that ρ_n is negligible and hence that $\mathbf{p}_c \approx \mathbf{s}_c$ and $\mathbf{v}_{ct} \approx \mathbf{v}_{sct}$; see Equations (4.20) and (4.58).

Contact Plate Pressure Differential

The quasi-static normal contact force acting on each side of the contact plate was found to be $k_{v,i} V_i = k_{v,j} V_j$ in magnitude. The force on each side is the resultant of the pressure acting at each

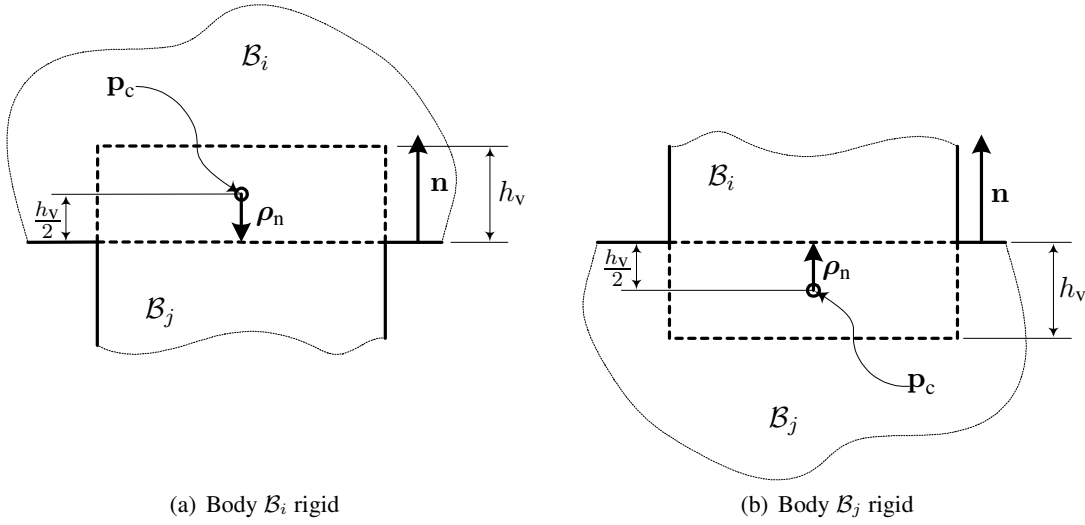


Figure 4.14: The contact plate normal offset ρ_n for rigid bodies.

infinitesimal surface element of the contact surface. This local pressure is directly a function of the local deformation depths $f_{s,i}(\mathbf{s})$ and $f_{s,j}(\mathbf{s})$ of the contact surface of each body. Hence, because the shapes of the bodies are arbitrary, $f_{s,i}(\mathbf{s})$ and $f_{s,j}(\mathbf{s})$ will in general be different. Consequently, the local pressure on each side of the force plate should not be assumed to be equal, i.e., $k_{v,i} f_{s,i}(\mathbf{s}) \neq k_{v,j} f_{s,j}(\mathbf{s})$. The resulting pressure differential has not been considered yet in the derivations of the proposed contact model. Its impact, if any, will now be investigated.

A new shape function $f_{s,p}(\mathbf{s})$ is introduced to help analyze the pressure differential behaviour. This shape function is defined as the shape the contact plate would assume if it was massless but not rigid at all, i.e., a completely compliant surface with no stiffness. Similarly to $f_{s,i}(\mathbf{s})$ and $f_{s,j}(\mathbf{s})$, $f_{s,p}(\mathbf{s})$ measures the distance of the flexible contact plate relative to the rigid contact plate position, and will be assumed positive in the direction of \mathbf{n} . Figure 4.15 shows an example of a flexible plate shape where the contact stiffness of both bodies is assumed to be roughly equal. The dashed line represents the rigid contact plate.

Because the flexible plate is not able to resist any normal pressure differential, the local pressure acting on each side of the flexible contact plate will be equal. Hence, $f_{s,p}(\mathbf{s})$ would satisfy

$$k_{v,i} (f_{s,i}(\mathbf{s}) + f_{s,p}(\mathbf{s})) = k_{v,j} (f_{s,j}(\mathbf{s}) - f_{s,p}(\mathbf{s})) . \quad (4.146)$$

Re-writing Equation (4.146) and integrating over the contact surface gives

$$\begin{aligned} (k_{v,i} + k_{v,j}) \int_S f_{s,p}(\mathbf{s}) dS &= k_{v,i} \int_S f_{s,i}(\mathbf{s}) dS - k_{v,j} \int_S f_{s,j}(\mathbf{s}) dS = 0 \\ &= k_{v,i} V_i - k_{v,j} V_j = 0 \end{aligned} \quad (4.147)$$

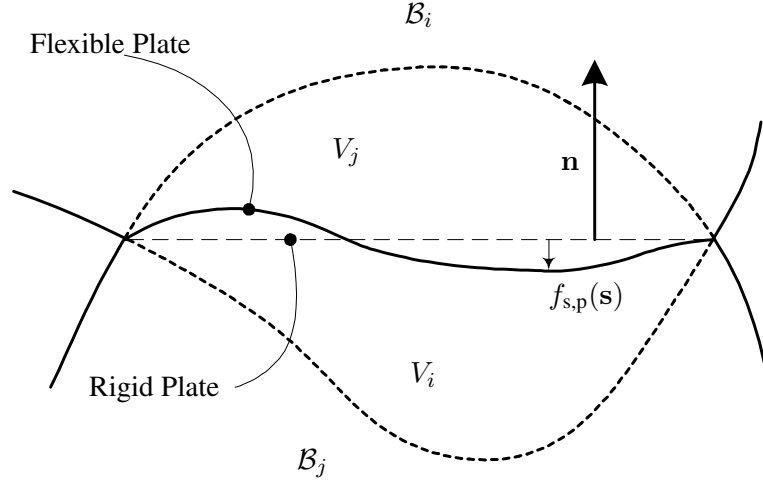


Figure 4.15: The flexible plate when $k_{v,i} \approx k_{v,j}$.

or

$$\int_S f_{s,p}(\mathbf{s}) dS = 0. \quad (4.148)$$

Equation (4.148) indicates that on average, the offset of the flexible contact surface with respect to the rigid one is zero.

Next, the torque produced by the pressure differential on the rigid plate is analyzed. Taking the cross-product on both sides of Equation (4.146) with $\boldsymbol{\rho}_t$ gives

$$(k_{v,i} + k_{v,j}) \int_S \boldsymbol{\rho}_t f_{s,p}(\mathbf{s}) dS \times \mathbf{n} = k_{v,i} \int_S \boldsymbol{\rho}_t f_{s,i}(\mathbf{s}) dS \times \mathbf{n} - k_{v,j} \int_S \boldsymbol{\rho}_t f_{s,j}(\mathbf{s}) dS \times \mathbf{n}. \quad (4.149)$$

Now, both integrals on the right hand-side of Equation (4.149) have been shown to be zero (see Equation (4.22)), and hence Equation (4.149) equals zero. Expressing $\boldsymbol{\rho}_t$ in terms of \mathbf{s} and \mathbf{s}_c in Equation (4.149) yields

$$\int_S \boldsymbol{\rho}_t f_{s,p}(\mathbf{s}) dS = \int_S \mathbf{s} f_{s,p}(\mathbf{s}) dS - \mathbf{s}_c \int_S f_{s,p}(\mathbf{s}) dS = 0. \quad (4.150)$$

Equation (4.150) shows that on average, the torque produced by the rigid contact plate about the centroid \mathbf{s}_c is zero. Furthermore, Equations (4.147) and (4.150) show that even though the contact plate is rigid, and therefore that the local pressure is different on each side of it, this has no impact on the net forces and torques produced by the deformation of the bodies. As a result, the contact plate can be assumed to be rigid and therefore perfectly flat, thereby allowing the tangential forces considered as being perpendicular to the normal ones.

Contact Plate Velocities

The analysis of the motion of the contact plate presented in Section 4.3.1 focused on deriving expressions relating the relative velocities of each deformable body \mathcal{B}_i and \mathcal{B}_j to the relative velocities of the entire volume of interference; see Equations (4.106), (4.110), (4.118) and (4.121). However, the velocities of the contact plate \mathbf{v}_p and $\boldsymbol{\omega}_p$ were not determined. This section introduces relationships defining these velocities in terms of the motion and stiffness of the bodies. These relationships will be shown to be consistent with a quasi-static process assumption.

In Section 3.2.1, it was observed that during the collision process, the energy is not dissipated through the action of a spring-damper type of surface deformation response. If the latter was true, the shape of the deformation would be affected by the normal relative velocity. Instead, the normal impact energy is dissipated by different phenomena whose effects on the shape of the deformed surfaces are neglected. As a result, the shape of the deformed surfaces has the shape of the quasi-static deformation, or in other words, the shape of the deformation is not affected by the normal velocity. Hence, the collision process is treated quasi-statically. This observation also applies to contact models based on Hertz theory, which is also based on a quasi-static process assumption; see Section 2.1.1.

With this observation in mind, the selection of a relationship defining the contact plate velocities becomes rather arbitrary: because the collision process is treated quasi-statically, the effect of the velocities is neglected. However, to include normal energy dissipation in the contact model, the effect of the velocities must nonetheless be taken into account. Hence, a relationship defining the relative body velocities is needed, but the definition must be consistent with the fact that the collision process is treated quasi-statically.

On the other hand, the model of the contact interaction must also be consistent with the expected physical behaviour. To determine the nature of this behaviour, it is first investigated in the extreme cases when one body is fully rigid and the other is compliant. In Section 4.2 the contact behaviour of a collision between a purely rigid body with a deformable one was investigated. It was observed that in this case, the contact plate was “attached” to the rigid body and that the deformation process involved only the compliant body. This behaviour will now be investigated in more detail.

First, the case where the body \mathcal{B}_i is fully rigid and body \mathcal{B}_j is compliant is considered. The contact plate is attached to \mathcal{B}_i and therefore $\boldsymbol{\omega}_p = \boldsymbol{\omega}_i$. As a result, the relative angular velocity between the plate and the body is zero,

$$\boldsymbol{\omega}_{r,i} = \boldsymbol{\omega}_p - \boldsymbol{\omega}_i = 0 \quad (\mathcal{B}_i \text{ rigid}) . \quad (4.151)$$

The velocity \mathbf{v}_p of the contact plate at \mathbf{s}_c is given as

$$\mathbf{v}_p = \mathbf{v}_i + \boldsymbol{\omega}_i \times (\mathbf{s}_c - \boldsymbol{\rho}_i) \quad (\mathcal{B}_i \text{ rigid}) . \quad (4.152)$$

To investigate $\mathbf{v}_{r,i}$, the motion $\mathbf{v}_{c,i}$ at the centroid $\mathbf{p}_{c,i}$ is first considered. Equation (4.98) gives $\mathbf{v}_{c,i}$ in terms of the plate and the body \mathcal{B}_i velocities. Replacing the definition from Equation (4.152) into Equation (4.98) and simplifying using Equation (4.20) yields $\mathbf{v}_{c,i} = 0$. Hence, the plate velocity relative to \mathcal{B}_i given by Equation (4.97) becomes

$$\mathbf{v}_{r,i} = \mathbf{v}_{c,i} + \boldsymbol{\omega}_{r,i} \times \boldsymbol{\rho}_{s,i} = 0 \quad (\mathcal{B}_i \text{ rigid}) \quad (4.153)$$

as expected since the contact plate is attached to \mathcal{B}_i . Next, the contact plate velocity relative to \mathcal{B}_j is found by replacing the definition for \mathbf{v}_p from Equation (4.152) into Equation (4.100) and noting that $\boldsymbol{\omega}_p = \boldsymbol{\omega}_i$, thus resulting in

$$\mathbf{v}_{r,j} = (\mathbf{v}_i + \boldsymbol{\omega}_i \times (\mathbf{s}_c - \mathbf{r}_i + \boldsymbol{\rho}_t)) - (\mathbf{v}_j + \boldsymbol{\omega}_j \times \boldsymbol{\rho}_j) \quad (\mathcal{B}_i \text{ rigid}) . \quad (4.154)$$

Recalling that $\boldsymbol{\rho}_t = \mathbf{s} - \mathbf{s}_c$ and that $\boldsymbol{\rho}_i = \mathbf{s} - \mathbf{r}_i$ (Equations (4.20) and (4.1)), Equation (4.154) simplifies to

$$\mathbf{v}_{r,j} = \mathbf{v}_r \quad (\mathcal{B}_i \text{ rigid}) , \quad (4.155)$$

where the definition of \mathbf{v}_r given in Equation (4.48) was invoked. The angular velocity of the plate relative to \mathcal{B}_j is found by replacing $\boldsymbol{\omega}_p = \boldsymbol{\omega}_i$ into Equation (4.101) yielding

$$\boldsymbol{\omega}_{r,j} = \boldsymbol{\omega}_i - \boldsymbol{\omega}_j = \boldsymbol{\omega}_r \quad (\mathcal{B}_i \text{ rigid}) . \quad (4.156)$$

Secondly, the case where body \mathcal{B}_j is fully rigid and body \mathcal{B}_i is compliant is studied. Here, the contact plate is attached to \mathcal{B}_j . Similarly to the case where \mathcal{B}_i was rigid, it can be shown that

$$\boldsymbol{\omega}_{r,j} = \boldsymbol{\omega}_p - \boldsymbol{\omega}_j = 0 \quad (\mathcal{B}_j \text{ rigid}) , \quad (4.157)$$

since $\boldsymbol{\omega}_p = \boldsymbol{\omega}_j$. The motion of the contact plate at \mathbf{s}_c is given by \mathbf{v}_p as

$$\mathbf{v}_p = \mathbf{v}_j + \boldsymbol{\omega}_j \times (\mathbf{s}_c - \boldsymbol{\rho}_j) \quad (\mathcal{B}_j \text{ rigid}) . \quad (4.158)$$

$\mathbf{v}_{c,j}$ can be shown to be zero, and hence

$$\mathbf{v}_{r,j} = \mathbf{v}_{c,j} + \boldsymbol{\omega}_{r,j} \times \boldsymbol{\rho}_{s,j} = 0 \quad (\mathcal{B}_j \text{ rigid}) . \quad (4.159)$$

The velocity of the contact plate relative to \mathcal{B}_i is given as

$$\mathbf{v}_{r,i} = (\mathbf{v}_i + \boldsymbol{\omega}_i \times \boldsymbol{\rho}_i) - (\mathbf{v}_j + \boldsymbol{\omega}_j \times \boldsymbol{\rho}_j) = -\mathbf{v}_r \quad (\mathcal{B}_j \text{ rigid}) , \quad (4.160)$$

and the angular velocity of the plate relative to \mathcal{B}_i is

$$\boldsymbol{\omega}_{r,i} = \boldsymbol{\omega}_j - \boldsymbol{\omega}_i = -\boldsymbol{\omega}_r \quad (\mathcal{B}_j \text{ rigid}) . \quad (4.161)$$

Summarizing, the results for the \mathcal{B}_i and \mathcal{B}_j rigid are

$$\left. \begin{array}{l} r_i = 0 \quad ; \quad r_j = 1 \\ \mathbf{v}_{r,i} = 0 \quad ; \quad \mathbf{v}_{r,j} = \mathbf{v}_r \\ \boldsymbol{\omega}_{r,i} = 0 \quad ; \quad \boldsymbol{\omega}_{r,j} = \boldsymbol{\omega}_r \end{array} \right\} \mathcal{B}_i \text{ rigid} , \quad (4.162)$$

$$\left. \begin{array}{l} r_i = 1 \quad ; \quad r_j = 0 \\ \mathbf{v}_{r,i} = -\mathbf{v}_r \quad ; \quad \mathbf{v}_{r,j} = 0 \\ \boldsymbol{\omega}_{r,i} = -\boldsymbol{\omega}_r \quad ; \quad \boldsymbol{\omega}_{r,j} = 0 \end{array} \right\} \mathcal{B}_j \text{ rigid} .$$

The following relationships for the relative body velocities are therefore proposed

$$\begin{aligned} \mathbf{v}_{r,i} &= -r_i \mathbf{v}_r \quad ; \quad \mathbf{v}_{r,j} = r_j \mathbf{v}_r , \\ \boldsymbol{\omega}_{r,i} &= -r_i \boldsymbol{\omega}_r \quad ; \quad \boldsymbol{\omega}_{r,j} = r_j \boldsymbol{\omega}_r . \end{aligned} \quad (4.163)$$

The relationships in Equation (4.163) satisfy all the conditions summarized in the Equations (4.162). They also satisfy the relationships from Equation (4.121) as follows

$$\begin{aligned} \mathbf{v}_r &= \mathbf{v}_{r,j} - \mathbf{v}_{r,i} = (r_i + r_j) \mathbf{v}_r = \mathbf{v}_r , \\ \boldsymbol{\omega}_r &= \boldsymbol{\omega}_{r,j} - \boldsymbol{\omega}_{r,i} = (r_i + r_j) \boldsymbol{\omega}_r = \boldsymbol{\omega}_r , \end{aligned} \quad (4.164)$$

since $r_i + r_j = 1$. For example, the case where $k_{v,i} = k_{v,j}$ is examined. The relationships in Equation (4.163) give

$$\begin{aligned} \mathbf{v}_{r,i} &= -\frac{1}{2} \mathbf{v}_r , \quad \mathbf{v}_{r,j} = \frac{1}{2} \mathbf{v}_r , \\ \boldsymbol{\omega}_{r,i} &= -\frac{1}{2} \boldsymbol{\omega}_r , \quad \boldsymbol{\omega}_{r,j} = \frac{1}{2} \boldsymbol{\omega}_r , \end{aligned} \quad (4.165)$$

and hence,

$$\begin{aligned} \mathbf{v}_{r,j} &= -\mathbf{v}_{r,i} , \\ \boldsymbol{\omega}_{r,j} &= -\boldsymbol{\omega}_{r,i} . \end{aligned} \quad (4.166)$$

When $k_{v,i} = k_{v,j}$, it is observed that the contact plate velocities are half of the relative translational and angular velocities of the bodies. As a result, the velocity of the bodies as perceived from the contact plate are equal and opposite. Figure 4.16 illustrates this case for the translational relative velocities.

The proposed relationships for the relative velocities can also be invoked to obtain equivalent

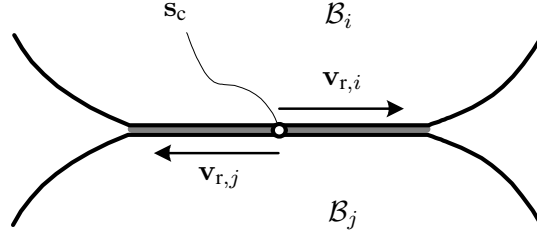


Figure 4.16: Body velocities relative to the contact plate for $k_{v,i} = k_{v,j}$.

relationships for the tangential and normal velocity components. The relationships for the normal components of the relative velocities are summarized as

$$\begin{aligned} \mathbf{v}_{\text{cn},i} &= v_{\text{cn},i} \mathbf{n}_i = -r_i \mathbf{v}_{\text{cn}} \quad ; \quad \mathbf{v}_{\text{cn},j} = v_{\text{cn},j} \mathbf{n}_j = r_j \mathbf{v}_{\text{cn}} \quad , \\ \boldsymbol{\omega}_{\text{n},i} &= \omega_{\text{n},i} \mathbf{n}_i = -r_i \boldsymbol{\omega}_{\text{n}} \quad ; \quad \boldsymbol{\omega}_{\text{n},j} = \omega_{\text{n},j} \mathbf{n}_j = r_j \boldsymbol{\omega}_{\text{n}} \quad , \end{aligned} \quad (4.167)$$

which can be expressed in scalar form as

$$\begin{aligned} v_{\text{cn},i} &= r_i v_{\text{cn}} \quad ; \quad v_{\text{cn},j} = r_j v_{\text{cn}} \quad , \\ \omega_{\text{n},i} &= r_i \omega_{\text{n}} \quad ; \quad \omega_{\text{n},j} = r_j \omega_{\text{n}} \quad , \end{aligned} \quad (4.168)$$

such that $v_{\text{cn},i} + v_{\text{cn},j} = (r_i + r_j) v_{\text{cn}} = v_{\text{cn}}$ and $\omega_{\text{n},i} + \omega_{\text{n},j} = (r_i + r_j) \omega_{\text{n}} = \omega_{\text{n}}$ as expected; see Equations (4.106) and (4.112). Similarly, the components of the relative velocities at \mathbf{s}_c in the tangential direction are obtained as

$$\begin{aligned} \mathbf{v}_{\text{sct},i} &= -r_i \mathbf{v}_{\text{sct}} \quad ; \quad \mathbf{v}_{\text{sct},j} = r_j \mathbf{v}_{\text{sct}} \quad , \\ \boldsymbol{\omega}_{\text{t},i} &= -r_i \boldsymbol{\omega}_{\text{t}} \quad ; \quad \boldsymbol{\omega}_{\text{t},j} = r_j \boldsymbol{\omega}_{\text{t}} \quad . \end{aligned} \quad (4.169)$$

Again, the proposed definition satisfies $\mathbf{v}_{\text{sct},j} - \mathbf{v}_{\text{sct},i} = (r_i + r_j) \mathbf{v}_{\text{sct}} = \mathbf{v}_{\text{sct}}$ and $\boldsymbol{\omega}_{\text{t},j} - \boldsymbol{\omega}_{\text{t},i} = (r_i + r_j) \boldsymbol{\omega}_{\text{t}} = \boldsymbol{\omega}_{\text{t}}$; see Equations (4.118) and (4.120).

The proposed relationships for the relative velocities guarantee that the relative velocities of the contact plate with respect to a rigid body are zero. This behaviour is consistent with the expectation of having zero deformation volume for the rigid body. If the plate was moving with respect to the rigid body, there would be a resulting volume of deformation. The proposed definitions also indicate that the relative plate velocities will be equal and opposite when the stiffness of the bodies is equal. This result is also consistent with the expected physical behaviour since the corresponding deformation volumes must be equal. Given that they share the same contact surface area, any change in contact surface velocity should be equally distributed between the two relative body velocities, such that the deformation volumes remain equal.

Hence, the proposed relative velocity relationships correspond to the expected physical behaviour. However, it has not been shown yet that the proposed relationships are also consistent

with the assumed quasi-static nature of the collision process. This latter condition will be tested when establishing the two deformable body contact model equations of the contact forces and moments.

4.3.3 Normal Force Model

To find the normal force acting on the contact plate, the quasi-static assumption is relaxed, such that the effect of the relative velocity between the contact plate and the bodies can also be considered. The modified Winkler elastic foundation model presented in Section 4.2.2 is used once more to obtain the local contact pressures caused by the deformation of \mathcal{B}_i and \mathcal{B}_j . The pressure $p_i(\mathbf{s})$ and $p_j(\mathbf{s})$ from bodies \mathcal{B}_i and \mathcal{B}_j acting on an infinitesimal surface element dS of the contact plate are given as

$$\begin{aligned} p_i(\mathbf{s}) &= \frac{df_{n,i}}{dS} = k_{v,i} f_{s,i}(\mathbf{s}) (1 + a_i v_{n,i}) , \\ p_j(\mathbf{s}) &= \frac{df_{n,j}}{dS} = k_{v,j} f_{s,j}(\mathbf{s}) (1 + a_j v_{n,j}) , \end{aligned} \quad (4.170)$$

where $f_{s,i}(\mathbf{s})$ and $f_{s,j}(\mathbf{s})$ are the normal elastic displacements of the surface of each body, and a_i and a_j are the hysteretic damping factors of \mathcal{B}_i and \mathcal{B}_j , respectively. The latter are a function of the coefficient of restitution and of the normal velocities $v_{n,i}^i$ and $v_{n,j}^i$ at the time of impact; see Equation (3.24). Integrating the contact pressures one each side of the contact plate yields

$$\begin{aligned} \mathbf{f}_{n,i} &= k_{v,i} V_i (1 + a_i v_{cn,i}) \mathbf{n}_i , \\ \mathbf{f}_{n,j} &= k_{v,j} V_j (1 + a_j v_{cn,j}) \mathbf{n}_j , \end{aligned} \quad (4.171)$$

where

$$\begin{aligned} a_i &= \frac{d}{e_{\text{eff}} v_{cn,i}^i} , \\ a_j &= \frac{d}{e_{\text{eff}} v_{cn,j}^i} , \end{aligned} \quad (4.172)$$

and $v_{cn,i}^i$ and $v_{cn,j}^i$ corresponds to initial normal impact velocity at \mathbf{s}_c . The relative normal velocity at the time of impact is governed by the same relationship as the normal relative velocity at any moment of the collision process. Hence, the relationships in Equation (4.168) are used to replace $v_{cn,i}^i$ and $v_{cn,j}^i$ in Equation (4.172), thus resulting in

$$\begin{aligned} a_i &= \frac{d}{e_{\text{eff}} r_i v_{cn}^i} , \\ a_j &= \frac{d}{e_{\text{eff}} r_j v_{cn}^i} . \end{aligned} \quad (4.173)$$

Similarly, the terms $v_{\text{cn},i}$ and $v_{\text{cn},j}$ in the equations for $\mathbf{f}_{\text{n},i}$ and $\mathbf{f}_{\text{n},j}$ can also be replaced by $r_i v_{\text{cn}}$ and $r_j v_{\text{cn}}$, respectively; see Equation (4.168). Substituting the definition for a_i and a_j in Equation (4.173) into the expressions for $\mathbf{f}_{\text{n},i}$ and $\mathbf{f}_{\text{n},j}$ in Equation (4.171) and simplifying the r_i and r_j terms yields

$$\begin{aligned}\mathbf{f}_{\text{n},i} &= f_{\text{n},i} \mathbf{n}_i = k_{\text{v},i} V_i (1 + a v_{\text{cn}}) \mathbf{n}_i , \\ \mathbf{f}_{\text{n},j} &= f_{\text{n},j} \mathbf{n}_j = k_{\text{v},j} V_j (1 + a v_{\text{cn}}) \mathbf{n}_j ,\end{aligned}\tag{4.174}$$

where a is defined as before (Equation (4.63)).

The contact plate was assumed to be massless. As a result, the sum of the forces and moments acting on it should always add up to zero. Summing the force in the normal direction gives $\mathbf{f}_{\text{n},i} + \mathbf{f}_{\text{n},j} = 0$. Expressing the result in scalar form in the \mathbf{n} direction gives

$$k_{\text{v},i} V_i (1 + a v_{\text{cn}}) = k_{\text{v},j} V_j (1 + a v_{\text{cn}}) ,\tag{4.175}$$

which indicates that $k_{\text{v},i} V_i = k_{\text{v},j} V_j$ for any value of v_{cn} , or in other words, the shape of the deformed surfaces is independent of the normal relative velocity. As a result, the shape of the deformed surfaces always exactly matches the shape of the quasi-static deformation, which implies that the resulting process is quasi-static. Hence, the proposed relative velocity relationships from Equation (4.163) yield a behaviour consistent with a quasi-static process assumption when the resulting contact model forces are examined in the normal direction. The result is also independent of r_i or r_j and, hence, it is valid for any possible combination of values for $k_{\text{v},i}$ and $k_{\text{v},j}$, including the cases where one body becomes fully rigid.

To obtain an expression for the normal force in terms of properties of the volume of interference, the force contribution from each side of the contact plate are added, namely,

$$2 \mathbf{f}_{\text{n}} = \mathbf{f}_{\text{n},j} - \mathbf{f}_{\text{n},i} = f_{\text{n},j} \mathbf{n}_j - f_{\text{n},i} \mathbf{n}_i = (f_{\text{n},i} + f_{\text{n},j}) \mathbf{n} .\tag{4.176}$$

Expressing the result in scalar form along the \mathbf{n} direction gives

$$2 f_{\text{n}} = (k_{\text{v},i} V_i + k_{\text{v},j} V_j) (1 + a v_{\text{cn}}) .\tag{4.177}$$

The definition of the equivalent stiffness from Equation (4.130) is used to simplify the above expression yielding

$$\mathbf{f}_{\text{n}} = f_{\text{n}} \mathbf{n} = k_{\text{v}} V (1 + a v_{\text{cn}}) \mathbf{n} ,\tag{4.178}$$

which is identical in form to the equation obtained for the one deformable body case (Equation (4.62)), except that here k_{v} now corresponds to the equivalent stiffness as defined in Equation (4.132).

4.3.4 Rolling Resistance Torque Model

The rolling resistance torque is produced by the tangential angular motion of the bodies relative to the contact plate. The torque is taken relative to the centroid of the volume of interference \mathbf{p}_c . The expressions for the rolling resistance torques acting on an infinitesimal surface element are

$$\begin{aligned} d\boldsymbol{\tau}_{r,i} &= \boldsymbol{\rho}_s \times d\mathbf{f}_{n,j} , \\ d\boldsymbol{\tau}_{r,j} &= \boldsymbol{\rho}_s \times d\mathbf{f}_{n,j} . \end{aligned} \quad (4.179)$$

The solution for Equation (4.64) can be applied here even though the surface element is referenced by $\boldsymbol{\rho}_s$ to \mathbf{p}_c instead of $\mathbf{p}_{c,i}$ and $\mathbf{p}_{c,j}$. Since these points are collinear, the equations apply nonetheless. Hence, integrating the torque on each side of the infinitesimal surface elements yields

$$\begin{aligned} \boldsymbol{\tau}_{r,i} &= k_{v,i} a_i \mathbf{J}_{s,i} \cdot \boldsymbol{\omega}_{t,i} , \\ \boldsymbol{\tau}_{r,j} &= k_{v,j} a_j \mathbf{J}_{s,j} \cdot \boldsymbol{\omega}_{t,j} . \end{aligned} \quad (4.180)$$

Since the contact plate is assumed massless, the rolling resistance torque from each side of the contact plate should cancel out, i.e., $-\boldsymbol{\tau}_{r,i} = \boldsymbol{\tau}_{r,j}$. Hence, substituting the definitions for a_i , a_j , $\mathbf{J}_{s,i}$, $\mathbf{J}_{s,j}$ (Equations (4.173) and (4.93)) and the relationships for $\boldsymbol{\omega}_{t,i}$ and $\boldsymbol{\omega}_{t,j}$ (Equation (4.169)), the following equation is obtained

$$-k_{v,i} \frac{d}{e_{\text{eff}} r_i v_{\text{cn}}^i} V_i \mathbf{J}_{\rho_s, \text{avg}} \cdot (-r_i \boldsymbol{\omega}_t) = k_{v,j} \frac{d}{e_{\text{eff}} r_j v_{\text{cn}}^j} V_j \mathbf{J}_{\rho_s, \text{avg}} \cdot (r_j \boldsymbol{\omega}_t) , \quad (4.181)$$

which simplifies into $k_{v,i} V_i = k_{v,j} V_j$. Hence, the rolling resistance torque equations indicate the proposed relative velocity relationships also result in a quasi-static process.

To express the rolling resistance torque in terms of the properties of the volume of interference, the torques from each side of the contact plate are added

$$\begin{aligned} 2 \boldsymbol{\tau}_r &= \boldsymbol{\tau}_{r,j} - \boldsymbol{\tau}_{r,i} , \\ &= k_{v,j} \frac{d}{e_{\text{eff}} r_j v_{\text{cn}}^j} V_j \mathbf{J}_{\rho_s, \text{avg}} \cdot (r_j \boldsymbol{\omega}_t) - k_{v,i} \frac{d}{e_{\text{eff}} r_i v_{\text{cn}}^i} V_i \mathbf{J}_{\rho_s, \text{avg}} \cdot (-r_i \boldsymbol{\omega}_t) , \\ &= a (k_{v,i} V_i + k_{v,j} V_j) \mathbf{J}_{\rho_s, \text{avg}} \cdot \boldsymbol{\omega}_t , \end{aligned} \quad (4.182)$$

where a is defined as before (Equation (4.63)) and \mathbf{J}_s was obtained using Equation (4.94). Substituting the definition for the equivalent stiffness (Equation (4.130)) yields

$$\boldsymbol{\tau}_r = k_v a \mathbf{J}_s \cdot \boldsymbol{\omega}_t , \quad (4.183)$$

which is identical to Equation (4.64) and where k_v corresponds to the equivalent stiffness as defined in Equation (4.132).

4.3.5 Tangential Friction Force Model

As in Section 4.2.4, a normal load and velocity frictional force element is considered to model the force of friction. The resulting friction force model thus corresponds to a load-dependent damper. The friction forces $\mathbf{f}_{t,i}$ and $\mathbf{f}_{t,j}$ acting on each side of the contact plate are given as

$$\begin{aligned} d\mathbf{f}_{t,i} &= \mu_i df_{n,i} \mathbf{v}_{t,i} , \\ d\mathbf{f}_{t,j} &= \mu_j df_{n,j} \mathbf{v}_{t,j} , \end{aligned} \quad (4.184)$$

where μ_i and μ_j are the same constant as in Equation (4.68), but correspond to the friction force acting between the contact plate and the bodies \mathcal{B}_i and \mathcal{B}_j , respectively. The friction force produced by an infinitesimal element of the contact surface is then integrated over the surface area, thus resulting in

$$\begin{aligned} \mathbf{f}_{t,i} &= \mu_i f_{n,i} \mathbf{v}_{sct,i} , \\ \mathbf{f}_{t,j} &= \mu_j f_{n,j} \mathbf{v}_{sct,j} . \end{aligned} \quad (4.185)$$

The contact plate is massless and therefore $-\mathbf{f}_{t,i} = \mathbf{f}_{t,j}$. However, $f_{n,i} = f_{n,j}$ and the tangential velocities $\mathbf{v}_{sct,i}$ and $\mathbf{v}_{sct,j}$ can be expressed in terms of \mathbf{v}_{sct} using the relationship from Equation (4.169). The resulting expression for $-\mathbf{f}_{t,i} = \mathbf{f}_{t,j}$ becomes

$$\begin{aligned} -\mu_i i f_{n,i} \mathbf{v}_{sct} &= \mu_j j f_{n,j} \mathbf{v}_{sct} , \\ \mu_i r_i f_n \mathbf{v}_{sct} &= \mu_j r_j f_n \mathbf{v}_{sct} , \end{aligned} \quad (4.186)$$

and, hence,

$$\mu_i r_i = \mu_j r_j . \quad (4.187)$$

Equation (4.187) is a condition that ensures the frictional forces acting on the contact plate are equal and opposite, thereby satisfying the requirement that the forces acting on a massless object must add up to zero. To obtain the friction force in terms of the properties of the volume of interference, the friction force from each side of the contact plate are added as follows

$$\begin{aligned} 2\mathbf{f}_t &= \mathbf{f}_{t,j} - \mathbf{f}_{t,i} \\ &= \mu_j \mathbf{v}_{sct,j} f_{n,j} - \mu_i \mathbf{v}_{sct,i} f_{n,i} \\ &= (\mu_i r_i + \mu_j r_j) f_n \mathbf{v}_{sct} . \end{aligned} \quad (4.188)$$

An equivalent damping factor μ is introduced as follows

$$2\mu = \mu_i r_i + \mu_j r_j , \quad (4.189)$$

such that

$$\begin{aligned}\mu_i &= \frac{1}{r_i} \mu, \\ \mu_j &= \frac{1}{r_j} \mu.\end{aligned}\tag{4.190}$$

Equation (4.190) indicates that $\mu_i = \mu_j$ when $k_{v,i} = k_{v,j}$. On the other hand, when one body is fully rigid, then the corresponding friction damping factor becomes infinite. For rigid bodies, the friction damping factors are given as

$$\begin{aligned}\left. \begin{aligned}\mu_i &= \infty \\ \mu_j &= \mu\end{aligned} \right\} \mathcal{B}_i \text{ rigid}, \\ \left. \begin{aligned}\mu_i &= \mu \\ \mu_j &= \infty\end{aligned} \right\} \mathcal{B}_j \text{ rigid}.\end{aligned}\tag{4.191}$$

The infinite friction damping factor values in Equation (4.191) indicate that the contact plate “sticks” to the rigid body and is not allowed to slide with respect to it. Hence, this result is completely consistent with the analysis so far which has assumed the contact plate is attached to the fully rigid body. On the other hand, the overall friction damping factor μ remains unaffected by the relative stiffness of the bodies. In other words, a change in value of $k_{v,i}$ and $k_{v,j}$ produce a corresponding change in value of μ_i and μ_j , such that μ remains constant. It is important to remember that the contact plate is a conceptual device introduced to facilitate the derivation and understanding of the contact model equations. It does not exist in reality, and only a single friction damping factor gives the corresponding friction force between the two bodies, i.e., μ .

Using the definition for the equivalent damping factor μ from Equation (4.189) to simplify Equation (4.188), the following expression for the tangential friction force is obtained as

$$\mathbf{f}_t = \mu f_n \mathbf{v}_{\text{sct}},\tag{4.192}$$

which is identical to Equation (4.75) for the one deformable body case.

4.3.6 Spinning Friction Torque Model

The spinning friction torque is obtained by considering the contributions of the spinning friction torques of each body as

$$\begin{aligned}d\boldsymbol{\tau}_{s,i} &= \boldsymbol{\rho}_t \times d\mathbf{f}_{t,j}, \\ d\boldsymbol{\tau}_{s,j} &= \boldsymbol{\rho}_t \times d\mathbf{f}_{t,i}.\end{aligned}\tag{4.193}$$

The solution for Equation (4.76) can be applied directly here since $\rho_{t,i} = \rho_{t,j} = \rho_t$. Hence, integrating the friction torque on each side of the infinitesimal surface elements yields

$$\begin{aligned}\tau_{s,i} &= \mu_i \frac{f_{n,i}}{V_i} \mathbf{J}_{s,i} \cdot \boldsymbol{\omega}_{n,i} , \\ \tau_{s,j} &= \mu_j \frac{f_{n,j}}{V_j} \mathbf{J}_{s,j} \cdot \boldsymbol{\omega}_{n,j} .\end{aligned}\tag{4.194}$$

Since the contact plate is massless, the sum of the spinning friction torques acting about \mathbf{n} should be zero. Hence, setting $-\tau_{s,i} = \tau_{s,j}$ and substituting the definitions for $\mathbf{J}_{s,i}$ and $\mathbf{J}_{s,j}$ from Equation (4.93), setting $f_{n,i} = f_{n,j} = f_n$ and applying relationship for the normal angular velocities (Equation (4.168)) yields

$$-\mu_i \frac{f_n}{V_i} V_i \mathbf{J}_{\rho_s, \text{avg}} \cdot (-r_i \boldsymbol{\omega}_n) = \mu_j \frac{f_n}{V_j} V_j \mathbf{J}_{\rho_s, \text{avg}} \cdot (r_j \boldsymbol{\omega}_n) ,\tag{4.195}$$

which reduces to Equation (4.187). Hence, the relationship between the friction damping factors for the tangential friction force balance is exactly the same for the spinning friction torque balance. As a result, it is concluded that satisfying the relationship in Equation (4.187) will guarantee that both the tangential friction force and spinning friction moment acting on the force plate add up to zero, thereby satisfying the force-moment balance requirement for a massless body.

The spinning friction torque can be expressed in terms of the properties of the volume of interference. To this end, the friction forces from each side of the contact plate are added. The result is

$$\begin{aligned}2\tau_s &= \tau_{s,j} - \tau_{s,i} , \\ &= \mu_j \frac{f_{n,j}}{V_j} \mathbf{J}_{s,j} \cdot \boldsymbol{\omega}_{n,j} - \mu_i \frac{f_{n,i}}{V_i} \mathbf{J}_{s,i} \cdot \boldsymbol{\omega}_{n,i} , \\ &= (1 + a v_{\text{cn}}) (\mu_i r_i k_{v,i} V_i + \mu_j r_j k_{v,j} V_j) \mathbf{J}_{\rho_s, \text{avg}} \cdot \boldsymbol{\omega}_n .\end{aligned}\tag{4.196}$$

However, Equation (4.190) gives $\mu_i r_i = \mu_j r_j = \mu$. Hence, using the definition for the equivalent stiffness (Equation (4.130)), Equation (4.196) reduces to

$$\begin{aligned}2\tau_s &= \mu (1 + a v_{\text{cn}}) (k_{v,i} V_i + k_{v,j} V_j) \mathbf{J}_{\rho_s, \text{avg}} \cdot \boldsymbol{\omega}_n , \\ &= 2\mu k_v (1 + a v_{\text{cn}}) V \mathbf{J}_{\rho_s, \text{avg}} \cdot \boldsymbol{\omega}_n ,\end{aligned}\tag{4.197}$$

Next, the definition of \mathbf{J}_s from Equation (4.94) is invoked and Equation (4.197) becomes simply

$$\tau_s = \mu \frac{f_n}{V} \mathbf{J}_s \cdot \boldsymbol{\omega}_n .\tag{4.198}$$

Equation (4.198) is identical to Equation (4.82).

4.3.7 Contact Normal

In Section 4.1.3 the concept of the contact plate was introduced to facilitate the theoretical analysis of the body-to-body interaction. The contact plate location was established — it passes near \mathbf{p}_c — but the direction of its surface normal \mathbf{n} is still undetermined, although it has been established that its orientation must satisfy $\mathbf{s}_{c,i} = \mathbf{s}_{c,j} = \mathbf{s}_c$ and, therefore, that $\boldsymbol{\rho}_{t,i} = \boldsymbol{\rho}_{t,j} = \boldsymbol{\rho}_t$. This subsection proposes a new and robust definition for \mathbf{n} .

The relationship $\boldsymbol{\rho}_{t,i} = \boldsymbol{\rho}_{t,j} = \boldsymbol{\rho}_t$ was used to obtain expressions relating the velocities of each body with respect to the contact plate to the relative velocities between the bodies; see Equations (4.109) and (4.117). In turn, these relationships were used to obtain expressions for the forces and torques acting on the contact plate, which were thereafter also expressed in terms of quantities pertaining to the entire volume of interference, i.e., V , \mathbf{p}_c and \mathbf{J}_s . Hence, the expressions derived for the volumetric contact model force and torque components already *include* the notion that $\mathbf{s}_{c,i} = \mathbf{s}_{c,j} = \mathbf{s}_c$ by definition. Consequently, the contact normal definition should be consistent with the expressions for the contact model force and torque components.

Now, Equation (4.82) gives the relationship for spinning friction torque, which depends both on the spinning angular velocity $\boldsymbol{\omega}_n$ and surface-inertia tensor \mathbf{J}_s . The resultant friction torque $\boldsymbol{\tau}_s$ must act to prevent the motion. Consequently, $\boldsymbol{\tau}_s$ is a vector that is collinear to the angular velocity vector $\boldsymbol{\omega}_n$ and points in the opposite direction. In other words, both $\boldsymbol{\omega}_n = \omega_n \mathbf{n}$ and $\boldsymbol{\tau}_s$ are parallel to the contact plate normal \mathbf{n} . If $\boldsymbol{\tau}_s$ was not parallel to \mathbf{n} , then the spinning friction would inevitably cause a tilting effect on the bodies with respect to each other, which is physically unreasonable because the friction from a flat contact plate cannot cause such a motion. Equation (4.198) is thus re-written in terms of the contact plate normal \mathbf{n} as follows,

$$\mathbf{J}_s \cdot \mathbf{n} = \mathbf{J}_v \cdot \mathbf{n} = \lambda_n \mathbf{n}, \quad \text{where} \quad \lambda_n = \frac{\tau_s V}{\mu f_n \omega_n} \quad (4.199)$$

and $\boldsymbol{\tau}_s$ is such that $\boldsymbol{\tau}_s = \tau_s \mathbf{n}$, i.e., is parallel to \mathbf{n} . Equation (4.199) shows that the determination of the contact normal is in fact a standard eigenvalue problem. That is, for Equation (4.199) to be true, \mathbf{n} must correspond to one of the three eigenvectors of \mathbf{J}_v . In fact, \mathbf{n} corresponds to one of the principal axes of \mathbf{J}_v .

To determine \mathbf{n} , the contact model implementation relies on a geometric estimate of the contact normal that is guaranteed to point outwards from the surface of \mathcal{B}_j and toward \mathcal{B}_i . Then, this estimate of \mathbf{n} is fed to an algorithm implementing the Inverse Iteration Method (IIM), which refines the estimate and returns the eigenvector closest to the geometric estimate, such that the vector is guaranteed to be pointing from \mathcal{B}_j toward \mathcal{B}_i . The implementation of the IIM for a 3×3 positive-definite symmetric matrix is simplified by the fact that a simple closed-form expression exists for the inverse of such a matrix.

With the proposed definition for the contact plate normal \mathbf{n} , it is easy to compute the corresponding radius of gyration r_{gyr} of the volume-inertia tensor about \mathbf{n} . The eigenvalue λ_n corre-

sponding to the eigenvector \mathbf{n} is found by taking the dot-product of Equation (4.199) with \mathbf{n} ,

$$\lambda_n = \mathbf{n} \cdot \mathbf{J}_v \cdot \mathbf{n} = \mathbf{n} \cdot \mathbf{J}_s \cdot \mathbf{n} = \mathbf{n} \cdot \int_S ((\boldsymbol{\rho}_s \cdot \boldsymbol{\rho}_s) \mathbf{I} - \boldsymbol{\rho}_s \boldsymbol{\rho}_s) f_s(\mathbf{s}) dS \cdot \mathbf{n} . \quad (4.200)$$

The average tensor $\mathbf{J}_{\rho_s, \text{avg}}$ can be used to find the radius of gyration r_{gyr} of \mathbf{J}_s about \mathbf{n} as follows

$$\lambda_n = \mathbf{n} \cdot \mathbf{J}_{\rho_s, \text{avg}} \cdot \mathbf{n} \int_S f_s(\mathbf{s}) dS = r_{\text{gyr}}^2 V \quad (4.201)$$

and therefore $r_{\text{gyr}} = \sqrt{\lambda_n / V}$. The radius of gyration r_{gyr} of \mathbf{J}_v about \mathbf{n} will be used for the derivations of the next section.

4.4 Volumetric Friction Model

This section adapts the bristle friction model introduced in Section 3.2.2 to the volumetric contact model. A key difference between the point contact model presented in Chapter 3 and the volumetric model introduced in this chapter is that the area of contact can no longer be assumed to be small. This difference has a significant impact on the behaviour of friction.

4.4.1 Coulomb Friction

In Section 3.2.2 a friction model that was both load and velocity dependent was introduced. Coulomb friction is a well-known phenomenon that is also load and velocity dependent (Coulomb friction acts against the direction of motion), but where the magnitude of the velocity does not play a role. To model this different phenomena, the infinitesimal friction element presented in Equation (4.75) is modified by normalizing the relative velocity term \mathbf{v}_t . The negative sign ensuring the friction force acts against the motion will be added at the end of the derivations. The infinitesimal Coulomb friction element $d\mathbf{f}_{\text{tc}}$ is written as

$$d\mathbf{f}_{\text{tc}} = \mu_C \frac{\mathbf{v}_t}{|\mathbf{v}_t|} df_n , \quad (4.202)$$

where μ_C is the Coulomb friction coefficient. The Equation (4.202) can be rearranged such that integration over the contact surface is done on both sides:

$$\int_S |\mathbf{v}_t| d\mathbf{f}_{\text{tc}} = \int_S \mu_C \mathbf{v}_t df_n . \quad (4.203)$$

The solution for the right-hand side of Equation (4.203) is given directly by Equation (4.75). Equation (4.57) shows that \mathbf{v}_t varies continuously across the contact surface as a function of $\boldsymbol{\rho}_s$. As a result, $|\mathbf{v}_t|$ also varies continuously across the contact surface and its value is always greater or equal to zero. The First Mean Value Theorem can therefore be invoked to find an average surface

velocity v_{avg} as

$$v_{\text{avg}} \int_S d\mathbf{f}_{\text{tc}} = \mu_C f_n \mathbf{v}_{\text{sct}} \quad (4.204)$$

and, therefore, the Coulomb friction force \mathbf{f}_{tc} is found to be

$$\mathbf{f}_{\text{tc}} = \mu_C f_n \frac{\mathbf{v}_{\text{sct}}}{|\mathbf{v}_{\text{sct}}|} C_v, \quad \text{where} \quad C_v = \frac{|\mathbf{v}_{\text{sct}}|}{v_{\text{avg}}}. \quad (4.205)$$

The quantity v_{avg} is a measure of the average relative translational velocity of all points on the contact surface. This average velocity is a function of the relative translational velocity of the bodies \mathcal{B}_i and \mathcal{B}_j , but also depends on the relative angular velocity since a rotational motion induces translational motion for any point on the contact surface that is away from the centre of the rotation. An expression for the value for v_{avg} will be introduced in Section 4.4.2.

Next, the effect of Coulomb friction on the spinning friction torque is investigated. As was done for the tangential Coulomb friction, the spinning friction of an infinitesimal surface element is considered

$$d\boldsymbol{\tau}_{\text{sc}} = \mu_C \boldsymbol{\rho}_s \times \frac{\mathbf{v}_t}{|\mathbf{v}_t|} df_n. \quad (4.206)$$

Once again, the magnitude of \mathbf{v}_t is carried over to the left-hand side of Equation (4.206) and an integration over the contact surface area is performed on both sides of the equation. The First Mean Value Theorem is invoked again, such that the magnitude of \mathbf{v}_t inside the integral is replaced by the average relative translational velocity v_{avg} . The solution for the right-hand side is given by Equation (4.82). The expression for $\boldsymbol{\tau}_{\text{sc}}$ is thus obtained as follows,

$$\boldsymbol{\tau}_{\text{sc}} = \frac{\mu_C f_n}{V v_{\text{avg}}} \mathbf{J}_s \cdot \boldsymbol{\omega}_n. \quad (4.207)$$

Equation (4.207) can be expressed in scalar form like Equation (4.199) since the torque caused by the Coulomb friction is also acting in the direction of \mathbf{n} , i.e., $\boldsymbol{\tau}_{\text{sc}} = \tau_{\text{sc}} \mathbf{n}$. Using the definition for the radius of gyration, Equation (4.207) becomes

$$\tau_{\text{sc}} = \mu_C r_{\text{gyr}} f_n \frac{\omega_n}{|\omega_n|} C_\omega, \quad \text{where} \quad C_\omega = \frac{r_{\text{gyr}} |\omega_n|}{v_{\text{avg}}}. \quad (4.208)$$

The factors C_v and C_ω on the right-hand side of Equations (4.205) and (4.208) are dimensionless and depend on v_{avg} . These terms directly affect the magnitude of the tangential force and spinning torque caused by the Coulomb friction. They are studied in the next section.

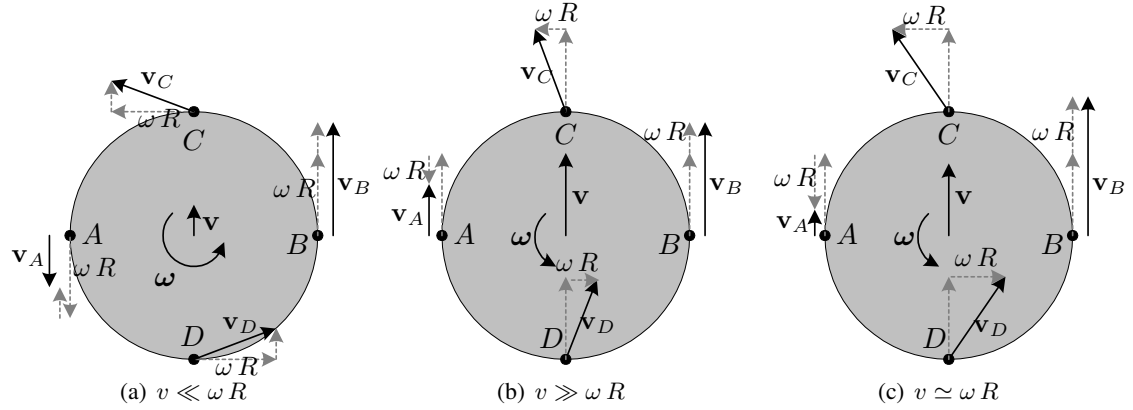


Figure 4.17: The Contensou effect.

4.4.2 Average Contact Surface Velocity

Contensou (1963) studied the behaviour of Coulomb friction for rapidly spinning objects and realized that the sliding Coulomb friction force vanishes when the ratio $\frac{v}{\omega R}$ tends to zero, where v is the tangential velocity magnitude, R the radius of the contact surface and ω is the normal angular velocity. Leine and Glocker (2003) modelled this effect as a set-valued force law which they called the Coulomb-Contensou friction. The behaviour of the Coulomb-Contensou friction, which establishes a direct relationship between the friction and the translational and angular velocities, will be referred here to as the Contensou effect. The discussion below will show that the Contensou effect reduces the Coulomb friction force or torque, and even eliminates them in some extreme cases.

It is interesting to observe that the Contensou effect appeared naturally in the derivations for the proposed Coulomb friction force and torque models. The Contensou effect on the sliding friction force was captured in the form of a dimensionless factor, namely C_v , which affects the magnitude of the tangential friction as a function of the relative surface velocities. The proposed contact model also associates a Contensou effect with the spinning friction torque. This latter effect is characterized by the factor C_ω which affects the magnitude of the spinning friction torque also as a function of the relative surface velocities. These two effects will now be investigated. For the purpose of the discussion, a simple circular contact surface will be considered.

Figures 4.17 presents a circular contact surface of radius R where the centre is moving with a relative translational velocity \mathbf{v} and rotating with a normal angular velocity ω . Let $v = |\mathbf{v}|$ and $\omega R = |\omega \times \rho_R|$, where ρ_R is a position vector for a point located on the circle radius with respect to the circle centre. v and ωR will be referred hereafter as the magnitude of the translational and angular component of the relative tangential velocity respectively; see Equation (4.57). The resulting translational velocities \mathbf{v}_A , \mathbf{v}_B , \mathbf{v}_C and \mathbf{v}_D of the four points labelled A , B , C and D located on the circle are shown also. The relative tangential velocity at each point is obtained by summing the translational and angular component vectors, as shown in grey.

The Contensou effect arises because the magnitude of the velocity does not affect the friction force, i.e., the Coulomb friction force is invariant to the magnitude of the velocity. The reduction of the sliding Coulomb friction force for $v \ll \omega R$ can be explained as follows. At each point, the Coulomb friction force acts against the local relative velocity direction. Figure 4.17(a) shows that the direction of the velocities \mathbf{v}_A and \mathbf{v}_B at points A and B is opposite when $v \ll \omega R$. If a uniform contact pressure is assumed, the Coulomb friction force at point A will counter-balance the force at point B . The two force directions are opposite at these points because the magnitude of the angular velocity component exceeds the magnitude of the translational velocity component. For the velocities at points C and D , it is seen that the direction of the velocities \mathbf{v}_C and \mathbf{v}_D will become perpendicular to \mathbf{v} as the ratio $\frac{v}{\omega R}$ tends to zero when $v \ll \omega R$. Hence, when considering the sliding friction force contribution of the four points, the total sliding friction force disappears because either the forces from different locations of the contact surface balance themselves out, or simply ‘lose’ their component acting against the relative translational velocity.

Next, the Contensou effect on the spinning torque caused by the Coulomb friction is studied. The torque generated by the Coulomb friction force acting at points A , B , C , and D about the centre of the circle is now considered. Figure 4.17(b) shows that velocity \mathbf{v}_A at A and \mathbf{v}_B at B have the same direction when $v \gg \omega R$. But since the points A and B are located at opposite sides of the centre of the circle, the produced torques about the centre of the circle are in opposite direction. Again, if a constant contact pressure is assumed, then the torques produced by the Coulomb friction at points A and B will cancel each other out. Also, when the ratio $\frac{\omega R}{v}$ tends to zero, then the relative tangential velocity of all points on the circle surface will have a velocity that is parallel to \mathbf{v} . Hence, as was observed with the points A and B , the torque produced at any point of the contact surface will always be cancelled-out by the torque produced by a point on the opposite side. The net impact of the Contensou effect in rotation is to eliminate the spinning friction torque between bodies when $v \gg \omega R$.

To simplify the discussion above, the observations on the behaviour of the Contensou effect were presented in a context where the contact pressure is uniform and the contact surface is circular. However, the Contensou effect occurs for non-uniform pressure distributions as well (Zhuravlev and Klimov, 2005). The conclusions on the Contensou effect can be extended to the general case, as indicated by the factors C_v and C_ω , which were obtained in the derivations of the proposed contact model without any assumption about the pressure distribution or the shape of the contact surface. The behaviour and relation of C_v and C_ω is examined next.

The discussion above focused on the fact that the Contensou effect reduces the Coulomb friction force or torque, and even eliminates them in some extreme cases. However, the Contensou effect never increases the Coulomb friction force or torque; that is, the Contensou effect does not amplify the magnitude of the Coulomb friction. Looking at the structure of Equations (4.205) and (4.208), it is clear that the maximum magnitudes of \mathbf{f}_{tc} and τ_{sc} are $\mu_C f_n$ and $\mu_C r_{\text{gyr}} f_n$ respectively.

Hence, it is concluded that

$$0 \leq C_v \leq 1 \quad ; \quad 0 \leq C_\omega \leq 1 . \quad (4.209)$$

Furthermore, C_v and C_ω are related as follows:

$$\begin{aligned} |\mathbf{v}_t| \ll r_{\text{gyr}} \omega_n &\Rightarrow C_v \rightarrow 0 \quad ; \quad C_\omega \rightarrow 1 , \\ |\mathbf{v}_t| \gg r_{\text{gyr}} \omega_n &\Rightarrow C_v \rightarrow 1 \quad ; \quad C_\omega \rightarrow 0 . \end{aligned} \quad (4.210)$$

Hence, a relationship that satisfies the constraints (4.209) and the behaviour summarized in Equation (4.210) must exist. The values of C_v and C_ω cannot be set arbitrarily or independently: the two values are related to one another. Also, by establishing the defining relationship between C_v and C_ω (Zhuravlev and Klimov, 2005), a correspondence between $|\mathbf{v}_t|$, $r_{\text{gyr}} |\omega_n|$ and v_{avg} will be obtained. Therefore, the following equation is proposed as a defining relationship between C_v and C_ω :

$$C_v^2 + C_\omega^2 = 1 . \quad (4.211)$$

Equation (4.211) satisfies both (4.209) and (4.210), and provides at the same time a definition for the average surface velocity v_{avg} introduced in Section 4.4.1 as follows,

$$v_{\text{avg}}^2 = \mathbf{v}_{\text{sct}} \cdot \mathbf{v}_{\text{sct}} + \omega_n \cdot \frac{\mathbf{J}_v}{V} \cdot \omega_n , \quad (4.212)$$

since

$$(r_{\text{gyr}} |\omega_n|)^2 = \omega_n \cdot \frac{\mathbf{J}_v}{V} \cdot \omega_n . \quad (4.213)$$

While the definition proposed in Equation (4.211) does satisfy the criteria (4.209) and (4.210), it is somewhat arbitrary. For example the relationship could have been defined without squaring C_v and/or C_ω and would have satisfied the criteria just as well. However, when the definition is examined from a geometric point of view, it can be shown to be justified. Figure 4.17(c) shows again the velocities \mathbf{v}_A , \mathbf{v}_B , \mathbf{v}_C and \mathbf{v}_D at the point A , B , C , and D respectively, of the circular contact area. Here, the tangential and angular components of the relative tangential velocity have comparable magnitudes. Figure 4.17(c) shows that the magnitude of the tangential velocity is the greatest at point B , when the tangential and angular components are parallel and have the same direction, and smallest at A when they are parallel but point in opposite direction.

On the other hand, the velocities \mathbf{v}_C and \mathbf{v}_D at the points C and D have the same magnitude, and correspond to the configuration where the translational and angular components of the velocities are perpendicular. \mathbf{v}_C and \mathbf{v}_D also correspond to the points where the angular component of the relative tangential velocity is rotated halfway between the positions giving the maximum value

for relative tangential velocity $|\mathbf{v}_B|$ and the minimum value $|\mathbf{v}_A|$. In this sense, the magnitude of the velocities at points C and D correspond to the average velocity of the points located on the circle. Velocity is a vectorial quantity and therefore it seems to be justified that the method used to find the average velocity should be based on vectorial analysis. The magnitude of \mathbf{v}_C and \mathbf{v}_D is given as

$$|\mathbf{v}_C|^2 = |\mathbf{v}_D|^2 = v^2 + (\omega R)^2, \quad (4.214)$$

which corresponds exactly to the definition for v_{avg} in Equation (4.212) when R is taken to correspond to r_{gyr} . It makes sense to use r_{gyr} as a measure for the average surface radius since the derivations have already shown that r_{gyr} correlates the friction force with the friction torque; see Equation (4.208). Here, r_{gyr} is used to correlate ω_n to an average translational velocity.

The proposed definition for v_{avg} can lead to the condition that $v_{\text{avg}} = 0$. This is problematic because it implies a possible division by zero in the calculation of C_v and C_ω ; see Equations (4.205) and (4.208). However, the definition for the average velocity was derived from observations on the behaviour of the Contensou effect in translation and rotation. But this effect exists only in the presence of relative motion between the objects. Hence, the relationship from Equation (4.211) is valid only for the case where there is relative sliding motion between the objects, i.e., when $v_{\text{avg}} \neq 0$. As a result, the definitions for C_v and C_ω in Equations (4.205) and (4.208) should be used only when the friction model is in the *slip*-mode. When the body surfaces are sticking to each other the Contensou effect disappears. Hence, when the body surfaces are sticking, $C_v \rightarrow 1$ and $C_\omega \rightarrow 1$ as $v_{\text{avg}} \rightarrow 0$. These two “modes” for the Contensou factor definitions will be implemented in the friction model.

4.4.3 Volumetric Bristle Force Model

To model stick-slip frictional effects, it is postulated that the two rigid bodies make contact through a large number of tiny elastic bristles located across the contact surface S ; see Figure 4.5. As was postulated in Section 3.2.2, the stiffness and damping of the bristles should be made proportional to the local normal load to reflect the fact that an increase in contact pressure causes the true contact area to increase and as a result that the surface asperities contact over a larger region. Since the stiffness and damping terms of the bristle model characterize the asperity surface interaction, they should therefore increase with the increase in the true area of contact, i.e., increase with the local normal load.

Hence, the infinitesimal friction force is modelled as a function of the local bristle deformation \mathbf{z} , deformation rate $\dot{\mathbf{z}}$, and normal contact load df_n . The friction force generated on the surface element from the bending of the bristles is described as

$$d\mathbf{f}_{\text{br}} = df_n (\sigma_0 \mathbf{z} + \sigma_1 \dot{\mathbf{z}}) = \sigma_0 \mathbf{z} df_n + \sigma_1 \dot{\mathbf{z}} df_n, \quad (4.215)$$

where σ_0 is the stiffness and σ_1 is the damping coefficient, as given in Section 3.2.2. During the sticking phase, the local bristle motion corresponds to the local relative body motion at s_c , hence

$$\dot{\mathbf{z}} = \dot{\mathbf{z}}_{s_c} + \boldsymbol{\omega}_n \times \boldsymbol{\rho}_t, \quad (4.216)$$

where $\dot{\mathbf{z}}_{s_c} = \mathbf{v}_{sct}$ corresponds to the relative tangential velocity at s_c . A similar expression for the local bristle deformation \mathbf{z} will be derived next.

The relative lateral displacement at any point on the contact surface can be expressed as a combination of the relative translational displacement \mathbf{z}_{s_c} at the centroid s_c and a relative rotation θ_n about s_c as follows

$$\mathbf{z} = \mathbf{z}_{s_c} + \theta_n \mathbf{n} \times \boldsymbol{\rho}_t = \mathbf{z}_{s_c} + \boldsymbol{\theta}_n \times \boldsymbol{\rho}_t, \quad (4.217)$$

where $\boldsymbol{\theta}_n = \theta_n \mathbf{n}$. Figure 4.18 shows the top view of a contact surface. The relative lateral displacement \mathbf{z} of an infinitesimal surface element dS is illustrated in terms of the displacement \mathbf{z}_{s_c} at s_c and the rotation θ_n about s_c .

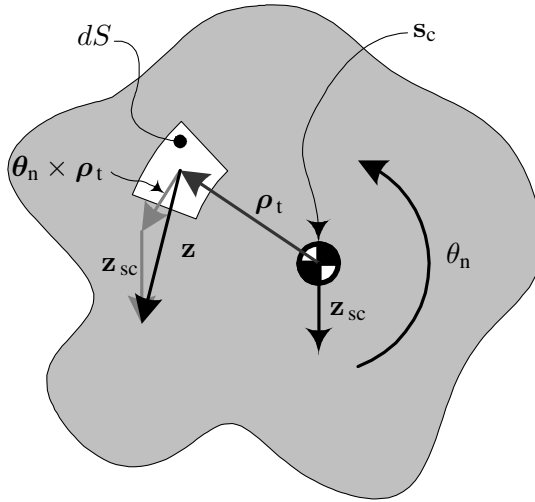


Figure 4.18: The bristle local deformation.

Equations (4.216) and (4.217) share the same vectorial structure: the first term deals with the motion at s_c and the second term gives the resulting motion at s induced by rotational motion about s_c . Here, motion is understood to mean lateral displacement and velocity for Equations (4.217) and (4.216), respectively. Clearly, the first term of Equation (4.216) is the time-derivative of the first term of Equation (4.217).

For the second term in the equations, it is observed that Equations (4.217) and (4.216) only deal with motions that are lateral to the surface. Hence, the only angular displacement that is of concern

is the one producing lateral motion, i.e., θ_n rotates about \mathbf{n} . As a result, the angular displacement about \mathbf{s}_c can be expressed as $\theta_n = \dot{\theta}_n \mathbf{n}$ as done in Equation (4.217). Furthermore, the bristle deformation models the micro-deformation of the surface asperities and, therefore, should always be small. Hence, the angle θ_n will be small and, as a result, it can be treated as a vectorial quantity.

4.4.4 Tangential Friction Force Model

To obtain the total bristle friction force acting over the contact surface the force for the infinitesimal surface element is integrated as

$$\mathbf{f}_{br} = \int_S d\mathbf{f}_{br} = \int_S \sigma_o \mathbf{z} df_n + \int_S \sigma_1 \dot{\mathbf{z}} df_n . \quad (4.218)$$

Given that $\dot{\mathbf{z}} = \mathbf{v}_t$ and considering that the equation defining \mathbf{z} has exactly the same structure as \mathbf{v}_t , the solution for the infinitesimal tangential friction force defined in Equation (4.68) can be used to solve both integrals, replacing μ by σ_o and σ_1 in the first and second integrals of Equation (4.218) respectively. The solution is

$$\mathbf{f}_{br} = f_n (\sigma_o \mathbf{z}_{sc} + \sigma_1 \dot{\mathbf{z}}_{sc}) . \quad (4.219)$$

Similarly as for the bristle friction model implementation presented in Section 3.2.2, the bristle state is defined at the velocity level and integrated to obtain local deformation \mathbf{z}_{sc} . The bristle dynamics model for $\dot{\mathbf{z}}_{sc}$ is formulated as two distinct sub-models: $\dot{\mathbf{z}}_{st}$ for the sticking regime and $\dot{\mathbf{z}}_{sl}$ for the sliding regime. A sticking-state function s is introduced to transition smoothly between the stick-slip friction regimes. The deformation rate is now expressed as

$$\dot{\mathbf{z}}_{sc} = s \dot{\mathbf{z}}_{st} + (1 - s) \dot{\mathbf{z}}_{sl} , \quad (4.220)$$

where

$$s = e^{-\frac{v_{avg}^2}{v_S^2}} \quad (4.221)$$

and v_S is the velocity at which the Stribeck effect occurs. The use of v_{avg} to determine s ensures that the friction model will be in slip mode whenever there is significant translational and/or rotational relative motion. When the friction state is in the stiction regime, the relative motion of the bristles should match exactly the relative motion of the rigid bodies at the contact surface. Hence, $\dot{\mathbf{z}}_{st}$ is defined as

$$\dot{\mathbf{z}}_{st} = \mathbf{v}_{sct} . \quad (4.222)$$

As discussed in the previous section, the definition for the Contensou factor C_v given in Equa-

tion (4.205) applies only when the body surfaces are sliding. When the surfaces are sticking, the factor should have a value of 1. This corresponds to the case where all the bristles on the contact surface are in contact and none are sliding, i.e., the full friction force should be in effect. A new term $C_{v,s}$ defined in terms of C_v is therefore introduced to handle the change in the sticking-state as follows

$$C_{v,s} = s + (1 - s) C_v, \quad (4.223)$$

where C_v is redefined to avoid any division by zero as

$$C_v = \begin{cases} \frac{|\mathbf{v}_{\text{sct}}|}{v_{\text{avg}}} & v_{\text{avg}} > v_\epsilon \\ \frac{|\mathbf{v}_{\text{sct}}|}{v_\epsilon} & v_{\text{avg}} \leq v_\epsilon \end{cases}, \quad (4.224)$$

where v_ϵ is given as before. Once again, a value at least 10 times smaller than v_S is recommended. A value of $v_S/100$ was used in the implementation. The sliding rate $\dot{\mathbf{z}}_{\text{sl}}$ is defined in terms of the Coulomb friction force \mathbf{f}_{tc} that acts while the two bodies are sliding with respect to each other. Coulomb friction acts in a direction opposite to the relative velocity \mathbf{v}_t between the two bodies and its magnitude is $\mu_C f_n$, where μ_C is the Coulomb friction coefficient. The friction force \mathbf{f}_{tc} from Equation (4.205) is modified by introducing the relaxed vector direction function dir_ϵ to avoid meaningless direction values when the vector magnitude is small

$$\mathbf{f}_{\text{tc}} = \mu_C f_n \text{dir}_\epsilon(\mathbf{v}_{\text{sct}}, v_\epsilon) C_{v,s}. \quad (4.225)$$

While the two rigid bodies are sliding on each other, the friction force \mathbf{f}_{br} applied by the bristle should be \mathbf{f}_{tc} . Setting Equation (4.219) equal to Equation (4.225) and solving for $\dot{\mathbf{z}}_{\text{sc}} \simeq \dot{\mathbf{z}}_{\text{sl}}$ yields

$$\dot{\mathbf{z}}_{\text{sl}} = \frac{1}{\sigma_1} \mu_C \text{dir}_\epsilon(\mathbf{v}_{\text{sct}}, v_\epsilon) C_{v,s} - \frac{\sigma_0}{\sigma_1} \mathbf{z}_{\text{sc}}. \quad (4.226)$$

Equation (4.226) is a first order ODE and has a time constant $\tau_{\text{br}} = \sigma_1/\sigma_0$. The bristle dynamics time constant τ_{br} controls how fast the bristles reach a steady-state deformation when two rigid bodies are moving at a constant relative velocity. To summarize, the bristle deformation rate is given as

$$\dot{\mathbf{z}}_{\text{sc}} = s \mathbf{v}_{\text{sct}} + (1 - s) \left(\frac{1}{\sigma_1} \mu_C \text{dir}_\epsilon(\mathbf{v}_{\text{sct}}, v_\epsilon) C_{v,s} - \frac{\sigma_0}{\sigma_1} \mathbf{z}_{\text{sc}} \right). \quad (4.227)$$

The dwell-time dynamics equations presented in Section 3.2.2 are used once again to obtain the maximum stiction coefficient μ_{max} . The maximum force f_{max} is then obtained by including the

Contensou dimensionless factor $C_{v,s}$ as

$$f_{\max} = \mu_{\max} f_n C_{v,s} . \quad (4.228)$$

The bristle friction force is saturated using $\text{sat}(\mathbf{f}_{\text{br}}, f_{\max}) = f_n \text{sat}(\sigma_o \mathbf{z}_{\text{sc}} + \sigma_1 \dot{\mathbf{z}}_{\text{sc}}, \mu_{\max} C_{v,s})$ and the bristle deformation rate is re-computed when the bristle force exceeds f_{\max} as

$$\dot{\mathbf{z}}_{\text{sc}} = \frac{1}{\sigma_1} \text{sat}(\sigma_o \mathbf{z}_{\text{sc}} + \sigma_1 \dot{\mathbf{z}}_{\text{sc}}, \mu_{\max} C_{v,s}) - \frac{\sigma_o}{\sigma_1} \mathbf{z}_{\text{sc}} . \quad (4.229)$$

Equation (4.229) shows that the bristle dynamics is independent of f_n , and is governed by τ_{br} which is constant. The tangential friction force \mathbf{f}_t opposing the velocity can now be computed. A term proportional to the relative tangential velocity is added to account for viscous friction so that

$$\mathbf{f}_t = -f_n (\text{sat}(\sigma_o \mathbf{z}_{\text{sc}} + \sigma_1 \dot{\mathbf{z}}_{\text{sc}}, \mu_{\max} C_{v,s}) + \sigma_2 \mathbf{v}_{\text{sct}}) , \quad (4.230)$$

where σ_2 is the viscous damping coefficient. Hence, the proposed friction model is again a seven parameter model, with exactly the same parameters as for the friction model presented in Section 3.2.2.

4.4.5 Spinning Friction Torque Model

To obtain the total bristle friction torque acting about \mathbf{p}_c , the torque for the infinitesimal surface element is integrated as follows

$$\boldsymbol{\tau}_{\text{br}} = \int_S \boldsymbol{\rho}_t \times d\mathbf{f}_{\text{br}} = \int_S \sigma_o \boldsymbol{\rho}_t \times \mathbf{z} df_n + \int_S \sigma_1 \boldsymbol{\rho}_t \times \dot{\mathbf{z}} df_n . \quad (4.231)$$

Again, given that $\dot{\mathbf{z}} = \mathbf{v}_t$ and taking into account that the equation defining \mathbf{z} has exactly the same structure as \mathbf{v}_t , the solution for the infinitesimal tangential friction torque defined in Equation (4.82) can be used to solve both integrals, replacing μ by σ_o and σ_1 in the first and second integrals of Equation (4.231) respectively. The solution is

$$\boldsymbol{\tau}_{\text{br}} = \frac{f_n}{V} \mathbf{J}_s \cdot (\sigma_o \boldsymbol{\theta}_n + \sigma_1 \dot{\boldsymbol{\theta}}_n) , \quad (4.232)$$

where $\boldsymbol{\theta}_n = \theta_n \mathbf{n}$ and $\dot{\boldsymbol{\theta}}_n = \dot{\theta}_n \mathbf{n}$. As was seen in Section 4.3.7 the spinning friction torque acts in the direction of the contact surface normal \mathbf{n} . Hence, it can be modelled as a 1-dimensional scalar phenomenon as illustrated by Equation (4.208). The bristle friction model is therefore adapted in the form of scalar expression based on the torsion angle θ_n , recalling that $\dot{\theta}_n = \omega_n$ for the sticking case. This angle corresponds to the relative rotation of the contacting surfaces of the two colliding bodies about \mathbf{s}_c . At any point in time, the deformation angle θ_n is assumed to be small, i.e., if the deformation angle becomes large the two bodies should no longer be considered as sticking to each

other. The scalar form of Equation (4.232) is given as

$$\tau_{br} = f_n r_{gyr}^2 \left(\sigma_0 \theta_n + \sigma_1 \dot{\theta}_n \right) , \quad (4.233)$$

where the definition for r_{gyr} from Equation (4.201) has been used to simplify the expression. Equation (4.233) can be interpreted as the torque produced by a bristle located at r_{gyr} from s_c , where the deformation is $r_{gyr} \theta_n$ and its rate is $r_{gyr} \dot{\theta}_n$. Equation (4.233) satisfies the Amontons law of friction which says that the friction should be proportional to the normal load f_n .

The spinning friction model is split into two sub-models for the slipping angular velocity $\dot{\theta}_{sl}$ and sticking angular velocity $\dot{\theta}_{st}$. The sticking state s is used to transition between them as

$$\dot{\theta}_n = s \dot{\theta}_{st} + (1 - s) \dot{\theta}_{sl} , \quad (4.234)$$

where s is defined as in Equation (4.221). In the tangential friction model, the sticking friction bristle velocity corresponded to the relative velocity between the bodies. Here, the bristle angular velocity is set to the relative angular velocity, i.e., $\dot{\theta}_{st} = \omega_n$.

Similar to the translational friction force model, the definition for the Contensou factor C_ω is modified to handle the change in the sticking-state as

$$C_{\omega,s} = s + (1 - s) C_\omega , \quad (4.235)$$

where C_ω is redefined to avoid any division by zero as follows

$$C_\omega = \begin{cases} \frac{r_{gyr} |\omega_n|}{v_{avg}} & v_{avg} > v_\epsilon \\ \frac{r_{gyr} |\omega_n|}{v_\epsilon} & v_{avg} \leq v_\epsilon \end{cases} . \quad (4.236)$$

For the sliding friction sub-model Equation (4.208) is expressed as follows

$$\tau_{sc} = \mu_C r_{gyr} f_n \operatorname{sgn}(\omega_n) C_{\omega,s} , \quad (4.237)$$

where the function $\operatorname{sgn}(\omega_n)$ returns the sign of ω_n when $\omega_n \neq 0$ and zero when $\omega_n = 0$. Setting Equation (4.233) equal to Equation (4.237) and solving for ω_n yields

$$\dot{\theta}_{sl} = \frac{\mu_C C_{\omega,s}}{\sigma_1 r_{gyr}} \operatorname{sgn}(\omega_n) - \frac{\sigma_0}{\sigma_1} \theta_n . \quad (4.238)$$

The bristle deformation rate for the spinning torque friction is thus given as

$$\dot{\theta}_n = s \omega_n + (1 - s) \left(\frac{\mu_C C_{\omega,s}}{\sigma_1 r_{gyr}} \operatorname{sgn}(\omega_n) - \frac{\sigma_0}{\sigma_1} \theta_n \right) . \quad (4.239)$$

The maximum torque the friction model can apply is found using μ_{max} and including the dimen-

sionless Contensou effect factor $C_{\omega,s}$ as

$$\tau_{\max} = \mu_{\max} r_{\text{gyr}} f_n C_{\omega,s} . \quad (4.240)$$

The spinning friction torque is saturated whenever the bristle torque exceeds the maximum spinning friction torque τ_{\max} . Thus, whenever $|\tau_{\text{br}}|$ exceeds τ_{\max} it is scaled to $\pm\tau_{\max}$, namely,

$$\text{sat}(\tau_{\text{br}}, \tau_{\max}) = r_{\text{gyr}}^2 f_n \text{sat}\left(\sigma_0 \theta_n + \sigma_1 \dot{\theta}_n, \frac{\mu_{\max} C_{\omega,s}}{r_{\text{gyr}}}\right) , \quad (4.241)$$

where the $\text{sat}()$ function is interpreted here as the scalar equivalent of Equation (3.39). When the scaling is needed, the angular deformation rate must be re-computed as

$$\dot{\theta}_n = \frac{1}{\sigma_1} \text{sat}\left(\sigma_0 \theta_n + \sigma_1 \dot{\theta}_n, \frac{\mu_{\max} C_{\omega,s}}{r_{\text{gyr}}}\right) - \frac{\sigma_0}{\sigma_1} \theta_n . \quad (4.242)$$

The spinning friction force τ_s opposing the angular velocity ω_n can now be computed. A term proportional to the relative angular velocity is added to account for viscous friction such that

$$\tau_s = -r_{\text{gyr}}^2 f_n \left(\text{sat}\left(\sigma_0 \theta_n + \sigma_1 \dot{\theta}_n, \frac{\mu_{\max} C_{\omega,s}}{r_{\text{gyr}}}\right) + \sigma_2 \omega_n \right) \mathbf{n} , \quad (4.243)$$

where σ_2 is the viscous damping coefficient. Note that r_{gyr} should not be zero unless the volume of interference itself is zero. When $V = 0$, the total contact force and moments should be zero in any case and therefore the condition for $r_{\text{gyr}} = 0$ can be avoided easily in the implementation. Hence, the proposed friction model is again a seven parameter model, with exactly the same parameters as for the friction model presented in Section 3.2.2.

4.5 Volumetric Contact Model Parameters

The parameters for the volumetric contact model are almost identical to the parameters for the point contact model presented in Chapter 3. For example, the point contact normal force model in Equation (3.19) has exactly the same form as the volumetric normal force models for the one deformable body model (Equation (4.62)) and the two deformable body model (Equation (4.178)). The only difference here is the stiffness term, which is $k x^p$ for the point contact model and $k_v V$ for the volumetric models. Here, k_v must be found experimentally.

The parameter for hysteretic damping factor is the same in all normal contact force models and can be selected using the same process as explained in Section 3.3.1. A numerical constraint relaxation is also included in the model implementation to avoid the artificial energy increase resulting from the error in contact time detection obtained with the Simulink fixed-step solvers. This constraint relaxation is implemented in exactly the same way as in Section 3.3.1, except that the inter-penetration depth x is replaced by the volume V of the volume of interference.

The rolling resistance torque of the volumetric contact model is proportional to the hysteretic damping term and, hence, no additional work is needed to select or identify parameters for this additional component of the contact model: its parameters are derived from the same basic parameter set as for the point contact model.

In the numerical implementation, the volume of interference is approximated by dividing the region where the two bodies collide into small cubes of known volume and counting the ones inside the volume of interference. The small cubes are called voxels. This implementation requires therefore that a voxel size threshold be specified. It is suggested to do the selection of the voxel size based on an estimate of a “small” force δf acting on the system. For example, in a simulation where a body falls on top of another, this small force could be selected in the range $10^{-3} m g$ to $10^{-6} m g$, where m is the mass of the falling body and g is the gravitational constant. Alternatively, for a robotic task requiring the application of forces of 50 N, the small force δf could be selected in the range $50 \cdot 10^{-3}$ N to $50 \cdot 10^{-6}$ N. In essence, δf should correspond to a non-zero force that has negligible effect on the dynamics of the system. Once the small force has been determined, the voxel size is selected as $(\delta f / k_v)^{\frac{1}{3}}$.

The contact normal \mathbf{n} is obtained by finding an eigenvector of \mathbf{J}_v closest to a geometric estimate provided by an LLG geometric function; see Section 2.3.2. The algorithm generating this geometric estimate guarantees the vector will always point from \mathcal{B}_j toward \mathcal{B}_i . The geometric estimate is then fed to an implementation of the inverse iteration method which requires three numerical parameters to be specified; see Appendix A. These parameters are: an angular convergence threshold θ_ϵ , an eigenvector estimate ratio r_n and a maximum number of iterations n_i . Values of 1 deg, 0.95 and 15 are suggested for θ_ϵ , r_n and n_i , respectively.

The volumetric friction model parameters correspond exactly to the parameters of the model presented in Section 3.2.2. Hence, they can be selected using the process presented in Section 3.3.2. Interestingly, the spinning friction model component requires no additional parameters to be specified and, hence, no additional parameters to be selected or identified. This feature greatly simplifies the use of the volumetric contact model, because it is based on a relatively limited parameter set which can be found through experimentation or selected based on simple guidelines.

Chapter 5

Numerical Simulation Results

An object-oriented framework written in C++ was created to support the implementation of the contact models presented in Chapters 3 and 4. Appendix A provides more details on this framework and explains how it is used to implement the proposed contact models. The C++ classes provide a single point interface to numerical simulation environments.

In this work, the contact models were used to create multibody simulations implemented in Simulink, a graphical simulation environment for systems where the dynamics equations are expressed in state-space form. The simulations, therefore, rely on the solvers available in this environment. The multibody dynamics are modelled using the Multibody Toolbox (MuT), an object-oriented multibody modelling software developed at the CSA that allows deriving the model properties symbolically and then exporting them into Matlab and Simulink; see Appendix B. The MuT was co-developed by the author and builds on the Symofros project (L'Archevêque et al., 2000).

This chapter presents the numerical simulation results of various multibody systems in contact, and illustrates the features and behaviour of the proposed contact models. The results for the point contact model from Chapter 3 are presented first and then those using the volumetric contact model from Chapter 4.

5.1 Point Contact Model

This section presents simulations involving bodies with non-conformal geometries. First, the behaviour of the normal contact sub-model is examined followed by simulation using the tangential friction sub-model. This section is concluded with a multibody simulation involving oblique frictional impact, thereby testing the combined behaviour of both sub-models.

5.1.1 Normal Contact Model

The behaviour of the hysteretic damping term for the normal force model presented in Chapter 3 was investigated. More specifically, a normal force model calculating the damping factor as a func-

tion of e_{eff} was implemented (Equation (3.23)), where e_{eff} is obtained using Equation (3.12). The ODE given in Equation (3.18) was solved over a single impact cycle. The results were generated in Simulink with the ode23s solver with relative and absolute error tolerances of 10^{-6} . This variable-step solver was chosen because it is designed to handle numerically stiff systems and the relatively stringent error tolerances ensure the results are very accurate. Identical results were also obtained using fixed-step solvers.

Figure 5.1 shows the ratio of e_{eff} to e_{emp} obtained using the model proposed by Hunt and Crossley (1975) for the impact of a sphere on a plane, and the model proposed in Section 3.2.1 based on the solution of the closed-form expression (Equation (3.23)). The figure shows the value of the ratio as a function of impact velocity, with $\alpha = 0.2$ s/m. Clearly, the damping model proposed in Section 3.2.1 yields a dynamic behaviour that is consistent with any given value of the coefficient of restitution, i.e., $e_{\text{eff}}/e_{\text{emp}}$ always equals 1. Hence, the model can also be used for plastic impacts, given that a function for the coefficient of restitution is provided. The model proposed by Hunt and Crossley (1975) is consistent with the given coefficient of restitution only when $v_n^i = 0$ (and $e = 1$ from Equation (3.12)), i.e., for perfectly elastic impacts.

Stoianovici and Hurmuzlu (1996) tuned the damping factor to obtain a good match between experimental and simulated results of a beam impacting a hard surface, without formal knowledge of the exact relationship between λ and e_{eff} . Instead, they varied λ to get the best possible match. The damping factor thus identified approximates the experimental behaviour only in the range of normal impact velocities used in the experiment. The damping factor model presented in Section 3.2.1 is not subject to this limitation since v_n^i can be varied over a wide range without reducing the accuracy of the approximation.

Figure 5.2 illustrates the contact force profile obtained using Equation (3.19) as a function of indentation depth for the same sphere-plane impact, for various restitution coefficients ranging from 0.1 to 1. The same solver and error tolerances were used. Notice that at large values of the restitution coefficient the damping in the compression and restitution phase is essentially symmetric. On the other hand, for low values of e_{eff} most of the energy (area inside the curve) is dissipated in the compression phase and the hysteretic damping becomes asymmetric.

5.1.2 Tangential Friction Model

Using the parameters given in Table 5.1, the friction model was used to simulate the response of a spring-mounted block sitting on a plate that is moved at a constant speed as shown in Figure 5.3. This experiment was first proposed by F.P. Bowden and L.L. Leben who built an apparatus to study the stick-slip process (Rabinowicz, 1956). To test the vectorized friction force model giving \mathbf{f}_t (Equation (3.42)), the motion direction is at 45 deg from the x -axis in the x - y plane, moving away from the origin, the spring constant is $k = 2$ N/m, the mass $m = 1$ kg and the gravitational constant $g = 10$ m/s². The numerical tolerance on velocity of the friction model was set to $v_\epsilon = v_S/100 = 10^{-5}$ m/s.

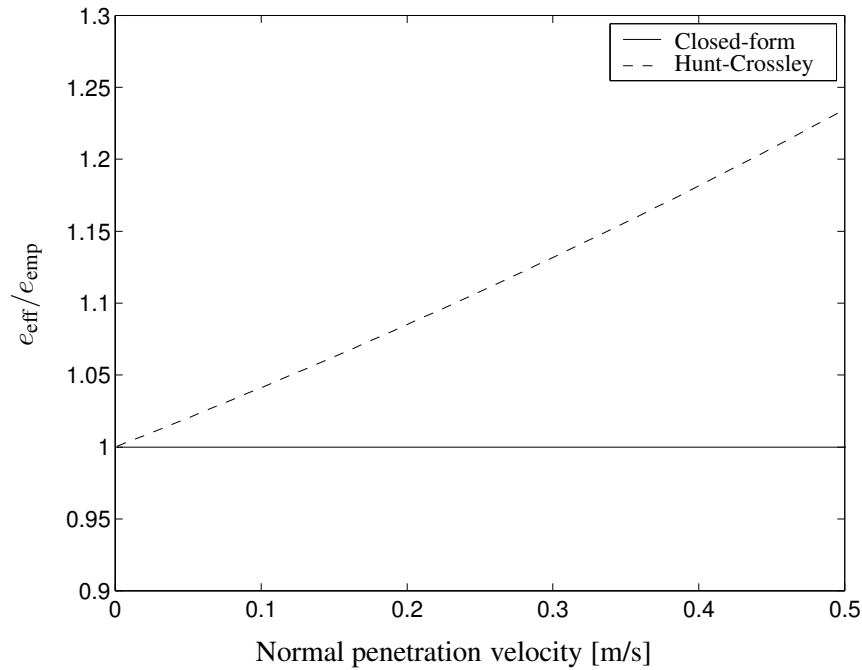


Figure 5.1: Effective coefficient of restitution for two models of d (mass: 0.454 kg; $k = 3.4 \cdot 10^{10} \text{ N/m}^{3/2}$; $\alpha = 0.2 \text{ s/m}$).

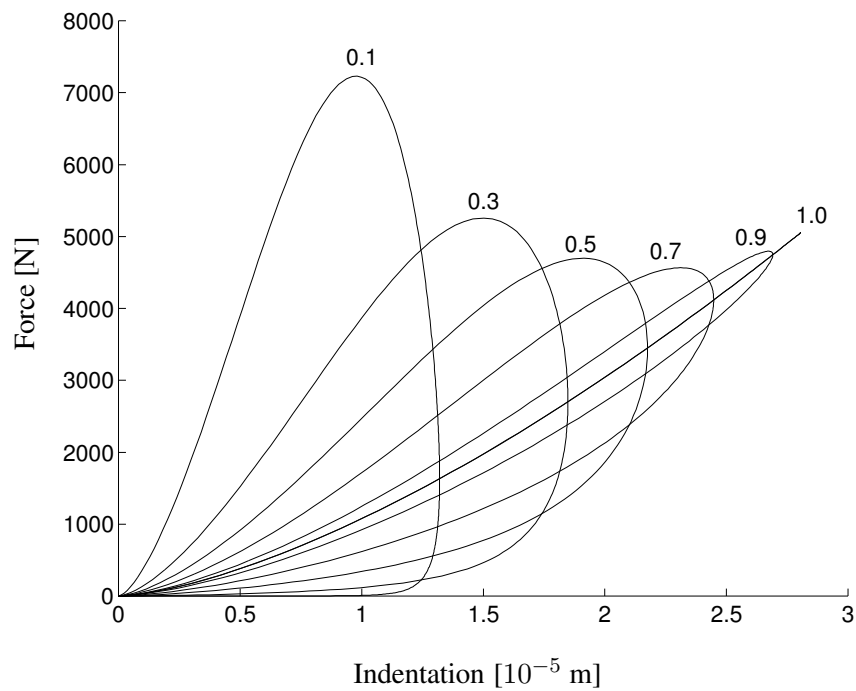


Figure 5.2: Contact force vs. indentation for various values of e_{eff} (mass: 0.454 kg; $k = 3.4 \cdot 10^{10} \text{ N/m}^{3/2}$).

μ_S	μ_C	$m g \sigma_0$	$m g \sigma_1$	$m g \sigma_2$	v_S	τ_{dw}
0.15	0.1	10^5 N/m	$\sqrt{10^5}$ Ns/m	0.1 Ns/m	0.001 m/s	2 s

Table 5.1: Friction model parameter values for Bowden and Leben stick-slip simulations.

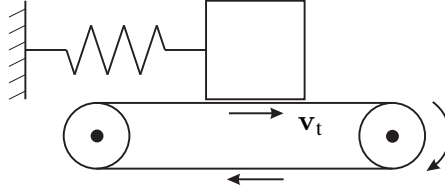


Figure 5.3: The Bowden and Leben stick-slip experimental apparatus.

The resulting ODE is $m \ddot{r} = -f_t$, where r is the position of the block with respect to the wall and $\dot{r} = v_t$. This time, the results were generated with the ode23t solver using the same error tolerances as before. There was no noticeable gain in performance between this solver and the ode23s; both appear to work well and produce the same results.

The simulation results show that the block sticks to the plate until the spring force is high enough to overcome the friction force, at which point the block slides in the opposite direction to the plate. The results were generated in Simulink using the ode23t solver using the same error tolerances as before and are plotted in Figures 5.4–5.6 for three different speeds of the plate. The position axes show the distance from the origin $|r|$ and the force axes correspond to the magnitude of the friction force $|f_t|$.

Note the sharp spikes in the friction curves corresponding to transitions between forward and reverse velocities of the block. When the plate is moving slowly, the position curve drops almost vertically as soon as the block starts sliding. Then, as the plate moves faster the amplitude of the oscillations decreases and the profile becomes similar to a sinusoidal wave. However, in all cases, the first peak of the friction profiles always extends up to the maximum stiction limit, a consequence of the dwell-time dynamics (the friction model is initialized in the “sticking” state). Subsequent peaks are of lesser magnitude for higher speeds of the plate, because there is not enough time for the stiction force to reach its maximum value of $\mu_S f_n$. This dynamic behaviour corresponds to the observations by Rabinowicz (1956). Also, the sudden drops in friction force indicate when a stick-slip transition occurred. The small “bump” in force thereafter is caused by the viscous damping term. It can be seen to peak when the position changes at the fastest rate.

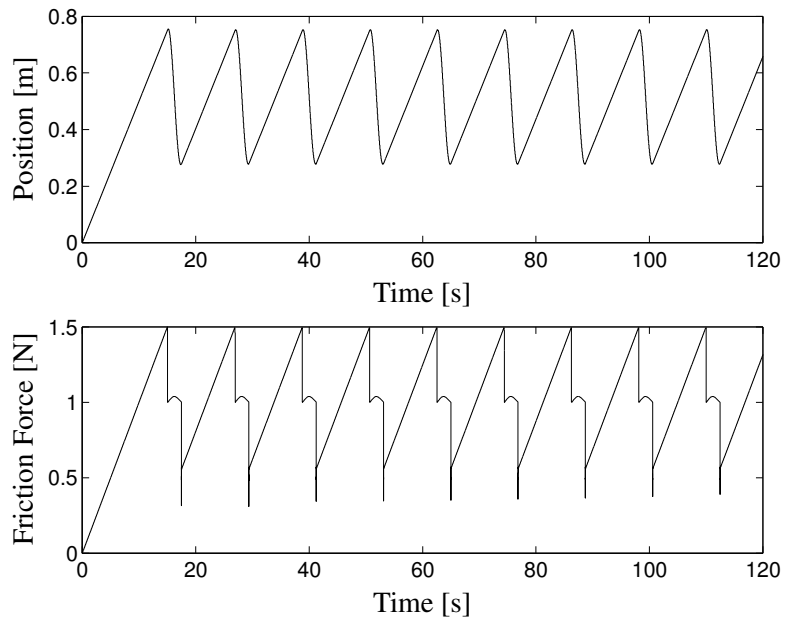


Figure 5.4: Bowden and Leben stick-slip experiment for $|\mathbf{v}_t| = 0.05$ m/s.

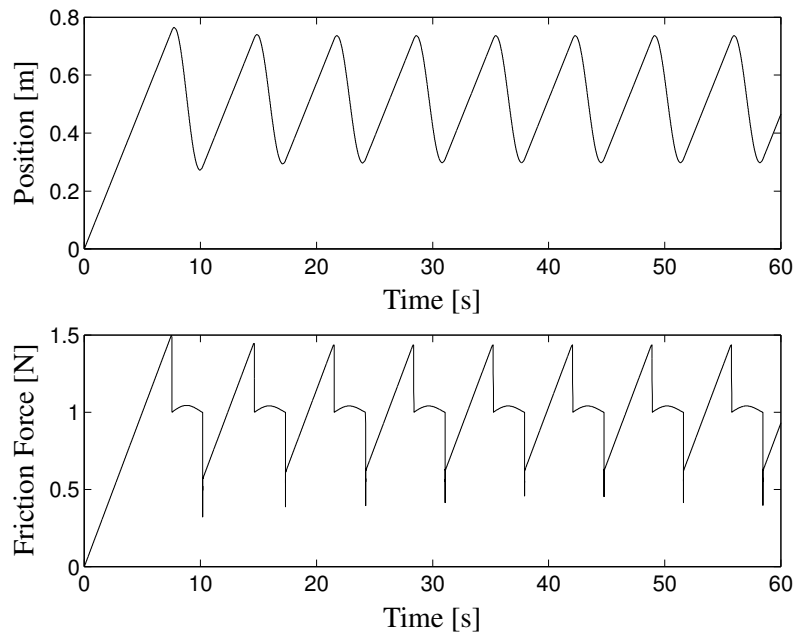


Figure 5.5: Bowden and Leben stick-slip experiment for $|\mathbf{v}_t| = 0.1$ m/s.

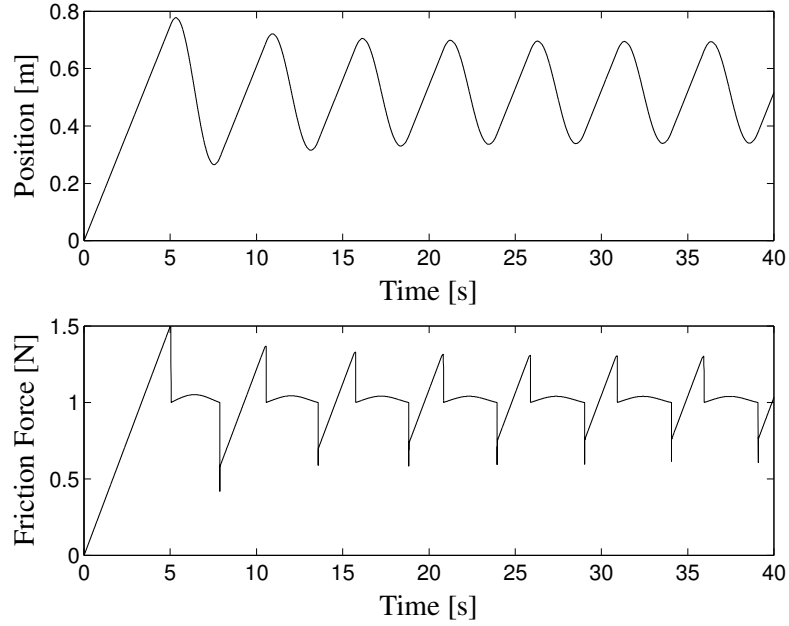


Figure 5.6: Bowden and Leben stick-slip experiment for $|\mathbf{v}_t| = 0.15$ m/s.

5.1.3 Multibody Dynamics Simulations

This section presents the numerical results for multibody dynamics simulations involving oblique impacts.

A Ball Falling on a Plane

A simulation model was implemented for a 2 kg ball, with 0.1 m radius colliding with an inclined plane. From the horizontal position, the plane is rotated 20 deg about the $+Y$ axis and its height h_j is set to 0.4 m; see Figure 3.1. The ball centre will therefore be around 0.5 m from the plane once it stops bouncing. Gravity $g = 9.81$ m/s² acts in the $-Z$ direction. The ball is dropped from a height of 2 m and is given an initial velocity of -1 m/s in the X direction and 0.5 m/s in the Y direction. The normal impact model with $k = 10^6$ N/m^{3/2} was set to have a constant coefficient of restitution of 0.5. The small velocity tolerance v_{small} was set to 0.001 m/s. The friction model parameters are shown in Table 5.2, and the numerical tolerance on velocity was set to $v_\epsilon = v_S/100 = 0.001$ m/s.

μ_S	μ_C	σ_o	σ_1	σ_2	v_S	τ_{dw}
0.45	0.4	10^5 1/m	10^4 s/m	0 s/m	0.1 m/s	0.01 s

Table 5.2: Friction model parameter values for the bouncing ball simulations.

The resulting motion is found by solving Euler's equation of motion for a free-floating rigid

body upon which the contact force \mathbf{f}_c is applied; see Equation (3.9). The simulation used the ode23s solver with error tolerances of 10^{-3} . It was observed that the solution obtained with these lower error tolerance settings were still very accurate when compared at the position level to results generated with the higher tolerance setting, i.e., 10^{-6} .

Figure 5.7 shows the three-dimensional trajectory of the ball centre, plotted in an xyz frame that is rotated with the plane. Thus, once the state of pure rolling has been reached, the only acceleration is $g \sin(20 \text{ deg})$ in the local x direction. The x and y components of the path are projected onto the $z = 0$ plane. Figure 5.8 gives the corresponding velocity profiles. The legend definition is the same for both sub-plots. Note that when pure rolling occurs (zero z velocity), the velocity in the y direction remains constant while the x component increases linearly, as expected. Note also that the angular velocities remain constant, except for the component in the y direction, which also increases linearly in agreement with $v = R\omega$. It can be seen that the two motions are coupled by the friction force that imposes a no-slip condition.

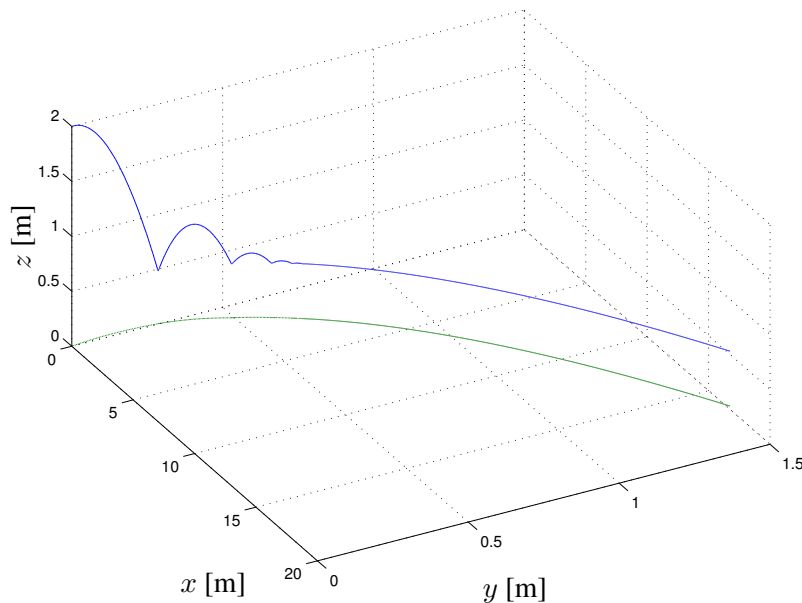


Figure 5.7: Trajectory of the ball impacting an inclined plane.

A Ball Falling in a Cylinder

The same ball was then dropped from a height of 0.5 m in Z on the inside surface of a 1 m radius cylinder aligned in the Y direction. All contact model parameters are identical as in the previous simulation. The ball was given an initial offset from the cylinder axis of 0.3 m in the X direction so that the first impact will cause motion in the $X-Z$ plane only. The simulation results were obtained in Simulink using the ode23s solver with error tolerances of 10^{-6} .

Figure 5.9 shows the resulting three-dimensional trajectory of the ball centre . The X and

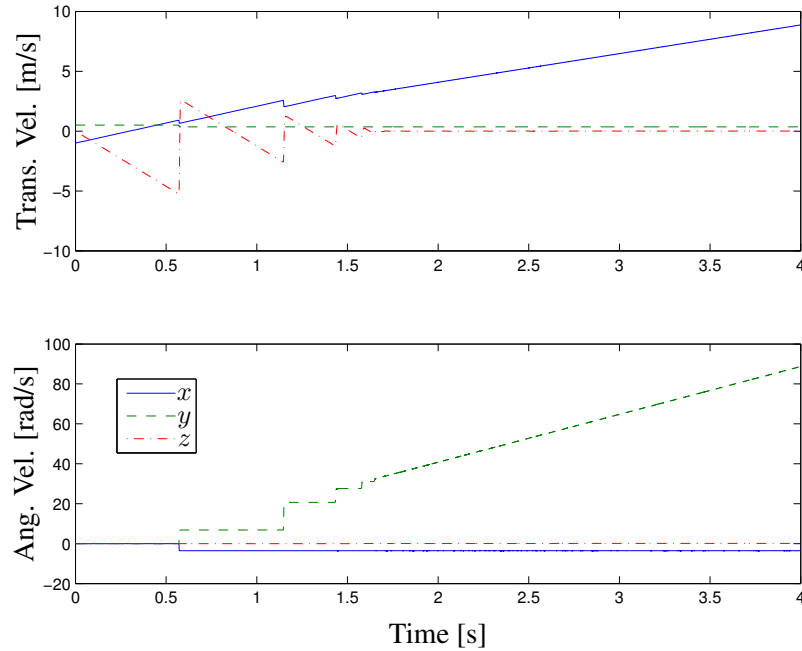


Figure 5.8: Ball impacting an inclined plane: velocity components vs. time.

Y components of the trajectory are shown below in the $Z = 0$ plane. Note the ball oscillations inside the cylinder, and the small penetration visible on the first impact. Figure 5.10 shows the velocity profiles. The angular velocity in the Y direction oscillates, while the other angular velocity components are zero. Again, there is coupling between the translational and rotational motions through the effect of the friction. It is seen that the model changes the orientation of the friction force to correctly impose the no-slip condition. Clearly, $v = R\omega$ holds during the rolling motion, e.g., $v = 1$ m/s when ω peaks at 10 rad/s.

The same simulation was then conducted with initial ball velocity of 0.3 m/s in the Y direction. Figure 5.11 plots the trajectory of the ball centre, with the X and Y components projected onto the $Z = 0$ plane. The ball oscillates as it rolls along the cylinder. Figure 5.12 presents the corresponding velocity profiles. As expected, a non-zero angular velocity in the Z direction results from the first impact, while the X component of angular velocity is no longer constant. Note also that the amplitude of the oscillation does not decay with time. This is to be expected since there are no spinning or rolling frictional effects included in the proposed contact model, and the tangential friction force does no work. Figure 5.13 shows the total energy of the sphere (kinetic and potential) and the contact model spring as a function of time. Clearly, energy is dissipated during the impact phase, but as soon as the sphere settles into pure rolling motion the energy is constant.

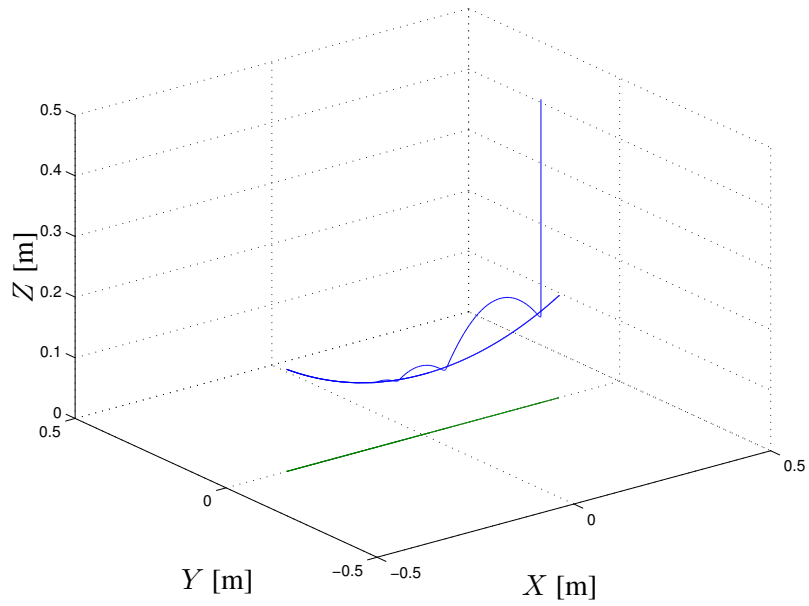


Figure 5.9: Trajectory of the ball impacting a cylinder (2D motion).

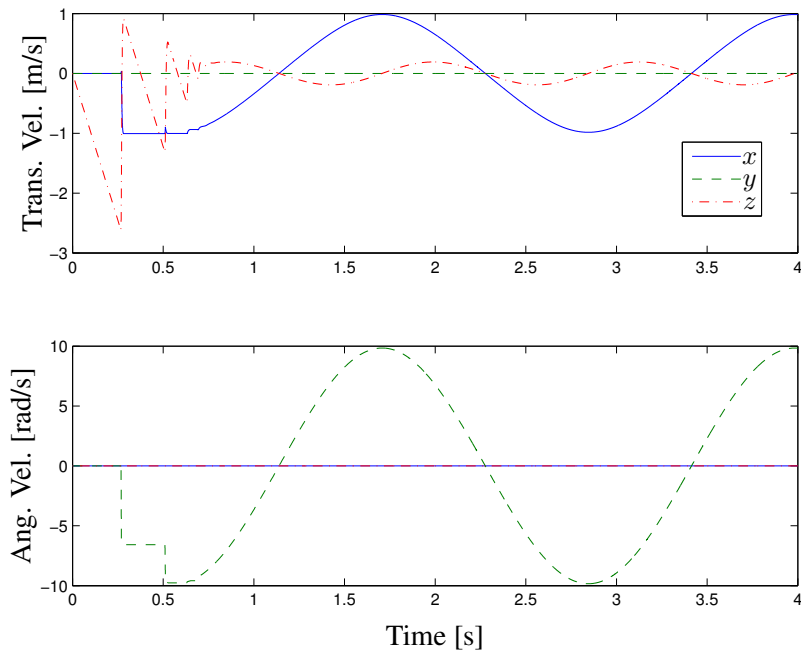


Figure 5.10: Ball impacting a cylinder: velocity components vs. time (2D motion).

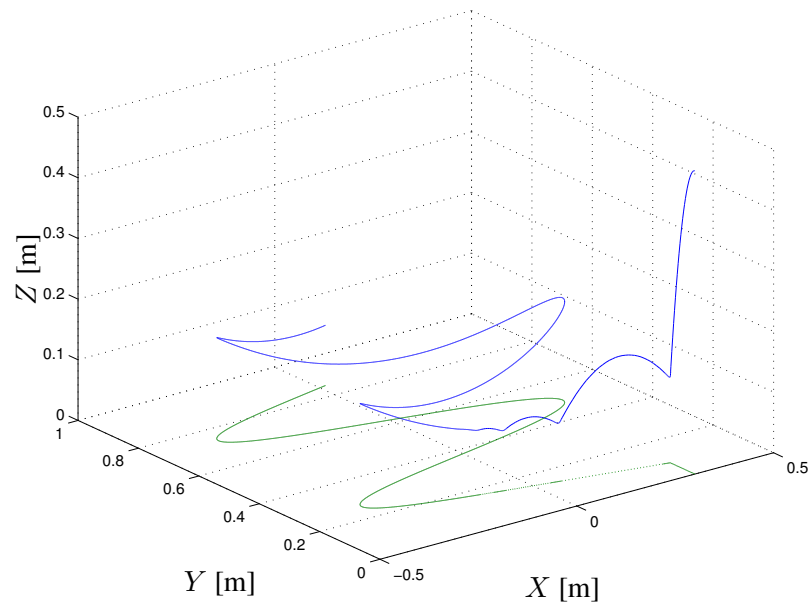


Figure 5.11: Trajectory of the ball impacting a cylinder (3D motion).

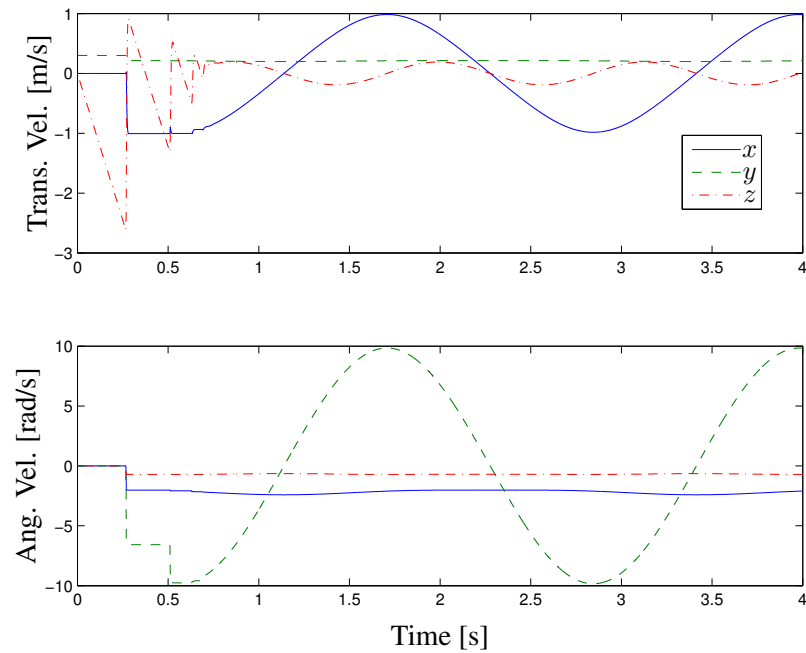


Figure 5.12: Ball impacting a cylinder: velocity components vs. time (3D motion).

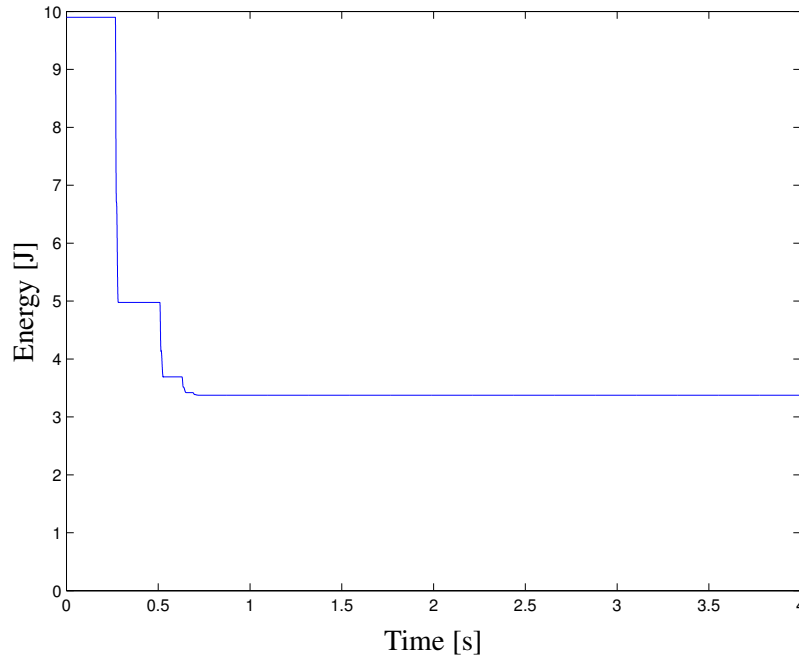


Figure 5.13: Ball impacting a cylinder: total system energy for 3D motion.

A Double Pendulum

Figure 5.14 presents the schematic diagram of a double pendulum, with a spring placed at the bottom to represent the surface compliance. The tip of the pendulum is allowed to hit the surface located 0.61 m below the first joint axis. The governing equations of motion were obtained using the MuT. The two coupled ODEs and the contact force model are then evaluated and solved numerically using the ode23s solver with error tolerances of 10^{-6} .

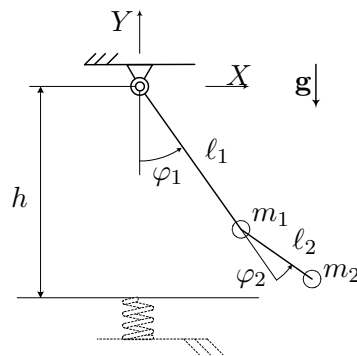


Figure 5.14: Double pendulum: schematic diagram ($\varphi_{o1} = 45 \text{ deg}$, $\varphi_{o2} = 0 \text{ deg}$, $\dot{\varphi}_{o1} = -120 \text{ deg/s}$, $\dot{\varphi}_{o2} = 130 \text{ deg/s}$, $l_1 = 0.5 \text{ m}$, $m_1 = 5.0 \text{ kg}$, $l_2 = 0.25 \text{ m}$, $m_2 = 2.0 \text{ kg}$, $g = 9.81 \text{ m/s}^2$, $h = 0.61 \text{ m}$).

The initial conditions listed in Figure 5.14 were selected to give the system a high kinetic energy with the tip of the pendulum moving toward the plane. To better illustrate the effects of the contact model on the system's response, the joints are modelled as frictionless. The normal impact model with $k = 10^9 \text{ N/m}^{3/2}$ was set to have a constant coefficient of restitution of 0.9. The small velocity tolerance v_{small} was set to 0.001 m/s. The friction model parameters are shown in Table 5.3 and the numerical tolerance on velocity was set to $v_\epsilon = v_S/100 = 0.001 \text{ m/s}$.

μ_S	μ_C	σ_o	σ_1	σ_2	v_S	τ_{dw}
0.15	0.12	10^5 1/m	$\sqrt{10^5} \text{ s/m}$	0 s/m	0.1 m/s	0.75 s

Table 5.3: Friction model parameter values for double pendulum simulation.

The resulting joint motion is plotted in Figures 5.15 and 5.16. The second joint motion first moves into the positive angles region, and finally settles at a negative angle around -65 deg. Figure 5.17 gives the corresponding tip motion in the X - Y plane as it moves from the initial position (marked by a circle) into the bouncing motion. It can be seen that after bouncing several times, the tip settles into a slowly decaying oscillatory motion in X .

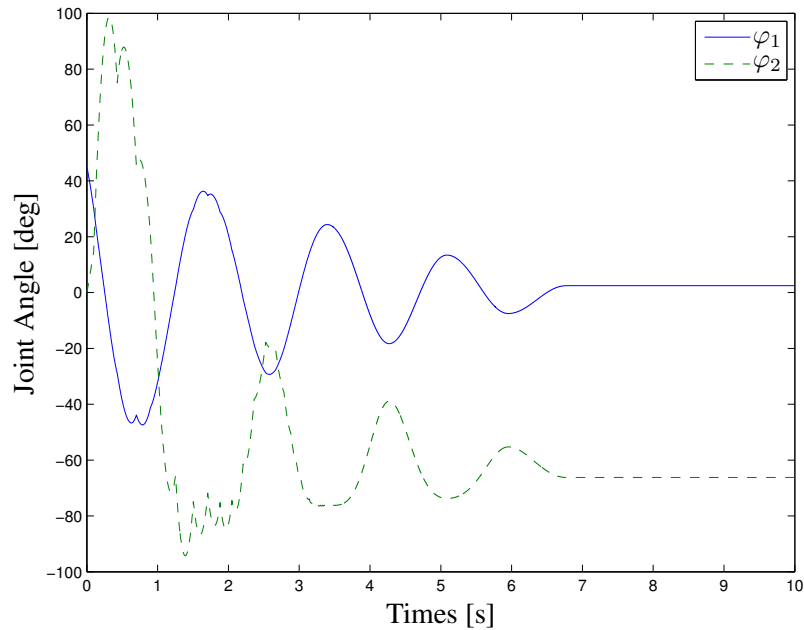


Figure 5.15: Double pendulum: joint positions.

Note that if the stick-slip effect was not included in the friction model, and if σ_2 was not zero, then the viscous damping term would have slowly dissipated the kinetic energy in the system. The final resting position would then be at the equilibrium where $\varphi_1 = 0 \text{ deg}$ since the surface is modelled as being perfectly horizontal, and therefore, cannot apply reaction forces perpendicular to gravity when it is frictionless. Instead, the stick-slip effect of the tangential friction model causes

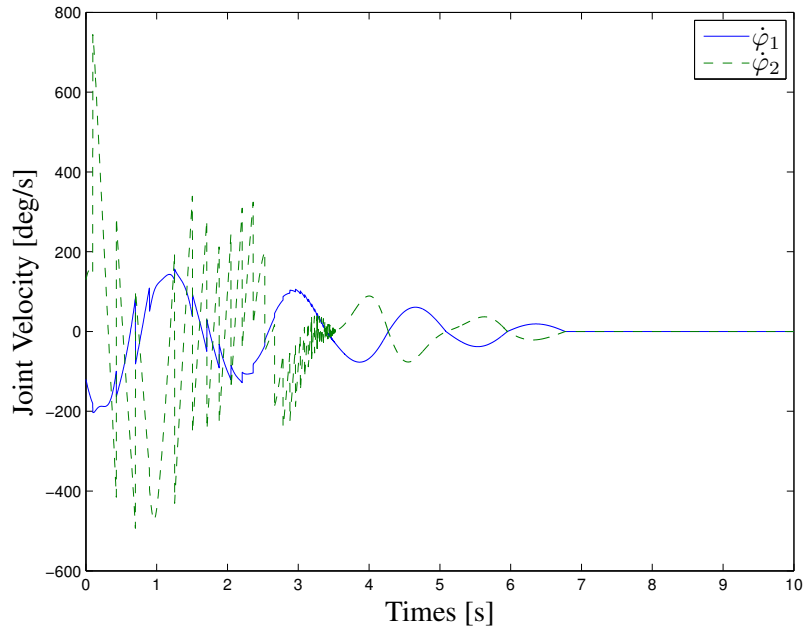
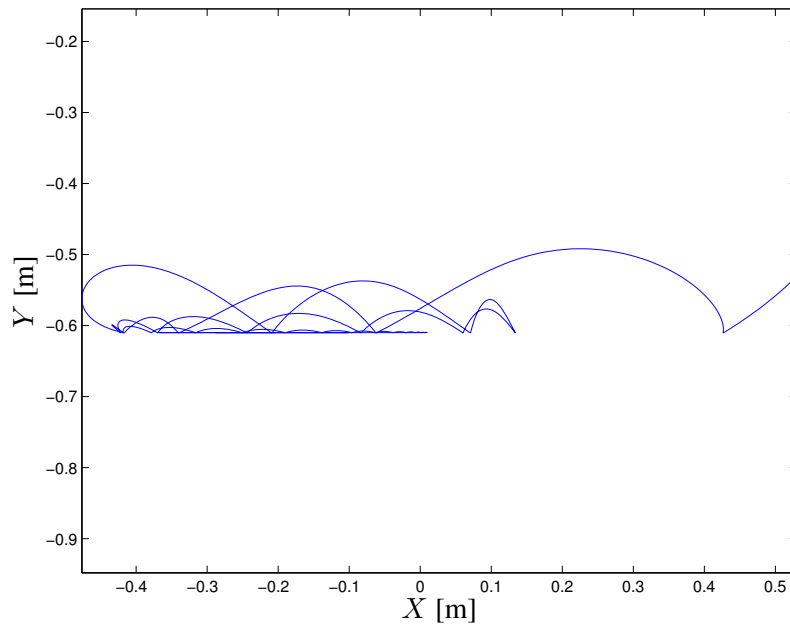


Figure 5.16: Double pendulum: joint velocities.

Figure 5.17: Double pendulum: X - Y plot of end-effector positions.

the final resting position of the first joint to be off-centre by 2.2 deg. Figure 5.18 shows that the friction model switches into the “sticking mode” after 6.5 s, as s_{dw} goes to 1. Figure 5.19 gives the time history of total system energy: it is constant in between collisions, drops rapidly when the tip bounces on the surface and then slowly decays down to a constant value.

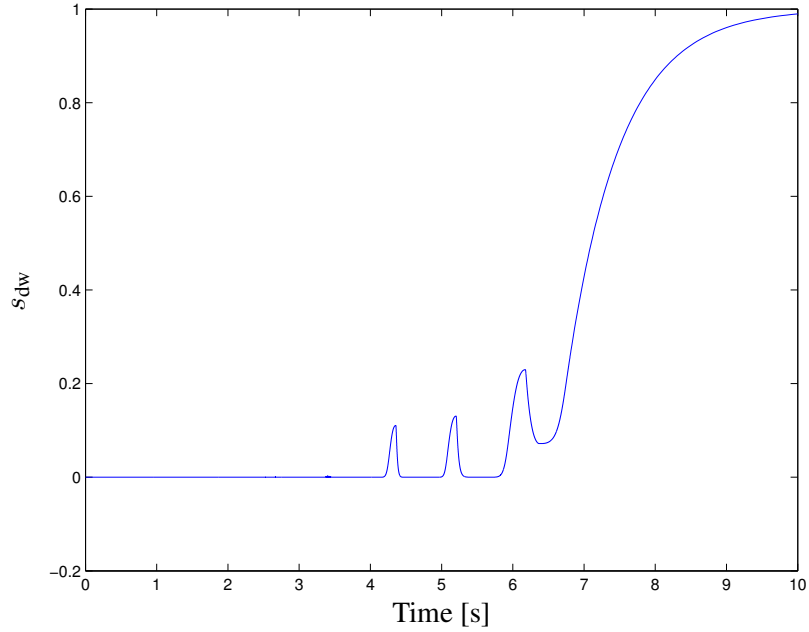


Figure 5.18: Double pendulum: dwell state s_{dw} of friction model.

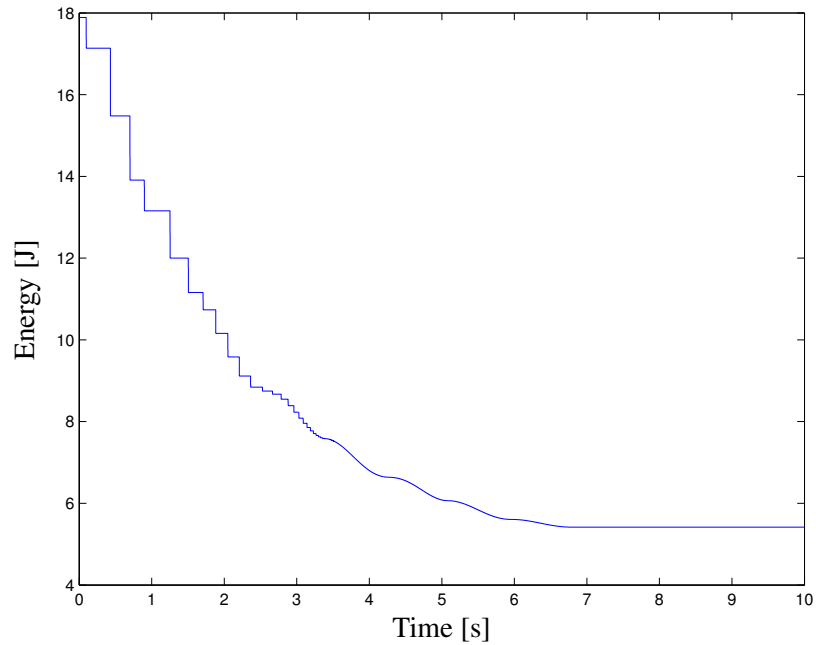


Figure 5.19: Double pendulum: total system energy.

The double pendulum model was then modified to match the benchmark simulation model from Ahmed et al. (1999) where $l_1 = l_2 = 1$ m, $m_1 = m_2 = 2$ kg and the link inertia are $J_1 = J_2 = 1/6$ kg m² about the centre of mass located in the middle of each link. The energy dissipation occurring over a single impact is studied at two pendulum configurations (a) at $\varphi_{o1} = 18$ deg,

$\varphi_{o2} = 12$ deg, and (b) at $\varphi_{o1} = 0$ deg, $\varphi_{o2} = 20.7$ deg. The initial velocities in both cases are $\dot{\varphi}_{o1} = \dot{\varphi}_{o2} = -1$ rad/s. The percentage of energy loss is computed for three different values of the coefficient of restitution, as a function of friction coefficient values. In the simulations, the values for μ_S and μ_C were set equal so that $\mu_S = \mu_C = \mu$, and vary from 0 to 1. The other contact model parameters are the same as before.

The results are given in Figures 5.20 and 5.21. The energy losses match perfectly the benchmark results, except for the $e = 0$ case, which cannot be implemented with the proposed contact model, as this results in a division by 0. Here, a value of $e = 0.01$ was used instead, and the resulting energy dissipation is very similar to the results for $e = 0$ of the benchmark simulation. Figure 5.21 indicates that for some values of μ the energy loss can be greater for higher values of e_{eff} , as in the benchmark simulation results.

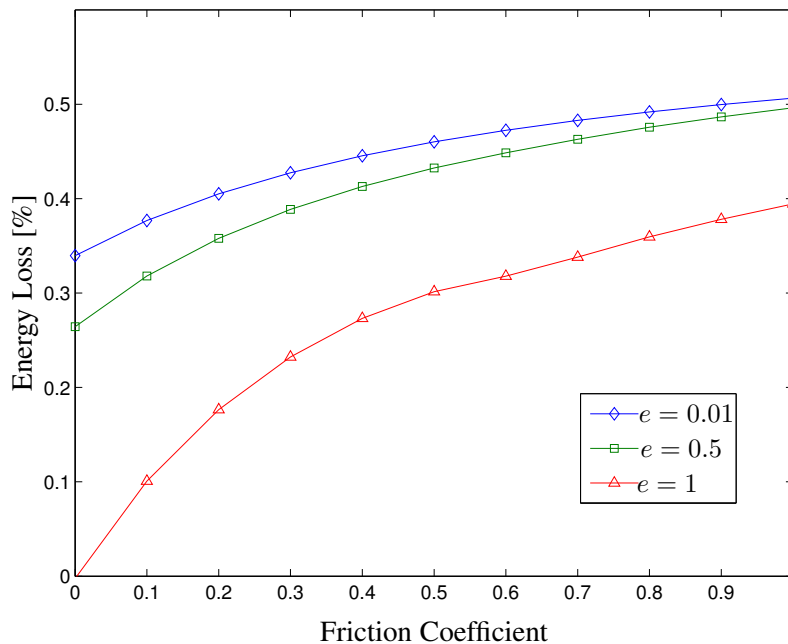


Figure 5.20: Benchmark double pendulum: energy loss vs. friction coefficient – case (a).

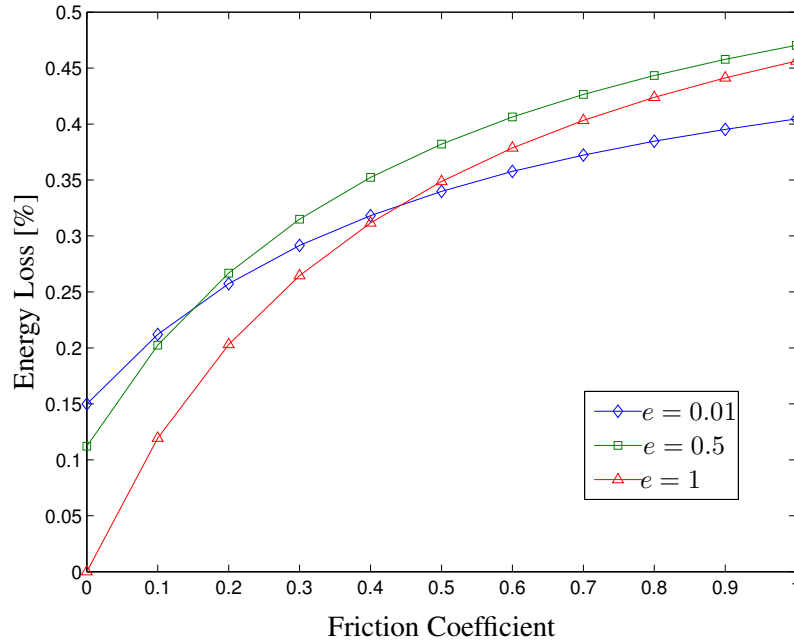


Figure 5.21: Benchmark double pendulum: energy loss vs. friction coefficient – case (b).

5.1.4 Experimental validation

This section¹ presents a comparison between experiments performed using the SMT manipulator introduced in Section 1.1.1 and a simulation of the SMT using the point contact model. The contact experiments involved a half-sphere object coming into contact with a flat plate. The plate is mounted on a 6-axis force-moment sensor and will be referred hereafter as the worksite force-plate. The selected geometric-pair satisfies the conditions for using a Hertz-based stiffness model, and hence the contact interaction can suitably be modelled using the point contact model. The half-sphere is made of aluminium and is mounted on top of a micro-fixtured specifically designed for the SMT gripper. The flat plate is also made of aluminium. Figure 5.22 show the key dimensions of the half-sphere payload, along with the geometric information of the worksite.

For the simulation, the normal impact model with $k = 2.5413 \cdot 10^8 \text{ N/m}^{3/2}$ was set to have a constant coefficient of restitution of 0.85. The small velocity tolerance v_{small} was set to 0.001 m/s. The version of the normal contact model used for the simulations in this section did not include the numerical relaxation feature discussed in Section 3.3.1. Since the impact velocities are very low in the experiments, this change has negligible effect, i.e., $x_{r,o}$ will be very small.

The friction model parameters are shown in Table 5.4 and the numerical tolerance on velocity was set to $v_\epsilon = v_S/100 = 0.001 \text{ m/s}$. The friction model used for the simulations in this section was based on a bristle model where the bristle stiffness and damping terms were not proportional

¹The work presented in this section was done in collaboration with Dr. Christian Lange at the CSA.

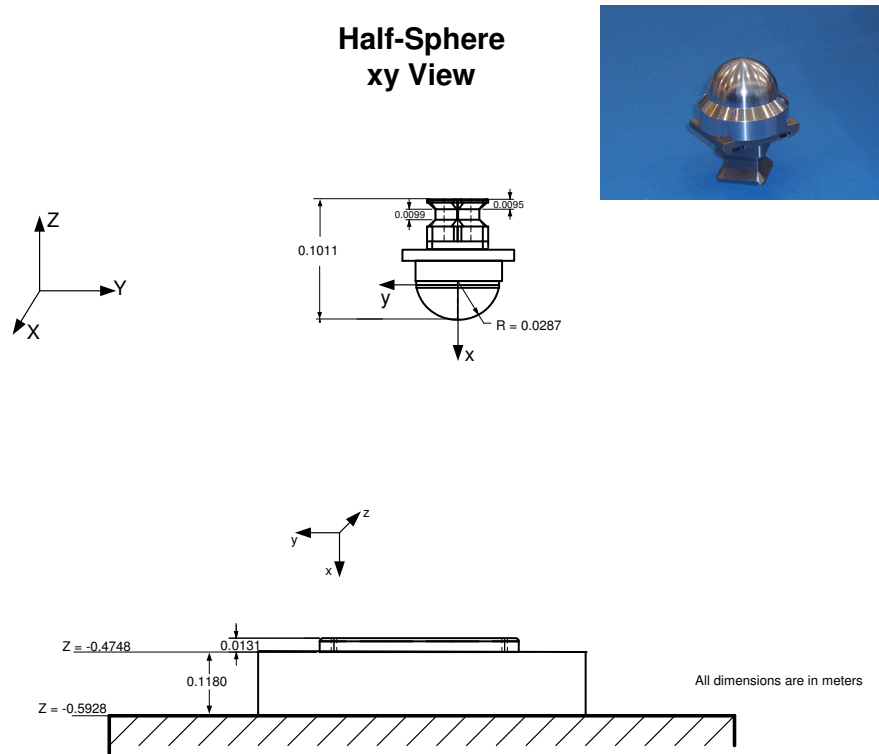


Figure 5.22: Dimensions and coordinate frame definition of the half-sphere and the worksite force-plate.

to the normal load. However, since the relative tangential motion is done under a constant normal load in the experiments, this has no significant impact on the simulation results, i.e., the effective bristle stiffness $\sigma_o^* = f_n \sigma_o$ and damping $\sigma_1^* = f_n \sigma_1$ are constant in this case.

μ_S	μ_C	σ_o^*	σ_1^*	σ_2^*	v_S	τ_{dw}
0.16	0.1	10^5 N/m	10^4 Ns/m	0 Ns/m	0.1 m/s	0.01 s

Table 5.4: Friction model parameter values for the contact experiment.

Description of experimental facility

To facilitate the planning and to ensure smooth operation of Dextre during contact related tasks, e.g., the insertion and extraction of Orbital Replacement Units (ORUs), the CSA has designed and built the on-ground SPDM Task Verification Facility (STVF). A description of STVF can be found in (Piedbœuf et al., 2000; Dupuis et al., 1998). Using a hardware-in-the-loop simulation (HLS) technique, the STVF Manipulator Test-bed (SMT) robot emulates the dynamics of the end-effector of the SPDM; see Figure 5.23.



Figure 5.23: The SMT and the worksite force-plate.

The SMT-robot is a highly rigid six degrees-of-freedom serial robot. The robot design is a typical backhoe configuration. The base shaft, upper arm and forearm segments are made of steel. The wrist members are made of aluminium. All manipulator joints include hydraulic actuators and position, load sensors and a torque sensor. The optical joint encoders (absolute position: 23 bit, incremental position: 23.5 bit after interpolation) have been selected such that they meet the end-effector resolution requirement of 0.5 mm and 0.05 degrees at the outside edge of the workspace together with the velocity sensing requirement of 1 mm/s and 0.1 deg/s. Since all joints except for the wrist rotate use cylinders, torque sensing is provided with load cells that attach to either the

cylinder clevises or cylinder bases. Where there are two cylinders on a joint, both are instrumented with load cells. On the wrist rotate joint, a 6-axis force-moment sensor measures the rotational moment directly.

The hydraulic actuators are controlled with servo-valves and the actuation pressure is provided by a constant-pressure pump. All of the hydraulic actuators on the SMT-robot are hydraulic cylinders, except for the wrist rotate. Shoulder and elbow joints use single cylinders. The swing, wrist pitch and wrist yaw joints each use dual cylinder arrangements. For the swing and wrist pitch joints, two hydraulic cylinders are connected via a linkage to drive the joint (a chain that straddles a sprocket under high pre-tension creating significant friction effects). For the wrist rotate joint, a direct drive hydraulic motor with good stall-torque characteristics is used. The robot was designed to handle payloads up to 100 kg.

The controller of the SMT-robot including the FMA scheme has been developed over many years to achieve a stable response with high position accuracy when it is in both in unconstrained and constrained motion. Further details of the STVF facility, which was utilized for this work, can be found in (Piedbœuf, 1996; Dupuis et al., 1998; Piedbœuf et al., 1998, 2000). It is also important to note that the SMT-robot has been designed to fulfil the requirements of the hardware-in-the-loop simulation. For this concept, the knowledge of the payload geometry and the compliance of the force-plates are not necessary. Furthermore, the adaptive controller itself compensates simplifications of the robot model utilized for the model-based control.

In general, the use of the SMT-robot to identify contact parameters seems a very good choice due to its high rigidity and precise joint encoders and load/force sensors and, most notably, its FMA motion control. This control allows insertion tasks in Cartesian velocity control mode without the risk of damaging the worksite, since the maximal applied force is bounded by the FMA and is proportional to the desired velocity. Nevertheless, as it turns out, besides the advantages of this system for safe contact experiments within a very controlled environment, certain properties of the robot hardware pose limits for the contact parameter identification for highly rigid contact pairs. Identifiable hardware restrictions are:

1. “Only” 23 bit joint encoders; these correspond to a maximal identifiable stiffness in the order of 10^7 N/m (assuming a maximum force-plate force of 400 N). Measured joint encoder noise translates into $2e-6$ m position noise;
2. Force plate sensor noise translates into 1 N force noise;
3. The force plate is not fully rigid and its compliance is difficult to model, which is necessary for comparison purposes with simulation results.
4. Joint load-cell sensors have experimentally determined DC offset and proportional gain. This is not a problem for the SMT-robot controller, but the measured signal is used later on to determine the applied joint torque and is one bench mark quantity for robot simulator performance.

Furthermore, the current SMT-robot control scheme guarantees a very good relative position accuracy of 0.2 mm. However, in terms of contact dynamics this poses certainly a limit when dealing with stiffness in the order of or above 10^6 N/m. Since the absolute position accuracy is by a factor of 10 less accurate, all experiments start from an inserted configuration and the motion is then defined relative to that one.

The controller implementation includes a low-level torque control loop at the joint level. The high-level motion control is realized using an acceleration-based control-law and guarantees a set point tracking up to 2 Hz. Furthermore, the adaptive torque control scheme yields a slightly different behaviour each time due to uncertainties in the initial pose. Therefore, it cannot be expected that the robot will be able to track steps or sharp transitions as they occur at initial impact of the contact pair. Finally, random processes and disturbances, e.g., numerical noise and uncertainties in the initial pose, yield for open but especially for closed-loop systems a slightly different behaviour each time as it will be shown for this test-bed in the results subsection.

Description of simulation environment

The SMT-robot simulator infrastructure is almost identical to the hardware-in-the-loop control software used for STVF, except that the hardware components, i.e., the SMT-robot itself, the contact pair (payload) interaction, and the force plate, are modelled as well. The space robot emulation part, i.e., the SPDM simulation, is disabled since it is not necessary.

The SMT is modelled as a serial chain of rigid links connected by ideal joints and with lumped masses. The multibody model is generated using Symofros (L'Archevêque et al., 2000; Piedbœuf, 1995). To reproduce the friction effects of the joints a friction model as described in Gonthier et al. (Gonthier et al., 2002, 2004) was used. The contact pair interaction was modelled using the point contact model with local compliance.

While the high-level model-based motion control is identical to the one of the SMT-robot, the low-level torque control does not exist. Assuming the latter to be perfect in simulation, the applied torque is set identical to the desired one computed by the high-level motion controller.

Based on this modelling approach, the following simplifications can be identified:

1. Link flexibility is not included;
2. Joint flexibility is not included;
3. Actuator dynamics (hydraulic fluid, valves, pipes) is not modelled;
4. No accurate identification of joint friction characteristics; simulation model parameters for the joint damping and joint friction were based on empirical values and subsequently tuned such that a stable simulation was obtained, while matching the free-space motion characteristics;

5. Uncertainties in robot kinematics and dynamics parameter identification; the kinematics and inertia parameters of the robot are initially derived from CAD drawings and then adjusted using kinematic and dynamic identification;
6. Force plate compliance is not modelled;
7. Joint load cells are not modelled; applied joint torque of SMT-robot is determined based on axial load sensors, then converted into the corresponding joint torque, if the load-cell offsets and gains are not accurately determined the nonlinear conversion function leads to non-constant torque difference.

The use of rigid body models for the robot, the contact pair and the force plate makes it necessary to lump all compliance into the local compliance of the contact model. This fact indicates that the contact model with its parameter set represents not only the physics of the local contact phenomena but is bound to comprise the compliance and dynamics of the overall structure of the test-bed. Therefore, the identified contact model and its parameters are inherently related to the facility used to identify them. Furthermore, the model is used (abused) to represent something it is not made for. Since the payload can be regarded as a compliance element (spring) connected in series to the test-bed compliance, this effect becomes significantly important if the stiffness of the payload is close to the one of the test-bed. As a result, the model cannot be expected to represent the transition phases (no-contact to contact) with a high fidelity due to this lumped-compliance approach.

Furthermore, it is important to note that the end-effector position of the robot, and therefore the payload position, is based on the joint encoder reading and the rigid-body forward kinematics. Hence, even if the robot end-effector does not move, since it is in rigid contact with a surface, the computed end-effector position will indicate a motion as a function of the link and joint flexibility. However, it was experimentally verified that this approach still leads to more accurate results than the available external camera system, i.e., OptoTrack made by Northern Digital Inc.² with calibration software made by Krypton³.

Experiments, simulation and results

In this section, the experiments and simulations with gradually increasing complexity are described. They were carried out to eventually accomplish a representative simulation of a contact task. To this end, free motion experiments, studies of the static stiffness of the test-bed and the payloads, single-point normal as well as single-point normal and tangential contact experiments were conducted before complex spatial contact scenarios were investigated. For each step, the objective, the approach taken as well as the results are presented below.

²www.northerndigital.ca

³www.krypton.be

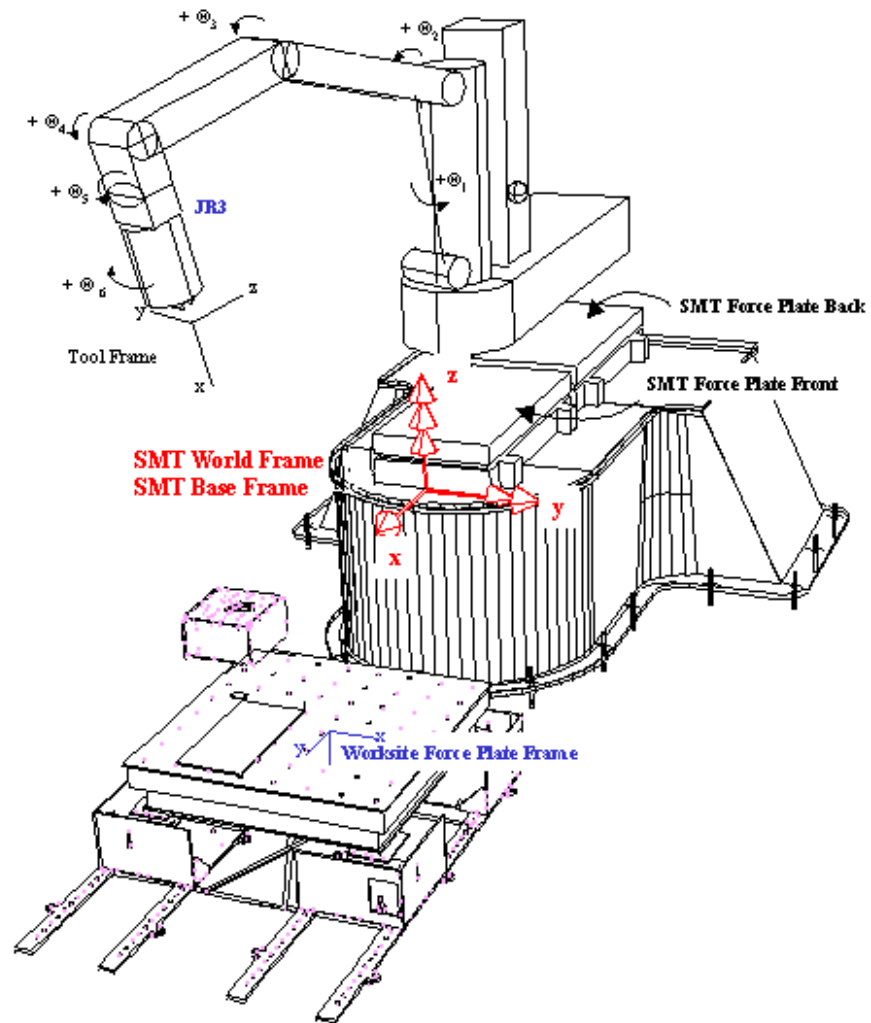


Figure 5.24: SMT-robot: frame definitions.

A. Unconstrained motion in joint position control mode

Objective: For the envisioned parameter estimation approach an identical — or more realistically, a similar — kinematics and dynamics response of the SMT-robot and the SMT-robot simulator is crucial. Therefore, this task is defined in order to verify the kinematics and dynamics response of the SMT-robot simulator in free motion. Benchmark criteria are: (a) primarily, agreement of motion (position, velocity) of the end-effector and (b) secondarily, agreement of the joint torques of the simulation versus the experimental data.

Approach: In order to obtain experimental results, the SMT-robot is driven along a pre-defined joint-position trajectory, whereby each joint position is commanded to move starting from the initial orientation by 10 degrees and then back to the initial configuration. Beginning with the first joint, each joint was rotated sequentially.

The same trajectory is then used to drive the SMT-robot simulator. Even though the SMT-robot simulator (including its controller) contains approximately 200 parameters, “only” an adjustment of the $6 \times 6 = 36$ joint friction parameters was considered to get a good match between the motion and torque signals of the SMT-robot and its simulator. The reason for this is the fact that all other model parameters are also used by the model-based controller of the SMT-robot itself, while the joint friction parameter are not. Hence, the controller related parameters were kept unchanged in order to not deteriorate the behaviour of the robot optimized for hardware-in-the-loop operations. However, one has to note that this set of controller related parameters is not necessarily the best possible choice in terms of model equivalence between SMT-robot and its simulator.

Results: The chosen joint friction parameters result into a SMT-robot simulator response very close to the one of the SMT-robot. The robot joints are labelled from base to tip as follows: swing (SW), shoulder (SH), elbow (EL), pitch (PI), yaw (YA) and roll (RO).

The time history of the joint positions and velocities, and the joint torques of the experiment and the simulation are shown in Figure 5.25 – 5.28, where *fb*, *sim* and *sp* indicate the feedback from the SMT-robot, the SMT-robot simulator and the controller set-point signals, respectively. From Figure 5.25 – 5.26 it is clearly apparent that both systems, i.e., the SMT-robot and the SMT-robot simulator, behave very similar in terms of motion signals. However, Figure 5.27 and Figure 5.28 (same signal but with adjusted DC offset) show that to generate with the robot-simulator the same motion pattern as with the SMT-robot slightly different joint torques have to be applied. The simplifications of the robot simulator mentioned previously and imperfections in the joint-friction model are responsible for this discrepancy. It should also be noted that the last joint (number 6) is particularly difficult to control in general and, hence, also to model due to its very small inertia, especially if no payload is attached.

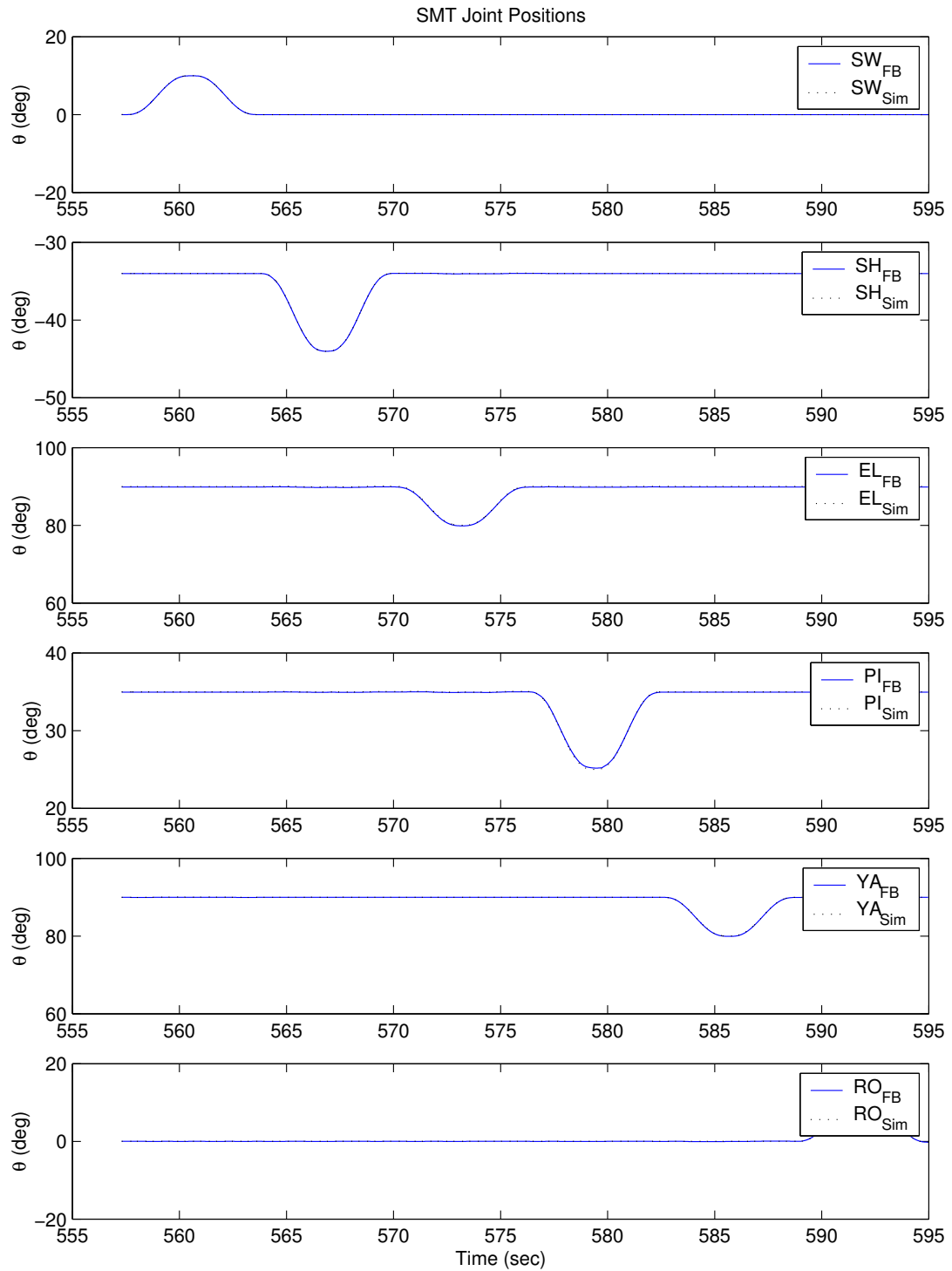


Figure 5.25: SMT joint positions (unconstrained motion).

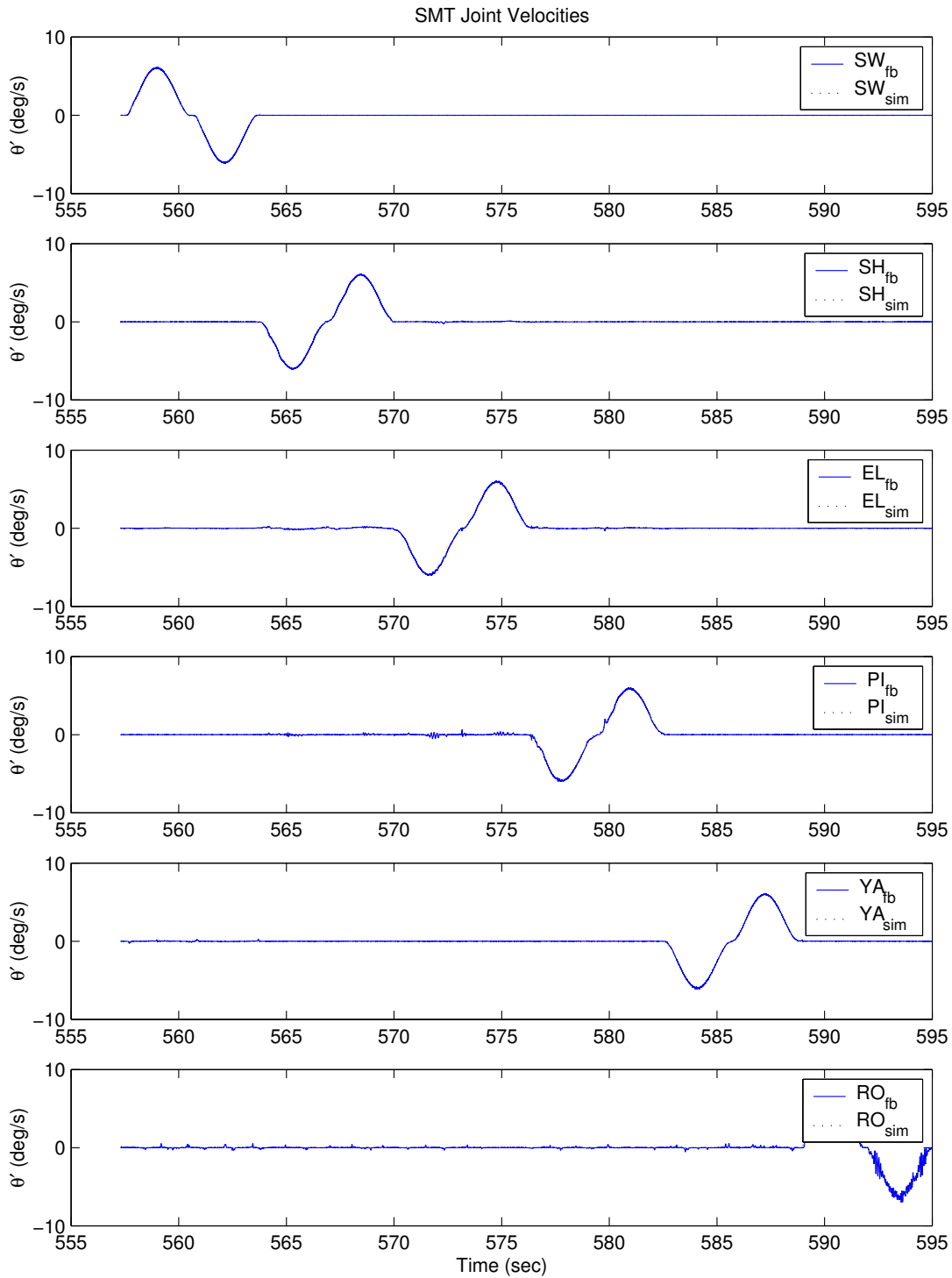


Figure 5.26: SMT joint velocities (unconstrained motion).

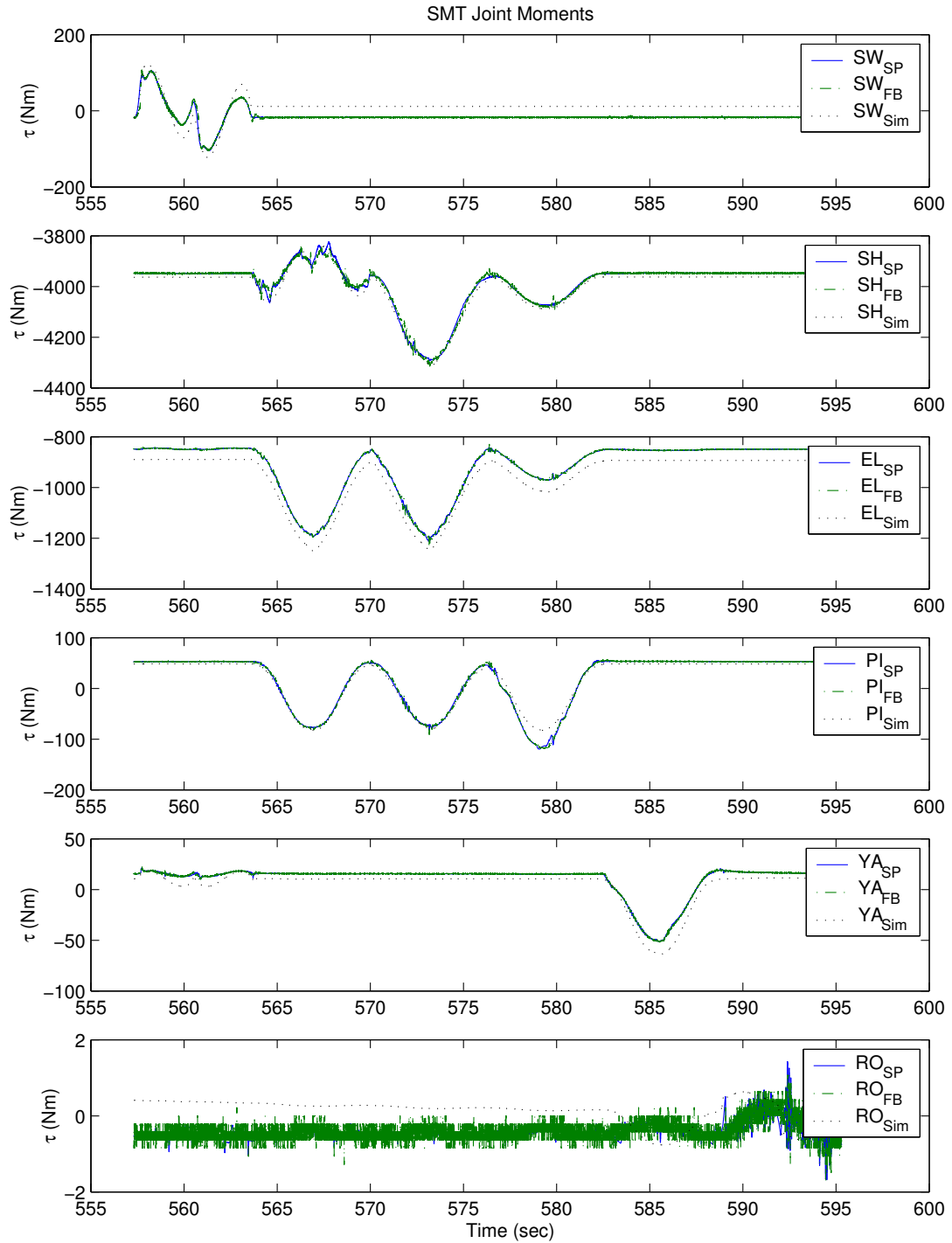


Figure 5.27: SMT joint moments (unconstrained motion).

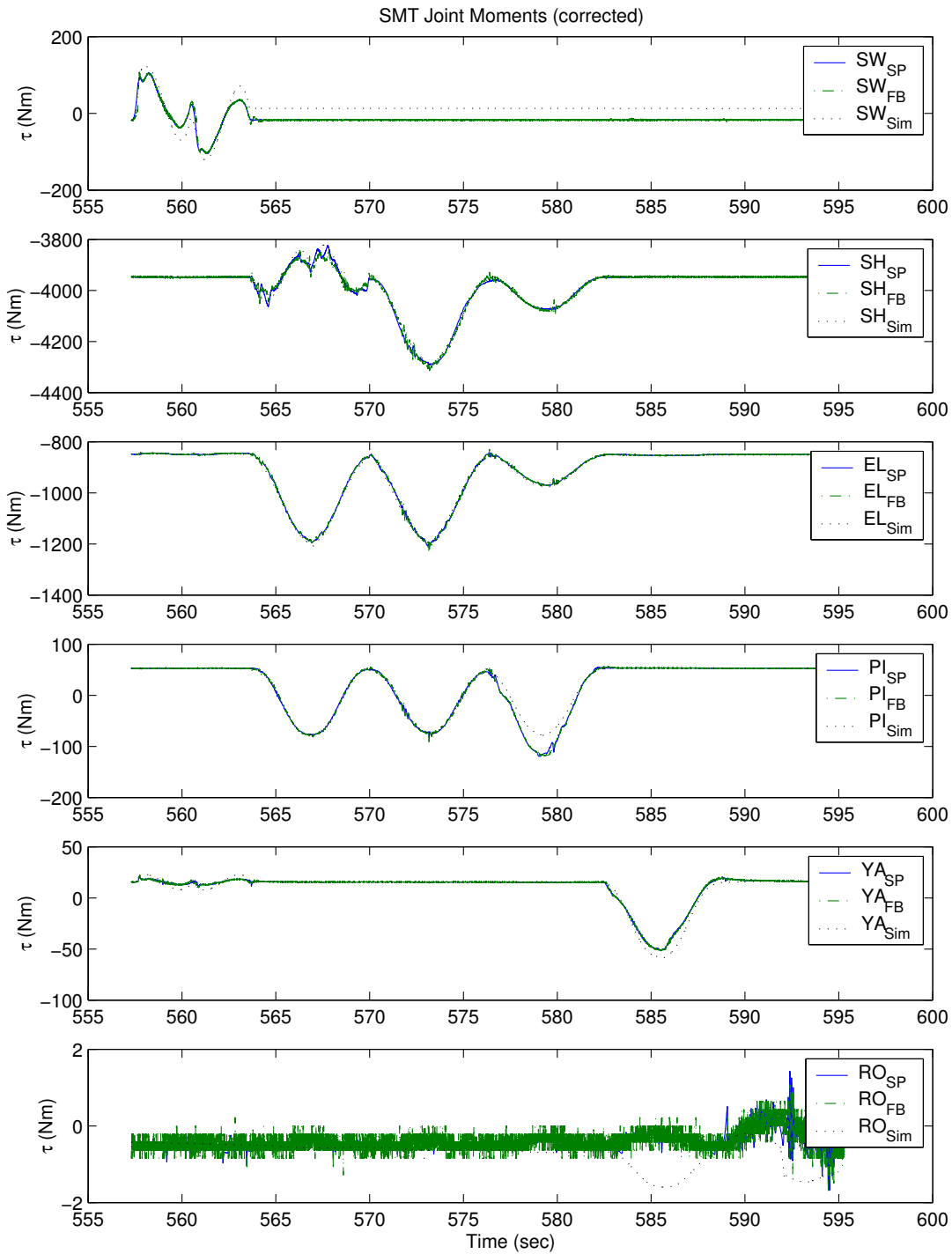


Figure 5.28: SMT joint moments (corrected) (unconstrained motion).

B. Single-point contact with only normal commanded motion

Objectives: The objective of this (and the next) task is to get more knowledge about the SMT-robot simulator with its contact model and its sensitivity to a change in contact model parameters. To make this as easy as possible the single-point contact with only normal commanded motion is investigated in a first step.

Approach: To obtain the experimental data, the SMT-robot was driven along a pre-defined Cartesian velocity trajectory under FMA control. The SMT-robot was put into a configuration such that the half-sphere was placed directly above the aluminium plate. Then it was repeatedly moved down with a velocity of $v_z = -2$ mm/s and up with $v_z = 1$ mm/s. On the simulation side, two different approaches were taken:

1. A kinematics simulation, i.e., the motion signals were directly fed into the contact model without any robot in the loop;
2. The pre-defined trajectory was run with the SMT-robot simulator;

Results: In case (1) it was possible to adjust the stiffness parameters of the nonlinear force model to get a match of the normal contact forces (z -direction). Although the commanded motion was only in the normal direction, tangential forces appear. This is caused by the fact that the performed motion is not perfectly normal and also that the robot end-effector and the force-plate orientation is not perfectly known in order to compensate for the tilting. After adjusting the z -position of the force-plate (and therewith the position of the fixed contact body) based on the contact period a stiffness value of $k = 2.5413 \cdot 10^8$ N/m^{3/2} was identified. Here one has to keep in mind that this number does not correspond to the physical value of the half-sphere but of the overall stiffness of the test-bed with the half-sphere.

Using these values case (2) was simulated, whereby the damping parameters were adjusted to get similar results compared to the experiment and a numerically stable simulation. Because of the complexity of the Simulink diagram implementing the simulation model of the SMT (recall that the same diagram is used to generate the control software for the real SMT), the simple ode1 solver (Euler) was used with a fixed-step size of 1 ms. A value of $e_{\text{eff}} = 0.85$ gives the best match between simulation and experiment. The resulting motion, torque and force-plate signals are given in Figure 5.29 – 5.30. Motion signals are given in the “SMT world frame” and forces are given in the “Worksite Force Plate Frame” (Figure 5.24). A very good match can be observed, even for the small contact forces in the contact plane, i.e., F_x and F_y and the moments. However, it is not possible to simulate the transition phase exactly. The actuator dynamics have a significant effect on the contact force during the impact phase but they have not been included in the simulation model of the SMT.

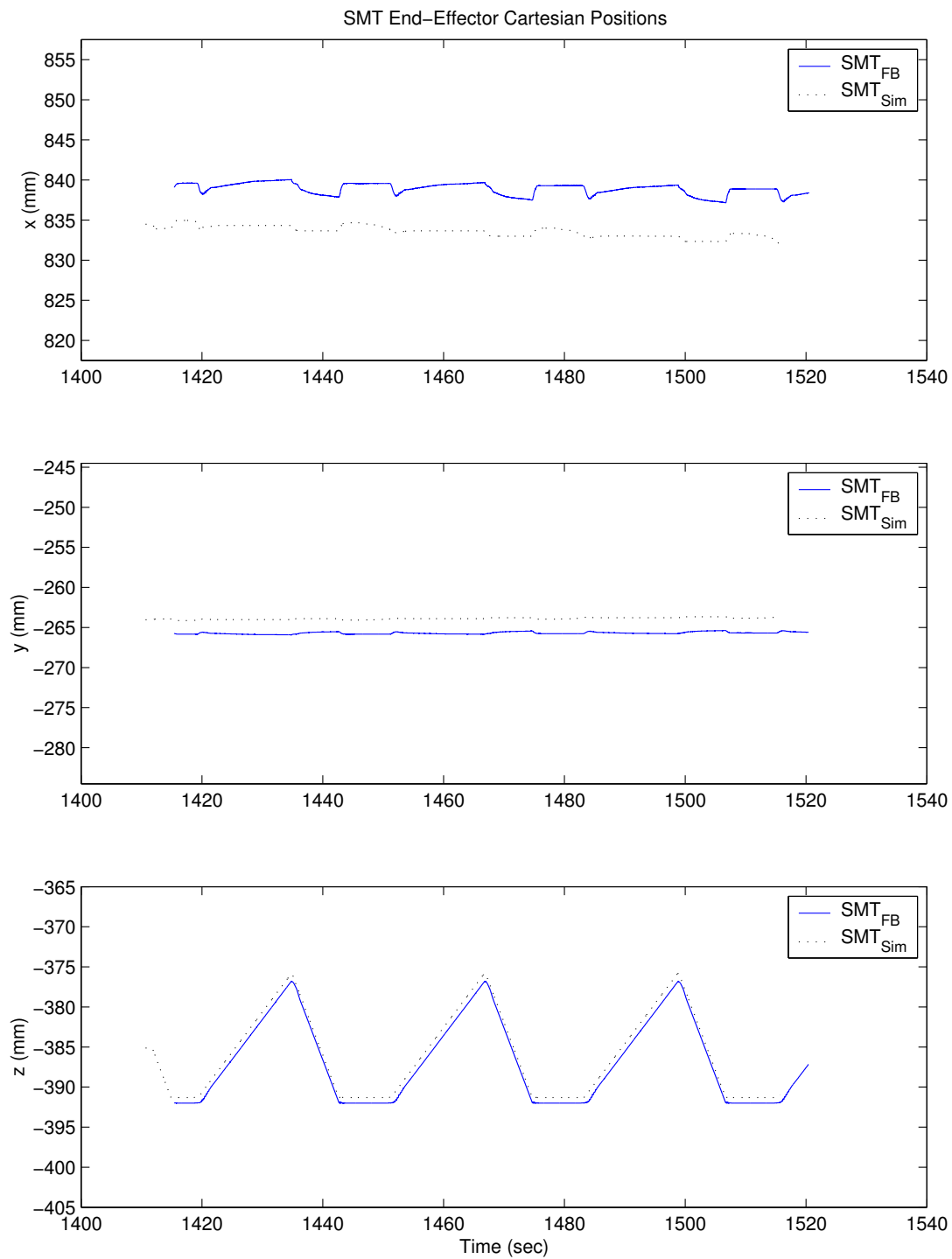


Figure 5.29: Cartesian position of SMT end-effector (normal motion only).

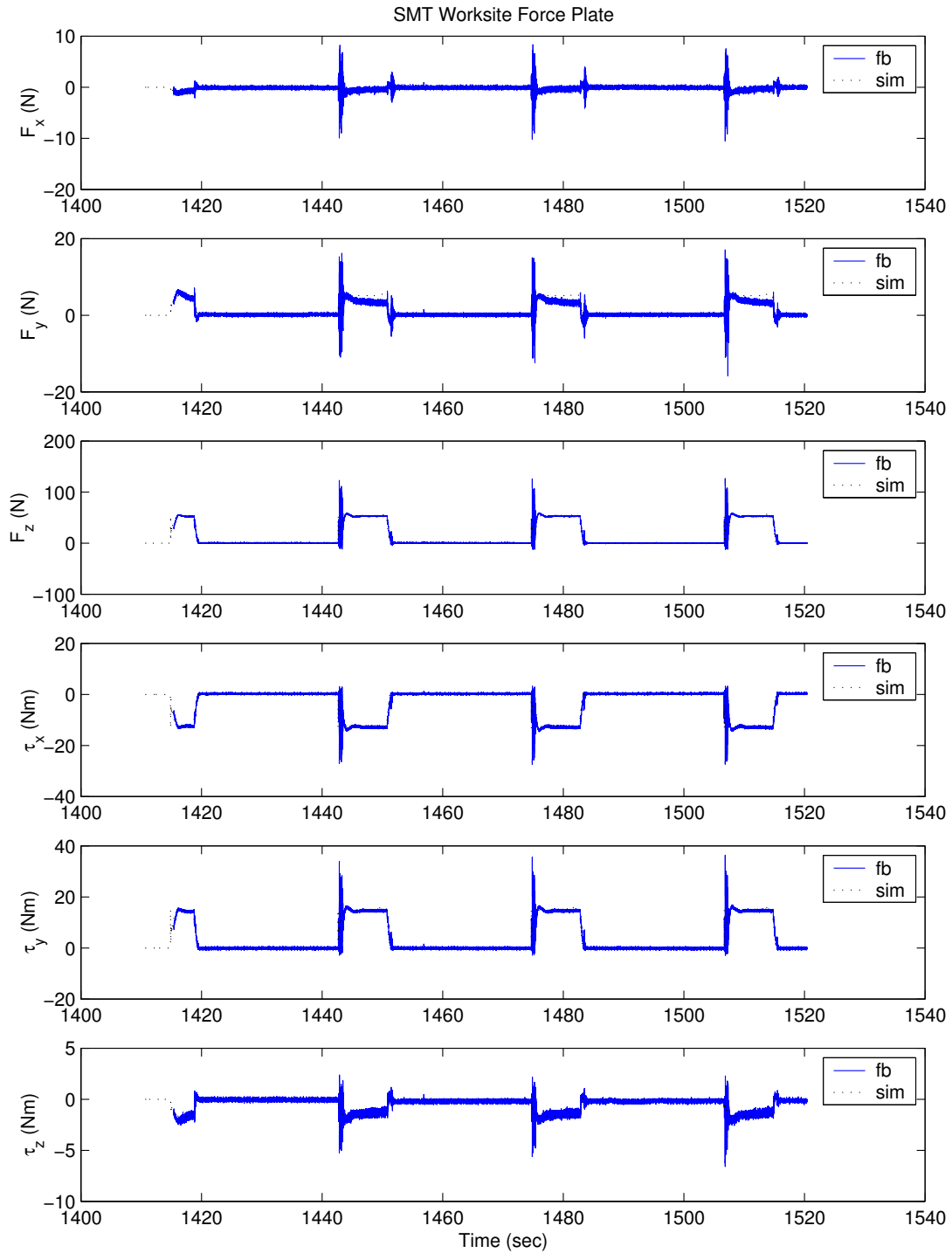


Figure 5.30: Worksite force-plate measurements (normal motion only).

C. Single-point contact with normal and tangential commanded motion

Objective: This task is defined in order to identify the static and kinetic friction coefficient to be used in the friction model for the half-sphere–plane contact.

Approach: For this task a similar approach was taken as for experiment *B* but this time two horizontal motion components (*y* and *x* direction) were additionally commanded. On the simulation side, an approach similar to experiment *B*(1) was tried, but failed since it turned out to be too complicated to find the proper orientation matrix for the force-plate with respect to the robot. In particular, it was found that this matrix as well as the force-plate position were time dependent. Hence, simulations similar to experiment *B*(2) were carried out. This approach (Cartesian velocity controlled motion with FMA) is a lot less stringent in terms of payload and worksite geometric uncertainties due to its compensating effects. The controller always tries to keep the reaction force constant and not the end-effector position. Regarding the FMA functionality, the critical matching criterion becomes slope of the contact force at impact rather than the contact force at steady state, since the later is controlled by the FMA. A steep slope corresponds to a large stiffness and a gentle slope to a small stiffness. The maximal force amplitude is always given by a FMA gain relating the desired velocity and the maximal force, i.e., in this case approximately 10 N per 1 mm/s, plus a 10 N dead-band.

Results: Figure 5.31–5.32 show the results of the single-point contact with normal and tangential commanded motion. Note that because it was not possible to determine the force-plate position and orientation with high accuracy, the time at which the contact phase starts and ends in the simulation cannot be synchronized with the experimental data for a single surface height/normal selection. Instead, the surface height was tuned so that the results are synchronized at the time contact is lost, for a given (assumed) surface normal direction.

Similar to the results obtained for the previously, a good match between simulated and experimental results can be observed for the motion signal. Values for μ_S and μ_C of 0.16 and 0.1 was found to give the best match. The other friction model parameters have little influence on the macro-level dynamics of the system, and were selected using the heuristic rules provided in Section 3.3.2.

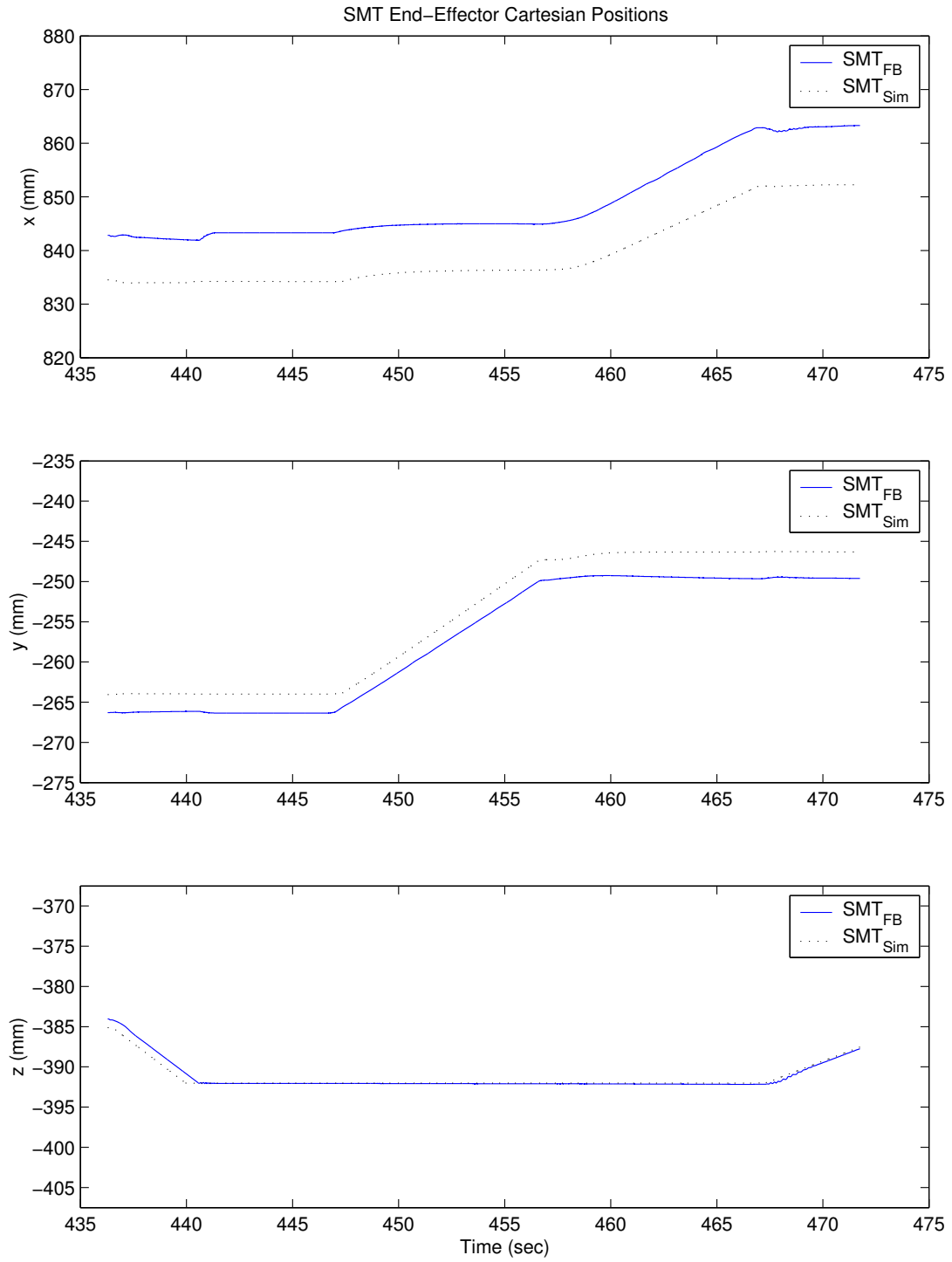


Figure 5.31: Cartesian position of SMT end-effector (normal and tangential motion).

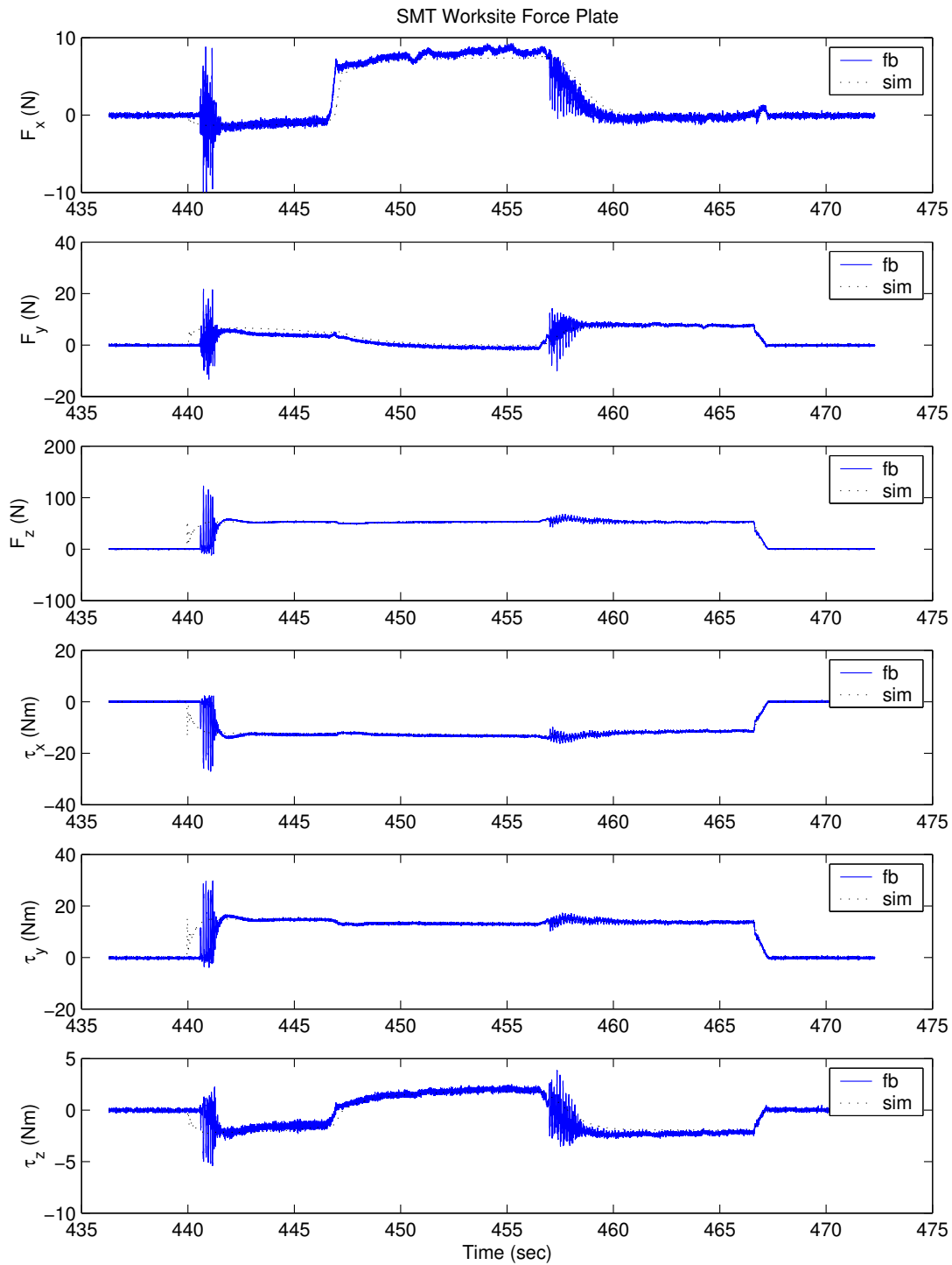


Figure 5.32: Worksite force-plate measurements (normal and tangential motion).

5.2 Volumetric Contact Model

The simulations presented in the previous section are considered again, but this time using the volumetric contact model presented in Chapter 4. The generality of the new contact model will first be illustrated using simple geometries and then with more complex ones. The implementation of the contact normal determination algorithm requires that the numerical parameters θ_ϵ , r_n and n_i be specified. The values of 1 deg, 0.95 and 15 for θ_ϵ , r_n and n_i respectively, were used for all the results presented in this section. These settings result in a very robust contact normal estimation and never required tweaking.

5.2.1 Simple Geometry Contacts

This subsection presents numerical results for simulation scenarios involving objects with fairly simple geometries. The selected scenarios are such that the contact forces and moments acting on the colliding bodies can be modelled using only one volumetric contact model. In other words, only a single contact plate needs to be inserted between the colliding objects to obtain an accurate representation of the contact interaction.

A Ball Falling in a Cylinder

The same simulation as in Section 5.1.3 for a ball bouncing inside a cylinder was implemented, but here the contributions from the normal force, rolling resistance torque, tangential friction force, and spinning friction torque sub-models were all included; see Equations (4.62), (4.67), (4.75) and (4.82). All the contact model parameters are the same except that the numerical value of the stiffness was increased by a factor of five to $k_v = 5 \cdot 10^6 \text{ N/m}^3$ to reduce the amount of rolling resistance torque. This torque increases with the size of the area of contact, and thus increases when the materials are less stiff. The numerical relaxation time constant τ_r was set to 1. A voxel size of 0.001 m was used. The fixed-step ode5 solver was used with a time-step size of 1 ms. This fixed-step solver was preferred over the variable-step solvers used previously in this chapter because reasonably accurate results could be obtained more quickly. A more detailed discussion that includes a comparison of the performance of fixed-step and variable-step solvers is presented later in this section.

An interesting feature of this simulation scenario is that the contact occurs between a convex shape—the ball—and a concave shape—the inside surface of the cylinder. In general, a single contact model should not be sufficient to accurately simulate the ball-cylinder interaction; see the discussion on modelling concave shapes in Section 4.1.2. However, the difference in radius is large—1 m vs. 0.1 m, and the cylinder surface “appears” almost flat in relation to the size of the ball; see Figure 5.33. As a result, using a single contact model is sufficient here, since the shape of the cylinder does not “wrap around” the ball sufficiently to cause significant interaction between the

normal and tangential forces. In other words, the flat-contact-surface assumption of the contact model can be transgressed up to a certain point, thereby allowing more modelling possibilities.

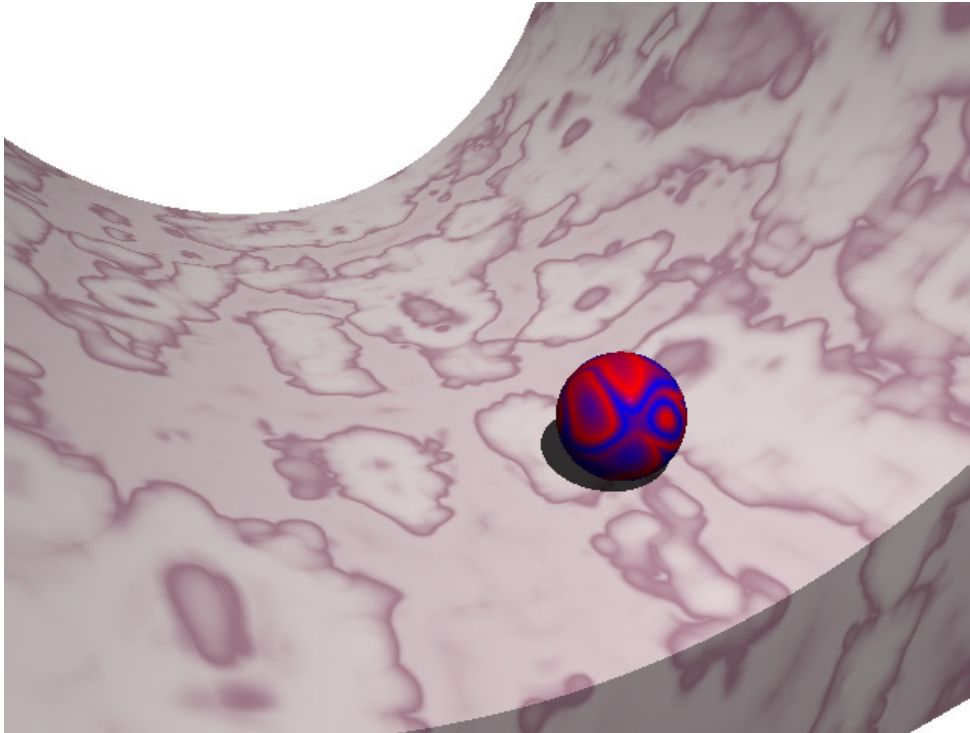


Figure 5.33: LLG model of the ball rolling in the cylinder.

This scenario also demonstrates a neat feature of the LLG technology: its natural capability to handle concave shapes indiscriminately from convex ones. Most contact dynamics modelling systems require concave shapes to be split up into convex ones. There are software packages available today that can automatically split a concave geometry into convex hulls. However, because it is based on projective primitives, the LLG technology does not need to distinguish between concave and convex. It only processes cells, which correspond to an intersection of projective primitives or simply a single projective primitive. The latter can be concave or convex. For example, a cylinder corresponds to the intersection of an infinite cylinder primitive with a biplane primitive. On the other hand, the cube-with-cylindrical-groove geometry shown in Figure 5.33 corresponds to the intersection of a box and the *dual* of a cylinder, i.e., a cylindrical hole in an infinite volume-space. The box is itself the intersection of three biplanes. The resulting geometry is still a single-cell shape, but is concave.

The results from the simulation are given in Figures 5.34 and 5.35. Note that no additional parameters were required to set up this simulation. In other words, the rolling resistance and spinning friction torque parameters are directly inferred from the parameters of the translational friction model, the normal damping coefficients and from the geometry of the colliding bodies. The results show the decays in both of the angular and translational velocities over time. Observe that the ball

eventually stops moving in the Y direction. Clearly, the rolling resistance and spinning friction torques act to prevent rotational motion, as expected. When, compared to the results obtained in Section 5.1.3 using the point contact model, it is clear that the torques produced by the volumetric contact model have a significant impact on the simulation results. These torques are not present in the point contact model and the ball never stopped rolling. Figure 5.36 shows the total system energy decaying over time, while the plot for the point contact model (Figure 5.13) shows the energy to be constant once the motion reach the pure rolling stage.

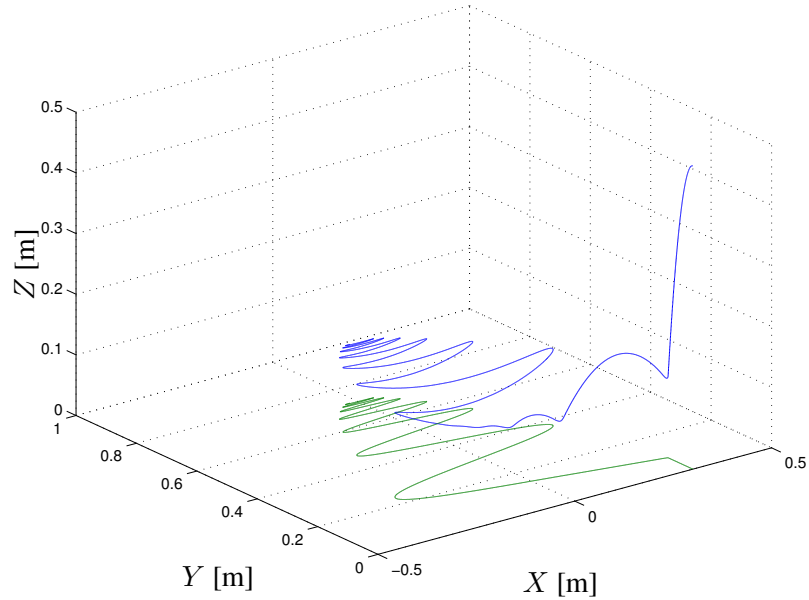


Figure 5.34: Trajectory of the ball impacting a cylinder (volumetric).

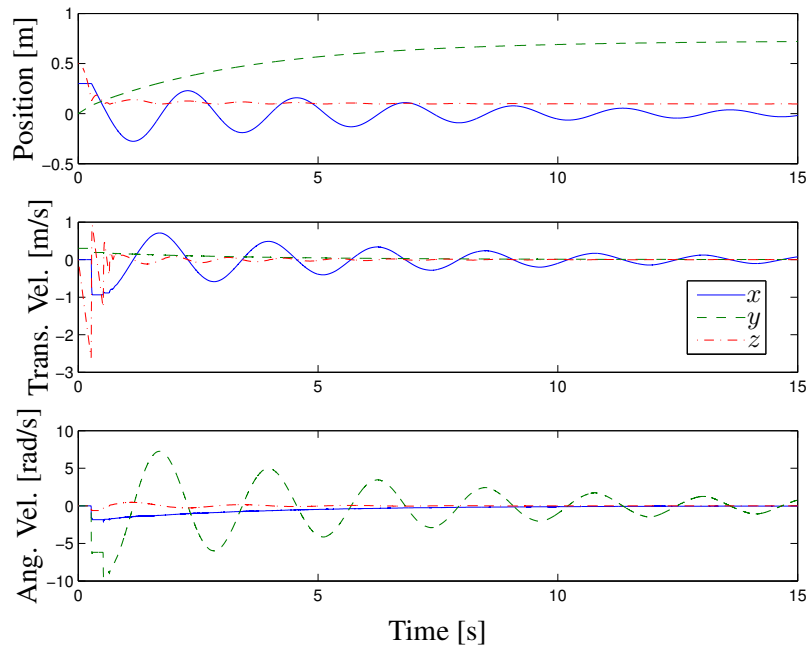


Figure 5.35: Ball impacting a cylinder: position and velocity components vs. time (volumetric).

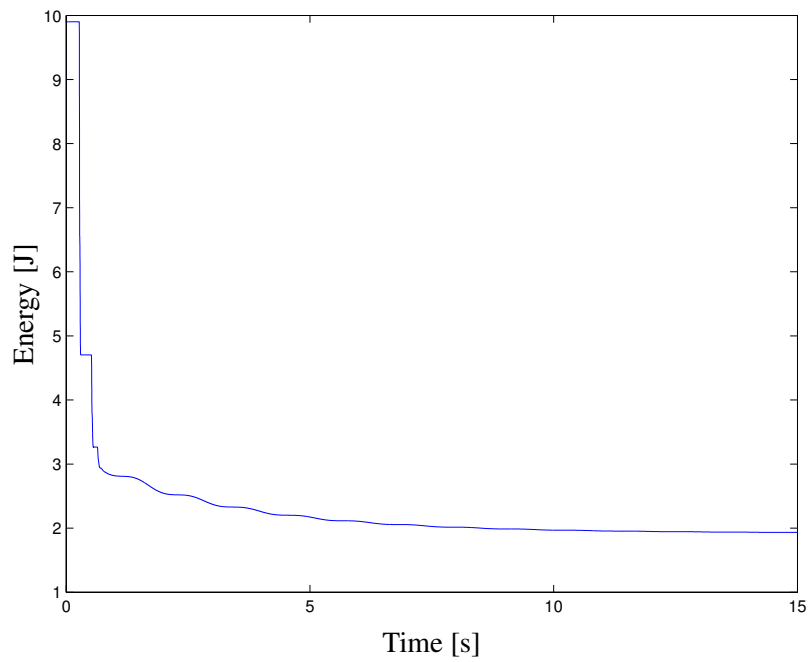


Figure 5.36: Ball impacting a cylinder: total system energy (volumetric).

A Ball Falling on a Table

The simulation of the 2 kg spinning ball bouncing on and rolling off a flat table is then considered. In particular, the contact interaction as the ball rolls off the edge of the table is analyzed; see Fig. 5.37. The ball is dropped from a height of 0.2 m in Z and is initially moving at 0.3 m/s in Y . It is also spinning at 3 rad/s around Z . Gravity acts in the $-Z$ direction and has a magnitude of 9.81 m/s^2 . The parameters for the normal contact model and friction model are given in Table 5.5 and Table 5.6, respectively. The numerical tolerance on velocity was set to $v_\epsilon = v_S/100 = 10^{-5} \text{ m/s}$.

The simulation is implemented in Simulink using the ode3 solver with a fixed step size of $5 \cdot 10^{-5} \text{ s}$. This step size is very small and was selected to obtain accurate results. A more detailed discussion investigating the performance of fixed-step and variable-step solvers using this simulation scenario is given in the next section. A smaller voxel size of $2 \cdot 10^{-4} \text{ m}$ was used to minimize the numerical noise associated with the voxel-discretization process used by the LLG geometric function to obtain the metrics of the volume of interference.

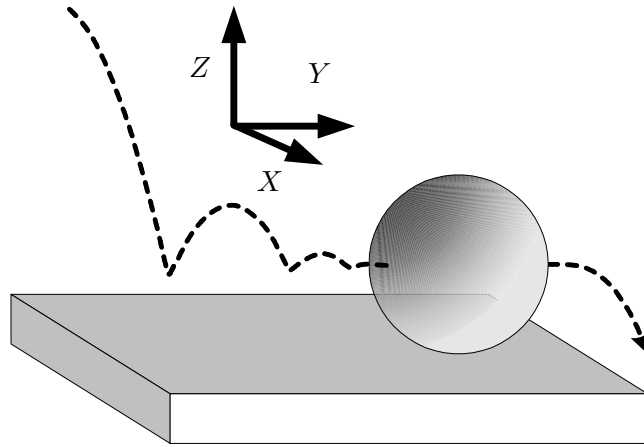


Figure 5.37: Trajectory of the ball impacting a table.

k_v	e_{eff}	v_{small}	τ_r
10^7 N/m^3	0.5	0.001 m/s	1 s

Table 5.5: Normal contact model parameter values for the ball impacting a table simulation.

μ_S	μ_C	σ_0	σ_1	σ_2	v_S	τ_{dw}
0.08	0.05	10^5 N/m	$\sqrt{10^5} \text{ Ns/m}$	0 Ns/m	0.001 m/s	0.3 s

Table 5.6: Friction model parameter values for the ball impacting a table simulation.

The time histories of the ball centre point velocities are given in Figure 5.38. The Z -velocity plot shows the ball bouncing two times, then settling into a rolling motion around 0.4 s and finally rolling off the table at 4 s. When in contact, the ball is observed to undergo a pure rolling motion. For example, during the first bounce, the X -angular velocity goes to from zero to -2 rad/s, while the Y -velocity changes from 0.3 m/s to 0.2 m/s. It is seen that the no-slip condition is enforced by the tangential friction such that $|v| = R|\omega|$, where v is the translational velocity and ω the angular velocity. There is no motion in the X -direction, and therefore the Y -angular velocity remains zero.

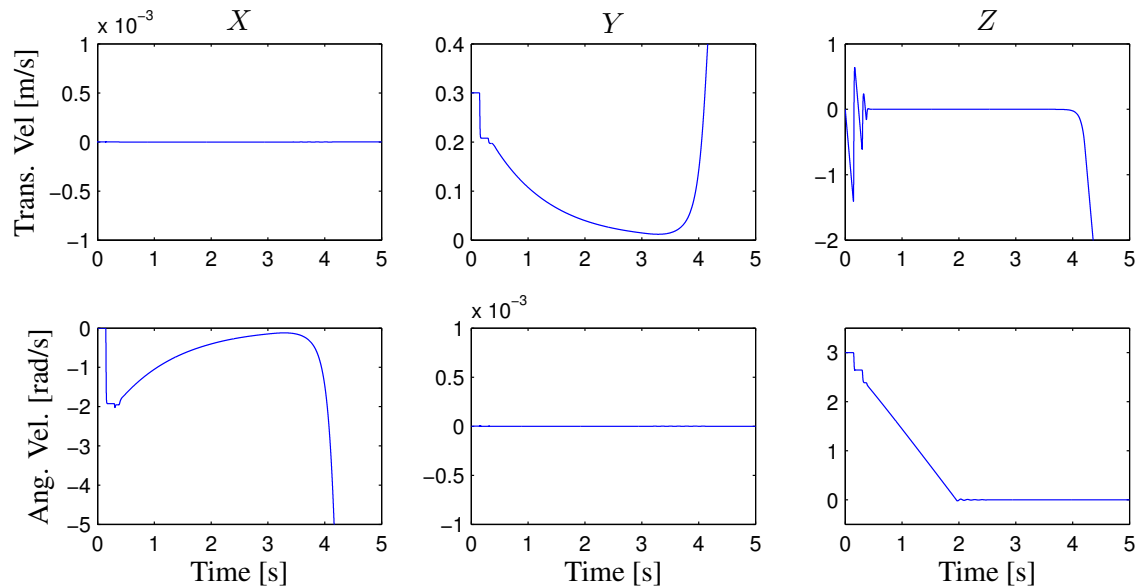


Figure 5.38: Ball impacting a table: ball centre motion.

The Z -angular velocity shows the effect of the spinning friction torque, as it reduces the angular velocity on each bounce, and then reduces it even further during the pure rolling motion until the ball stops spinning at 1.9 s. The spinning velocity decreases linearly under the influence of a constant spinning torque; see Equation (4.208). The contact model rolling resistance torque acts to reduce the $-X$ -angular velocity before the ball starts reaching the edge of the table at 3.5 s. During this phase, the rolling angular velocity decreases exponentially, indicating a first order ODE decay as is expected since the rolling resistance torque is in fact a damping torque; see Equation (4.67). Since the ball is in pure rolling during this part of the simulation, the Y -translational velocity also features the exponential decay behaviour. Then, as the ball rolls over the edge, the $-X$ -angular velocity increases significantly.

Figures 5.39 and 5.40 show the resulting forces and moments acting at the ball centre. The force f_x in the X -direction and moment τ_y in the Y -direction are not shown because they are zero. The f_z force history in the Z -direction clearly show the three impacts when the ball hits the table surface, then the force becomes constant as the ball rolls along the table. When the ball reaches

the edge of the table, the force “turns down” to zero as the ball rolls over the edge. The f_y force history in the Y -direction shows two negative “spikes” when the ball bounces initially. These force impulses get the ball rotating about the X -axis. As the ball settles into the rolling motion f_y is almost zero. It has a small non-zero value caused by the rolling resistance torque. When the ball rolls over the edge, f_y becomes positive as it pushes the ball away from the table edge.

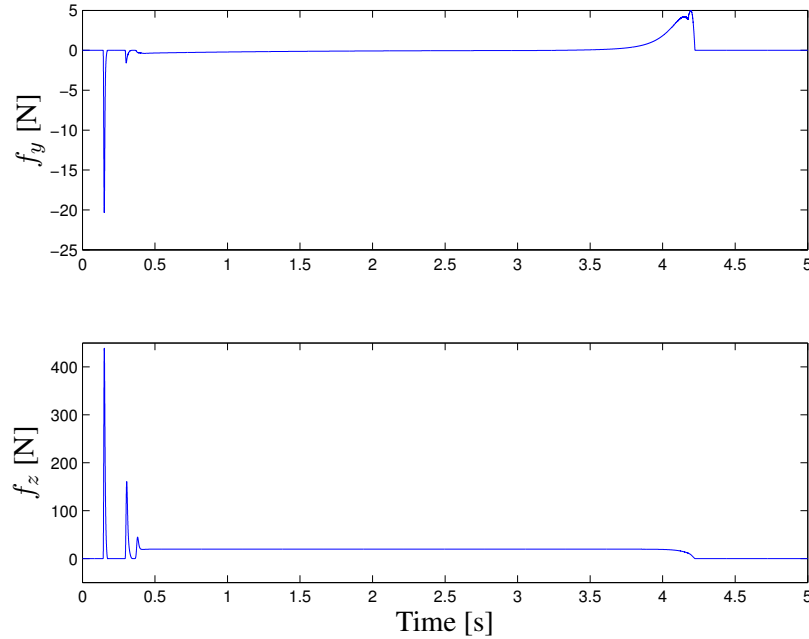


Figure 5.39: Ball impacting a table: forces acting at the ball centre.

The τ_x moment history in the X -direction show two moment spikes corresponding to the f_y spikes, and which initiate the rolling motion of the ball. τ_x then has a small positive value acting to slow down the rotational motion of the ball, i.e., the rolling resistance torque. A negative x -moment is applied as the ball rolls over the edge. The Z -moment τ_z acts to reduce the Z -angular velocity upon the impacts, and then with a constant negative torque value once the ball settles in the rolling motion. Once it stops spinning about the z -axis at 2 s, τ_z goes to zero. The oscillations visible thereafter illustrate the effect of the bristle dynamics of the friction model.

The time history of the angle θ_y of the contact normal as defined by Equation (4.199) with respect to the Y -axis is given in Figure 5.41. It is observed that the contact normal smoothly transitions from a vertical direction and tilts toward the $+Y$ axis as the ball rolls over the edge. A small numerical glitch can be seen at the end of the contact phase at around 4.3 s. Since the contact volume is extremely small at that point in time, i.e., the ball is about to lift off the surface, the geometric estimate algorithm is less accurate.

Figure 5.42 shows the time history of the dwell-stick state s_{dw} . The ball appears to undergo pure rolling motion as soon as it lands after the second bounce at 0.4 s but it is still spinning about the Z -axis until 2 s. The dwell state s_{dw} only starts increasing after 1.8 s, when the spinning

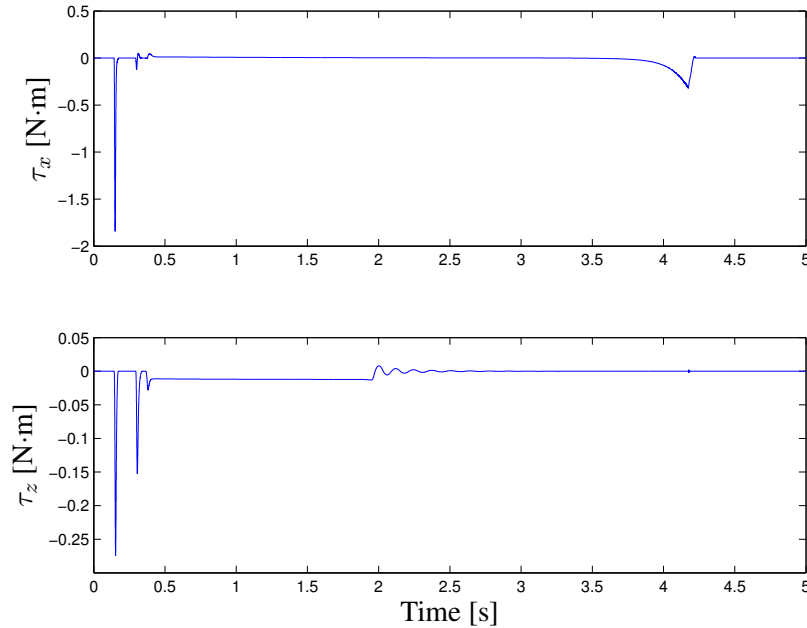


Figure 5.40: Ball impacting a table: moments acting at the ball centre.

angular velocity is almost zero. Here, the contribution of the angular velocity of the ball in v_{avg} keeps the average velocity value above that of the Stribeck velocity v_S even though the relative translational velocity is zero due to the pure rolling motion. Then, once the relative velocity is small both in translation and rotation, the dwell-stick state increases gradually up to 1, the “stick” mode. The rise of s_{dw} is driven by the time constant τ_{dw} of 0.3 s. As the ball rolls off the edge of the table, it starts slipping at 4.3 s and the dwell-stick state immediately comes back to zero.

The total energy of the system is shown in Figure 5.43. The energy is dissipating quickly during the impact phases due to the normal damping term. After 0.4 s the energy loss comes from the rolling resistance torque. The total energy of the system remains constant after the ball falls.

Numerical Solver Performance

Simulink offers two categories of solvers to compute simulations results: fixed-step and variable-step solvers. The ode15s, ode23s, ode23t, and ode23tb variable-step solvers are designed to handle numerically stiff problems and must rely on a numerically generated Jacobian matrix to obtain the solution at each time-step; the state-space formulation imposed by Simulink precludes obtaining the Jacobian matrix symbolically.

The advantage of using variable-step solvers is that in theory, these solvers allow the accuracy of the solution to be controlled via the error tolerances setting. Therefore, in this discussion, it will be assumed that the most accurate result is obtained using a variable-step solver with the most stringent specification for the error tolerances, and when the increase in numerical precision requirement produces no significant change in the dynamic behaviour. It is expected that a variable-

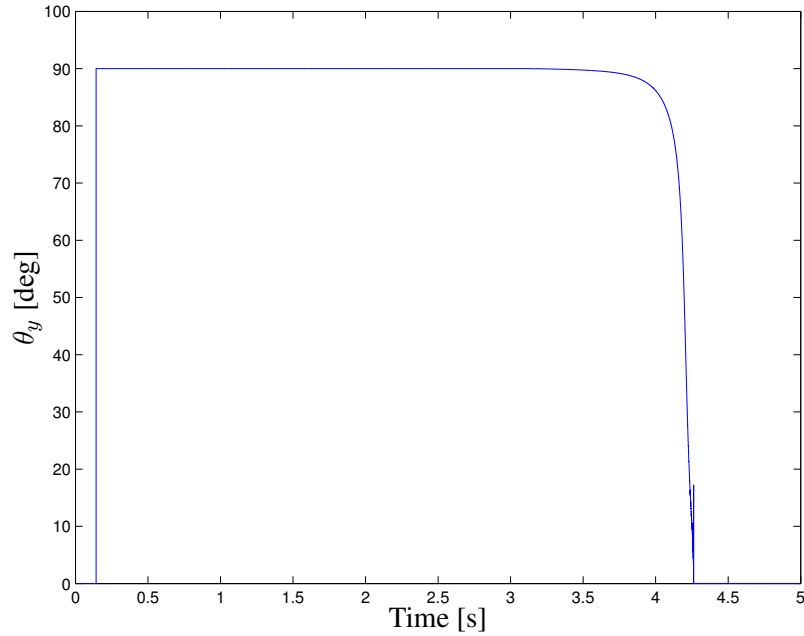


Figure 5.41: Ball impacting a table: contact normal angle relative to the Y -axis.

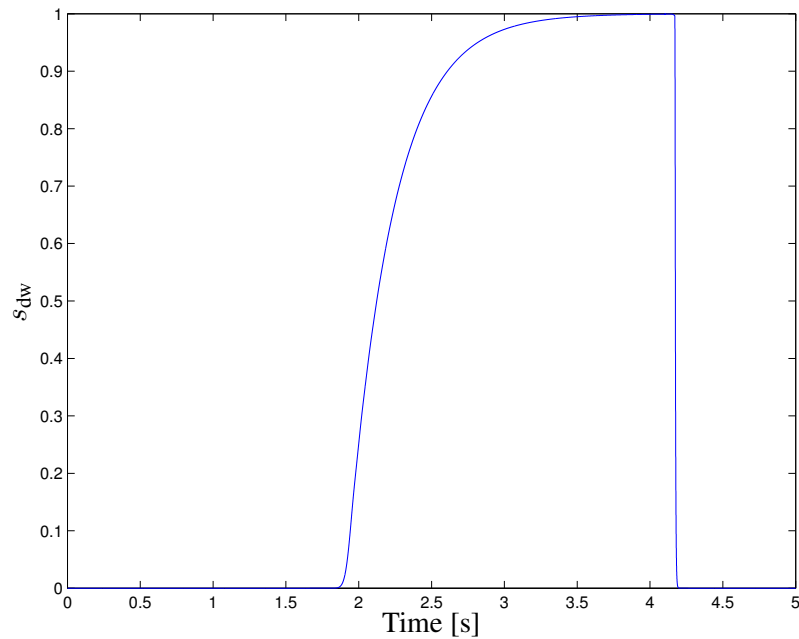


Figure 5.42: Ball impacting a table: dwell state s_{dw} of the friction model.

step solver with high error tolerances will yield the same results as a fixed-step solver with a very small time-step.

For the results previously presented in this chapter, the relative and absolute error tolerances were set very strictly, i.e., 10^{-6} , to ensure the provided results are accurate. Relaxing these error

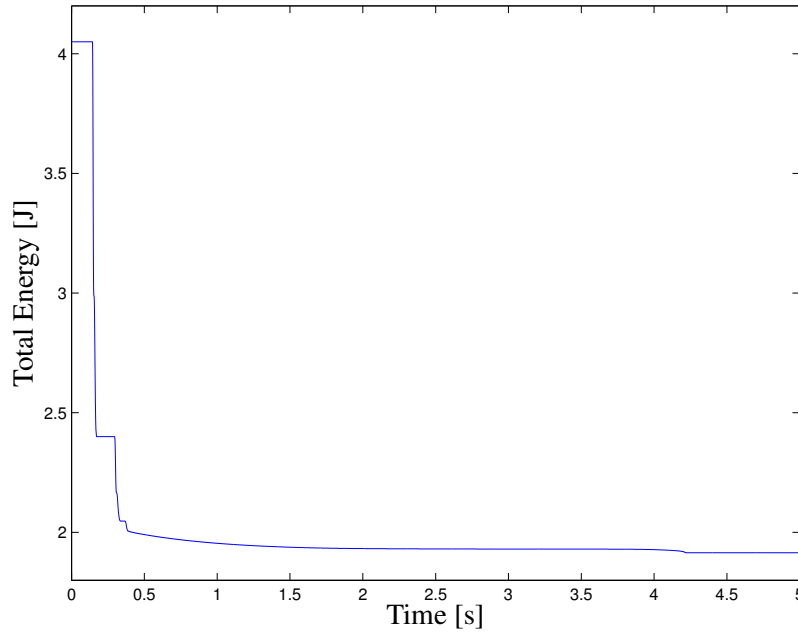


Figure 5.43: Ball impacting a table: total system energy.

tolerances allow the solvers to take larger time-steps, thereby reducing the total time required to run the simulation. There results a trade-off between the simulation run-time and its accuracy. On the other hand, fixed-step solvers only allow the size of the time step to be selected and offer no other way to control the simulation accuracy. Consequently, a very small time-step size must be selected to obtain very accurate results, as was done for the ball-table simulation in the previous section. Hence, a priori, the variable-step solvers appear to be more effective to obtain fast and accurate results, since it takes small time-steps only when needed. However, in practise it was found that the fixed-step solvers are more reliable in obtaining an accurate simulation with a reasonable run-time. This indicates an apparent weakness of the Simulink variable-step solvers to tackle this kind of system dynamics.

The simulation of the ball falling on the table presented in the previous section is considered again, but this time using different solvers and solver settings. When the simulation was set up, various solver settings were tried. In all cases, the generated results were very similar for the initial part of the simulation from 0 to 3.5 s when the ball bounces on the surface of the table and then settles into the pure rolling motion. However, the part of the simulation where the balls rolls over the edge of the table yielded clearly different simulation results for different solver settings. Hence, the period of the simulation from 3.5 to 4.5 s is investigated in more detail.

As the ball rolls over the edge of the table, the direction of the contact normal changes: it starts off being vertical and gradually tilts down. Figure 5.41 indicates that the change in direction occurs smoothly and without any discontinuity. As this happens, the bristle deformation dynamics must also “track” this change of direction, such that the direction of the deformation \mathbf{z} is maintained

tangential to the normal; see Equation (4.227). This ensures that the friction force always acts tangentially to the contact normal direction. If the numerical solvers obtain an incorrect or inaccurate solution for the bristle deformation, this may introduce an artificial coupling between the normal and tangential force.

Figure 5.44 plots the time history of f_z obtained using the solver ode23tb with error tolerances of 10^{-5} , 10^{-6} and 10^{-7} . Figure 5.45 gives the corresponding total system energy, which includes both the kinetic and potential energies. When the error tolerances are set to 10^{-5} a deviation in generated force can be observed at 4.2 s and a large increase in system energy. Since no external non-conservative force is acting on the system, the energy should never increase. Hence, the solver returns incorrect results for these settings.

The case when the error tolerances are set to 10^{-6} is significantly better and the resulting energy profile shows no large increase in energy. However, when looking more closely at the generated force profile (see Figure 5.46) it can be seen that there are oscillations in the force that are much less present in the case when the error tolerances are set to 10^{-7} . The energy profile also exhibits an increase in total system energy around 4.25 s; see Figure 5.47. Hence, the results using ode23tb with error tolerances of 10^{-6} are better but are still incorrect.

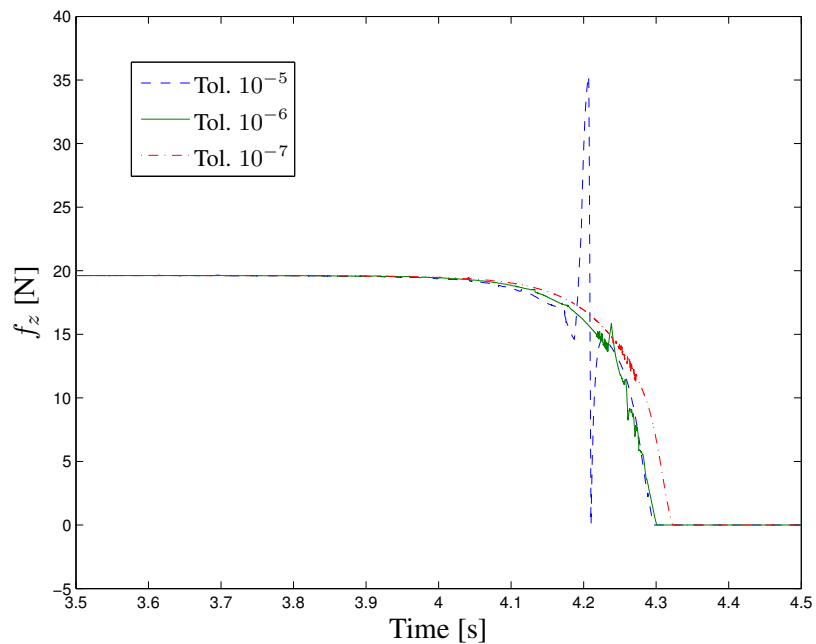


Figure 5.44: Simulation results using ode23tb: force in Z .

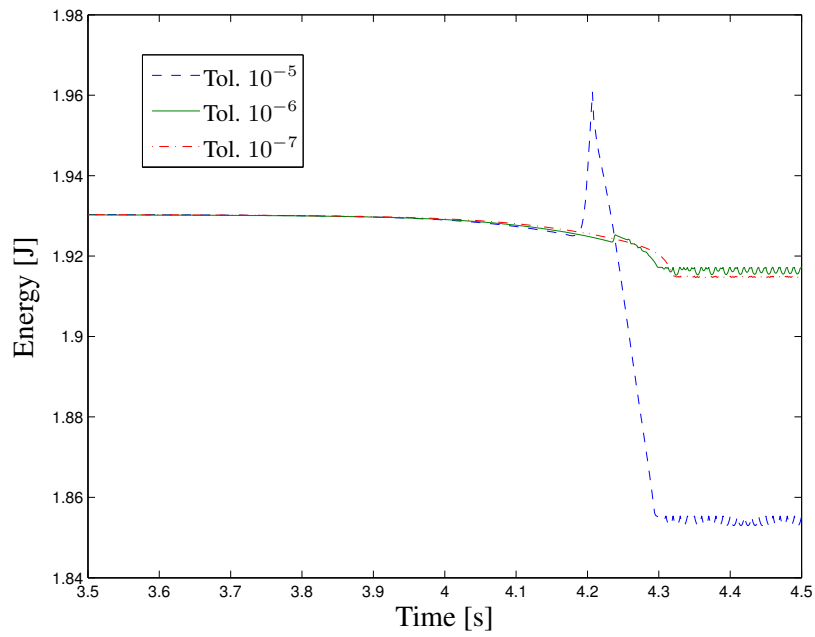
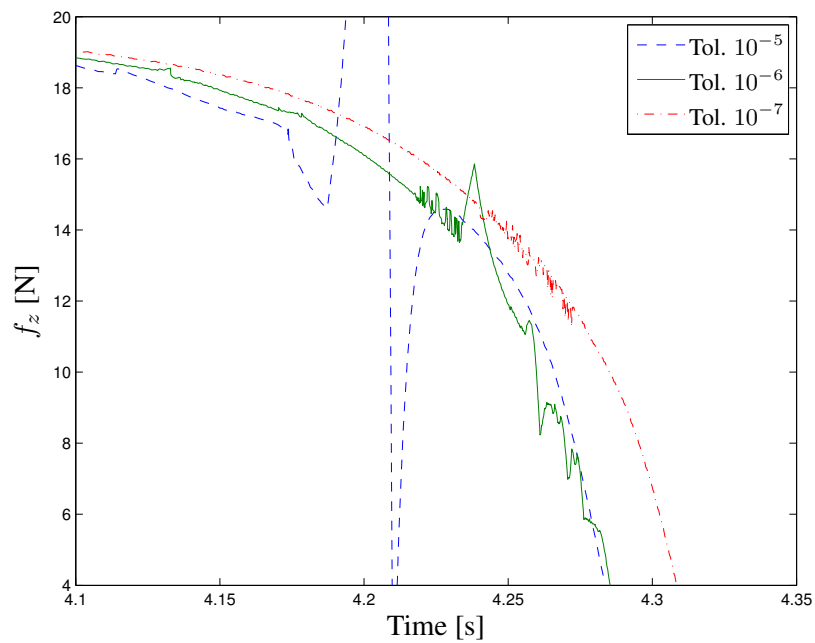


Figure 5.45: Simulation results using ode23tb: total system energy.

Figure 5.46: Simulation results using ode23tb: force in Z – zoomed.

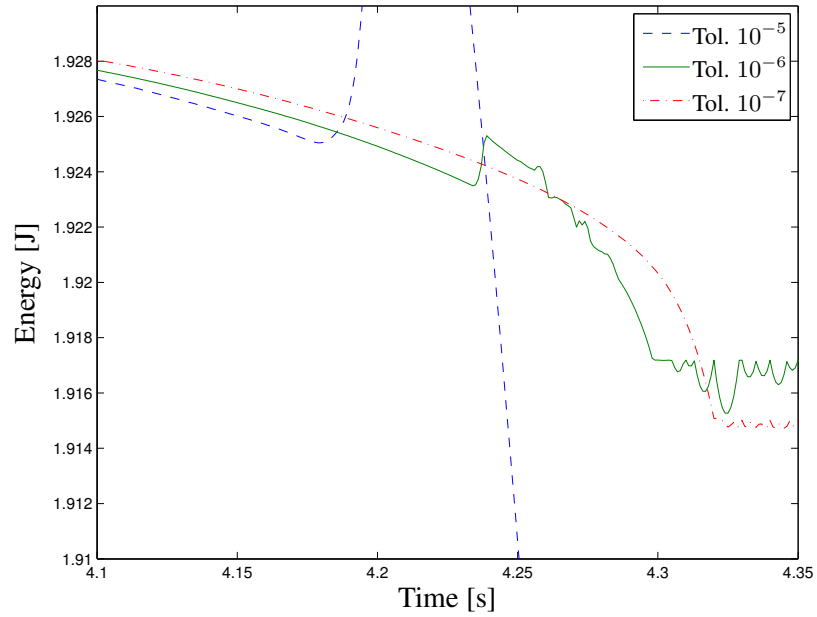


Figure 5.47: Simulation results using ode23tb: total system energy – zoomed.

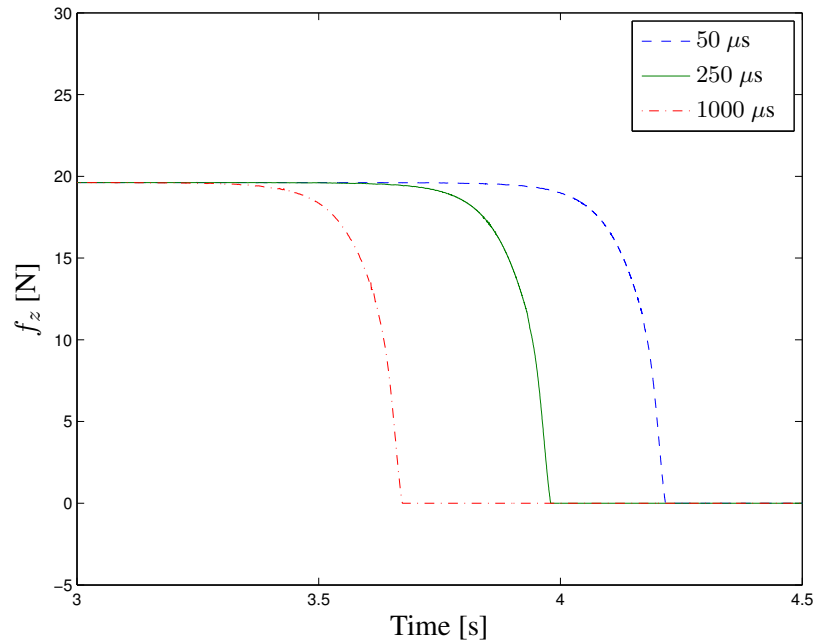


Figure 5.48: Simulation results using ode3: force in Z .

Next, a similar investigation was performed using the ode3 fixed-step solver using time-step sizes of $50 \mu\text{s}$, $250 \mu\text{s}$ and $1000 \mu\text{s}$. The results are given in Figures 5.48 and 5.49. All curves appear very similar even though the time-step size changes by a factor of 20. Most importantly, even with a time step size of 1 ms, there is no increase in total system energy. On the other hand,

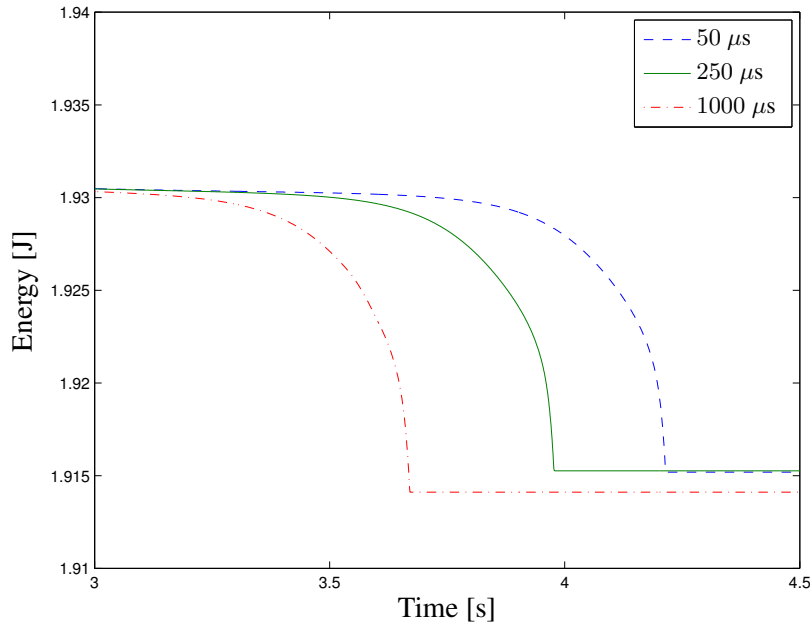


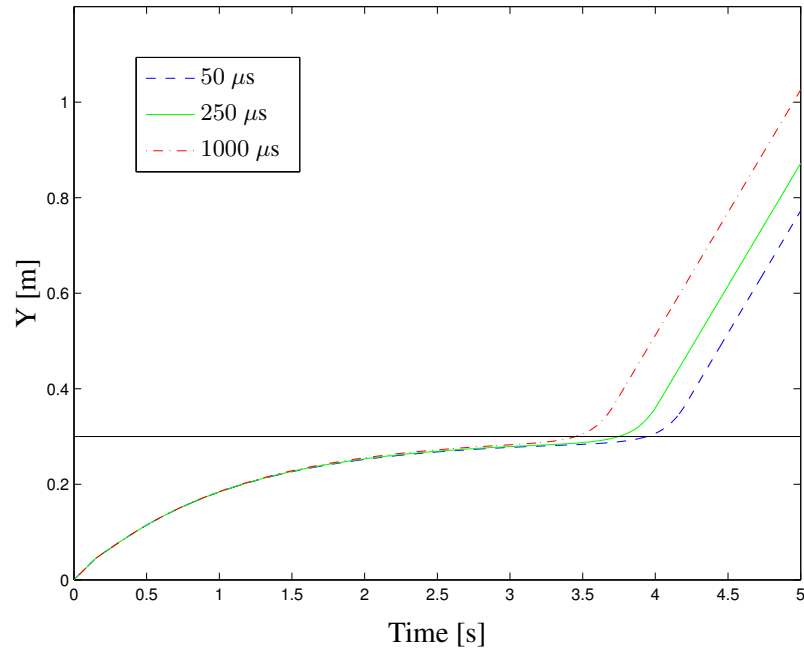
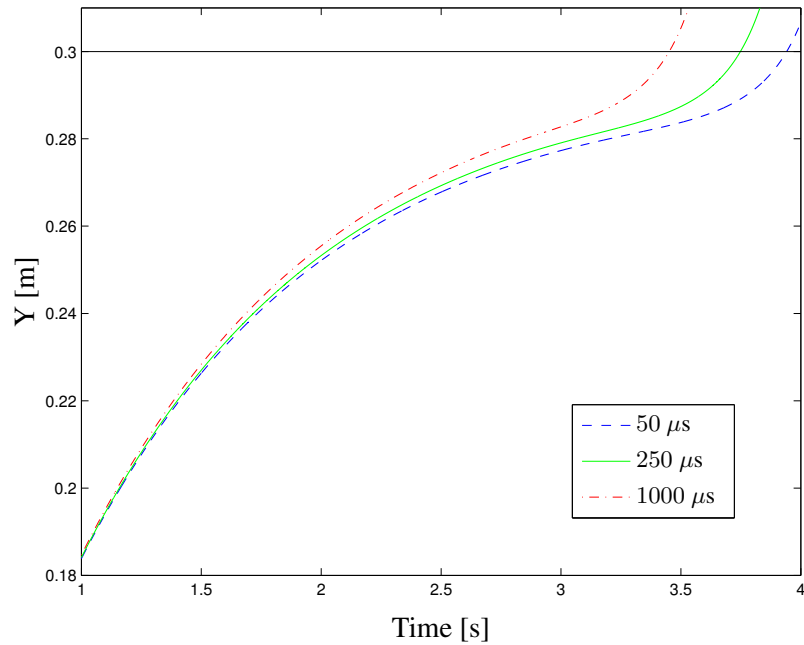
Figure 5.49: Simulation results using ode3: total system energy.

large time offsets separate the curves; the curves have nearly identical shapes, but do not occur at the same point in time.

The time offsets are caused by the accumulation of small errors in the predicted positions, and this has a significant impact on the moment at which the ball starts tilting over the edge of the table. This latter motion corresponds to the part in the force and energy curves where the slope changes from horizontal down to nearly vertical. The simulation results for all three simulations give a Y -translational velocity of 0.197 m/s at 0.35 s, i.e., the moment just after that last impact when the lasting contact is initiated. Hence, at that point in time, the simulation results are nearly identical. However, as the ball moves toward the edge, the simulation results from the three simulations start diverging slightly.

Figure 5.50 presents the motion of the centre of ball toward the edge in the Y -direction obtained using the three solver time-step sizes. The edge is located at $Y = 0.3$ m, and is indicated in the figure by a solid horizontal line. It can be seen that the Y -position curve obtained using a time step of 1000 μs is slightly above the other two, thereby indicating the velocity obtained using this time-step size is slightly higher than the one obtained in the other two simulations. Similarly, the Y -position predictions obtained using a time-step size of 250 μs are also slightly higher than those obtained using the time-step size of 50 μs . The small position differences can be better seen in Figure 5.51, where a magnified view of Figure 5.50 for the portion of the curves where the ball rolls over the edge is given.

The point where the ball starts tilting down corresponds to the point of inflection of the curves at around $Y = 0.28$ m. Figure 5.51 shows that the ball starts tilting down at exactly the same

Figure 5.50: Y -position of the ball centre over time.Figure 5.51: Y -position of the ball centre over time – zoomed.

point in space in all three curves, but it reaches that point at a significantly different times. In the simulation scenario, the location of the edge was selected such that the ball has nearly lost all of its Y -velocity before it rolls off the edge of the table. That particular choice of scenario therefore

amplifies the difference in the curves; since the velocity is very small at the time the ball reaches the edge, a small difference in position results in a large difference in time for the onset of the ball tilting motion. Hence, the large time offset between the curves can be explained by the accumulation of numerical errors and the selection of the particular simulation scenario.

The phenomenon observed here is that large changes in simulation results can be caused by seemingly minute changes in parameter or simulation settings. This phenomenon is characteristic of multibody simulation involving contact dynamics. Here, a small change in the solver time-step size causes a big time difference between the curves, e.g., the difference between the $250 \mu\text{s}$ time-step and the $50 \mu\text{s}$ time-step is only $200 \mu\text{s}$, but the offset of the curves is about 0.2 s , or 1000 times larger.

Figures 5.52 and 5.53 present a comparison of f_z and the total energy results obtained using the ode23tb variable-step solver with error tolerances of 10^{-7} and the ode3 fixed-step solver with a time-step of $50 \mu\text{s}$. The results have a very similar shape, but have a time offset which can be explained as before. As expected, the plots indicate the fixed-step solver results obtained using the smallest time step are closest to the results from the variable step solver.

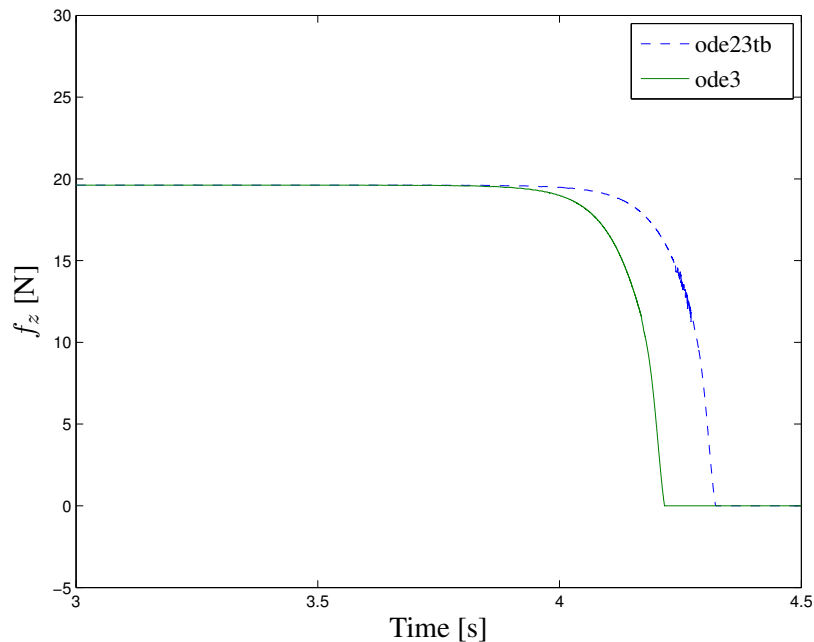


Figure 5.52: Simulation results comparison: force in Z .

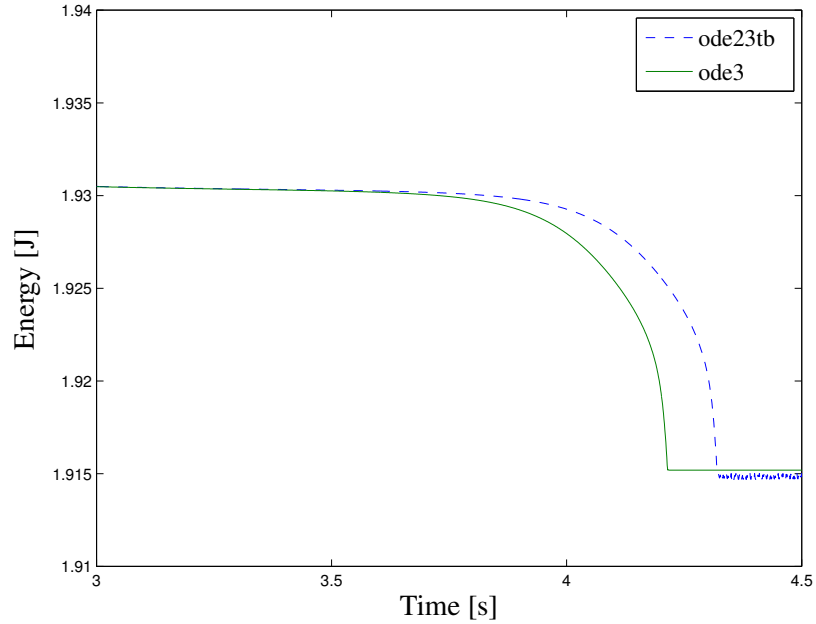


Figure 5.53: Simulation results comparison: total system energy.

5.2.2 Complex Geometry Contacts

The simulation results presented so far have only included objects with simple geometries. However, the volumetric modelling approach makes no assumption on the actual shape of the objects and hence it can be used to model contact for a wide range of object shapes. The model however imposes that the contact plate is flat, thereby requiring the contact geometries to be “cut” into smaller segments to ensure the overall contact model is accurate; see Section 4.1.2. This restriction can be somewhat “transgressed”, as shown in Section 5.2.1. However, there are cases where the model must be segmented into smaller sub-components. This section presents the results for such models.

The object-oriented framework created to support the implementation of the contact models also includes a mechanism to process these segmented geometric models automatically. Because the parts of the segmented objects do not move with respect to each other, the implementation can therefore be optimized by processing all the segmented parts as a whole, and only process the sub-parts that are effectively in contact. These segmented models are referred to as *cellular* models; their sub-components are *cells*. The LLG volumetric processing routines have been optimized to operate on pairs of cells. A cell is defined as being a single projective primitive, or the intersection of a number of such primitives. A cell can never be the union of projective primitives.

A cellular contact model was therefore implemented to support the modelling of contact between multi-cell objects. This contact model acts as a container for an array of internal volumetric contact models, referred hereafter as contact sub-models. However, each of these sub-models is a

full-fledged volumetric contact model with its own states and properties. The contact sub-models only share the constant contact model parameters, e.g., the volumetric stiffness. The implementation of the cellular contact model includes a mechanism that tracks which cell pairs are in contact and assigns them to a specific contact sub-model. It also detects when new cell-pairs come into contact or when contact is lost, and activates or de-activates the contact sub-models accordingly. A more detailed discussion of the cellular contact model implementation is given in Appendix A.

This section presents the simulation results for two cellular objects. This first object is a Tippe-Top. It is fairly simple object and could have been implemented by simply using two separate contact models for the two spherical parts. Its contact model was nonetheless implemented using the cellular infrastructure and the simulation results are compared to results from the literature. The second object is a truly complicated geometry and makes full use of the cellular model optimizations.

A Tippe-Top Simulation

The Tippe-Top model used by Friedl (1997) and Leine and Glocker (2003) was implemented using a free-floating body model to which the contact force and torque from the proposed model are applied. The dimensions are $r_1 = 15$ mm, $r_2 = 5$ mm, $a_1 = 3$ mm and $a_2 = 16$ mm; see Figure 5.54. The Tippe-Top has a mass of $6 \cdot 10^{-3}$ kg. Gravity acts in the negative Z -direction with a magnitude of 9.81 m/s².

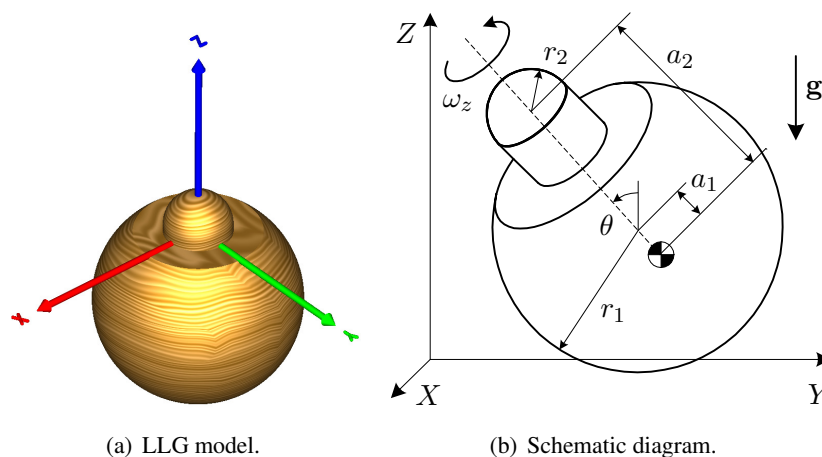


Figure 5.54: The Tippe-Top geometry.

The parameters for the contact model are given in Table 5.7. The stiffness was selected to obtain a circular contact surface with a radius of 0.5 mm when the sphere of radius r_1 is resting on the ground, as in Leine and Glocker (2003). The damping factor value was chosen close to 1 to minimize the amount of energy dissipated during contact by the normal damping force and the rolling resistance torque. These modes of energy dissipation are not included in the reference

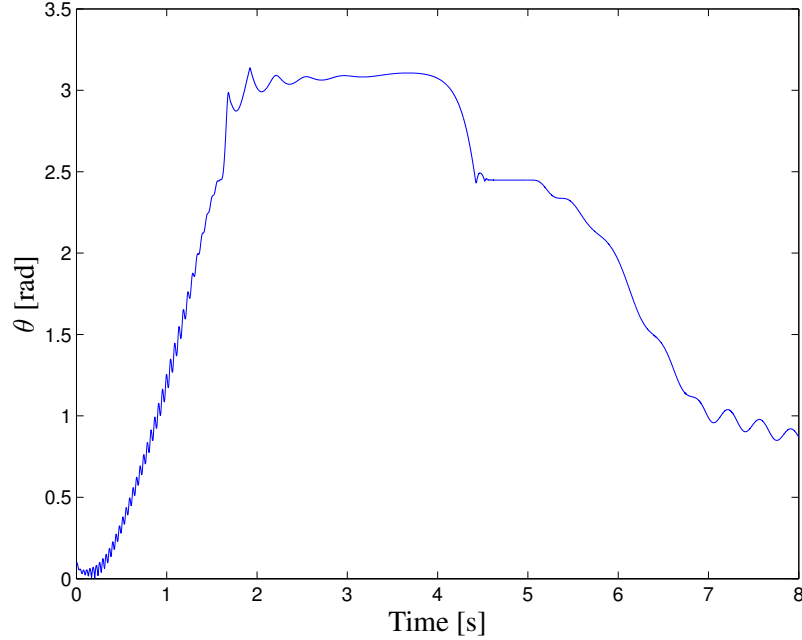


Figure 5.55: Time-history of the inclination of the Tippe-Top (original).

simulation models. The parameters for the friction model are summarized Table 5.8. The numerical tolerance on velocity was set to $v_\epsilon = v_S/100 = 10^{-5}$ m/s. The voxel size was set to $2 \cdot 10^{-5}$ m.

k_v	e_{eff}	v_{small}	τ_r
$1.798 \cdot 10^{10}$ N/m ³	0.975	10^{-4} m/s	1 s

Table 5.7: Normal contact model parameter values for the Tippe-Top simulations.

μ_S	μ_C	σ_o	σ_1	σ_2	v_S	τ_{dw}
0.3	0.3	10^5 1/m	$\sqrt{10^5}$ s/m	0 s/m	0.001 m/s	0.01 s

Table 5.8: Friction model parameter values for the Tippe-Top simulations.

Figure 5.55 presents the resulting Tippe-Top orientation time-history using the contact model proposed in this work and referred hereafter as the ‘original’ model. The Tippe-Top is given an initial angle offset of 0.1 rad from the vertical. The initial z -angular velocity ω_z about the spin axis of the Tippe-Top which was 180 rad/s in the reference simulation was increased to 200 rad/s. The plot shows the angle θ varying from 0.1 down to 0 rad (straight up position) at 0.15 s. Then the Tippe-Top gradually start tilting and eventually flips over at 1.6 s. It stays upside down until 4 s, at which point it falls and starts to tilt back up as it gradually loses its angular momentum.

Figure 5.56 shows the results for the same simulation but with a reduced initial angular velocity ω_z of 185 rad/s, and where the contact model spinning friction torque has been scaled by a

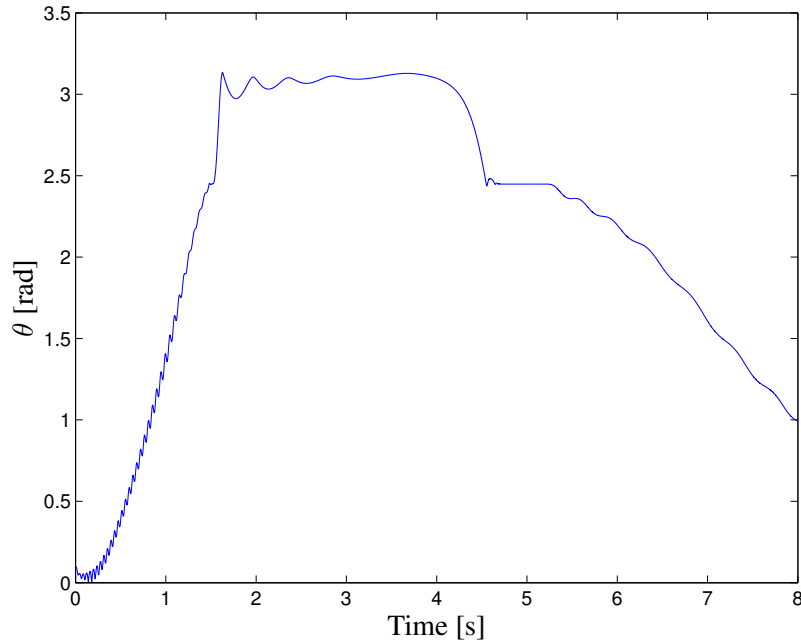


Figure 5.56: Time-history of the inclination of the Tippe-Top (modified).

factor of 0.65. The results for this ‘modified’ contact model are now very close to the results from Leine and Glocker (2003). This indicates that the proposed contact model has a spinning friction torque about 35% greater than the reference simulation, which was using a set-valued force law of the Coulomb-Contensou friction. Experimental investigation will be required to determine which model yields the more accurate results. Also, the initial ω_z is still 5 rad/s greater than in the reference simulation scenario. The extra momentum is required to overcome the additional energy dissipation effects present in the proposed contact model and not in the reference simulation. Figure 5.57 gives the time histories of the global Z -angular velocity Ω_z for the original and modified simulation models. Clearly, the original model angular velocity decreases more quickly over time. The modified model initial angular velocity velocity was tuned such that the Tippe-Top angular velocity, right after it flips over, is an approximate match to that of the reference simulation.

The overall behaviour of the Tippe-Top simulation implemented using the proposed contact model is consistent with the reference simulations and with observed physical behaviour. It remains to be determined which model has the more accurate estimate for the spinning friction torque. It should be noted that the proposed contact model was not specifically designed to simulate a Tippe-Top. Rather, it is a general purpose contact model that is able to reproduce with reasonable fidelity the dynamic behaviour obtained with dedicated and specialized Tippe-Top simulation models.

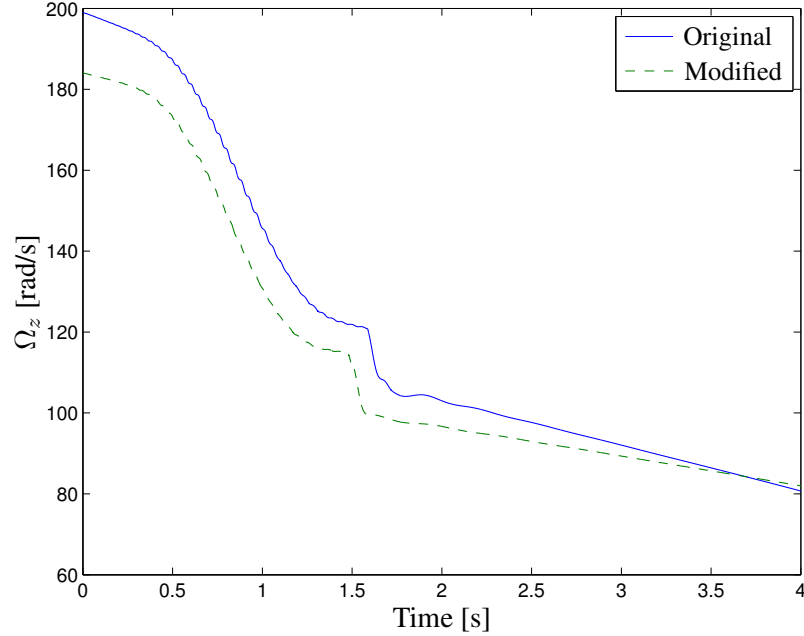


Figure 5.57: Time-history of the global Z -angular velocity Ω_z .

A Falling Battery Box

A simulation model using an approximate model of the battery box shown in Figure 4.1 was implemented. The LLG models for battery box and its worksite seen in Figure 2.3 were used to implement the simulation of a free-floating battery box falling into its worksite under the action of a 1 m/s^2 gravity in the X -direction. The LLG models are presented in Figure 5.58 along with their corresponding axis definitions. These were selected such that they overlap perfectly when the battery box is fully inserted into the worksite frame. The world frame reference axes X , Y , and Z are aligned with the worksite frame.

The battery box was assumed to have a mass of 100 kg and was dropped from the initial position $r_o = [-0.35 \ 0 \ -0.095]^T \text{ m}$. The box was also rotated by 2 deg about the Y -direction and then 2 deg about the rotated x -direction. The parameters for the normal contact model and friction model are given in Table 5.9 and Table 5.10, respectively. The simulation was run using the ode3 fixed-step solver with a step-size of $250 \ \mu\text{s}$. The translational and angular velocities at the battery box frame origin are given in Figures 5.59 and 5.60. The corresponding forces and moments, acting at the battery box frame and resolved in the worksite frame, are shown in Figures 5.61 and 5.62.

k_v	e_{eff}	v_{small}	τ_r
10^9 N/m^3	0.6	10^{-4} m/s	1 s

Table 5.9: Normal contact model parameter values for the falling battery box simulation.

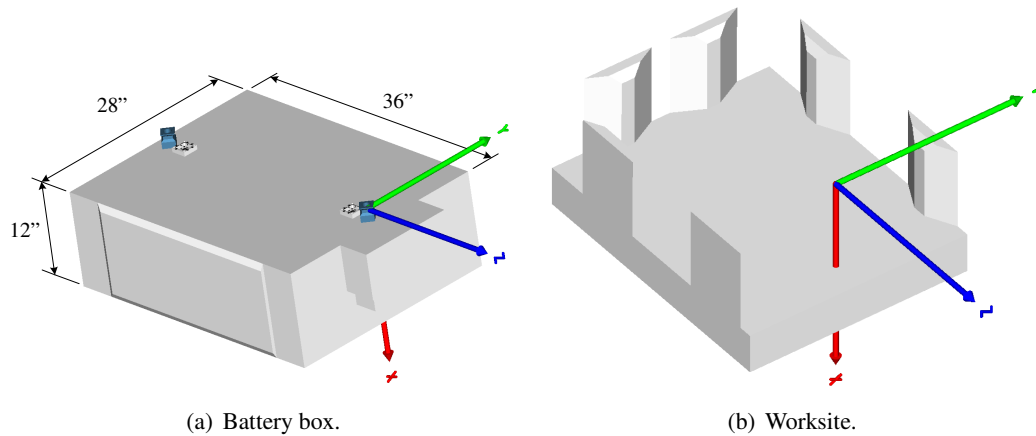


Figure 5.58: Cellular LLG models for a battery box and its worksite.

μ_S	μ_C	σ_o	σ_1	σ_2	v_S	τ_{dw}
0.3	0.3	10^5 1/m	$\sqrt{10^5}$ s/m	0 s/m	0.1 m/s	0.001 s

Table 5.10: Friction model parameter values for the falling battery box simulation.

Because of the complexity of the interaction, it is not possible to explain in detail the nature of the variations in velocities and forces. It can be observed from the velocity plots that the initial velocity is zero and increases in the $+X$ -direction under the action of gravity. Once the contacts occur, both the translational and angular velocities fluctuate back and forth around zero and eventually go to zero as the battery box comes to rest inside the worksite after 2 s.

The force and moment plots indicates that many impacts occur with the largest one being in the X -direction. Figure 5.63 shows that f_x eventually settles at -100 N, as expected since gravity acts in the $+X$ -direction and has a magnitude of 1 m/s^2 . The high frequency oscillations apparent in the latter figure are the result of the high contact stiffness. Here, the battery box is lying flat on the bottom surface of the worksite. The resulting contact area is therefore large, and since the contact stiffness of the volumetric model is proportional to the contact surface, the resulting contact stiffness becomes large as well.

Figure 5.64 presents LLG-rendered images of the battery box as it falls into the worksite. The images are ordered from left to right and from top to bottom. The images correspond to time increments of 0.2 s.

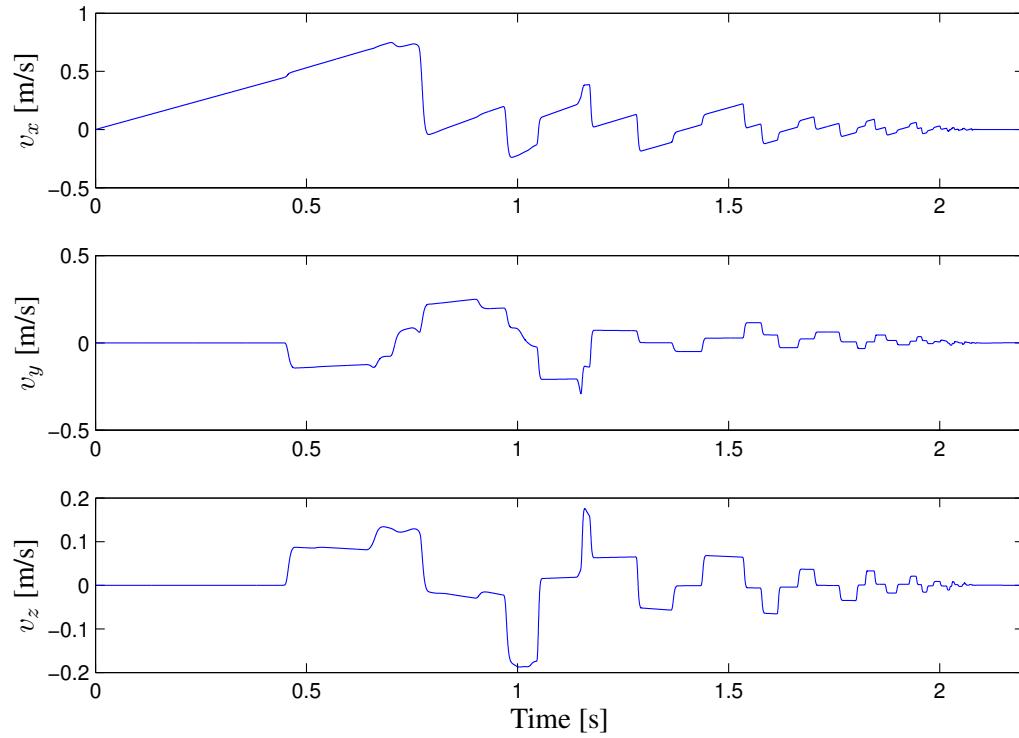


Figure 5.59: The battery box translational velocities.

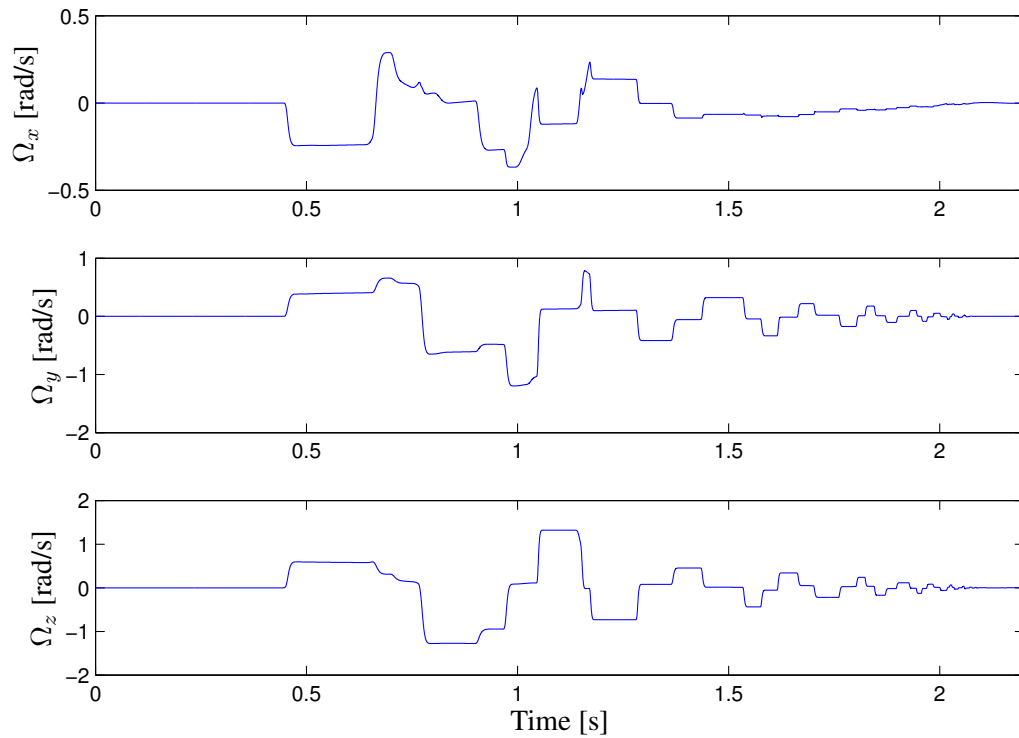


Figure 5.60: The battery box angular velocities.

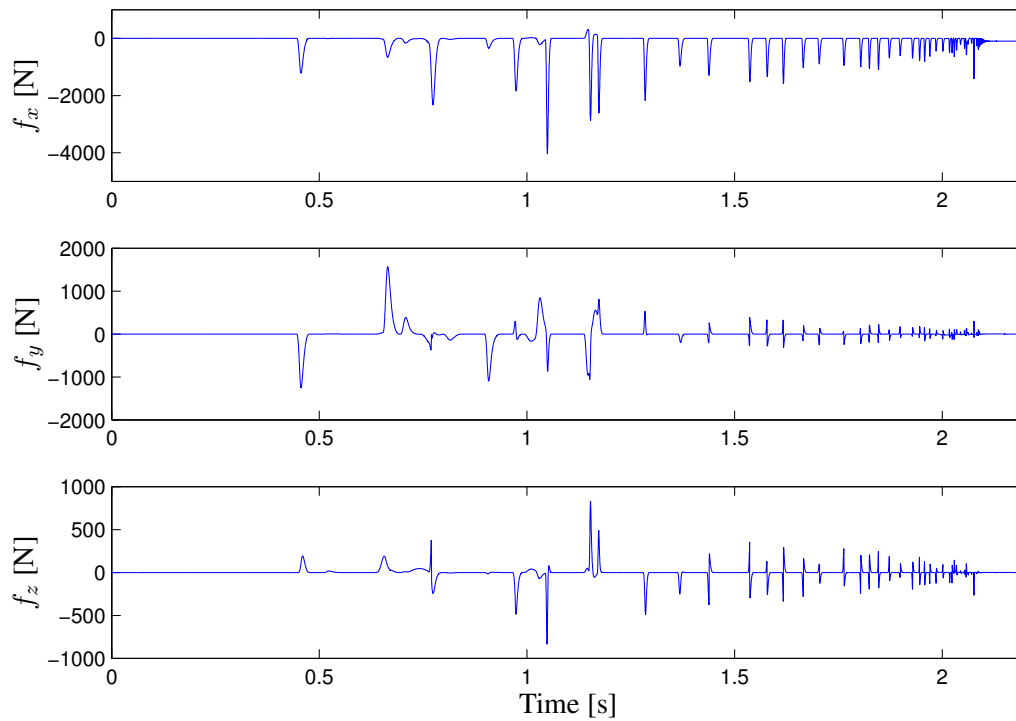


Figure 5.61: The battery box forces at the micro-fixture.

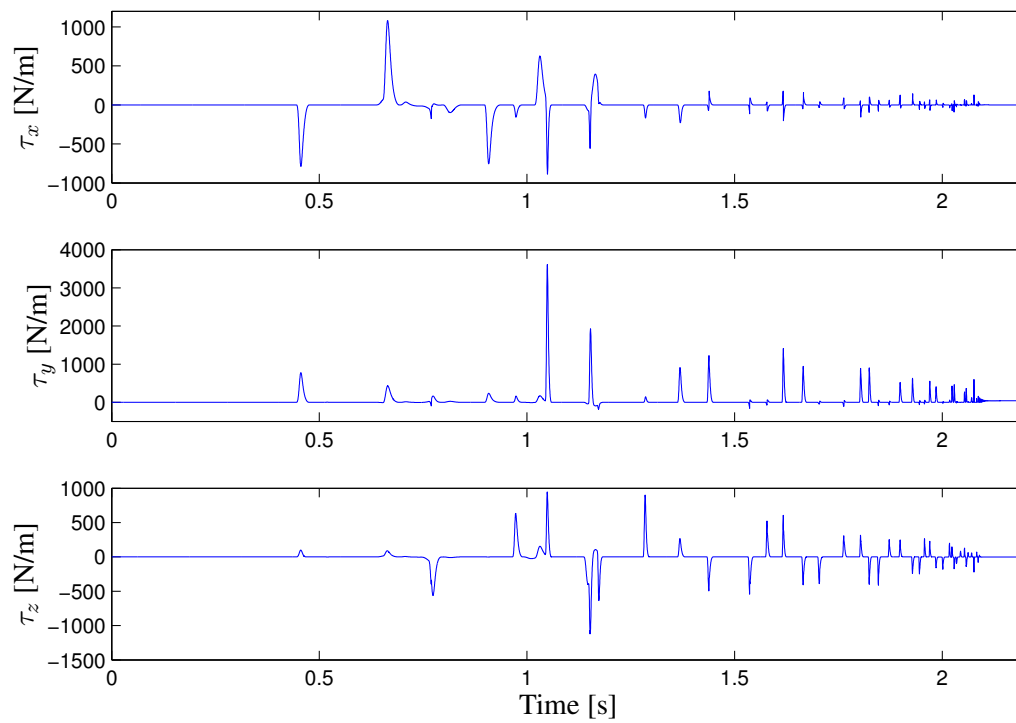


Figure 5.62: The battery box moments at the micro-fixture.

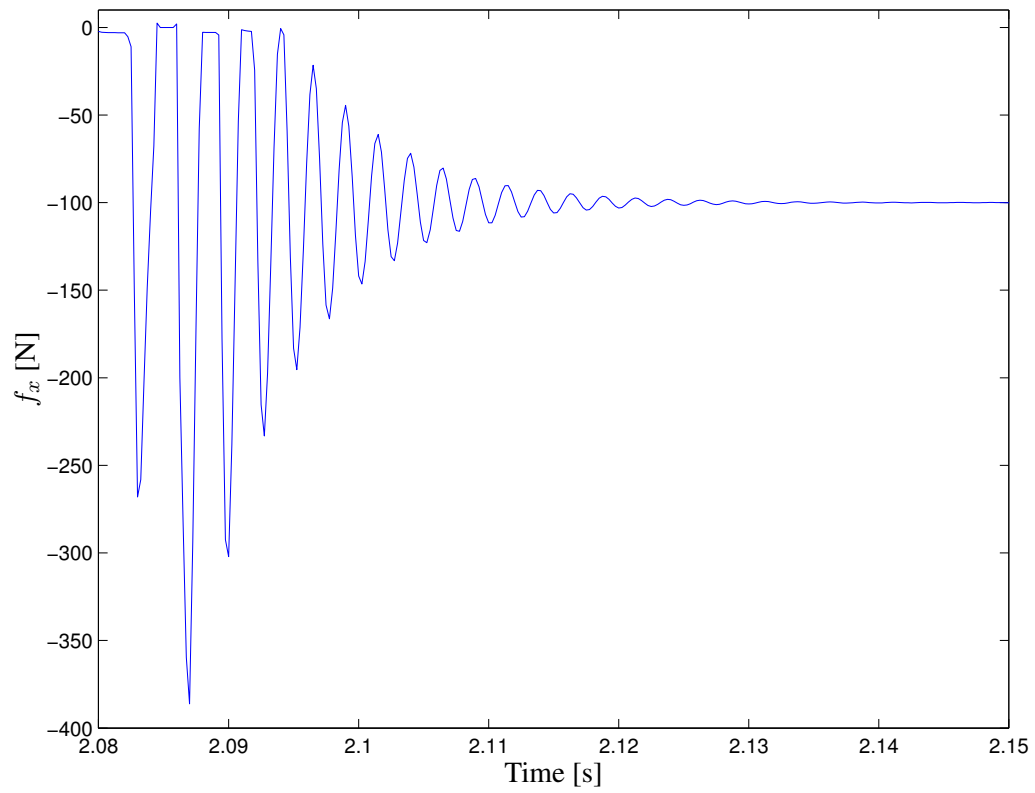


Figure 5.63: The battery box force in X – zoomed.

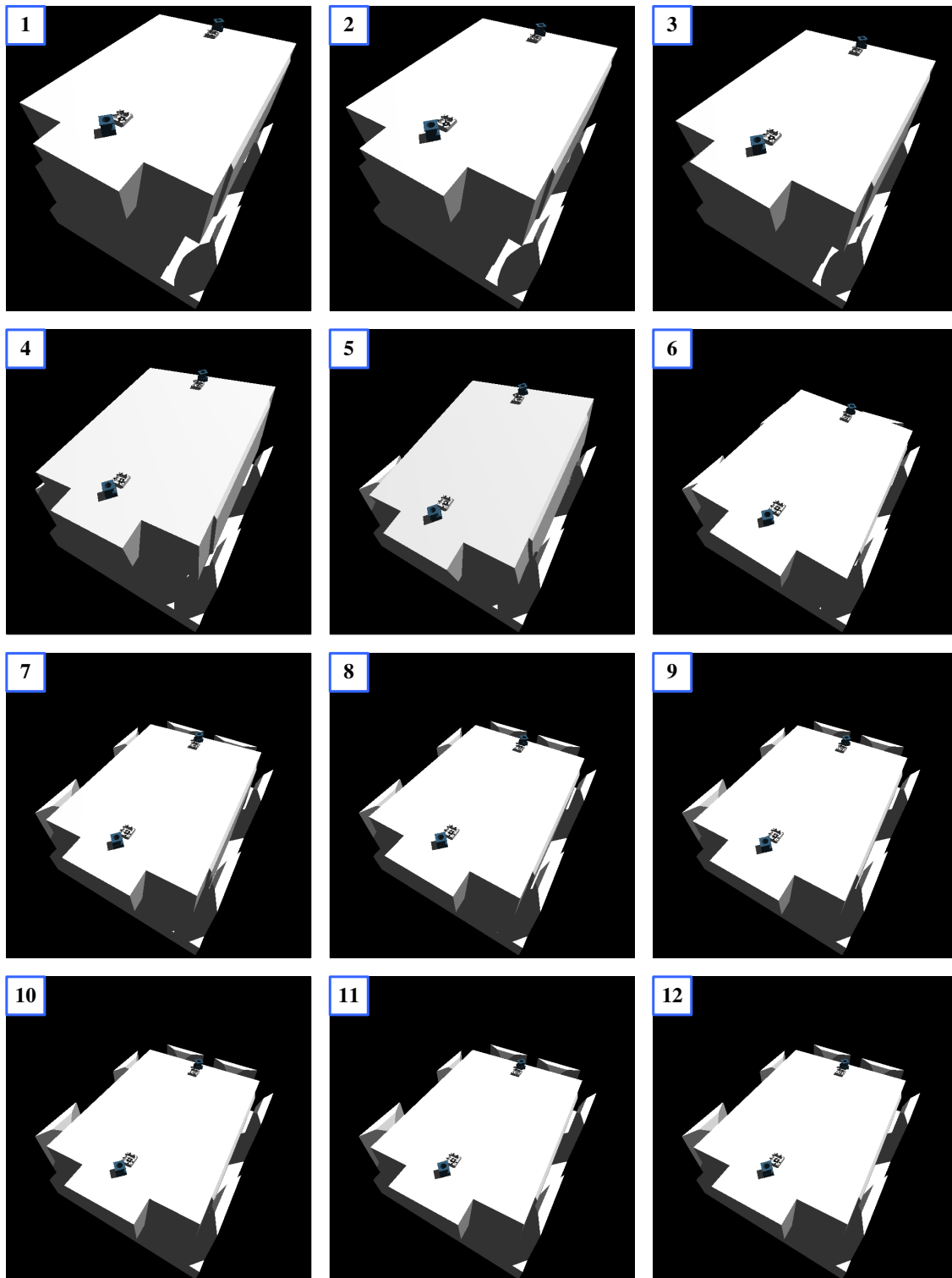


Figure 5.64: The battery box falling into the worksite.

Chapter 6

Conclusions

This thesis presented a general contact dynamics modelling system. This system could be used to support the task planning process for space-based manipulator systems. It is able to generate accurate and reliable simulation results quickly, such that an operation engineer can investigate multiple contact dynamics simulation scenarios within a few hours. The contact models used in this system are chosen such that the parameters related to physical quantities can be identified experimentally, or through analysis based on the material properties. Similarly, the numerical parameters can be either selected automatically, or by using the provided heuristic rules that indicate the range of appropriate values ensuring the simulations results will be qualitatively correct.

The literature survey showed that contact models based on the material compliance were the most suitable for the intended use of the contact models. However, it was demonstrated that the current state-of-the-art compliant contact dynamics modelling systems failed to reproduce rudimentary contact behaviour as soon as the colliding body geometries were no longer simple, and in particular whenever the resulting contact surface became large. Additionally, it was shown that the contact model parameters could not always be related to a physical property. Finally, it was observed that many contact dynamics modelling systems relied on geometric description systems based on polygons and that the simulated contact behaviour was affected by this geometric approximation.

This thesis introduced a flexible contact dynamics modelling framework. A contact dynamics modelling system compatible with the Simulink simulation environment from The MathWorks Inc. was developed under this framework. Two types of contact models were implemented in the system, and the detailed derivations for these models were presented in the thesis. First, a contact model based on Hertz theory was proposed to tackle simulations involving bodies with smooth non-conformal surfaces. The proposed point contact model includes normal damping and tangential friction. It also assumes the contact surface is small, such that the contact force is assumed to be acting through a point, i.e., the moments generated across the contact surface are neglected. A second contact model based on the Winkler elastic foundation model was then proposed to deal with a larger class of geometries. This so-called volumetric contact model is suitable for a broad

range of contact geometries, as long as the contact surface can be approximated as being flat. A method to deal with objects where this latter approximation is not reasonable was also presented. In the volumetric contact model, the effect of the contact pressure distribution across the contact surface is accounted for in the form of the rolling resistance torque and spinning friction torque.

In both cases, the contact model equations were derived from first principles, and the behaviour of each contact model characteristic was studied and simulated. When available, the simulation results were compared with benchmark results from the literature. Experimental validation of the point contact model was performed using the STVF at the CSA. The details of the contributions from this thesis are given next.

6.1 Review of the Contributions

The contributions from this work fall in three categories: the theory and simulation results for the point contact model, the theory and simulation results for the volumetric contact model, and the novel software architecture used to seamlessly integrate these models under a common framework.

6.1.1 Point Contact Model

Chapter 3 introduced a contact model suitable for modelling collisions between objects with non-conformal geometries. Since it is based on Hertz theory, the contacting surfaces must be smooth and without discontinuity, i.e., no corners or sharp edges. The contact model is composed of two sub-models: one for the normal contact force and one for the tangential friction force.

The normal contact force model takes the form of a non-linear spring with a hysteretic damping term. This type of non-linear spring-damper model has been shown to agree with experimental data (Hunt and Crossley, 1975; Stoianovici and Hurmuzlu, 1996). The derivations demonstrated that the damping factor could be defined in such a way that the normal energy dissipation could be controlled via a single parameter. It was shown that this parameter value could be determined as a function of the coefficient of restitution. The so-called dimensionless damping factor equation can be solved off-line since it describes a constant one-to-one mapping between the coefficient of restitution e_{eff} and the dimensionless damping factor d . Section 5.1.1 showed that the impact response obtained using the proposed damping factor definition gives exactly the expected coefficient of restitution. As a result, the model can be used to match any experimentally observed behaviour of the coefficient of restitution (Goldsmith, 1960). Finally, the proposed method of defining the damping factor makes it easy to obtain this parameter experimentally by simply measuring the coefficient of restitution.

A seven-parameter bristle friction model was proposed in Section 3.2.2. The model is a generalization of the bristle friction models proposed by Canudas de Wit et al. (1995) and de Carufel et al. (2000). In particular, it was adapted to the context of 3-dimensional frictional impact modelling with introduction of load-dependent bristle stiffness and damping terms, and with the expression

of the bristle deformation in vectorial form. The model features a dwell-time stiction force dependency and was shown to be able to reproduce the dynamic nature of the friction phenomenon (Section 5.1.2). Section 3.3.2 proposed methods to identify the friction model parameters, and also showed how to simplify the selection process depending on the required level of modelling fidelity.

The model behaviour was then investigated for oblique impacts. Numerical simulation examples of a ball impacting a plane and the interior surface of a cylinder under the action of gravity were provided in Section 5.1.3. The resulting dynamic behaviour is physically realistic and satisfies the no-slip condition once the state of pure rolling is reached. The resulting total energy of the simulated systems was analyzed and the results show the energy decaying until a steady-state and constant energy motion is obtained. These results were expected results since no external non-conservative force was acting on the systems.

The model was also used to simulate the collision of the tip of a double pendulum on a plane. The results showed the dynamic characteristic of the friction model and the total system energy behaving as expected. The double pendulum model was then modified to match a benchmark model in the literature (Ahmed et al., 1999) and the simulation results were found to be in good agreement.

Finally, the results from a simulation of the six degrees-of-freedom STVF manipulator holding a half-spherical payload and coming into contact with a flat plate were compared with experimentally obtained data using the STVF at the CSA. Even though the experimental facility features some significant limitations regarding the identification of contact model parameters, it was possible to obtain a very good correspondence between the simulated and experimental results. The performed experiments allowed the identification of the normal contact stiffness and damping as well the stiction and Coulomb friction coefficients.

6.1.2 Volumetric Contact Model

In Chapter 4, a contact model based on volumetric properties was presented. The model properties were derived assuming the elastic behaviour of the contacting objects can be approximated using a modified Winkler elastic foundation model, and that the contact surface is approximately flat. A method was proposed to deal with concave geometries when the latter approximation is not necessarily valid.

The proposed contact model was derived from first principles. The concept of a contact plate was introduced as a mechanism to “measure” the contact forces and torques acting between the bodies. The case where one body is deformable and the other has a rigid and flat contact surface was first investigated. An expression defining the contact pressure as a function of the shape of the colliding surfaces was defined. It was then analytically integrated over the contact area, such that the overall body-to-body contact force was obtained. It was shown that this contact force can be expressed in terms of the volumetric properties of the *volume of interference* between the two bodies, defined as the volume spanned by the intersection of the two undeformed geometries of

the colliding bodies. The properties of interest are: the volume of the volume of interference, the position of its centroid, and its inertia tensor taken about the centroid.

The analysis provided additional insight into two separate components of the contact force. First, the pressure acting on the contact surface between the two bodies produces a normal contact force and a rolling resistance torque. Second, the friction acting across the contact surface causes a tangential friction force and a spinning friction torque. Hence, the proposed model includes normal contact force and damping, rolling resistance torque and tangential and spinning friction force and torque. It features a contact stiffness proportional to the contact area and leads automatically to the correct selection of the point of action of the force.

The collision between two deformable bodies was then investigated. The contact model equations were shown to be nearly identical to the case where only one body is deformable, with the exception that the contact stiffness corresponds to an equivalent stiffness. The latter is computed as a function of the two body stiffnesses. Hence, the two deformable body contact model is also based on the same volumetric properties as the model for the one deformable body. The contact plate was also used to obtain the direction of the contact surface normal. It was shown that the contact normal corresponds to one of the eigenvectors of the volume of interference inertia tensor. This definition is not arbitrary and is based on the mechanical analysis of the action of the contact pressure across the contact surface.

The investigation also examined how the Coulomb friction is affected by the relative motion of the objects. The concept of average surface velocity was introduced. It accounts for both the relative translational and angular motions of the contacting surfaces. The average surface velocity was then used to find dimensionless factors that relate friction force and spinning torque caused by the Coulomb friction. These latter factors were labelled the Contensou factors in reference to the work of P. Contensou (1963). Also, the radius of gyration of the inertia tensor of the volume of interference about the contact normal was shown to correlate the spinning Coulomb friction torque to the translational Coulomb friction force.

A volumetric version of the seven-parameter bristle friction model was then introduced. It includes both the tangential friction force and spinning friction torque. The model is identical in form to the friction model for the point contact models, but with a few modifications. Here, the bristle force was obtained by analytical integration of the bristle deformations across the contact surface and the stick-slip transitions are triggered by the average surface velocity. The model also includes an extra state to account for the bristle deformation in torsion. Finally, the Contensou factors switch between a “stick” mode where the maximum friction force and torque are applied and a slip mode, where the relative motion of the contacting surfaces affects the magnitude of the friction force and torque. This switch is also triggered by the average surface velocity.

The proposed model is not restricted to contact situations where the bodies have non-conformal geometries, but can be used for any geometric pair with reasonably flat contact area. The behaviour of volumetric contact model was first compared to the one obtained with the point contact model

for simulation scenario of the ball was falling on the inside surface of a cylinder (Section 5.2.1). The resulting dynamic behaviour is physically realistic and satisfies the no-slip condition. It was observed that the effect of the rolling resistance torque is to dissipate rotational energy such that the motion of the ball is eventually stopped. In contrast, the simulation results obtained with the point contact model showed the ball rolling-on forever (Section 5.1.3).

The numerical simulation of a ball bouncing on a flat table surface and then rolling off the edge of the table was then presented. The simulation results demonstrated the contact model features, i.e., the normal contact force and damping, the rolling resistance torque, and the tangential friction force and spinning friction torque. The simulation results also showed the total system energy decaying in time until the ball fell over the edge of the table, as expected. However, the results obtained with the variable-step solvers in Simulink were not always accurate, unless stringent error tolerances were used. On the other hand, the simple explicit fixed-step solver yielded accurate results with a correct energetic behaviour, even with a relatively large step size. However, the selected simulation scenario was such that numerical error accumulated during the lasting contact phase of the motion caused large time offset between the curves generated using different time-step sizes.

The numerical simulation of a Tippe-Top was presented and the results were compared to a specialized Tippe-Top simulation model from the literature. This simulation scenario was selected because of the influence of the Contensou effect on the results. The results were shown to be consistent with the reference simulations and with observed physical behaviour. The spinning friction torque of the proposed contact model was about 35% greater than in the reference simulation. It remains to be determined which model has the more accurate estimate for the spinning friction torque. However, it was observed that even though the volumetric contact model is a general-purpose contact model, it was still able to reproduce with reasonable fidelity the dynamic behaviour obtained with dedicated and specialized Tippe-Top simulation models.

The contact model can be used as a general-purpose tool to model contact dynamics for a broad range of object shapes because the volumetric quantities that serve as input to the contact model can be determined for any object shape, and even when the contacting surfaces involve edges or corners. To illustrate this capability, the simulation of a battery box falling into its worksite was implemented. This simulation involves objects with very complex geometries and where the contact normals cannot always be intuitively determined. The results were presented in Section 5.2.2 and were shown to be qualitatively correct.

6.1.3 Implementation Framework

Although not reported in detail in the present document, an important contribution of the work accomplished in this research is the implementation of an open-architecture object-oriented framework that facilitates the creation of contact models based on compliance and their integration into a numerical simulation environment. Appendix A provides more details on the framework and

explains how it is used to implement a number of variations of the proposed contact models.

The novelty in the proposed approach is to segment the contact dynamics modelling process into distinct model components, and design each such component as a stand-alone software object. Then, various instances of the component can be easily combined into a contact model to create completely new contact models. The user is not restricted to changing the contact model settings or parameters; the contact model itself can be changed. In essence, the contact model object acts as a container for the geometric pair, normal contact and friction model objects that can be mixed in any combination to create new categories of contact models. The process of combining the contact model components is straightforward and can be accomplished by writing a few simple lines of code, a matter which takes at most a few minutes; see Section A.5.

6.2 General Comments

The goal of this work was to develop a robust, reliable, flexible and easy to use contact dynamics modelling system. From the theoretical stand-point, the point contact model should be used whenever the simulation involves smooth and rounded objects. The volumetric model theory is based on the Winkler elastic foundation model that gives only a rough approximation of the true deformation behaviour of contacting elastic bodies. Hence, the Hertz theory model is more accurate, but is also much more restrictive in the type of geometries that are allowed.

On the other hand, the volumetric model can work with a much larger class of geometries. Besides the fact that the point contact model does not include the modelling of the rolling resistance and spinning friction torques, the main difference between the volumetric and the point contact model is in the normal contact force model. More precisely, the difference resides in the formulation of the stiffness equation, i.e., the force versus penetration relationship. In an operational context, there are programmatic reasons which often prevent this relationship from being known accurately, e.g., access to payloads, and the force versus penetration curve must be guessed instead. As a result, the concern will shift from trying to obtain the accurate behaviour to trying to determine bounds for these force-penetration curves. In this context, the approximate nature of the foundation model is not a serious limitation after all since approximate scenarios will often be used.

Moreover, significant benefits can be gained from using the volumetric contact model. This model is much more detailed and includes the effects of many more phenomena occurring during contact, and in particular when the contact surface area is significant. To the best knowledge of the author, the model proposed here is the only model to have a sophisticated dynamic friction model that includes the Contensou effect in translation and in rotation, and the only one that defines the direction of the contact normal based on the mechanical analysis of the contact phenomena rather than using some arbitrary definition or “rule”.

Furthermore, the choice of the LLG solid modelling technology has yielded significant benefits.

First, because this is a volume-based geometric system, it was easily and naturally adapted to generate the volume metrics required as input by the contact model. Secondly, because it uses an exact representation of geometry, the modelling of rolling contact is accurate and not subject to the artificial geometric “noise” incurred by geometric modelling systems based on polygons.

To obtain the volume metrics, the LLG function does need to do a discretization of the volume of interference: it needs to split volume of interference into voxels to count them. Hence, the accuracy of the obtained volume metrics is always limited by the size of the voxels. Obviously, when the requested voxel size is very small, the time to obtain the volume metrics will be unreasonable. On the other hand, the returned value is volume, and hence it is proportional to the cube of the voxel size; it quickly becomes accurate for not-so-small values of the voxel size, e.g., the volume of a voxel of size 10^{-3} m is 10^{-9} m³, which gives a force of 1 N for a stiffness of 10^9 N/m³. Another important point is that the LLG voxelization is always done on the exact geometries. It is only a local discretization that always converges to the true shape. Polygonal models instead do the discretization beforehand, e.g., the sphere is modelled with a set of triangular facets; hence is impossible to get back to the true shape.

Finally, the volumetric contact model is the only approach that yields a consistent contact force evaluation that is independent of how the volume of a geometry is broken down into smaller pieces. In other words, if a volume must be split into different cells to get an accurate contact model, its total volume remains the same. This implies that when another object interacts with this broken-down volume, the total contact force between the two objects will remain the same because the total volume of interference between the two bodies remains the same, no matter how finely the broken-down volume is cut. This observation holds true for the bristle stiffness and damping models as well. Because they are both proportional to the normal contact force, and therefore to the volume, the total bristle force and stiffness will remain the same for any resolution of volume discretization. Hence, the total tangential friction force will also remain the same.

6.3 Future Work

The contact modelling approach proposed in this thesis lays solid foundations for building a comprehensive contact dynamics simulation system. However, one of the key difficulties in creating accurate and reliable contact models is obtaining good values for the contact model parameters. Sections 3.3 and 4.5 briefly discussed ways to obtain or estimate these parameters. The discussion was limited to describing a general way of obtaining these values but obviously the work involved is significant. One would need to design or find the appropriate experimental apparatus and define a detailed experimental protocol to obtain each parameter. Moreover, obtaining the contact parameters for objects that are already built is an even more challenging task. In addition to the contact stiffness and damping, one must factor-in the effects of structural stiffness and damping. Further research is required to bring together a parametric identification facility that would allow fast and

accurate parameter determination.

Furthermore, some features of the volumetric contact model must be validated experimentally. In Section 5.2.2, it was observed that the contact model spinning friction torque was 35% higher than in the reference simulation. The predicted spinning friction magnitude needs to be validated experimentally. In particular, the model predicts that the Coulomb friction spinning torque can be obtained by multiplying the Coulomb friction force by the radius of gyration of the volume of interference inertia tensor. This relationship needs to be tested. The dynamic behaviour of the Contensou effect, characterized in the contact model by the Contensou factors C_v and C_ω also needs to be verified.

Another area where significant improvements are achievable is in the LLG technology itself. Fast, efficient and accurate collision detection systems have been the subject of extensive research over the past two decades, but the work has mainly focused on obtaining the distance between non-colliding objects. More recently, many fast methods have been proposed to measure the interpenetration distance between two colliding objects. However, little research has been performed on finding methods to efficiently characterize the volume of interference. The LLG technology uses the voxelization approach, but other methods may be faster or even more accurate, such as analytic or semi-analytic methods. LLG is now focusing on parallelizing geometric algorithms to target multi-CPU platforms. The currently used voxelization algorithms are based on a recursive-tree decomposition of the volume and are therefore naturally suited for an adaption to a parallel processing paradigm. LLG claims that huge gains in processing speed are already possible.

Alternatively, the volume accuracy could be generated with a fixed number of digits of precision instead of a fixed voxel size, thereby lowering the accuracy requirements during the impact phase of the contact where the inter-penetration volume is the largest. In other words, when the volume of interference is large there is no need to go down to the smallest voxel size to obtain an accurate estimate of the volume.

As was observed in Section 5.2.1, the performance of the numerical solvers can vary significantly. It is recommended to investigate other numerical methods to find one that is well suited for this type of system dynamics. In particular, the implicit methods such as Hilber-Hughes-Taylor developed initially for finite element problems might be very efficient at tackling the contact dynamics simulations. The simulation results showed that some solvers were poorly tracking the solution and that the corresponding system energy was becoming incorrect. The solver performance could also be optimized by improving the numerical scaling of the states. Another alternative would be to examine energy-preserving solvers, which can track the energy flow in and out of the system to ensure the solution is energetically correct.

Finally, although the contact modelling approach presented in this work is targeted toward the simulation of robotic tasks, it is clear the methodology is applicable for a much wider use. Possible applications are the modelling of bio-mechanical systems, such as foot-ground interactions (Millard et al., 2007). The contact model could be refined to include the skin visco-elastic

behaviour and also to model bodies that are globally deforming, e.g., the toes of a foot bending.

Bibliography

- Agar, J., Sharf, I., Lange, C. and Gonthier, Y.: 2005, Contact parameter estimation with a space robot verification facility, *Proceedings of IDETC'05, ASME 2005 International Design Engineering Technical Conferences & Computers and Information in Engineering Conference*, Long Beach, California, USA. DETC2005-84346.
- Aghili, F., Dupuis, E., Martin, E. and Piedbœuf, J.-C.: 2001, Force/Moment accommodation control for tele-operated manipulators performing contact tasks in stiff environment, *Proceedings of the 2001 IEEE/RSJ International Conference on Intelligent Robotics and Systems*, Maui, Hawaii, USA, pp. 2227 – 2233.
- Aghili, F., Dupuis, E. and Namvar, M.: 2004, Analysis and synthesis of an impedance scheme for emulation of space robots, *ASTRA Workshop*, ESTEC, Noordwijk.
- Aghili, F., Dupuis, E., Piedbœuf, J.-C. and de Carufel, J.: 1999, Hardware-in-the-loop simulations of robots performing contact tasks, in M. Perry (ed.), *Fifth International Symposium on Artificial Intelligence, Robotics & Automation in Space i-SAIRAS 1999*, ESA Publication Division, Noordwijk, The Netherlands, pp. 583–588.
- Ahmed, S., Lankarani, H. M. and Pereira, M. F. O. S.: 1999, Frictional impact analysis in open-loop multibody mechanical systems, *Transactions of the ASME Journal of Mechanical Design* **121**, 119–127.
- Alexandroff, V. M. and Pozharskii, D. A.: 2001, *Three-Dimensional Contact Problems*, Kluwer Academic Publishers, Dordrecht, The Netherlands.
- Ananthakrishnan, S., Teders, R. and Alder, K.: 1996, Role of estimation in real-time contact dynamics enhancement of space station engineering facility, *IEEE Robotics & Automation Magazine* pp. 20–28.
- Armstrong, B.: 1991, *Control machine friction*, Kluwer Academic.
- Armstrong-Helouvry, B., Dupont, P. and Canudas de Wit, C.: 1994, A survey of models, analysis tools and compensation methods for the control of machines with friction, *Automatica* **30**(7), 1083–1138.

- Avitzur, B., Huang, C. K. and Zhu, Y. D.: 1984, A friction model based on the upper-bound approach to the ridge and sublayer deformation, *Wear* **95**, 59–77.
- Bailey, A. R. and Sayles, R. S.: 1991, Effect of roughness and sliding friction on contact stresses, *ASME Journal of Tribology* **113**(3), 729–738.
- Barber, J. R.: 1992, *Elasticity*, Kluwer Academic Publishers, Dordrecht, The Netherlands.
- Battle, J. A.: 1993, On Newton's and Poisson's rules of percussive dynamics, *Transactions of the ASME Journal of Applied Mechanics* **60**, 376–381.
- Bell, R. and Burdekin, M.: 1969, An investigation into the mechanism of frictional damping of machine tools slideways, *Proceedings of the Institute of Mechanical Engineers, Applied Mechanics Group* **184**(59), 1088–1096.
- Bennewitz, R.: 2007, Friction force microscopy, in E. Gnecco and E. Meyer (eds), *Fundamentals of Friction and Wear on the Nanoscale*, Springer-Verlag, Berlin, pp. 1–14.
- Bowden, F. P. and Tabor, D.: 1939, The area of contact between stationary and moving surfaces, *Proceedings of the Royal Society, Series A* **169**, 391–413.
- Brogliato, B.: 1996, *Nonsmooth impact mechanics*, Springer, London.
- Cameron, S.: 1997, Enhancing GJK: Computing minimum penetration distances between convex polyhedra, *Proceedings International conference on Robotics and Automation*, IEEE.
- Canudas de Wit, C., Olson, H., Astrom, K. J. and Lischinsky, P.: 1995, A new model for control of systems with friction, *IEEE Transaction on Automatic Control* **40**(3), 419–425.
- Chang, W. R., Etsion, I. and Bogy, D. B.: 1987, An elastic-plastic model for the contact of rough surfaces, *ASME Journal of Tribology* **109**(1), 257–263.
- Chang, W. R. and Ling, F. F.: 1992, Normal impact model on rough surfaces, *ASME Journal of Tribology* **114**(2), 439–447.
- Contensou, P.: 1963, Couplage entre frottement de glissement et frottement de pivotement dans la théorie de la toupie, in H. Ziegler (ed.), *Kreiselp Probleme und Gyrodynamics*, IUTAM Symposium Celerina, 1962, Springer-Verlag, Berlin, pp. 201–216.
- Dahl, P. R.: 1968, A solid friction model, *Technical Report TOR-158*, The Aerospace Corporation.
- de Carufel, J., Touzin, S. and Bergeron, C.: 2000, CDMLib reference manual, *Technical report*, Canadian Space Agency.

- Doyon, M., Martin, E., Gonthier, Y., Lange, C., L'Archevêque, R., Bedziouk, S. and Piedboeuf, J.-C.: 2004, On orbit real-time simulation of the ISS mobile servicing system, *Proceedings of the International Astronautical Congress*, Vancouver, Canada. IAC-04-IAA.A.5.03.
- Dupuis, E., Ouellet, A., Doyon, M., Aghili, F. and Piedbœuf, J.-C.: 1998, Control system prototyping for the STVF manipulator testbed, *Proceedings of the First IFAC Workshop on Space Robotics*.
- Eberhard, P.: 1999, Collision detection and contact approaches for a hybrid multibody system / finite element simulation, in F. Pfeiffer and C. Glocker (eds), *Symposium on Unilateral Multibody Contacts*, Vol. 72 of *Solid Mechanics and its Applications*, IUTAM, Kluwer Academic Publishers, pp. 193–203.
- Fischer-Cripps, A. C.: 2000, *Introduction to Contact Mechanics*, Springer-Verlag, New-York.
- Friedl, C.: 1997, *Der Stehaufkreisel*, Master's thesis, Universität Augsburg.
- Gilbert, E. G., Johnson, D. W. and Keerthi, S. S.: 1988, A fast procedure for computing the distance between complex objects in three-dimensional space, *IEEE Journal of Robotics and Automation* **4**(2), 193–203.
- Gladwell, G. M. L.: 1980, *Contact problems in the classical theory of elasticity*, Sijthoff and Noordhoff International Publishers B.V., Alphen aan de Rijn, The Netherlands.
- Glocker, C.: 2001, *Set-Valued Force Laws — Dynamics of Non-smooth Systems*, Springer, Berlin.
- Glocker, C. and Pfeiffer, F.: 1992, Dynamical systems with unilateral contacts, *Nonlinear Dynamics* **3**, 107–115.
- Goldsmith, W.: 1960, *Impact: The Theory and Physical Behavior of Colliding Solids*, Edward Arnold Ltd., London, U.K.
- Gonthier, Y. and Lange, C.: 2006, MuT Matlab/Simulink/RTW user's guide, *Technical Report CSA-ST-SSA-2006-004*, Canadian Space Agency.
- Gonthier, Y., McPhee, J., Lange, C. and Piedbœuf, J.-C.: 2002, A regularized contact model with asymmetric damping and dwell-time dependent friction, *CSME Forum 2002 SCGM*, Queen's University, Kingston, Ontario.
- Gonthier, Y., McPhee, J., Lange, C. and Piedbœuf, J.-C.: 2004, A regularized contact model with asymmetric damping and dwell-time dependent friction, *Multibody System Dynamics* **11**(3), 209–233.
- Greenwood, J. A. and Williamson, J. B. P.: 1966, Contact of nominally flat surfaces, *Proceeding of the Royal Society, Series A* **295**, 300–319.

- Han, I. and Gilmore, B. J.: 1993, Multi-body impact motion with friction—analysis, simulation, and experimental validation, *ASME Journal of Mechanical Design* **115**, 412–422.
- Hasegawa, S. and Sato, M.: 2004, Real-time rigid body simulation for haptic interactions based on contact volume of polygonal objects, *EUROGRAPHICS* **23**(3), 529–538.
- Heidelberger, B., Teschner, M., Keiser, R., Mueller, M. and Gross, M.: 2004, Consistent penetration depth estimation for deformable collision response, *Proceedings of Vision, Modeling, Visualization VMV'04*, Stanford, USA, pp. 339–346.
- Hertz, H.: 1896, *Miscellaneous Papers by H. Hertz*, Eds. Johns and Schott, London.
- Hess, D. P. and Soom, A.: 1990, Friction at a lubricated line of contact operations at oscillatory sliding velocities, *ASME Journal of Tribology* **112**(1), 147–152.
- Hippmann, G.: 2004, An algorithm for compliant contact between complexly shaped bodies, *Multi-body System Dynamics* **12**(4), 345–362.
- Hotz, G., Kerzmann, A., Lennerz, C., Schmid, R., Schömer, E. and Warken, T.: 1999, Calculation of contact force, *VRST* pp. 180–181.
- Hu, B. and Schiehlen: 2003, Multi-scale simulation for impact systems: From wave propagation to rigid-body motion, *Archive of Applied Mechanics* **72**, 885–898.
- Hunt, K. H. and Crossley, F. R. E.: 1975, Coefficient of restitution interpreted as damping in vibroimpact, *Transactions of the ASME Journal of Applied Mechanics* **42**, 440–445. Series E.
- Jimenez, P., Thomas, F. and Torras, C.: 2001, 3D collision detection: A survey, *Computers & Graphics* **25**(2), 269–285.
- Johnson, K. L.: 1985, *Contact Mechanics*, Cambridge University Press, London.
- Keckskeméthy, A., Lange, C. and Grabner, G.: 2000, Efficient modeling of rigid-body impacts between cylinder end faces using the regularized approach, *Proceedings of the 9th German-Japanese Seminar. Nonlinear Problems in Dynamical Systems — Theory and Applications*, Straelen, Germany.
- Keller, J. B.: 1986, Impact with friction, *ASME Journal of Applied Mechanics* **53**, 1–4.
- Khulief, Y. A. and Shabana, A. A.: 1987, A continuous force model for the impact analysis of flexible multibody systems, *Mechanism and Machine Theory* **22**(3), 213–224.
- Klarbring, A.: 1990, Examples of non-uniqueness and non-existence of solutions to quasistatic contact problems with friction, *Ingenieur-Archiv* **60**, 529–541.

- Kövecses, J., Kovács, L. L. and Stéphan, G.: 2007, Dynamics modelling and stability of robotic systems with discrete-time force control, *Archive of Applied Mechanics (Ingenieur Archiv)* **77**(7), 293–299.
- Krenn, R. and Schäfer, B.: 1999, Limitations of hardware-in-the-loop simulations of space robotics dynamics using industrial robots, in M. Perry (ed.), *Fifth International Symposium on Artificial Intelligence, Robotics & Automation in Space i-SAIRAS 1999*, ESA Publication Division, Noordwijk, The Netherlands, pp. 681–686.
- Lange, C. and Gonthier, Y.: 2003, Contact dynamics toolkit (CDT) contact parameter estimation, *Technical Report CSA-TR-2002-0007*, Canadian Space Agency.
- Lange, C. and Gonthier, Y.: 2006a, Multibody system editor (MSE) user's guide, *Technical Report CSA-ST-SSA-2006-003*, Canadian Space Agency.
- Lange, C. and Gonthier, Y.: 2006b, Multibody Toolbox (MuT) user's guide, *Technical Report CSA-ST-SSA-2006-002*, Canadian Space Agency.
- Lankarani, H.: 1996, Contact/impact dynamics applied to crash analysis, *Proceedings of the NATOI-ASI on Crashworthiness of Transportation Systems: Structural Impact and Occupant Protection*, Vol. 1, Tróia, Portugal, pp. 255–283.
- Lankarani, H. M. and Nikravesh, P. E.: 1988, Application of the canonical equations of motion in problems of constrained multibody systems with intermittent motion, *ASME Design Automation Conference*, ASME, Orlando (Florida). ASME-Paper No. 88-DAC-51.
- Lankarani, H. M. and Nikravesh, P. E.: 1990, A contact force model with hysteresis damping for impact analysis of multibody systems, *ASME Journal of Mechanical Design* **112**, 369–376.
- Lankarani, H. M. and Pereira, M. F. O. S.: 2001, Treatment of impact with friction in planar multibody mechanical systems, *Multibody System Dynamics* **6**(3), 203–227.
- L'Archevêque, R., Doyon, M., Piedbœuf, J.-C. and Gonthier, Y.: 2000, SYMOFROS: Software architecture and real time issues, *DASIA 2000 - Data Systems in Aerospace*, Vol. SP-457, ESA, Montreal, Canada, pp. 41–46.
- Laursen, T. A. and Simo, J. C.: 1993, A continuum-based finite element formulation for the implicit solution of multibody, large deformation frictional contact problems, *International Journal for Numerical Methods in Engineering* **36**, 3451–3485.
- Leine, R. I. and Glocker, C.: 2003, A set-valued force law for spatial Coulomb-Contensou friction, *European Journal of Mechanics* **22**(2), 193–216.
- Lichtenberg, A. and Liebermann, M.: 1992, *Regular and Chaotic Dynamics*, Springer Verlag, New York.

- Lin, M. and Gottschalk, S.: 1998, Collision detection between geometric models: A survey, in R. Cripps (ed.), *The Proceedings of IMA Conference on Mathematics of Surfaces*, University of Birmingham, pp. 37–56.
- Lüder, J.: 2000, *Ein Beitrag zur Modellbildung von reibungsbehafteten Kontakten mit wechselnden Strukturen in Mehrkörpersystemen*, Berichte aus dem Maschinenbau, Shaker Verlag, Aachen.
- Ma, O.: 2000, CDT – a general contact dynamics toolkit, *Proceedings of the 31st International Symposium on Robotics*, Montreal, Canada, pp. 468–473.
- Ma, O., Buhariwala, K., Roger, N., MacLean, J. and Carr, R.: 1997, MDSF- A generic development and simulation facility for flexible, complex robotic systems, *Robotica* **15**, 49–62.
- Majumbar, A. and Bhushan, B.: 1991, Fractal model of elastic-plastic contact between rough surfaces, *ASME Journal of Tribology* **113**(2), 1–11.
- Mann, J. B., Farris, T. N. and Chandrasekar, S.: 1994, Effects of friction on contact of transverse ground surfaces, *ASME Journal of Tribology* **116**(2), 430–437.
- Marhefka, D. W. and Orin, D. E.: 1999, A compliant contact model with nonlinear damping for simulation of robotic systems, *IEEE Transactions on Systems, Man and Cybernetics - Part A: Systems and Humans* **29**(6), 566–572.
- Martin, E., Doyon, M., Gaudreau, D., Gonthier, Y., Lange, C. and Piedbœuf, J.-C.: 2004, On the validation of the STVF facility for ground verification of Dextre tasks, *Proceedings of the International Astronautical Congress*, Vancouver, Canada. IAC-04-T.P.08.
- Millard, M., McPhee, J. and Kubica, E.: 2007, Multi-step forward dynamic gait simulation, *EC-COMAS Multibody Dynamics Conference*, Milano, Italy.
- Mirtich, B.: 1998, Rigid body contact: Collision detection to force computation, Technical Report, TR-98-01, Mitsubishi Electric Research Laboratory.
- Mirtich, B. and Canny, J.: 1995, Impulse-based simulation of rigid bodies, *Proceedings of the 1995 Symposium on Interactive 3D Graphics*, pp. 181–188.
- Nguyen, T., Wang, J., Hwand, J. and Alder, K.: 1991, Force accommodation control of the space shuttle remote manipulator system: A unique problem, *1991 IEEE International Conference on Robotics and Automation*, Sacramento, CA, pp. 2510–2515.
- O'Brien, J. F.: 2000, *Graphical Modeling and Animation of Fracture*, PhD thesis, Georgia Institute of Technology.
- Pfeiffer, F. and Glocker, C.: 1996, *Multibody dynamics with unilateral contacts*, Wiley, New York.

- Piedbœuf, J.-C.: 1995, SYMOFROS: Symbolic modelling of flexible robots and simulation, *Proceedings of the AAS/AIAA Astrodynamics Conference*, Halifax, Nova-Scotia, Canada, pp. 949–968. Paper AAS 95-359.
- Piedbœuf, J.-C.: 1996, Modelling flexible robots with maple, *Maple Tech: The Maple Technical Newsletter* **3**(1), 38–47.
- Piedbœuf, J.-C., Aghili, F., Doyon, M., Gonthier, Y., Martin, E. and Zhu, W.-H.: 2001, Emulation of space robot through hardware-in-the-loop simulation, *The 6th International Symposium on Artificial Intelligence and Robotics & Automation in Space: i-SAIRAS 2001*, Canadian Space Agency, St-Hubert, Quebec, Canada.
- Piedbœuf, J.-C., de Carufel, J., Aghili, F. and Dupuis, E.: 1999, Task verification facility for the Canadian special purpose dextrous manipulator, *1999 IEEE International Conference on Robotics and Automation*, Detroit, Michigan, pp. 1077–1083.
- Piedbœuf, J.-C., Dupuis, E. and de Carufel, J.: 1998, STVF concept document, *Technical Report CSA-SS-ST-016*, Canadian Space Agency, St-Hubert, Quebec.
- Piedbœuf, J.-C., Dupuis, E., Martin, E., Doyon, M. and Rey, D.: 2000, STVF: SPDM task verification facility, *Proceedings of the 31st International Symposium on Robotics ISR'2000*, Montreal, Canada, pp. 510–515.
- Puso, M. A. and Laursen, T. A.: 2004, A mortar segment-to-segment frictional contact method for large deformations, *Computer Methods in Applied Mechanics and Engineering* **193**, 4891–4913.
- Rabinowicz, E.: 1956, Stick and slip, *Scientific American* **194**(5), 109–118.
- Rebele, B., Schaefer, B., Albu-Schaeffer, A., Bertleff, W. and Landzettel, K.: 2006, Robotic joints and contact dynamics experiments: Lessons learned from ROKVISS, *9th ESA Workshop on Advanced Space Technologies for Robotics and Automation*, ESTEC, Noordwijk, the Netherlands, pp. 33–40.
- Rigney, D. A. and Hirth, J. P.: 1979, Plastic deformation and sliding friction on contact stresses, *Wear* **53**, 345–370.
- Rotgé, J.-F.: 1997, *L'Arithmétique des Formes: une introduction à la logique de l'espace*, PhD thesis, Université de Montréal.
- Rotgé, J.-F. and Farret, J.: 2007, Universal solid 3D format for high performance urban simulation, *Urban Remote Sensing Joint Event*, Proceedings of the IEEE, Paris, France, pp. 1–10.
- Sharf, I., Gilardi, G. and Crawford, C.: 2002, Identification of friction coefficient for constrained robotic tasks, *Transactions ASME Journal Dynamic Systems, Measurement, and Control* **124**(4), 529–538.

- Sharf, I. and Nahon, M.: 1995, Interference distance calculation for two objects bounded by quadratic surfaces, *Proceedings of the 1995 ASME Design Engineering Technical Conferences*, Vol. DE-Vol.82, Volume 1, pp. 634–641.
- Sharf, I. and Zhang, Y.: 2006, A contact force solution for non-colliding contact dynamics simulation, *Multibody System Dynamics* **16**(3), 263–290.
- Stieber, M., Sachdev, S. and Lymer, J.: 2000, Robotics architecture of the mobile servicing system for the International Space Station, *Proceeding of the 31st International Symposium on Robotics (ISR 2000)*, Canadian Federation of Robotics, Montreal, Quebec, pp. 416–421.
- Stoianovici, D. and Hurmuzlu, Y.: 1996, A critical study of the applicability of rigid-body collision theory, *ASME Journal of Applied Mechanics* **63**, 307–316.
- Stronge, W. J.: 2000, *Impact Mechanics*, Cambridge University Press.
- Szabó, I.: 1987, *Einführung in die Technische Mechanik, Wissenschaft und Kultur*, Vol. 32, Birkhäuser Verlag, Basel, Boston, Stuttgart.
- Tenaglia, C. A., Orin, D. E., LaFarge, R. A. and Lewis, C.: 1999, Toward development of generalized contact algorithm for polyhedral objects, *Proceedings of the 1999 IEEE International Conference on Robotics & Automation*, IEEE, pp. 2887–2892.
- Timoshenko, S. P. and Goodier, J. N.: 1970, *Theory of Elasticity*, McGraw-Hill, New-York.
- Van Den Bergen, G.: 1999, A fast and robust GJK implementation for collision detection of convex objects, *Journal of Graphics Tools* **4**(2), 7–25.
- Van Den Bergen, G.: 2001, Proximity queries and penetration depth computation on 3D game objects, *Proceedings of the 2001 Game Developers Conference*.
- Vielsack, P.: 1996, Regularisierung des Haftzustandes bei Coulombscher Reibung, *Zeitschrift für angewandte Mathematik und Mechanik* **8**(76), 439–446.
- Wang, J., Mukherji, R., Ficocelli, M., Ogilvie, A. and Rice, C.: 2006, Contact dynamics simulations for robotic servicing of hubble space telescope, in P. Motaghedi (ed.), *Proceedings of SPIE*, Vol. 622106 of *Modeling, Simulation, and Verification of Space-based System III*.
- Wang, Y. and Mason, M. T.: 1992, Two-dimensional rigid-body collisions with friction, *ASME Journal of Applied Mechanics* **59**(3), 635–642.
- Whittaker, E. T.: 1937, *Analytical Dynamics*, 4th edn, Cambridge University Press, London.
- Zhang, Y. and Sharf, I.: 2004, Compliant force modeling for impact analysis, *Proceedings of DETC'04, 2004 ASME Design Engineering Technical Conference*, Salt Lake City, Utah, USA.

- Zhu, W.-H., Piedbœuf, J.-C. and Gonthier, Y.: 2002, Emulation of a space robot using a hydraulic manipulator on ground, *IEEE 2002 International Conference on Robotics and Automation*, Washington, DC, pp. 2315 – 2320.
- Zhuravlev, V. P. and Klimov, D. M.: 2005, The model of dry friction in the problem of the rolling of rigid bodies, *Mechanics of solids* **40**(6), 117–127.

Appendix A

Contact Model Implementation Architecture

This section presents an object-oriented framework written in C++ that facilitates the creation of contact models based on compliance. The framework was used to implement a contact dynamics simulation toolbox and is part of the MuT software package described in Appendix B. The framework provides a standardized structure to implement the components of a contact model, such that they can be easily combined to create specialized contact models. The framework includes interface utilities that facilitates the integration of the contact models into a numeric simulation environment. In particular, a standard C-code interface function for the Simulink simulation environment from The MathWorks, Inc. was implemented. The framework also includes utilities to automatically compute all model input quantities and map the model force outputs to the respective body frames. This feature allows the user to focus on the specific details of the contact model being implemented without having to consider how the contact model will be integrated in a numerical multibody simulation environment.

A.1 Contact Model Components

In the proposed framework, the contact models are created by adding the contact model components to a standard contact model container class. The components of the contact model are: the geometric-pair component and the force model component(s). Each component is designed as a stand-alone software object. The geometric-pair component holds all of the information regarding the geometries of the simulated objects, and includes standard methods to query this information. It also provides methods to apply the forces and torques computed by the force model components to the objects. The force model components fall into two categories: the normal contact models and the friction models. These latter components contain the implementation of the contact models described in this thesis.

All contact model component are defined with a standard interface and, hence, they can be combined in different ways to create a variety of contact models. The user is not restricted to changing the contact model settings or parameters; the contact model itself can be changed. Each contact model includes one geometric-pair component and one or two force model components. Any force model can be used in conjunction with any geometric pair, thus allowing a large variety of contact models to be created. The process of combining the contact model components is straightforward and can be accomplished by writing a few lines pre-processor instructions, as shown in Section A.5.

Each contact model component includes a set of component-specific and user-selected constant parameters, e.g., a sphere radius, a spring stiffness constant. Standardized methods are provided to set and read these values. In addition the force model components can have the following attributes:

- States,
- Internal parameters.

The internal parameters are used to store contact model specific information, e.g., the velocity at the time of impact. This basic set of attributes is sufficient to allow the implementation of a many different contact model components. The model components are explained next.

A.1.1 Geometric-Pair Components

The force model components require specific kinematics information to compute the output of their respective models, e.g., inter-penetration depth or volume, relative tangential velocity. This kinematics information is provided by the geometric-pair components. However, depending on the algorithms implemented by the force model components, the list of kinematics information needed by the force components may change from one model to another. For example, a contact model that includes a tangential friction model will need to have the relative tangential velocity evaluated at each time step, whereas a model that has no friction will not. Hence, the geometric-pair component has a built-in kinematics-task registration system that ensures that the geometric-pair object will always compute the necessary kinematics information.

Upon instantiation of the geometric pair object, each force model registers the list of kinematics tasks it needs. The kinematics task list is divided into two categories: the mandatory and the optional kinematics information. The mandatory kinematics information must be provided by all instances of the geometric-pair components. The list of mandatory kinematics tasks includes the following elements:

- **Boolean collision test:** collision is happening or not.
- **Minimal contact distance and penetration measure** $[x]$: gives a positive value when the colliding bodies are not touching and negative value when there is inter-penetration. This

function is needed when using a solver that tries to detect the exact time at which the contact is initiated (scalar).

- **Contact normal** [\mathbf{n}]: normal of the contact plane pointing from body \mathcal{B}_j toward body \mathcal{B}_i (vector).
- **Point of action** [\mathbf{p}_a]: the location of the point where the contact force-moment pair is applied to each body. The position is given with respect to the inertial ‘world’ frame (vector).
- **Compliance measure** [$|x|^p$ or V]: a value that is a function of the geometries and to which the normal contact force is directly proportional (scalar).
- **Compliance measure tolerance**: needed if force model algorithm implementation requires a test to zero (scalar: zero by default).
- **Inter-penetration volume inertia tensor** [\mathbf{J}_v]: needed for volume-based contact models only (matrix: zero by default).

All vectorial quantities should be resolved in the inertial ‘world’ frame. The optional kinematics information list includes:

- Magnitude of the relative velocity in the direction of the contact plane normal (scalar).
- Relative velocity normal to contact plane (vector).
- Relative velocity tangential to the contact plane (vector).
- Magnitude of the relative angular velocity in the direction of the contact plane normal (scalar).
- Relative angular velocity normal to contact plane (vector).
- Relative angular velocity tangential to the contact plane (vector).

The force components use the kinematics information provided by the geometric-pair components to calculate their respective force and/or moments contributions. However, the force models do not have access to any other geometric information regarding the objects in contact. Hence, to apply the resulting force and/or moments computed by the force model, the geometric-pair component includes the `applyForce()` and `applyMoment()` utility functions that correctly apply a force and moment of equal magnitude and opposite direction to the objects and maps these to their respective body frames.

In the presented framework, the geometric-pair component itself can be composed of a combination of many sub-geometric-pairs, as long as all the required kinematics information are properly computed. This will lead to situations where there are multiple contact sites for a same geometric-pair component. However, separate contact models must be set up for each contact sites. Hence, the total number of states and internal parameters will increase accordingly since each contact model

must have its own states and internal parameters. To this end, the function call `getNumPairs()` is provided to allow the contact model container class to properly set its total number of states and internal parameters.

A.1.2 Force Components

The force model components contain the implementation of normal contact and friction models, e.g., the models presented in Chapters 3 and 4. Each force model component has a utility function `setKinematicTasks()` that returns the flags indicating the additional kinematics information needed for the implemented model. The force components also provide additional information with the `getNumStates()` and `getNumInternalParam()` functions that return the number of states and number of internal parameters used by each model implementation, respectively. This information is needed by the contact model container class to correctly initialize and assign the parameters and states corresponding to each force model.

`computeForce()` is main function of the force model components. For the normal contact models, this function returns the normal contact force magnitude. For the friction model components, the normal contact force is provided as an additional parameter. A function to compute the states derivative must be defined if the model has states. The force components also have methods to reset the model states.

A.1.3 Contact Model Container

The contact model container classes serve as general-purpose utilities to “assemble” the contact model components and provide a single-point interface to the numerical simulation environment. There are two types of containers: the frictionless contact models and the frictional contact models. The implementation of the two is identical, except that the frictional contact model implementation includes additional steps to process the friction model.

The contact model container automatically manages the internal parameters of the contact model and the state arrays from the simulation environment. The components are only given access to their respective states and internal parameters. Hence, the implementation of the force models is not affected by the number of states and parameters of the other force models in the contact model. Consequently, the user does not need to worry about the other contact model components when implementing a new contact model component, i.e., the components can be assembled in any combination.

Furthermore, the framework allows for geometric-pair components to be composed of multiple sub-geometric-pairs. This situation occurs when dealing with colliding bodies composed of multiple sub-parts (as in complex LLG models). The contact model algorithms (with and without friction) adapt themselves to the number of pairs involved and automatically update the number of states and adapt the state-array indexing scheme to automatically assign the states to their corre-

sponding contact model. As a result, the contact model is able to process the multiple contact site interactions that may be occurring between two complexly-shaped bodies.

The implementation of the normal contact and friction models was covered in the main body of the thesis. The next section presents the equations for a few simple geometric-pair models.

A.2 Geometric-Pair Models for the Point Contact Model

This section presents the equations for the implementation of geometric-pairs for simple geometries. The equations assume a point contact scenario and are therefore suitable for the force models presented in Chapter 3. The compliance measure of the four geometric-pair models presented in this section is given as $|x|^{3/2}$, and the boolean collision test simply verifies the condition $x < 0$ to detect a collision. The minimal distance and penetration measure is also given by x . The sections for the implementation of each geometric-pair will thus present how x , \mathbf{n} and \mathbf{p}_a are calculated.

A.2.1 Sphere-Plane

The sphere-plane pair was used in Chapter 3 to introduce the notion of the point of action of the contact force. The sphere-plane pair model assumes the sphere is attached to the frame \mathcal{K}_i of body \mathcal{B}_i and the plane is attached to the frame \mathcal{K}_j of body \mathcal{B}_j . The geometric parameters are defined as follows: the sphere radius R and its position \mathbf{p}_{sph} relative to the origin of \mathcal{K}_i , and the plane normal \mathbf{n} and its height h_j along \mathbf{n} with respect to \mathcal{K}_j ; see Figure A.1. The one-dimensional vector $P_{\text{sphere-plane}}$ specifying the constant geometric parameters of the sphere-plane geometric-pair is ordered as follows:

$$P_{\text{sphere-plane}} = [R, [\mathbf{p}_{\text{sph}}]_i^T, [\mathbf{n}]_j^T, h_j], \quad (\text{A.1})$$

where the subscripts i and j indicate the frame in which the components of the vector are resolved in. The point of action location with respect to \mathcal{K}_w is given by \mathbf{p}_a as

$$\mathbf{p}_a = \mathbf{r}_i + \mathbf{p}_{\text{sph}} - R \mathbf{n}. \quad (\text{A.2})$$

The height x of the point of action with respect to the plane is given by

$$x = (\mathbf{p}_a - \mathbf{r}_j) \cdot \mathbf{n} - h_j, \quad (\text{A.3})$$

which is the expression for the penetration depth needed to evaluate the compliance measure given in Equation (2.1). This same expression can be used to detect contact, i.e., when $x \leq 0$, so a separate collision detection algorithm is not needed for this case.

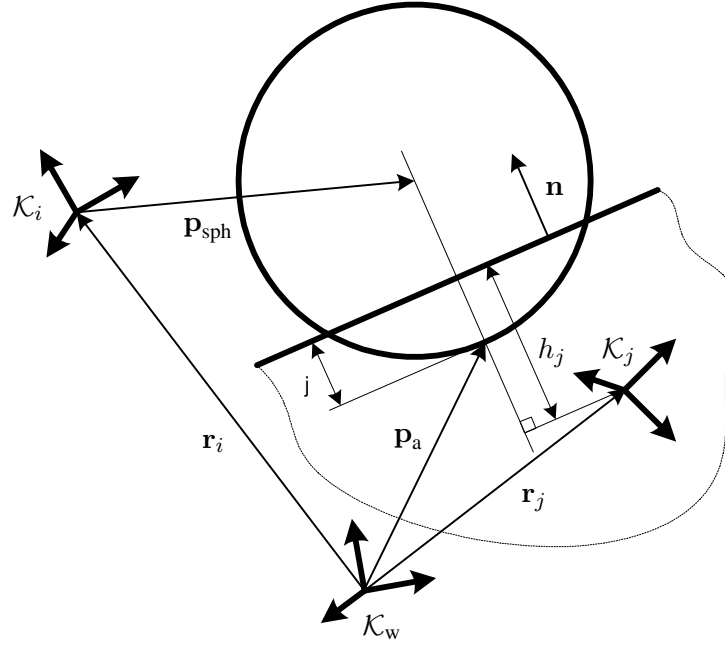


Figure A.1: Schematic diagram for the sphere-plane pair.

A.2.2 Sphere-Edge

A geometric model for the sphere-edge pair was also implemented. The edge is defined as the intersection of two infinite planes. Since this does not constitute a smooth surface, the Hertz theory is not applicable. However, depending on the simulation fidelity requirements, this contact model may be suitable as an approximation. The proposed implementation guarantees a smooth change in contact normal direction as the sphere moves over the edge. Figure A.2 illustrates the sphere-edge pair and a few vectors which will be defined next.

As in the preceding section, the sphere geometry is defined by its radius R and the location of its centre \mathbf{p}_{sph} relative to \mathcal{K}_i . The edge is defined by a point located somewhere along the intersection of the two planes. The position of this point is specified relative to \mathcal{K}_j by \mathbf{p}_{edge} . The planes are labelled 1 and 2, and their respective normals are \mathbf{n}_1 and \mathbf{n}_2 . The one-dimensional vector $P_{\text{sphere-edge}}$ specifying the constant geometric parameters of the sphere-edge geometric-pair is ordered as follows:

$$P_{\text{sphere-edge}} = [R, [\mathbf{p}_{\text{sph}}]_i^T, [\mathbf{p}_{\text{edge}}]_j^T, [\mathbf{n}_1]_j^T, [\mathbf{n}_2]_j^T, \epsilon] , \quad (\text{A.4})$$

where ϵ is a numerical tolerance. A typical value for ϵ is 10^{-6} . To obtain the kinematics information for the sphere-edge pair, the problem is divided into distinct cases. For each case a local normal and plane height are computed. Once \mathbf{n} and h_j have been identified, the kinematics information is computed as before using Equations (A.2) and (A.3). In other words, the sphere-edge model is

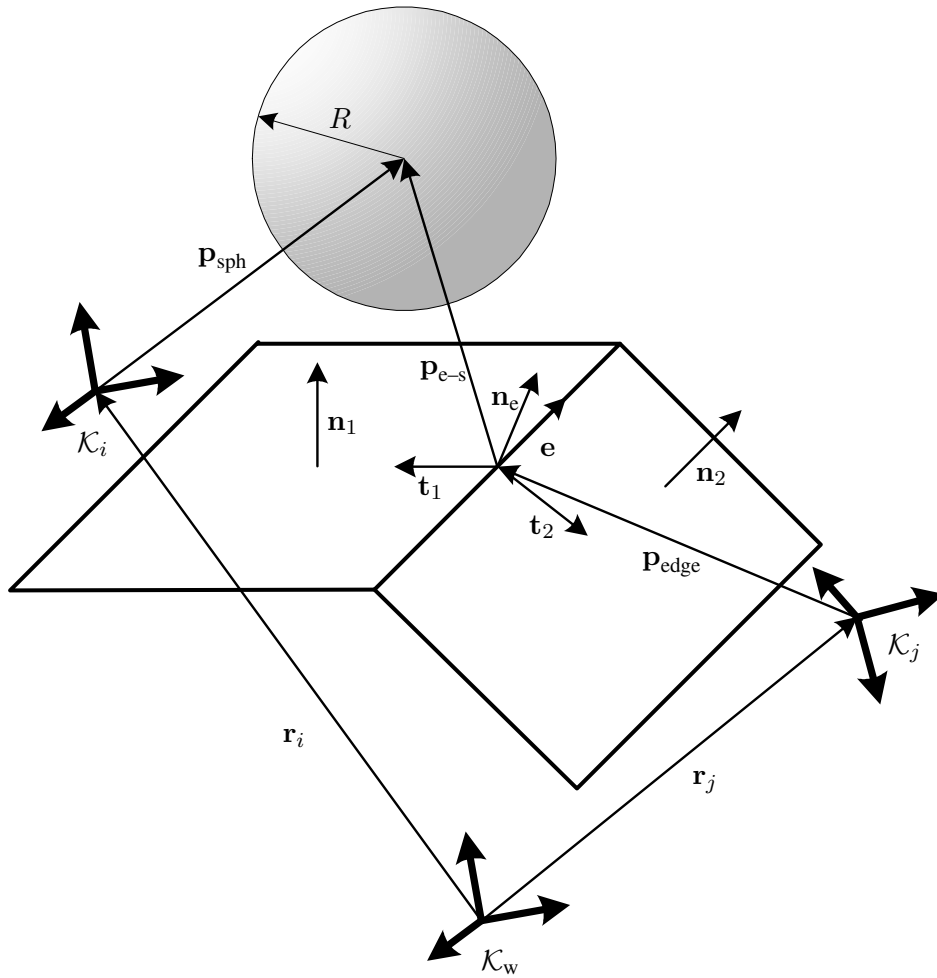


Figure A.2: Schematic diagram for the sphere-edge pair.

“converted” into a local sphere-plane model. The plane heights h_1 and h_2 of the plane 1 and 2 are computed as $h_1 = \mathbf{p}_{\text{edge}} \cdot \mathbf{n}_1$ and $h_2 = \mathbf{p}_{\text{edge}} \cdot \mathbf{n}_2$ respectively. The criteria used to select each case are based on certain quantities which are defined next.

First, the edge normal vector \mathbf{n}_e is defined as

$$\mathbf{n}_e = \frac{\mathbf{n}_1 + \mathbf{n}_2}{|\mathbf{n}_1 + \mathbf{n}_2|}. \quad (\text{A.5})$$

The direction of \mathbf{n}_e is halfway between the directions of \mathbf{n}_1 and \mathbf{n}_2 ; see Figure A.2. Next, the edge direction vector \mathbf{e} is defined as

$$\mathbf{e} = \frac{\mathbf{n}_1 \times \mathbf{n}_2}{|\mathbf{n}_1 \times \mathbf{n}_2|}, \quad (\text{A.6})$$

where it is assumed that \mathbf{n}_1 and \mathbf{n}_2 are not parallel and, hence, the cross-product yields a non-zero

vector. The parallel case can be avoided by checking if $|\mathbf{n}_1 \times \mathbf{n}_2| > \epsilon$. If not, then this implies that the two planes are essentially parallel, and the sphere-edge can be treated simply as a sphere-plane pair with a contact normal \mathbf{n}_e and a plane height $h_e = \mathbf{p}_{\text{edge}} \cdot \mathbf{n}_e$.

When the two planes are at an angle, the plane tangential vectors \mathbf{t}_1 and \mathbf{t}_2 can be defined as

$$\begin{aligned} \mathbf{t}_1 &= \mathbf{n}_1 \times \mathbf{e} \\ \mathbf{t}_2 &= \mathbf{e} \times \mathbf{n}_2 \end{aligned} \quad (\text{A.7})$$

Similarly, the direction vector \mathbf{t}_e tangential to \mathbf{n}_e is given as

$$\mathbf{t}_e = \mathbf{n}_e \times \mathbf{e} . \quad (\text{A.8})$$

The location of the sphere relative to the edge is given by \mathbf{p}_{e-s} as

$$\mathbf{p}_{e-s} = \mathbf{r}_i + \mathbf{p}_{\text{sph}} - \mathbf{r}_j - \mathbf{p}_{\text{edge}} . \quad (\text{A.9})$$

Figure A.3(a) shows cross-section views of the edge with the new vector definitions for an arbitrary position \mathbf{p}_{e-s} of the sphere relative to the edge.

The relative position vector \mathbf{p}_{e-s} is used to decide how the contact normal will be computed. When $\mathbf{p}_{e-s} \cdot \mathbf{n}_1 < 0$ and $\mathbf{p}_{e-s} \cdot \mathbf{n}_2 < 0$, the centre of the sphere is located below the contact surfaces of the edge. This case is illustrated in Figure A.3(b), with the grey area corresponding to the possible locations of \mathbf{p}_{e-s} under the contact surfaces. Here, it is easy to distinguish which contact normal to use: when the centre of the sphere is located to the left of the dashed line, \mathbf{n} should be set to \mathbf{n}_1 and h_j to h_1 , and when the centre of the sphere is to the right of the line, \mathbf{n} should be set to \mathbf{n}_2 and h_j to h_2 . Mathematically, this observation implies that when $\mathbf{p}_{e-s} \cdot \mathbf{t}_e > 0$, $\mathbf{n} = \mathbf{n}_1$ and $h_j = h_1$ or, otherwise, $\mathbf{n} = \mathbf{n}_2$ and $h_j = h_2$.

When the centre of the sphere is above the contact surface, it can be either above one of the two planes, or above the edge. If it is located above plane 1 then $\mathbf{p}_{e-s} \cdot \mathbf{t}_1 > 0$, and \mathbf{n} should be set to \mathbf{n}_1 and $h_j = h_1$. If $\mathbf{p}_{e-s} \cdot \mathbf{t}_2 > 0$, then \mathbf{n} should be set to \mathbf{n}_2 and $h_j = h_2$. These cases are shown in Figure A.3(c).

The case when the sphere is over the edge must be handled carefully. As the sphere moves from being on-top of one plane, say plane 1, and then goes over the edge and finally moves over to plane 2, the contact normal direction must change smoothly from \mathbf{n}_1 to \mathbf{n}_2 . Figure A.3(d) illustrates this situation. To obtain a smooth transition of the contact normal when the sphere is located over the edge, the normal is defined as

$$\mathbf{n} = (\mathbf{I} - \mathbf{E}) \frac{\mathbf{p}_{e-s}}{|\mathbf{p}_{e-s}|} , \quad (\text{A.10})$$

where $\mathbf{E} = \mathbf{e}\mathbf{e}$ is the dyadic operator projecting any vector onto \mathbf{e} . Hence, $(\mathbf{I} - \mathbf{E})$ finds the projection perpendicular to \mathbf{e} . When \mathbf{p}_{e-s} is directly above \mathbf{p}_{edge} in the direction of \mathbf{n}_1 , the definition

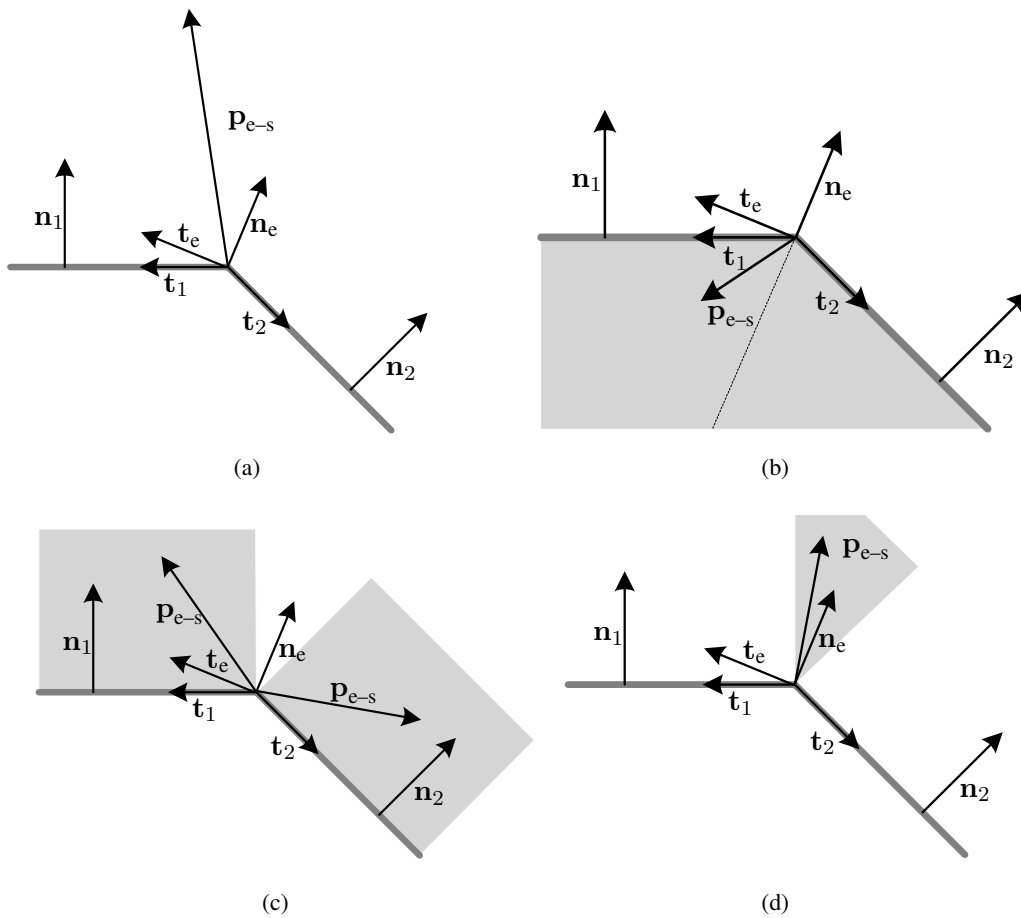


Figure A.3: Sphere-edge pair cross-section.

above yields $\mathbf{n} = \mathbf{n}_1$. The plane height should be set to $h_j = \mathbf{p}_{\text{edge}} \cdot \mathbf{n}$.

However, the proposed definition includes the condition when $|\mathbf{p}_{e-s}|$ is very small or zero, and hence may result in a division by zero. To have a robust implementation, a test is added to verify the magnitude of $|\mathbf{p}_{e-s}|$. If it is smaller than the threshold ϵ , the normal is simply set to \mathbf{n}_e and h_j to h_e . This case corresponds to the condition when the sphere centre is located near and above the edge. It should also be noted that the location of \mathbf{p}_{edge} should be selected near the expected location of contact. If it is very far from the contact site, this will have a detrimental effect on the accuracy of the calculations.

A.2.3 Sphere-Cylinder

The sphere-cylinder geometric-pair was used to implement the ball bouncing on the inside surface of a cylinder in Section 5.1.3. However, the geometric pair implementation can also deal with the

case of the sphere being located on the outside surface of the cylinder. The latter case is obtained by simply specifying a positive value for the radius instead of a negative one.

As in the preceding sections, the sphere geometry is defined by its radius R and the location of its centre \mathbf{p}_{sph} relative to \mathcal{K}_i . The cylinder is described using a point located somewhere along its central axis and a radius r . The position of this point relative to \mathcal{K}_j is specified by \mathbf{p}_{cyl} . The axis direction is given by \mathbf{a} . The one-dimensional vector $P_{\text{sphere-cylinder}}$ specifying the constant geometric parameters of the sphere-cylinder geometric-pair is ordered as follows:

$$P_{\text{sphere-cylinder}} = [R, [\mathbf{p}_{\text{sph}}]_i, [\mathbf{p}_{\text{cyl}}]_j^T, [\mathbf{a}]_j^T, r] . \quad (\text{A.11})$$

To obtain the geometric-pair kinematics information, the following vectors are defined. The position of the sphere relative to the cylinder is $\mathbf{p}_{\text{c-s}}$ and is given as

$$\mathbf{p}_{\text{c-s}} = \mathbf{r}_i + \mathbf{p}_{\text{sph}} - \mathbf{r}_j - \mathbf{p}_{\text{cyl}} . \quad (\text{A.12})$$

The vector $\mathbf{p}_{\text{c-s}}$ can be decomposed into $\mathbf{p}_{\text{c-s,a}}$, the component of $\mathbf{p}_{\text{c-s}}$ parallel to the cylinder axis \mathbf{a} , and $\mathbf{p}_{\text{c-s,p}}$, the component of $\mathbf{p}_{\text{c-s}}$ perpendicular to the cylinder axis \mathbf{a} ; see Figure A.4. The latter is found as follows

$$\mathbf{p}_{\text{c-s,p}} = (\mathbf{I} - \mathbf{A}) \mathbf{p}_{\text{c-s}} , \quad (\text{A.13})$$

where $\mathbf{A} = \mathbf{a}\mathbf{a}$ is the dyadic operator projecting any vector onto \mathbf{a} .

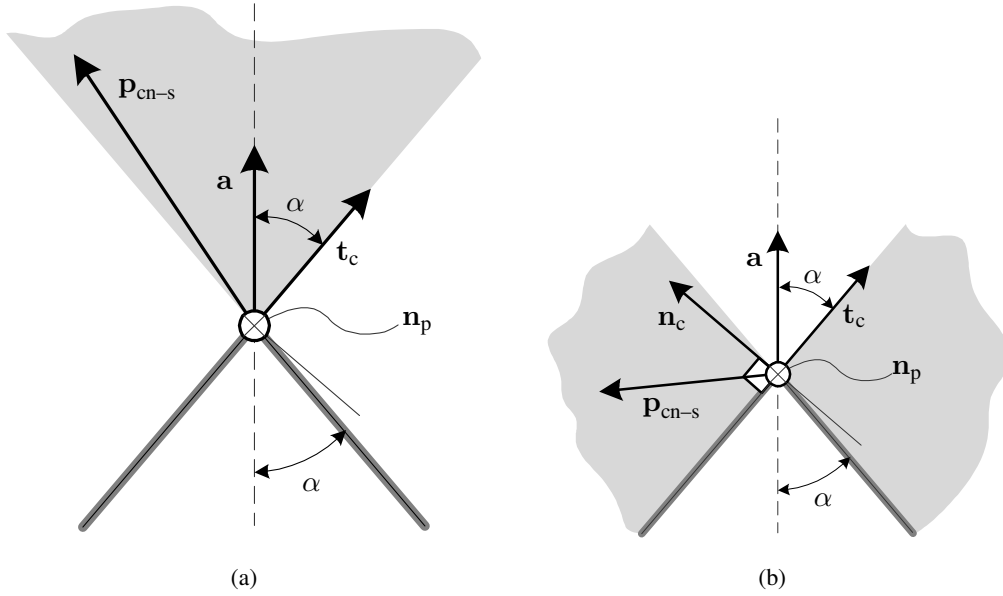
The contact normal is obtained using $\mathbf{p}_{\text{c-s,p}}$ and its direction is selected based on whether the sphere should be impacting the inside surface of the cylinder ($r \leq 0$) or the outside surface of the cylinder ($r > 0$). The contact normal \mathbf{n} is therefore defined as

$$\mathbf{n} = \begin{cases} \frac{\mathbf{p}_{\text{c-s,p}}}{|\mathbf{p}_{\text{c-s,p}}|} , & r > 0 \\ -\frac{\mathbf{p}_{\text{c-s,p}}}{|\mathbf{p}_{\text{c-s,p}}|} , & r \leq 0 \end{cases} . \quad (\text{A.14})$$

Similarly, the penetration depth is also computed differently for the two separate cases

$$x = \begin{cases} |\mathbf{p}_{\text{c-s,p}}| - R - r , & r > 0 \\ -|\mathbf{p}_{\text{c-s,p}}| - R - r , & r \leq 0 \end{cases} . \quad (\text{A.15})$$

The point of action is always located at a distance R from the sphere centre, hence it is determined using Equation (A.2). Note that the case when $|\mathbf{p}_{\text{c-s,p}}| = 0$ is not treated because the direction of the contact normal cannot be found. This corresponds to the centre of the sphere being located on the central axis of the cylinder. Hence, this situation should be avoided in the simulation scenarios.

Figure A.6: Sphere-cone pair cross-section in the $\mathbf{p}_{\text{cn-s}}-\mathbf{a}$ plane.

The vector \mathbf{n}_p is perpendicular to the plane defined by $\mathbf{p}_{\text{cn-s}}$ and \mathbf{a} . The case when $|\mathbf{p}_{\text{cn-s}} \times \mathbf{a}| < \epsilon$ occurs when the sphere centre is located very near the central axis of the cone and above or below its apex. In this case, \mathbf{n}_p should not be evaluated. The normal \mathbf{n} is then simply set as \mathbf{a} and the penetration depth is computed as

$$x = \begin{cases} \mathbf{p}_{\text{cn-s}} \cdot \mathbf{a} - R & \mathbf{p}_{\text{cn-s}} \cdot \mathbf{a} > 0 \\ \mathbf{p}_{\text{cn-s}} \cdot \mathbf{a} \sin(\alpha) - R & \mathbf{p}_{\text{cn-s}} \cdot \mathbf{a} \leq 0 \end{cases}, \quad (\text{A.20})$$

where the $\sin(\alpha)$ term has been added for the case where the centre of the sphere is located inside the cylinder. This scaling avoids a discontinuity as the sphere rolls over the tip of the cone from one side to the other. When the sphere is on the side of the cone, its depth is measured in a direction perpendicular to the surface and not along \mathbf{a} .

If the sphere centre does not lie along the central axis of the cone, \mathbf{n}_p can be computed without any possibility of numerical problems, i.e., division by zero. In this case, the cone surface tangential vector \mathbf{t}_c is found using

$$\mathbf{t}_c = \mathbf{R}(\mathbf{n}_p, \alpha) \mathbf{a}, \quad (\text{A.21})$$

where $\mathbf{R}(\mathbf{n}_p, \alpha)$ is a matrix rotating \mathbf{a} about \mathbf{n}_p by α . Hence, the resulting vector \mathbf{t}_c lies in the plane defined by $\mathbf{p}_{\text{cn-s}}$ and \mathbf{a} and is tangential to the cone surface; see Figure A.6. Note that if $\beta = \pi$, then $\alpha = \pi/2$ and the cone surface tangential vector is simply perpendicular to \mathbf{a} , i.e., the cone becomes a plane.

Once the cone surface tangential vector is determined, it is used to distinguish two cases for the evaluation of the contact normal and the penetration depth. When the sphere is on top of the cone, i.e., it is above the apex of the cone, then $\mathbf{p}_{\text{cn-s}} \cdot \mathbf{t}_c > 0$; see Figure A.6(a). The shaded grey area indicates the possible locations for the centre of the sphere. Here, the contact normal corresponds to the direction from the apex of the cone to the centre of the sphere,

$$\mathbf{n} = \begin{cases} \frac{\mathbf{p}_{\text{cn-s}}}{|\mathbf{p}_{\text{cn-s}}|} & , \quad \mathbf{p}_{\text{cn-s}} \cdot \mathbf{a} > 0 \\ -\frac{\mathbf{p}_{\text{cn-s}}}{|\mathbf{p}_{\text{cn-s}}|} & , \quad \mathbf{p}_{\text{cn-s}} \cdot \mathbf{a} \leq 0 \end{cases} , \quad (\text{A.22})$$

where the condition depending on \mathbf{a} has been added to ensure that \mathbf{n} is always pointing out of the cone. The situation where $|\mathbf{p}_{\text{cn-s}}|$ is small or zero has already been considered when treating the condition that $|\mathbf{p}_{\text{cn-s}} \times \mathbf{a}| < \epsilon$. Hence, at this point in the geometric-pair algorithm implementation, $|\mathbf{p}_{\text{cn-s}}|$ has a none negligible magnitude such that the definition for \mathbf{n} above can always be evaluated. The penetration depth is given as

$$x = \mathbf{p}_{\text{cn-s}} \cdot \mathbf{n} - R . \quad (\text{A.23})$$

When the sphere is not located above the tip of the cone, the contact normal is perpendicular to the surface of the cone. Figure A.6(b) shows the possible locations of the centre of the sphere in the shaded grey area. This region satisfies the condition that $\mathbf{p}_{\text{cn-s}} \cdot \mathbf{t}_c \leq 0$. The normal to the cone surface \mathbf{n}_c is obtained using

$$\mathbf{n}_c = \mathbf{t}_c \times \mathbf{n}_p . \quad (\text{A.24})$$

Hence, when $\mathbf{p}_{\text{cn-s}} \cdot \mathbf{t}_c \leq 0$ then $\mathbf{n} = \mathbf{n}_c$ and the penetration depth, in turn, is found using Equation (A.23).

A.3 Volumetric Contact Model

This section presents an implementation of the two-deformable body contact model presented in Chapters 4. In the derivation of this contact model, it was shown the the two deformable body contact model equations were identical to the one deformable body ones, with the exception that the contact stiffness coefficient was interpreted differently. Hence for the implementation, a single stiffness coefficient k_v will be used and it will be left to the user to set this parameter correctly. The definition of the contact normal from the two deformable body model will also be used because it is more general and can readily be implemented without requiring extra geometric information. The tensor \mathbf{J}_s will be approximated by \mathbf{J}_v ; see Section 4.2.1. Finally, the contact model implementation assumes the inter-penetration depth to be small, and therefore that $\mathbf{v}_{\text{sct}} \approx \mathbf{v}_{\text{ct}}$.

A.3.1 LLG Polynomial Geometry Model

The Parallel Geometry Inc. (LLG) polynomial technology is a solid modelling system based on a pure mathematical representation of geometry. With this technology, a cylinder is described exactly as a cylinder, a sphere is exactly a sphere, etc. Polygons are *not* used to model and display geometries, unless their geometry are truly polygonal in nature. A short background on the technology was given in Section 2.3.2.

The LLG models take the form of an ASCII text file written in the functional programming language Scheme. The Scheme .scm files are then processed by the LLG Scheme interpreter and result in .sl files. The latter are referred to as “compiled model files” and contain the result of the execution of the Scheme model file. For example, a Scheme file may contain a program that reproduces a given volumes many time. In the Scheme file, the volume may be described only once, and a recursive loop may be set up to generate its many incarnations. On the other hand, the corresponding .sl file will contain the data for each of the volume instances. Hence, the .sl file contains an explicit description of the object geometries.

A.3.2 Geometric and Collision Metric Functions

The suite of collision detection and collision metrics functions developed by LLG for the CSA take as input the .sl file. The Matlab function script `MuT_createCollisionObject()` processes the .scm file to create the .sl file. This function also obtains the number of cells in the polynomial geometry and computes the volume metrics for the entire geometry, i.e., the total volume and the corresponding centroid location and moment of inertia tensor. These latter informations are used by the free-floating body block implementation in Simulink to model the motion of the geometry as a single rigid body. The Matlab script `MuT_createCollisionObject()` takes as input the name of the Scheme model file and returns a Matlab structure containing all the relevant information regarding the geometry. Information on how to use this function is provided in the on-line help.

The volumetric information is obtained by decomposing the geometry into voxels, and counting contribution from each voxel toward the total geometry volume, centroid location and inertia tensor. The voxel-decomposition algorithm used by the LLG implementation relies on statistical information of the content of each voxel to do a recursive octree decomposition. The resulting voxel representation is therefore a variable resolution data structure. A voxel size limit is specified to stop the recursive decomposition. This limit is set to 10^{-3} by default, but can be changed. A scaling parameter can also be defined to convert the geometric model reference unit into the unit system used by the user. Its default value is set to 1.

The voxel-decomposition algorithm starts by identifying a box around the volume of interest. In the case of the collision metrics functions, the starting box corresponds to the intersection of the two geometry boxes. The volume is then analyzed and statistical information about its content is

obtained. When it is decided that the voxel is of mixed-type, i.e., it is partially inside and partially outside the volume of the geometry, it decomposed into 8 equal voxels.

The voxel-decomposition algorithm is also capable of handling *concave* shapes. Because it relies on statistical information about the content of the voxel rather than simply looking at the corners of the cube, it can determine that a voxels is of mixed-type even when all corners of the voxel are located inside the volume of the geometry. Hence, a concave shape will force the algorithm to sub-divide the voxels until it finds only voxels located entirely inside the volume of the geometry. The details of the statistical voxel-type determination algorithm is proprietary information to LLG. Another advantage of the statistical approach is that it is also used to estimate how much a voxel is filled by the volume of the geometry. This extra information is taken into account when computing the total volume of the geometry and, hence, the resulting volume is estimated with a much better accuracy then if it was estimated using only the voxels contained inside the volume.

The LLG functions return the moment of inertia of the volume $\mathbf{J}_{v,w}$ of the geometry about the ‘world’ reference frame. Hence, the volume-inertia tensor \mathbf{J}_v with respect to the centroid of the volume is obtained as follows

$$[\mathbf{J}_v]_w = [\mathbf{J}_{v,w}]_w - V \left([\mathbf{p}_c]_w^T [\mathbf{p}_c]_w [\mathbf{I}] - [\mathbf{p}_c]_w [\mathbf{p}_c]_w^T \right), \quad (\text{A.25})$$

where $[\mathbf{I}]$ is the identity matrix and $[\mathbf{p}_c]_w$ is the position of the centroid of the volume relative to the ‘world’ frame and resolved in the ‘world’ frame. The vector $[\mathbf{p}_c]_w$ is computed by the LLG functions. The location of the point of action is simply

$$\mathbf{p}_a = \mathbf{p}_c. \quad (\text{A.26})$$

The LLG functions provide a boolean test function to detect when two geometries are overlapping. A function returning the minimal distance between the geometries when they are *not* colliding was also provided. However, there is no function available that returns an estimate of the inter-penetration depth. It is therefore estimated as $x = -V^{\frac{1}{3}}$. This definition ensures the minimal distance and inter-penetration depth function is a continuous function around the time of collision and crosses zero at the time the contact initially occurs. The Simulink variable step solvers use this function to find the exact time contact is initiated. Fixed-step solver do not try to detect this exact time and hence, the computer implementation is such that only the boolean collision test is called when using the fixed-step solvers. The boolean test is much faster than the minimal distance test. Finally, the volumetric contact model also needs to get an estimate for the contact surface normal \mathbf{n} . This is covered in the next section.

A.3.3 Contact Normal

The contact surface normal \mathbf{n} is found using the inverse iteration method (IIM). This algorithm takes as input an estimate of the eigenvector direction and iterates toward the closest eigenvector. The convergence of the iterations using this algorithm is much faster than with the power iteration method. It also guarantees that the algorithm will converge to the eigenvector closest to the estimate. The implementation of the IIM can be made even more efficient here because the matrix for which the eigenvector is sought is a 3x3 positive-definite symmetric matrix. A simple closed-form solution for the inverse of such a matrix exists. For a 3x3 symmetric matrix \mathbf{A} is given as

$$\mathbf{A} = \begin{bmatrix} a_{11} & a_{12} & a_{13} \\ a_{12} & a_{22} & a_{23} \\ a_{13} & a_{23} & a_{33} \end{bmatrix}, \quad (\text{A.27})$$

the inverse of \mathbf{A} is

$$\mathbf{A}^{-1} = \frac{1}{\text{denom}} \begin{bmatrix} a_{22}a_{33} - a_{23}^2 & -a_{12}a_{33} + a_{13}a_{23} & a_{12}a_{23} - a_{13}a_{22} \\ -a_{12}a_{33} + a_{13}a_{23} & -a_{13}^2 + a_{11}a_{33} & -a_{11}a_{23} + a_{13}a_{12} \\ a_{12}a_{23} - a_{13}a_{22} & -a_{11}a_{23} + a_{13}a_{12} & -a_{12}^2 + a_{11}a_{22} \end{bmatrix}, \quad (\text{A.28})$$

where

$$\text{denom} = 2 a_{13}a_{12}a_{23} - a_{13}^2a_{22} - a_{12}^2a_{33} + a_{11}a_{22}a_{33} - a_{11}a_{23}^2. \quad (\text{A.29})$$

The IIM implementation stops iterating toward the eigenvector when the maximum number of iteration n_i has been reached, or when the following condition is met

$$\mathbf{n}_{\text{est}}(n) \cdot \mathbf{n}_{\text{est}}(n-1) > 1 - \frac{\theta_\epsilon^2}{2}, \quad (\text{A.30})$$

or, in other words, when the angle between the current eigenvector estimate $\mathbf{n}_{\text{est}}(n)$ and the previous one $\mathbf{n}_{\text{est}}(n-1)$ is less than θ_ϵ , and θ_ϵ is a small angle tolerance. Note that because θ_ϵ is small, its cosine is $1 - \theta_\epsilon^2/2$.

The IIM starts from an initial guess of the eigenvector and iterates toward the closest eigenvector. This initial guess $\mathbf{n}_{\text{guess}}$ is given as a combination of a geometric estimate \mathbf{n}_{geo} of the contact normal and of the eigenvector found in the previous time step \mathbf{n}_{prev} . The LLG algorithm generating this geometric estimate guarantees the vector will always point from \mathcal{B}_j toward \mathcal{B}_i . The contact surface normal guess is generated using

$$\mathbf{n}_{\text{guess}} = (1 - r_n) \mathbf{n}_{\text{geo}} + r_n \mathbf{n}_{\text{prev}}, \quad (\text{A.31})$$

where r_n is a ratio that controls how much of the eigenvector found in the previous time-step

should be used to generate the eigenvector starting guess. This feature was added to help the contact normal change smoothly over time. At the first point in time where the contact is detected, the guess is simply set to $\mathbf{n}_{\text{guess}} = \mathbf{n}_{\text{geo}}$.

A.4 Complex Geometries

A contact model designed to deal with more complex geometries was also implemented. The complex polynomial geometries are characterized by the fact that there are made of multiple cells. Each cell corresponds to the intersection of projective polynomial primitives or is simply a single projective polynomial primitive, e.g., a sphere geometry has only one cell in the LLG system. The number of cells of a given geometry can be obtained when the Scheme model file is compiled.

The contact model capable of handling these cellular object is called the *cellular* contact model. Here, the collision metrics are obtained for each colliding cell-pair of the objects and not in terms of the overall object interaction. In other words, separate contact models are *assigned* to each cell-pair in collision. These will be referred hereafter as contact sub-models, but constitute in fact a full-fledged implementation of the volumetric contact model, complete with all of its forces and torques components. Hence, it becomes imperative to keep track of which cells are in collision and to which contact model a cell-pair combination is assigned. This section described the algorithm implemented for this purpose.

Each cell in a LLG model is assigned a unique identifier number (ID). The numbers are assigned from zero to the total number of cells minus 1. Hence, the cell IDs can be used as index to a 2-dimensional matrix matching the index of a contact model to a cell ID-pair. Similarly, when a contact model index is assigned to a specific cell-pair, the ID numbers of these cells can also be stored. As a result, it is possible to know to which contact model a cell-pair is assigned to, and reversely, to which cell-pair a contact model is assigned to. The processing of these indexes is accomplished by the cellular LLG-pair object.

The cellular contact model uses the `getNumPairs()` function of the cellular LLG-pair object to determine the number of contact models needed, and then registers the necessary number of states with the simulation system, e.g., Simulink, and allocates memory for the internal parameters of each contact model. The contact model objects are themselves only aware of the constant parameters of the contact model. Hence, the contact-model-specific information is stored in the cellular contact model container class and not in the contact model itself. As a result, the cellular contact model does not need to be given extra force model components for its implementation, i.e., a frictionless cellular contact model container class only needs 1 normal contact force model component.

To correctly process the contact sub-models assigned to each cell-pair, the cellular contact model relies on cell-pair information lists provided by the cellular LLG-pair object. This object includes additional utilities that store and list the cell-pairs in contact and compare this list to the

previous state of the cellular LLG-pair object. It also keeps track of the contact model indexes, i.e., the number used to reference one of the contact sub-models. The following lists are provided:

- New cell-pairs: the list of cell-pairs in contact during the current time-step, but that were not in contact in the previous time-step.
- Found cell-pairs: the list of cell-pairs currently in contact, but also in contact in the previous time-step.
- Current cell-pairs: the full list of cell-pairs currently in contact.
- Lost cell-pairs: the list of cell-pairs that were in contact during the previous time step, but are no longer in contact.
- De-activated contact indexes: the list of currently unused contact model indexes's.

The cellular LLG-pair object keeps track of which contact model index is assigned to which cell-pair ID. It also keeps track of which contact model indexes are currently used and those that are currently de-activated. The cellular contact model process for each time step is given as follows:

1. Updated the LLG-pair object list information.
2. Parse through the list of lost cell-pairs and reset the contact models.
3. If the objects are not colliding (0 cell-pairs in contact), return, otherwise, go to the next step.
4. Process new contacts: parse through the list of newly found cell-pairs, assign an available contact model to them, initialize it and calculate and apply the contact forces and moments from the force model(s) to the objects.
5. Process on-going contacts: parse through the list of found cell-pairs, calculate and apply the contact forces and moments from the force model(s) to the objects.

The lost cell-pair list is processed first because this can make a previously used contact model available for a newly discovered cell-pair in contact. The cellular contact model obtains the contact sub-model indexes from the LLG-pair object. All contact model and cell-pair indexes are managed from inside this object and the cellular contact only has to connect the contact model index to the corresponding force model component. A similar process is implemented to process the function computing the contact sub-model state derivatives. The contact model state derivatives are found as follows:

1. Process on-going contacts: parse through the list of current cell-pairs, and compute the state derivatives of each contact model.
2. Parse through the list de-activated contact indexes and reset the contact model state derivatives.

Hence, the cellular contact models simply rely on the volumetric contact model implementation of the single-cell-pair contact model. The management of all indexes is handled by the cellular LLG-pair object and the cellular contact models take care of assigning the proper states and internal parameters to process each contact sub-model. The only difference between the frictional cellular contact model and the frictionless one is that an extra force model needs to be processed. Examples of contact models C-code files are given next.

A.5 Contact Model C-Code Examples

This section presents a few examples of user-created contact models. The presented files end with a pre-processor `#include` statement that links-in a standard S-Function file using the defined macros. The user only needs to change the code shown here to create new/different contact models from available contact model components.

Figure A.7 gives an example of the C-code creating a sphere-cone contact model using a normal contact model component that includes numerical constraint relaxation and a bristle friction model component with dwell-time dependency.

```
#define S_FUNCTION_NAME  sfun_cd_sphcne_wrbrdw  // must match the filename

// include and specify geometric pair model
#include "MuT_SphereConePair.hpp"
#define GEO_MODEL_NAME      MuT_SphereConePair
#define NUM_PARAM_GEO      NUM_PARAM_SPHERE_CONE_PAIR

// include and specify normal contact force model
#include "MuT_PointContact_RelaxedHystereticDamping.hpp"
#define CONTACT_MODEL_NAME  MuT_PointContact_RelaxedHystereticDamping
#define NUM_PARAM_CONTACT  NUM_PARAM_POINTCONTACT_RELAXED_HYSTERETIC_DAMPING

// include and specify friction model to be used (comment out if no friction)
#include "MuT_PointFriction_BristleModelWithDwellTime.hpp"
#define FRICTION_MODEL_NAME MuT_PointFriction_BristleModelWithDwellTime
#define NUM_PARAM_FRIC     NUM_PARAM_POINTFRICTION_BRISTLE_MODEL_WITH_DWELL_TIME

// total number of continuous states (contact model + friction model)
#define NUM_STATE_CONT NUM_STATE_POINTCONTACT_RELAXED_HYSTERETIC_DAMPING + \
    NUM_STATE_POINTFRICTION_BRISTLE_MODEL_WITH_DWELL_TIME

#include "MuT_cd_model.cpp"
```

Figure A.7: C-code for a frictional sphere-cone contact model.

Next, the C-code for a frictionless sphere-edge contact model is given in Figure A.8. The model uses that same normal contact model as the previous example. Notice that the section concerning the friction model was simply commented out, and that the number of states corresponds to the number of states of the normal contact model.

```

#define S_FUNCTION_NAME  sfun_cd_sphedg_nofric  // must match the filename

// include and specify geometric pair model
#include "MuT_SphereEdgePair.hpp"
#define GEO_MODEL_NAME    MuT_SphereEdgePair
#define NUM_PARAM_GEO    NUM_PARAM_SPHERE_EDGE_PAIR

// include and specify normal contact force model
#include "MuT_PointContact_HystereticDamping.hpp"
#define CONTACT_MODEL_NAME MuT_PointContact_HystereticDamping
#define NUM_PARAM_CONTACT NUM_PARAM_POINTCONTACT_HYSTERETIC_DAMPING

// include and specify friction model to be used (comment out if no friction)
// #include "MuT_BristleModelWithDwellTime.hpp"
// #define FRICTION_MODEL_NAME MuT_PointFriction_BristleModelWithDwellTime
// #define NUM_PARAM_FRIC      NUM_PARAM_POINTFRICTION_BRISTLE_MODEL_WITH_DWELL_TIME

// total number of continuous states (contact model + friction model)
#define NUM_STATE_CONT    NUM_STATE_POINTCONTACT_HYSTERETIC_DAMPING

#include "MuT_cd_model.cpp"

```

Figure A.8: C-code for a frictionless sphere-edge contact model.

The last C-code example is for an LLG Scheme model. The contact model includes the volumetric version of the normal contact model with numerical constraint relaxation and the volumetric friction model. The standard S-Function file `MuT_cd_model.cpp` was modified for the LLG Scheme model to allow the model to be described by file names instead of being characterized by an array of numerical parameters. It has been replaced by the `MuT_cd_sgdl_model.cpp` file. Figure A.9 shows the corresponding C-code.

```

#define S_FUNCTION_NAME  sfun_cd_sgdl_wrbrdw  // must match the filename

// include and specify normal contact force model
#include "MuT_VolumetricContact_RelaxedHystereticDamping.hpp"
#define CONTACT_MODEL_NAME MuT_VolumetricContact_RelaxedHystereticDamping
#define NUM_PARAM_CONTACT NUM_PARAM_VOLUMETRICCONTACT_RELAXED_HYSTERETIC_DAMPING

// include and specify friction model to be used (comment out if no friction)
#include "MuT_VolumetricFriction_BristleModelWithDwellTime.hpp"
#define FRICTION_MODEL_NAME MuT_VolumetricFriction_BristleModelWithDwellTime
#define NUM_PARAM_FRIC      NUM_PARAM_VOLUMETRICFRICTION_BRISTLE_MODEL_WITH_DWELL_TIME

// total number of continuous states (contact model + friction model)
#define NUM_STATE_CONT
NUM_STATE_VOLUMETRICCONTACT_RELAXED_HYSTERETIC_DAMPING \\
    + NUM_STATE_VOLUMETRICFRICTION_BRISTLE_MODEL_WITH_DWELL_TIME

#include "MuT_cd_sgdl_model.cpp"

```

Figure A.9: C-code for a frictional LLG-pair contact model.

A.6 Simulink Diagram Example

The results of sphere-cylinder simulation presented in Section 5.1.3 were generated using the Simulink numerical simulation environment from The MathWorks, Inc. The corresponding diagram is given in Figure A.10. The image shows the contact model block “Sphere-Cylinder with Friction” generating contact forces and moments. These are then fed to the “Free-Floating Body Forward Dynamics” block that contains a numeric implementation of Euler’s equations of motion. This block computes the accelerations, velocities and positions resulting from the action of the forces and torques. In turn, the positions and velocities given as input the the contact model, and so forth. A block was also implemented to compute the total system energy. The compressive energy stored in the spring of the contact model is obtained by numerically integrating the compressive power $P = -f_k v_n$ over time.

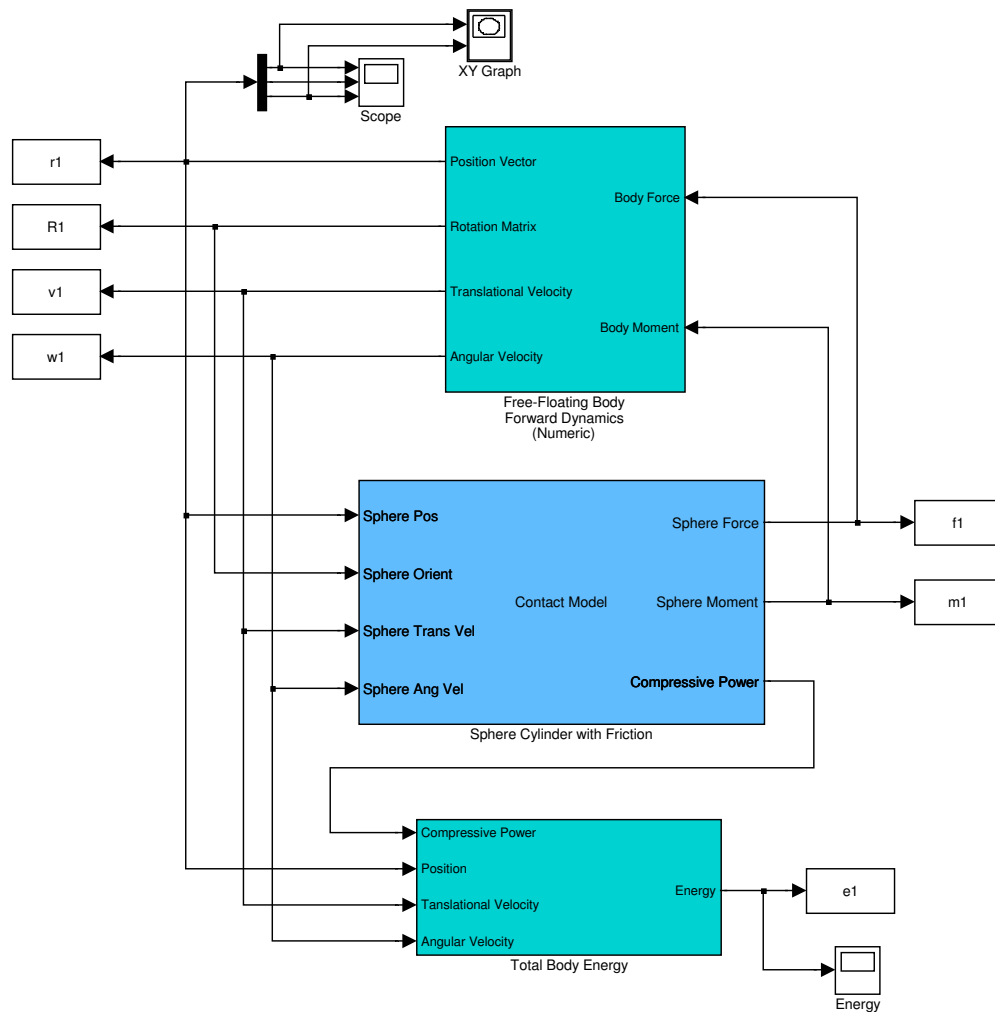


Figure A.10: Simulink diagram for the ball-cylinder simulation using the point contact model.

Appendix B

The Multibody Toolbox (MuT)

This appendix gives a high-level overview of the Multibody toolbox (MuT) and its implementation philosophy. The MuT is a non-commercial software package developed by the Robotics Section at the CSA to support internal projects. The reader is referred to the MuT documentation for a more detailed description (Lange and Gonthier, 2006a,b; Gonthier and Lange, 2006).

B.1 Executive Summary

- MuT is a set of tools that, if used sequentially, provide symbolic and numeric multibody systems modelling capabilities to generate customizable sets of model functions, and the exporting of these functions to NRT and RT execution environment, e.g. for real-time model-based control or simulation.
- MuT was designed to be easy to integrate with other multibody software packages through clearly defined interfaces. These interfaces allow MuT to take advantage of the specific tool within each external software package.
- MuT is based on state-of-the-art software engineering principles and incorporates advanced modelling and simulation techniques.

B.2 Description

The Multibody Toolbox (MuT) is a framework allowing the integration of different multibody software packages under a common environment, to generate software solutions to tackle real-life engineering problems, and to seamlessly port these solutions into a real-time operating environment (with focus on space robotics). This framework permits the leveraging of the expertise embedded within different software packages, thus reducing the need to "re-invent the wheel" each time a new feature is required.

The MuT framework is a combination of the Maple symbolic processing environment for modelling the multibody system, and the Matlab/Simulink/Real-Time Workshop (RTW) for the execution environment. The MuT concept is to characterize the multibody model behaviour by defining a number of model functions, e.g., the mass matrix of the system. These are obtained symbolically in the Maple environment and are then ported into the execution environment in the form of automatically generated C-code functions which can be queried either from the Matlab command prompt or placed in the Simulink simulation environment, and are designed to be compatible with the RTW, such that stand alone executable can be created automatically.

In the MuT frameworks no assumptions are made about which model functions were selected by the user to be generated and exported to the execution environment. It is the responsibility of the user to select or set-up these functions. MuT provides a flexible and open infrastructure that makes it easy to select and include into a common modelling framework all model functions, whether these are generated using the built-in symbolic modelling environment or from any external modelling software package. By design, MuT has clearly defined access points that allow externally obtained model functions to be inserted into the MuT framework, such that creating interfaces to external software packages is a simple and straightforward process. In effect, the MuT framework does not distinguish from where or how the model functions were obtained, i.e. there are no special cases.

Furthermore, since Maple allows the multibody models to be processed symbolically or numerically, it provides the versatility of creating symbolic or numeric model function, and MuT takes advantage of this additional flexibility. Hence, each MuT model can have different model functions associated with it in the execution environment, these model function can correspond to a symbolically derived modelling process or a numerical one, and these different model functions can come from different sources, i.e. not exclusively from the MuT symbolic modelling environment.

The MuT exporting process is scalable, transparent and requires no special knowledge on the part of the user, except knowing how to use Maple, and a basic-level understanding of multibody dynamics if modelling a multibody system. It was designed to allow model functions to be easily and automatically exported right up to the real-time execution environment. The framework relies on a simple process to export the model functions, and uses only standard Matlab/Simulink/RTW utilities to do so, such that compatibility with forthcoming releases of Matlab/Simulink/RTW is maximized. The framework architecture is presented in the next section.

B.3 Framework

The Multibody Toolbox Framework:

- Facilitates the creation of new formulations (analytical, numerical or hybrid) by providing topology management, a convenient model interface and basic kinematic and kinetostatic toolboxes for any given model.

- Features an object-oriented architecture that simplifies integration of new modelling components (based on standard component templates), functions (e.g., identification (kinematics, dynamics), CoG, variable mass, sensitivity analysis, parametric studies, optimization), and support implementation of these new functions right up to the RT-OS execution environment.
- Uses a general XML component template that allows new components to be added or modified without changing the existing formulations code, thus simplifying the component integration and validation process.
- Was designed with a modular structure that simplifies code modification and maintenance.
- Was designed to efficiently generate code in C based on simple code-generation templates ensuring maintainability and compatibility with changing versions of execution environment.
- Provides an infrastructure to do benchmark comparisons of different modelling algorithms (efficiency, stability).